Highly sensitive nanoSQUIDs for investigations of magnetic nanoparticles

Dissertation
der Mathematisch-Naturwissenschaftlichen Fakultät
der Eberhard Karls Universität Tübingen
zur Erlangung des Grades eines
Doktors der Naturwissenschaften
(Dr. rer. nat.)

vorgelegt von
Benedikt Müller
aus Tübingen

Tübingen
2020

Gedruckt mit Genehmigung der Mathematisch-Naturwissenschaftlichen Fakultät der Eberhard Karls Universität Tübingen.

Tag der mündl. Qualifikation:	22.05.2020
Dekan:	Prof. Dr. Wolfgang Rosenstiel
1. Berichterstatter:	Prof. Dr. Dieter Kölle
2. Berichterstatter:	Prof. Dr. Reinhold Kleiner

Abstract

Measurements on magnetic nanoparticles (MNPs) are very relevant for research as well as for applications, since they can, on the one hand, contribute to a deeper understanding of nanomagnetism and, on the other hand, lots of technical or clinical applications of MNPs require precise knowledge of their properties. For the characterization of single MNPs, tiny signals have to be detected in huge magnetic background fields, a task that can be achieved by using superconducting quantum interference devices that are miniaturized to the submicron range (nanoSQUIDs).

The first part of this thesis deals with the usage of nanoSQUIDs, based on the high critical temperature superconductor $YBa_2Cu_3O_7$ (YBCO), in magnetization reversal measurements on different MNPs. First, the magnetization reversal of an iron nanowire embedded in a carbon nanotube is investigated. Further measurements are performed on cobalt MNPs that were fabricated by focused electron-beam-induced deposition. For cobalt nanowires, an increase in the cobalt content as well as the saturation magnetization of the wires after thermal annealing is shown. For cobalt particles with radii $\lesssim 100\,\mathrm{nm}$ that are directly grown on the nanoSQUIDs, measurements at temperatures between $0.3\,\mathrm{K}$ and $80\,\mathrm{K}$ verify a thermally assisted reversal of the magnetization, which partly takes place by formation of a magnetic vortex state.

In the second part of this thesis, different studies for the improvement of future nanoSQUIDs are conducted. By simultaneously measuring the magnetiza-

tion reversal of a MNP in all 3 spatial directions, the anisotropic magnetic properties of the MNP can be fully captured. The general feasibility of such measurements using nanoSQUIDs is shown in the characterization of a vector nanoSQUID that is realized by combination of three niobium-based nanoSQUIDs.

However, transferring this approach to YBCO is not possible with the current grain boundary-based Josephson junctions (JJs) of YBCO nanoSQUIDs for topological reasons. Therefore, JJs that can be induced in YBCO by irradiation with a focused helium ion beam are fabricated and characterized in this thesis. The position of such junctions can be defined by the location of irradiation, and adjustments of the electronic properties are possible by choice of the irradiation dose. For irradiation with a sufficiently high dose, superconductivity is suppressed completely, which enables defining the geometry of electronic structures without removal of material.

Furthermore, artificial pinning centers for Abrikosov vortices can be created by local suppression of superconductivity. The focused helium ion beam allows for fabrication of pinning arrays with spacings below 100 nm. The characterization of such ultradense pinning arrays in magnetic fields reveals matching effects at temperatures significantly below the critical temperature, which confirms strong pinning of vortices at the pinning centers. Therefore, such pinning centers could be used to improve the low-frequency flux noise of YBCO nanoSQUIDs in magnetic fields.

Kurzfassung

Messungen an magnetischen Nanopartikeln (MNP) sind sowohl aus wissenschaftlicher Sicht als auch für Anwendungen sehr relevant, da sie zum einen zum tieferen Verständnis des Nanomagnetismus beitragen können und zum anderen für eine Vielzahl von technischen oder medizinischen Anwendungen von MNP die möglichst genaue Kenntnis ihrer Eigenschaften erforderlich ist. Zur Charakterisierung einzelner MNP müssen kleinste Signale in hohen magnetischen Hintergrundfeldern detektiert werden, wofür sich bis in den Submikrometer-Bereich miniaturisierte supraleitende Quanteninterferometer (nanoSQUIDs) eignen.

Der erste Teil dieser Arbeit befasst sich mit dem Einsatz von nanoSQUIDs aus dem Hochtemperatur-Supraleiter $YBa_2Cu_3O_7$ (YBCO) für Messungen der Magnetisierungsumkehr verschiedener MNP. Zuerst wird die Magnetisierungsumkehr eines Eisen-Nanodrahtes, der in ein Kohlenstoff-Nanoröhrchen eingebettet ist, untersucht. Weitere Messungen befassen sich mit MNP aus Kobalt, die mittels fokussierter Elektronenstrahlabscheidung hergestellt wurden. An Kobalt-Nanodrähten wird gezeigt, dass durch thermische Nachbehandlung sowohl der Kobalt-Gehalt als auch die Sättigungsmagnetisierung der Drähte gesteigert werden kann. Für direkt auf nanoSQUIDs abgeschiedene Kobalt-Partikel mit Radien $\lesssim 100\,\mathrm{nm}$ kann durch Messungen bei Temperaturen zwischen $0.3\,\mathrm{K}$ und $80\,\mathrm{K}$ eine thermisch unterstützte Magnetisierungsumkehr nachgewiesen werden, die teilweise auch mittels Bildung eines magnetischen Vortex-Zustandes stattfindet.

Im zweiten Teil der Arbeit werden verschiedene Studien durchgeführt, die zur Verbesserung zukünftiger nanoSQUIDs beitragen sollen. Durch simultane Messung der Magnetisierungsumkehr eines MNP in allen 3 Raumrichtungen können die anisotropen magnetischen Eigenschaften des MNP vollständig erfasst werden. Die prinzipielle Machbarkeit solcher Messungen mittels nanoSQUIDs wird durch die Charakterisierung eines Vektor-nanoSQUIDs gezeigt, das aus einer Kombination von drei aus Niob hergestellten nanoSQUIDs besteht.

Die Umsetzung eines solchen Konzeptes in YBCO ist mit den aktuellen, auf Korngrenzen basierenden Josephsonkontakten (JK) der YBCO nanoSQUIDs jedoch aus topologischen Gründen nicht möglich. Deshalb werden in dieser Arbeit JK, die durch Bestrahlung mit einem fokussierten Helium-Ionenstrahl in YBCO erzeugt werden können, hergestellt und charakterisiert. Die Position solcher Kontakte kann durch den Ort der Bestrahlung bestimmt werden, zudem wird eine Anpassung der elektrischen Eigenschaften durch Wahl der Bestrahlungsdosis ermöglicht. Bei Bestrahlung mit einer hinreichend hohen Dosis wird die Supraleitung vollständig unterdrückt, sodass die Geometrie von elektronischen Strukturen ohne Materialabtrag definiert werden kann.

Außerdem können durch lokale Unterdrückung der Supraleitung künstliche Pinningzentren für Abrikosov-Flusswirbel erzeugt werden. Durch den fokussierten Helium-Ionenstrahl können regelmäßige Gitter aus Pinningzentren mit Abständen unter 100 nm hergestellt werden. Bei der Charakterisierung solcher ultra-dichten Pinninggitter in Magnetfeldern zeigen sich auch bei Tem-

peraturen deutlich unterhalb der kritischen Temperatur Kommensurabilitätseffekte, die das Vorliegen stark gepinnter Flusswirbel an den Pinningzentren belegen. Damit könnten solche Pinningzentren eingesetzt werden, um das niederfrequente Flussrauschen von YBCO nanoSQUIDs in Magnetfeldern zu verbessern.

List of Publications

This is a cumulative thesis based on the 9 publications listed below. Publications 1 to 4 describe magnetometry experiments on single magnetic nanoparticles using $YBa_2Cu_3O_7$ nanoSQUIDs, whereas publications 5 to 8 showcase novel ideas and techniques for the development of future nanoSQUIDs. Publication 9 is a review of the activities described in publications 1 to 3, 5 and 6 as well as further activities using Nb nanoSQUIDs, which are not part of this thesis.

Summaries and descriptions of contributions for all publications can be found in chapter 2. The publications themselves are appended at the very end of this thesis.

nanoSQUID magnetometry of individual magnetic nanoparticles

Publication 1 T. Schwarz, R. Wölbing, C. F. Reiche, **B. Müller**, M. J. Martínez-Pérez, T. Mühl, B. Büchner, R. Kleiner, and D. Koelle
Low-Noise $YBa_2Cu_3O_7$ Nano-SQUIDs for Performing Magnetization-Reversal Measurements on Magnetic Nanoparticles
Phys. Rev. Applied **3**, 044011 (2015)

Publication 2 M. J. Martínez-Pérez, J. Pablo-Navarro, **B. Müller**, R. Kleiner, C. Magén, D. Koelle, J. M. de Teresa, and J. Sesé
NanoSQUID Magnetometry on Individual As-grown and Annealed Co Nanowires at Variable Temperature
Nano Lett. **18**, 7674-7682 (2018)

Publication 3 M. J. Martínez-Pérez, **B. Müller**, D. Schwebius, D. Korinski, R. Kleiner, J. Sesé, and D. Koelle
NanoSQUID magnetometry of individual cobalt nanoparticles grown by focused electron beam induced deposition
Supercond. Sci. Technol. **30**, 024003 (2017)

Publication 4 M. J. Martínez-Pérez, **B. Müller**, J. Lin, L. A. Rodriguez, E. Snoeck, R. Kleiner, J. Sesé, and D. Koelle
Magnetic vortex nucleation and annihilation in bi-stable ultra-small ferromagnetic particles
Nanoscale **12**, 2587-2595 (2020)

Preparatory studies for future nanoSQUIDs

Publication 5 M. J. Martínez-Pérez, D. Gella, **B. Müller**, V. Morosh, R. Wölbing, J. Sesé, O. Kieler, R. Kleiner, and D. Koelle
Three-Axis Vector Nano Superconducting Quantum Interference Device
ACS Nano **10**, 8308-8315 (2016)

Publication 6 **B. Müller**, M. Karrer, F. Limberger, M. Becker, B. Schröppel, C. J. Burkhardt, R. Kleiner, E. Goldobin, and D. Koelle
Josephson Junctions and SQUIDs Created by Focused Helium-Ion-Beam Irradiation of $YBa_2Cu_3O_7$
Phys. Rev. Applied **11**, 044082 (2019)

Publication 7 B. Aichner, **B. Müller**, M. Karrer, V. R. Misko, F. Limberger, K. L. Mletschnig, M. Dosmailov, J. D. Pedarnig, F. Nori, R. Kleiner, D. Koelle, and W. Lang
Ultradense Tailored Vortex Pinning Arrays in Superconducting $YBa_2Cu_3O_{7-\delta}$ *Thin Films Created by Focused He Ion Beam Irradiation for Fluxonics Applications*
ACS Appl. Nano Mater. **2**, 5108-5115 (2019)

Publication 8 B. Aichner, K. L. Mletschnig, **B. Müller**, M. Karrer, M. Dosmailov, J. D. Pedarnig, R. Kleiner, D. Koelle, and W. Lang
Angular magnetic-field dependence of vortex matching in pinning lattices fabricated by focused or masked helium ion beam irradiation of superconducting $YBa_2Cu_3O_{7-\delta}$ thin films
Low Temp. Phys. **46**, 331-337 (2020)

Review article

Publication 9 **B. Müller**, J. Lin, J. Linek, M. Karrer, F. Limberger, L. Koch, E. Goldobin, R. Kleiner, D. Koelle, V. Morosh, T. Weimann, O. F. Kieler, J. Sesé, M. J. Martínez-Pérez
$YBa_2Cu_3O_7$ and Nb NanoSQUIDs for the investigation of Magnetization Reversal of Individual Magnetic Nanoparticles
2019 IEEE International Superconductive Electronics Conference (ISEC) Proceedings (2019);
DOI: 10.1109/ISEC46533.2019.8990906

Publications not included in this thesis

Publication I J. Lin, **B. Müller**, J. Linek, M. Karrer, M. Wenzel, M. J. Martínez-Pérez, R. Kleiner, and D. Koelle
$YBa_2Cu_3O_7$ nano superconducting quantum interference devices on MgO bicrystal substrates
Nanoscale **12**, 5658-5668 (2020)

Publication II L. Thiel, D. Rohner, M. Ganzhorn, P. Appel, E. Neu, **B. Müller**, R. Kleiner, D. Koelle, and P. Maletinsky
Quantitative nanoscale vortex imaging using a cryogenic quantum magnetometer
Nat. Nanotechnol. **11**, 677-681 (2016)

Publication III D. Rohner, L. Thiel, **B. Müller**, M. Kasperczyk, R. Kleiner, D. Koelle, and P. Maletinsky
Real-Space Probing of the Local Magnetic Response of Thin-Film Superconductors Using Single Spin Magnetometry
Sensors **18**, 3790 (2018)

Publication IV V. Morosh, J. Linek, **B. Müller**, M. J. Martínez-Pérez, S. Wolter, T. Weimann, J. Beyer, T. Schurig, O. Kieler, A. B. Zorin, R. Kleiner, and D. Koelle
Transport and noise properties of sub-100-nm planar Nb Josephson junctions with metallic HfTi barrier for nanoSQUID applications
submitted to Phys. Rev. Applied

Publication V J. Linek, **B. Müller**, D. Korinski, M. Wyszynski, M. Milosevic, E. Goldobin, D. Koelle, and R. Kleiner
On the coupling of magnetic moments to SQUIDs
in preparation

Contents

Chapter 1

Introduction

Nanomagnetism is a very appealing field of research. On the one hand, there are phenomena like, for example, macroscopic quantum tunneling of the magnetization [1], offering the possibility to address fundamental scientific questions like the only insufficiently understood transition between the classical and the quantum regime. On the other hand, magnetic nanoparticles (MNP) are of great interest for technological applications like data storage [2], non-volatile memory [3], or ferrofluids in industrial applications [4], as well as biological applications in contrast agents [5], drug targeting [6] or hyperthermia cancer treatments [7, 8].

In macroscopic ferromagnets below their Curie temperature (and also ferrimagnets below the Néel temperature), the formation of multiple magnetic domains separated by domain walls

contributes to the minimization of the total energy by reducing the stray field at the expense of higher exchange energy and magnetocrystalline anisotropy energy [9]. However, if the size of the magnet is reduced, the formation of domain walls becomes energetically unfavorable, resulting in a single magnetic domain stretching over the magnet's entire volume. For many ferromagnetic materials, the critical diameter for this transition is in the range of 5-1000 nm for spherical particles [9]. Depending on the magnetic hardness of the material, the existence of a magnetic vortex state between the single and multi-domain state is also possible [9].

The orientation of such a MNP's magnetic moment is defined by the anisotropy of the particle, which consists of contributions from magnetocrystalline and surface anisotropy, as well as shape anisotropy if the MNP has a non-spherical shape [10]. This results in the existence of an easy axis for the magnetization, to which the magnetic moment of the particle will align in parallel or antiparallel manner in the case of such an uniaxial anisotropy. In general, there can also be additional preferred axes of magnetization. The parallel and antiparallel configurations are separated by an energy barrier $\Delta E = KV$ with the anisotropy constant K and particle volume V. This is schematically illustrated in Fig. 1.1(a). For very small particles, the height of this energy barrier can be lower than the thermal energy $k_{\mathrm{B}}T$, with temperature T and the Boltzmann constant k_{B}, so that the magnetization is not stable above a certain blocking temperature; the particle is then in a so-called superparamagnetic state [11].

For MNPs with a stable magnetization, the magnetization

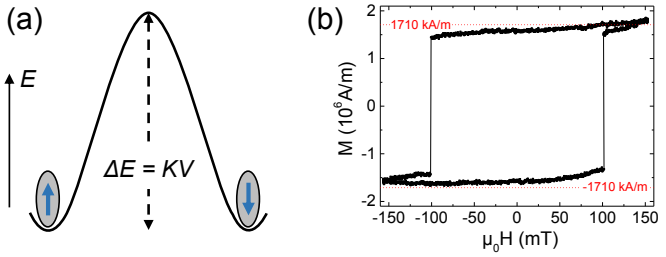

Figure 1.1: (a) Schematic illustration of the energy barrier for magnetization reversal for a MNP with uniaxial anisotropy. (b) Magnetic hysteresis loop $M(H)$ of an Fe nanowire. Panel (b) adapted from appended publication 1.

can be reversed by application of an external magnetic field H in the direction opposite to the current magnetization. Upon increasing H, the energy of the antiparallel orientation is increased and the energy of the parallel orientation is lowered until the energy barrier can be overcome at the switching field H_{sw} and the magnetization is reversed. By measuring the magnetization M as a function of the applied magnetic field H, a magnetic hysteresis loop $M(H)$ can be recorded. Fig. 1.1(b) shows such a hysteresis loop, which was measured on an Fe nanowire. From such hysteresis loops, a multitude of informations can be obtained, such as the domain configuration, saturation magnetization, switching and coercive field or the mechanism for magnetization reversal [12].

For magnets with several magnetic domains, magnetization reversal takes place by nucleation, propagation and annihila-

tion of domain walls. In single-domain MNPs the reversal can be achieved by different processes [12]. The simplest process is reversal via uniform rotation of the magnetization according to the model of Stoner and Wohlfarth [13]. Other processes are non-uniform, like the curling mode reversal [14] or the less common buckling and fanning modes [9]. The influence of thermal fluctuations on the magnetization reversal can be described by the Néel-Brown model, which has been adapted for predictions of the switching field by Kurkijärvi [15].

Different methods can be used for experimental investigations of MNPs, like spin-polarized scanning tunneling microscopy [16], electron holography [17], magnetic resonance force microscopy [18], torque magnetometry [19] or magneto-optical detection using nitrogen-vacancy centers in diamond [20–22]. However, direct recording of magnetic hysteresis loops of single MNPs is possible only with Hall bars [23–25] or miniaturized superconducting quantum interference devices (SQUIDs), an approach that was pioneered by Wernsdorfer *et al.* [26]. This approach is also followed by the group of Reinhold Kleiner and Dieter Kölle in Tübingen and by this thesis.

A direct current (dc) SQUID consists of a superconducting loop which is intersected by two Josephson junctions (JJs). Thus, two fundamental effects in superconductivity are combined: The fluxoid quantization in a superconducting loop [27, 28] and the Josephson effect [29]. If the device is biased with a current slightly above its critical supercurrent I_c, the voltage drop V across the SQUID is modulated with the externally applied magnetic flux Φ. This modulation $V(\Phi)$ oscillates periodically with the magnetic flux quantum $\Phi_0 \approx 2.068 \times 10^{-15}\,\mathrm{V\,s}$,

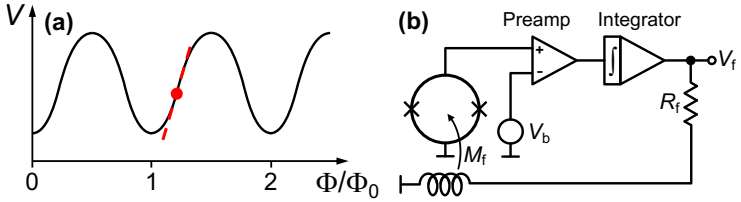

Figure 1.2: (a) Schematic illustration of the $V(\Phi)$ curve in a dc SQUID (black). Optimum working point and transfer function shown in red. (b) Basic circuit diagram of a flux-locked loop.

as shown schematically by the black curve in Fig. 1.2(a). This allows the usage of SQUIDs as flux-to-voltage converters and makes them the most sensitive detectors for magnetic flux. The highest sensitivity is reached for a working point where the slope of the $V(\Phi)$ curve is maximum, as indicated by the red dashed line and dot in Fig. 1.2(a). This defines the transfer function $V_\Phi = (\partial V/\partial \Phi)_{\max}$. Achieving a linear correlation between flux and voltage instead of an oscillating signal is possible by usage of a flux-locked loop (FLL) circuit, like shown schematically in Fig 1.2(b). Via a feedback inductance M_f, the flux detected by the SQUID is compensated, so that the device is always operated at the optimum working point. The feedback voltage V_f across a feedback resistance R_f is then used as output signal, which corresponds to the flux detected by the SQUID via $V_\mathrm{f} = \Phi\, R_\mathrm{f}/M_\mathrm{f}$. The sensitivity of a SQUID is limited by the noise of the SQUID itself, since signals below this intrinsic noise level cannot be detected. The measured spectral density of the root mean square

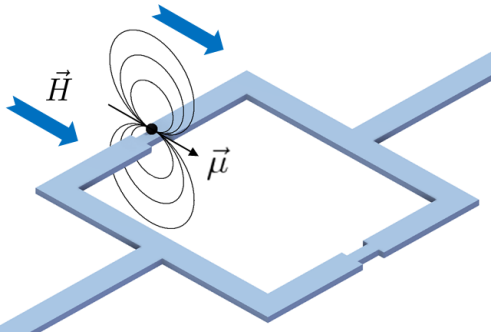

Figure 1.3: Schematic illustration of a nanoSQUID detecting the stray field of a particle with magnetic moment $\vec{\mu}$ in an external magnetic field $\vec{H}$.

(rms) voltage noise $S_V^{1/2}$ corresponds to a spectral density of flux noise $S_\Phi^{1/2} = S_V^{1/2}/|V_\Phi|$. For conventional SQUIDs, one finds typically $S_\Phi^{1/2} \gtrsim 1\,\mu\Phi_0/\mathrm{Hz}^{1/2}$.

In order to measure magnetic hysteresis loops of magnetic nanoparticles, strongly miniaturized SQUIDs (nanoSQUIDs) can be used [30], as is schematically shown in Fig 1.3: The MNP with magnetic moment $\vec{\mu}$ is placed on the SQUID loop, and to change the magnetization an external magnetic field $\vec{H}$ is applied in the loop plane. Ideally, no flux is then coupled to the SQUID by $\vec{H}$, and only the stray field of the MNP is detected. Thus, the challenging task of measuring the small magnetic signal originating from a single particle in a strong background field up to the Tesla range [12] can be achieved. Enhancing the signal by performing measurements on ensembles of MNPs is

possible, but has several drawbacks, like possible interactions between the particles, which can greatly complicate the interpretation of results, or the loss of information on anisotropy by averaging over different particle orientations. These problems can be avoided by measurements of single MNPs like the ones discussed in this thesis.

The main figure of merit for nanoSQUIDs is the spin sensitivity $S_\mu^{1/2} = S_\Phi^{1/2}/\phi_\mu$, given by the flux noise $S_\Phi^{1/2}$ divided by the coupling factor ϕ_μ. The spin sensitivity quantifies the minimum magnetic moment (in units of the Bohr magneton μ_B) that can be detected by a nanoSQUID within a 1 Hz bandwidth. In the limit of thermal white noise, the flux noise scales as $S_\Phi \propto L/I_0R$ [31] with the SQUID inductance L and the characteristic voltage $V_\mathrm{c} = I_0R$ given by the critical current I_0 times normal state resistance R per single junction. Lowering L in order to optimize $S_\mu^{1/2}$ is one of the main motivations for further miniaturization of SQUIDs. The coupling factor $\phi_\mu = \Phi/|\vec{\mu}|$ expresses the amount of flux coupled to the SQUID loop by a magnetic moment $\vec{\mu}$ and depends on the geometry of the SQUID loop as well as on the position and orientation of $\vec{\mu}$, which is why it is usually estimated either via magnetostatic considerations [32–34] or numerical methods [35–39]. ϕ_μ can be increased by positioning the MNP as close as possible to an as thin and narrow as possible constriction in the loop - however, such a constriction comes with a large kinetic inductance [40], which in turn leads to increased flux noise. For nanoSQUIDs with grain boundary (GB) JJs, an optimized geometry with respect to $S_\mu^{1/2}$ has been found by numerical simulations [38].

Different types of nanoSQUIDs have been realized within the last years, overviews can be found for example in Refs. [41–43]. Many devices are made from metallic superconductors like Nb, Al or Pb with constriction-type JJs. Although impressive results for spin sensitivity $S_\mu^{1/2} < 1\,\mu_\mathrm{B}/\mathrm{Hz}^{1/2}$ and flux noise $S_\Phi^{1/2} = 50\,\mathrm{n}\Phi_0/\mathrm{Hz}^{1/2}$ have been achieved [44], these devices are restricted to narrow intervals of the applicable magnetic field and temperature due to the lack of flux feedback structures and critical temperatures $T_\mathrm{c} < 10\,\mathrm{K}$ of the materials used.

In the Tübingen group, nanoSQUIDs based on the cuprate superconductor $YBa_2Cu_3O_7$ (YBCO) have been developed [37, 45]. This material offers the advantages of a high critical temperature $T_\mathrm{c} \approx 90\,\mathrm{K}$ and a high critical field, allowing for nanoSQUIDs that can be operated in magnetic fields up to 3 T [45]. These devices are fabricated by pulsed laser deposition (PLD) of YBCO onto a $SrTiO_3$ (STO) bicrystal substrate and subsequent electron beam evaporation of a Au layer. Coarse patterning is done by optical lithography and Ar ion beam milling, followed by final patterning of the SQUID geometry using Ga focused ion beam milling (FIB) [37]. This results in a device with GB JJs that are shunted by the Au layer, yielding non-hysteretic current-voltage characteristics (IVCs). Further, an additional constriction is added to the layout, serving as an integrated inductance for flux feedback via a modulation current I_mod and as area of maximized ϕ_μ for a MNP [45]. Devices on MgO substrates have also been realized [46], however this thesis focuses on devices on STO. A scanning electron microscopy (SEM) image of such a YBCO nanoSQUID is shown in Fig. 1.4.

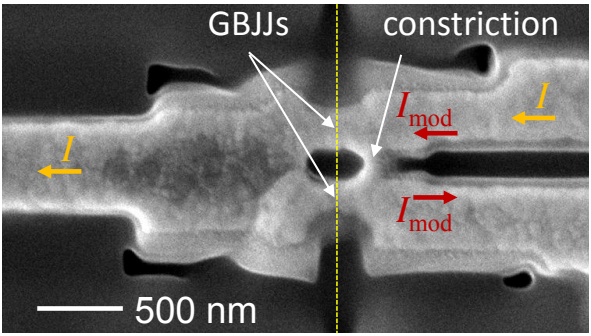

Figure 1.4: SEM image of a YBCO nanoSQUID. The dashed yellow line indicates the position of the grain boundary. Arrows indicate the paths for bias current I (orange) and modulation current I_{mod} (red). Figure from appended publication 1. © 2015 American Physical Society.

The use of nanoSQUIDs for magnetometry on single MNPs is one of the goals of this thesis. In **section 2.1**, 4 publications treating this topic are summarized. In these publications, YBCO nanoSQUIDs are used to record hysteresis loops of different nanomagnets. **Publication 1** deals with the magnetization reversal of an Fe nanowire (NW) embedded into a carbon nanotube (CNT), which was positioned close to the nanoSQUID using nanomanipulators. The particles investigated in **publications 2 to 4** are Co NWs and nanodisks that were grown on top of the sample surface by focused electron-beam-induced deposition (FEBID). In this method, $Co_2(CO)_8$ is brought into an SEM/FIB system as a precursor gas, which can be decom-

posed by the focused electron beam [47]. This results in Co-rich magnetic nanostructures with tunable properties [48, 49] at the precise position of the electron beam focus on the sample.

Section 2.2 of this thesis deals with ideas and methods for the design and fabrication of further optimized nanoSQUIDs. An inherent limitation of the measurements discussed before is their one-dimensional character, which means only one vector component of the MNP's three-dimensional magnetic moment $\vec{\mu}$ is captured by the nanoSQUID. Thus, the information gathered in such measurements is always incomplete. This limitation can greatly complicate or even prevent making precise statements, especially on the anisotropic properties of the MNP. A possible solution to this drawback is shown in **publication 5**, where a three-axis vector nanoSQUID is presented. This device consists of 3 mutually orthogonal Nb nanoSQUID loops with sandwich-type Nb/HfTi/Nb JJs [50]. The Nb nanoSQUIDs feature integrated flux feedback structures and can be operated in magnetic fields up to 0.5 T [51]. A major drawback to this approach is the critical temperature $T_c = 9.2\,\mathrm{K}$ of Nb, which sets an upper limit to the operation temperature of such devices.

Transferring this approach to YBCO in order to make use of the higher critical temperature and larger upper critical magnetic field is, however, not possible with bicrystal-based GB junctions, because the positioning of JJs is only possible along the single grain boundary line. Further, YBCO structures crossing that line do always contain a junction. These limitations of the bicrystal-based GB JJ technology largely restrict the possible layouts and make designs like the three-axis vector nanoSQUID presented in publication 5 topologically impossi-

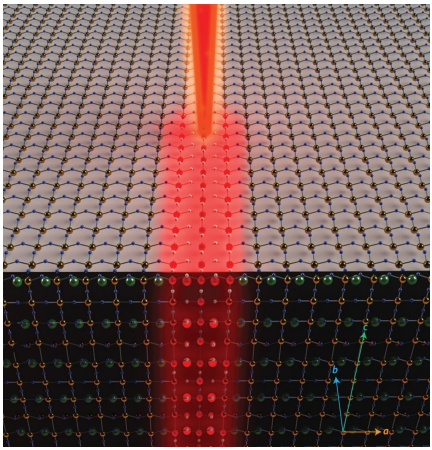

Figure 1.5: Artistic representation of the creation of a Josephson junction in YBCO with a focused He ion beam. Figure reprinted by permission from Springer Nature: S. A. Cybart *et al.*, Nano Josephson superconducting tunnel junctions in $YBa_2Cu_3O_{7-\delta}$ directly patterned with a focused helium ion beam. Nature Nanotechnology **10**, 598-602 (2015), © 2015.

ble. In 2015, however, Cybart and co-workers [52] successfully demonstrated an alternative approach for the fabrication of JJs in YBCO: irradiation with a focused He ion beam (He-FIB). This method allows to locally suppress the superconductivity in YBCO with nanometric precision at arbitrary positions, and can thus overcome the topological limitations inherent with the use of bicrystals. An artistic representation of the irradiation process is shown in Fig. 1.5.

In the helium ion microscope (HIM), a finely focused He ion beam is scanned across the sample surface for imaging [53–55]. Compared to scanning electron microscopy, a better spatial resolution ($< 0.5\,\mathrm{nm}$) can be achieved due to the smaller excited sample volume. The He ion beam is formed at an atomically sharp tungsten tip in a gas field ion source (GFIS) [53] and then trimmed and focused to the sample surface by electrostatic ion optics, resulting in a large depth of focus. Additional use of an electron flood gun can prevent charging of the sample, which enables imaging of insulating samples [54]. FIB milling is also possible, yielding nanometric spatial resolution [56] without sample contamination, both of which can not be achieved by conventional Ga-FIB using a liquid metal ion source.

The creation of Josephson barriers in cuprates by local irradiation with high-energy electrons [57–60], protons [60], neon ions [61–63] or oxygen ions [64, 65] has always struggled with the quality of the produced JJs, since the barriers produced by irradiation show widths of up to 100 nm [63]. This results in lower I_0R values and greater excess currents compared to GB based JJs [55]. With the invention of the GFIS, irradiation with He ions at sub-nm resolution has become possible, which enables the fabrication of JJs with thin barriers in YBCO [52, 66]. Nanopatterning without removal of material is also possible by irradiation with a high He ion dose [67–69]. **Publication 6** contains a systematic study on the scaling of electrical transport parameters of He-FIB JJs with the irradiation dose. Recently, devices produced by He-FIB irradiation are applied to THz detection [70] and magnetization measurements on ensembles of MNPs [71].

Another promising application of the local suppression of superconductivity in YBCO using He-FIB irradiation is the creation of artificial pinning centers for Abrikosov vortices [72]. Due to their non-superconducting core, it is energetically favorable for these vortices to be located at positions with reduced condensation energy of the superconductor, which means at positions with weakened or suppressed superconductivity. Such pinning sites can be intrinsic defects in the material, but may also be introduced artificially [73, 74]. A current flow in the superconductor exerts a Lorentz force on the vortices, which limits the maximum supercurrent due to depinning of the vortices followed by dissipative vortex motion. Increasing the critical current I_c by stronger vortex pinning is one of the main motivations for the research done on this topic.

For regular pinning arrays, matching effects occur when the applied magnetic field B fulfills the matching condition $B_k = k\Phi_0/A$, where A is the area of one unit cell of the array and k is the number of pinning sites within A. At these matching fields, the energy required to deform the vortex lattice is minimized, which leads to enhanced pinning [75] and local maxima in $I_c(B)$, as shown in Fig. 1.6. Here, the 200 nm lattice constant of the square array corresponds to a matching field $B_1 = 52\,\mathrm{mT}$.

Pinning arrays have been realized by different methods, for example via magnetic structures [76–79] or antidots (holes) [80–87] in metallic superconductors. In YBCO, pinning centers can be induced by high-energy irradiation with heavy ions [88, 89], the use of antidots [90] or masked ion beam structuring (MIBS) [91–97] using light ions. However, matching effects can only be observed, if the London penetration depth λ_L,

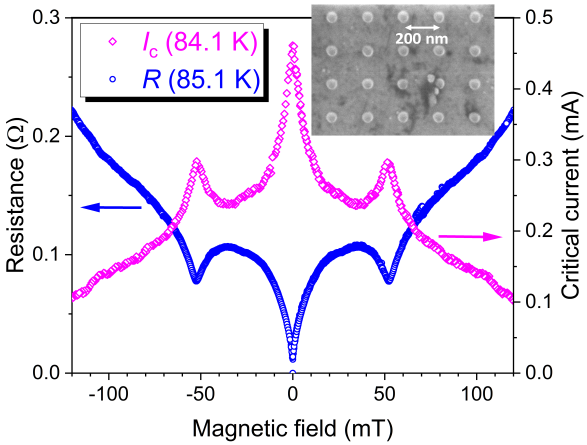

Figure 1.6: $I_c(B)$ (pink) and $R(B)$ (blue) of a square pinning array in YBCO with a 200 nm lattice constant (see HIM image inset). Figure from supplemental material of appended publication 7. © 2019 American Chemical Society.

defining the distance for magnetic vortex-vortex interaction, is larger than the distance between neighbouring pinning sites and, additionally, the intrinsic pinning is weaker than pinning to the array. Since λ_L diverges at the superconducting critical temperature, matching effects are typically investigated near T_c, with only few exceptions [84, 98, 99]. In the case of YBCO, intrinsic pinning on edge and screw dislocations with typical distances of 300 nm [100] is dominant for temperatures up to almost T_c.

The finely focused helium ion beam of the HIM offers the possibility to create pinning arrays in YBCO with lattice constants below both the characteristic distance of intrinsic pinning and the low-temperature λ_L. **Publications 7 and 8** describe the fabrication and characterization of such ultradense pinning arrays with strong pinning at temperatures significantly below T_c. Such strong pinning of vortices at artificial pinning centers can reduce low-frequency noise in YBCO SQUIDs [101] and might therefore also be used to improve the high-field performance of future YBCO nanoSQUIDs.

Chapter 2

Summary of publications and contributions

This chapter gives a summary for each of the appended publications. Each summary is followed by a description of author contributions.

2.1 nanoSQUID magnetometry of individual magnetic nanoparticles

Publications 1 through 4 are examples of nanoSQUID magnetometry experiments performed within this thesis on single magnetic nanostructures. The magnetic particles under investigation are an Fe nanowire in publication 1, Co nanowires which were annealed at different temperatures in publication 2, and Co nanodisks grown by FEBID in publications 3 and 4.

2.1.1 Publication 1: Low-Noise $YBa_2Cu_3O_7$ Nano-SQUIDs for Performing Magnetization-Reversal Measurements on Magnetic Nanoparticles

In this publication, among other results, a proof-of-principle magnetization reversal measurement on a magnetic nanowire is presented.

The first part of the work describes the fabrication and characterization of optimized YBCO nanoSQUIDs. By incorporation of results obtained from a numerical optimization study [38] into the fabrication process, nanoSQUIDs with optimized geometric parameters were fabricated and characterized. Compared to previous devices [37, 45], the optimized SQUIDs are made from thicker films and have smaller loops with wider junctions, resulting in lower inductances (down to $L = 3.9\,\mathrm{pH}$) and higher characteristic voltages (up to $V_c = 1.9\,\mathrm{mV}$ at $T = 4.2\,\mathrm{K}$).

The measured rms spectral density of flux noise for one device is shown in Fig. 2.1.

The spectrum measured in open loop mode (Fig. 2.1(a)) is governed by frequency-dependent noise with a $1/f$-like scaling up to the cutoff frequency of the electronics at $f \approx 7\,\mathrm{MHz}$. Thus, we can only give an upper limit for the white flux noise level, yielding a very low value $S_{\Phi,\mathrm{w}}^{1/2} < 50\,\mathrm{n}\Phi_0/\mathrm{Hz}^{1/2}$. This is the lowest value reported so far for a YBCO SQUID and among the lowest flux noise levels of SQUIDs in general [44, 102–104]. With a calculated coupling factor $\phi_\mu = 13\,\mathrm{n}\Phi_0/\mu_\mathrm{B}$ for a point-like MNP at distance $z = 10\,\mathrm{nm}$ above the constriction, the spin sensitivity of this optimized device is better than $4\,\mu_\mathrm{B}/\mathrm{Hz}^{1/2}$. However, the typical frequencies in practical magnetization-reversal measurements are on the order $f \lesssim 1\,\mathrm{Hz}$, so that the low high-frequency noise level is of limited use only. In order to shed more light on the origin of the frequency-dependent noise sources, further measurements were done with dc bias and also with bias reversal (BR) [105] to eliminate the noise originating from critical current fluctuations (see Fig. 2.1(b)). With the BR technique, the noise level is reduced compared to the dc spectrum, but for frequencies lower than a few kHz a strong frequency dependence remains, neither arising from critical current fluctuations nor from the movement of Abrikosov vortices, which can be ruled out due to the narrow linewidths and the magnetically shielded measurement environment. Thus, the low-frequency excess noise must have another origin. This origin is not known yet, and also noise measurements at different temperatures do not show any systematic behavior, as shown in the supplemental

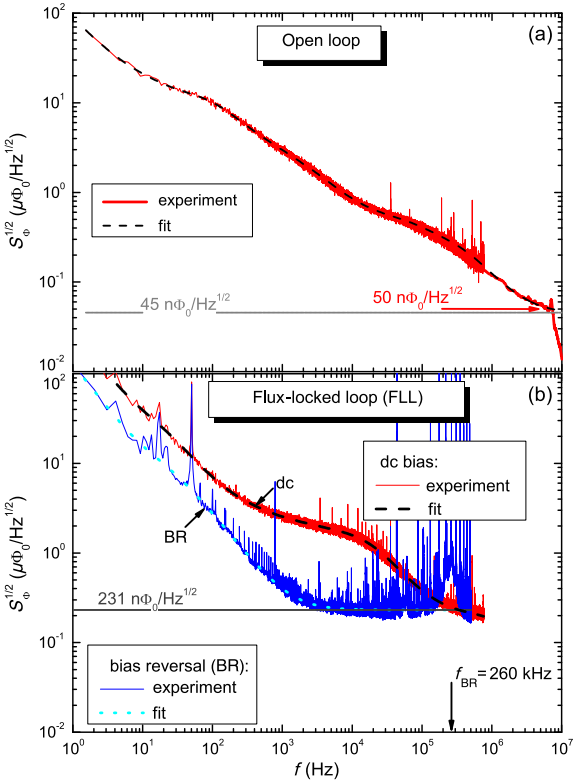

Figure 2.1: Flux noise spectra of an optimized nanoSQUID, measured in open-loop mode (a) and flux-locked loop mode (b) with dc bias (red) and bias reversal (blue). The dashed lines are fits to the measured spectra with white noise levels as indicated by the horizontal lines. Figure from appended publication 1.

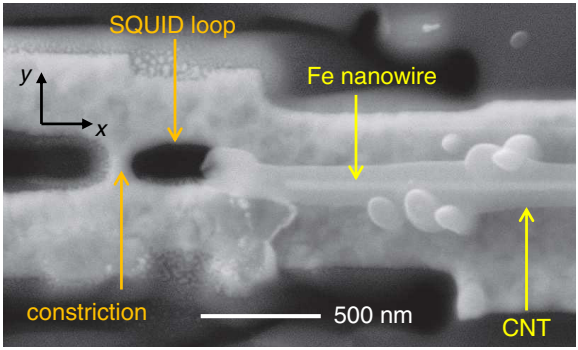

Figure 2.2: SEM image of a CNT-encapsulated Fe nanowire positioned close to a YBCO nanoSQUID. Figure from appended publication 1.

material of publication 1. A possible candidate are the magnetic moments of oxygen vacancies in the STO substrate [106] that might be caused by the FIB milling process [107].

In the second part of this publication, the magnetization reversal of an Fe nanowire encapsulated in a carbon nanotube (CNT) [108–111] is investigated. In Fig. 2.2, an SEM image of the CNT positioned close to a YBCO nanoSQUID is shown. The easy axis of the Fe nanowire is aligned along the x axis (perpendicular to the grain boundary plane) with misalignment angles $\lesssim 4°$ and distances of $\sim 0.3\,\mu$m to the SQUID hole in both the x and z direction. The diameter and length of the Fe nanowire are 39 nm and $\sim 14\,\mu$m, respectively.

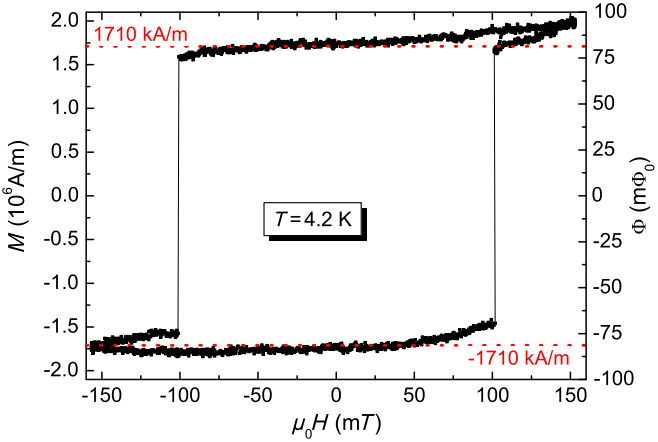

Figure 2.3: Hysteresis loop $\Phi(H)$ of an Fe nanowire detected with a YBCO nanoSQUID. Figure from appended publication 1. © 2015 American Physical Society.

The magnetic hysteresis loop measured with the nanoSQUID while applying a magnetic field along the x direction is shown in Fig. 2.3. Reversal of the wire magnetization can clearly be identified as large jumps of the flux signal at fields $\pm 101\,\mathrm{mT}$, which matches the predicted value of 103 mT for a reversal via curling mode [112] very well. Furthermore, we can calculate the total flux coupled to the SQUID by integrating the coupling factor obtained from numerical simulations [113–115] over the volume of the wire, yielding an expected flux signal $\Phi_\mathrm{s} = 81.4\,\mathrm{m}\Phi_0$ when using a literature value of $M_\mathrm{s} = 1710\,\mathrm{kA/m}$ [116] for the

saturation magnetization of iron. This also agrees very well with the measurement, as indicated by the red dotted lines in Fig. 2.3. The signal-to-noise ratio of this nanoSQUID-based measurement is on the order of 100, about an order of magnitude better than similar measurements performed with a micro-Hall sensor [111].

Contributions

This work was done in collaboration with the group of B. Büchner at the Leibnitz Institute for Solid State and Materials Research IFW Dresden, who provided the Fe CNT and its positioning on the SQUID. The nanoSQUIDs were fabricated by T. Schwarz, who also optimized the setup and did the measurements at 4.2 K. Furthermore, he assisted in the simulations for the determination of the coupling factor and the measurements at variable temperature. R. Wölbing optimized the 4.2 K setup and did the simulations of the coupling factor. M. J. Martínez-Pérez assisted in the 4.2 K measurements and interpretation of the results. I improved the setup for measurements at variable temperature, performed these measurements and assisted in the measurements at 4.2 K. I provided analysis of the noise spectra at variable temperature and wrote according parts of the manuscript.

2.1.2 Publication 2: NanoSQUID Magnetometry on Individual As-grown and Annealed Co Nanowires at Variable Temperature

Publication 2 is a comparative study on the magnetic properties of Co nanowires, using YBCO nanoSQUIDs as sensors to trace out the magnetization hysteresis loops at different temperatures.

As shown in Ref. [117], the structural and magnetic properties of FEBID-grown Co NWs can be modified by annealing them at different temperatures. Measurements of the Co content performed by electron energy loss spectroscopy during scanning transmission electron microscopy (STEM-EELS), for example, show that the composition of the wires can be increased from $\sim$ 70 atom % of Co for an as-grown NW to $>$ 90 atom % by annealing at 600 °C, with the saturation magnetization rising at the same time from 0.8 T to 1.6 T as estimated by electron holography.

In publication 2, the magnetic properties of as-grown and annealed Co NWs are investigated in more detail by nanoSQUID magnetometry. After growth on a Cu TEM grid, the wires are separated by FIB-cutting the grid, followed by the annealing step. Four wires are annealed for 100 min in ultra-high vacuum at temperatures of 150, 300, 450 and 600 °C, denoted as 150-, 300-, 450- and 600-NW, respectively, while one wire is kept at room temperature (RT-NW). A nanomanipulator is then used to position the wires with their Cu carriers close to the SQUIDs and to align the wire axes parallelly to the substrate and perpen-

dicularly to the GB plane with the JJs, as shown in Fig. 2.4(a). Subsequently, $\Phi(H)$ hysteresis loops at temperatures from 1.4-80 K are recorded for each sample by sweeping the magnetic field in the direction of the wire axis while operating the SQUID in FLL mode. 30-50 hysteresis loops are measured for each temperature. Fig. 2.4(b) shows 5 representative loops for each wire obtained at 15 K, whereas in panel (c) the mean hysteresis loops after averaging over 30-50 field sweeps are presented.

The results from these measurements suggest a classification of the NWs into 3 groups:

The RT-NW shows multiple steps in the magnetization reversal and a large scattering of the nucleation field H_n, observed for different temperatures. These are clear signs for a high structural disorder of the magnetic material, leading to a spin glass-like behavior due to magnetic frustration between the multiple magnetic domains. Structural disorder is also evidenced from the TEM analysis without any peaks in the fast Fourier transform (FFT) image, as shown in Fig. 2.5(b). STEM-EELS reveals an almost homogeneous distribution of Co, C and oxygen atoms inside the NW, as well as a 5-10 nm thick oxidized layer at the surface (cf. Fig. 2.5(c)). The purity p of the wire, denoting its Co content, can be determined, independently from the STEM-EELS measurement, by evaluation of the total flux Φ_exp captured by the nanoSQUID. To do this, the coupling factor is calculated numerically using the software package 3D-MLSI [113–115] and averaged over the magnetic volume of the NW as determined from SEM imaging, yielding an effective coupling factor ϕ_NW. The purity can then be calculated via $p = \Phi_\mathrm{exp}/\phi_\mathrm{NW} V_\mathrm{mag} M_\mathrm{s}$, with the bulk saturation magneti-

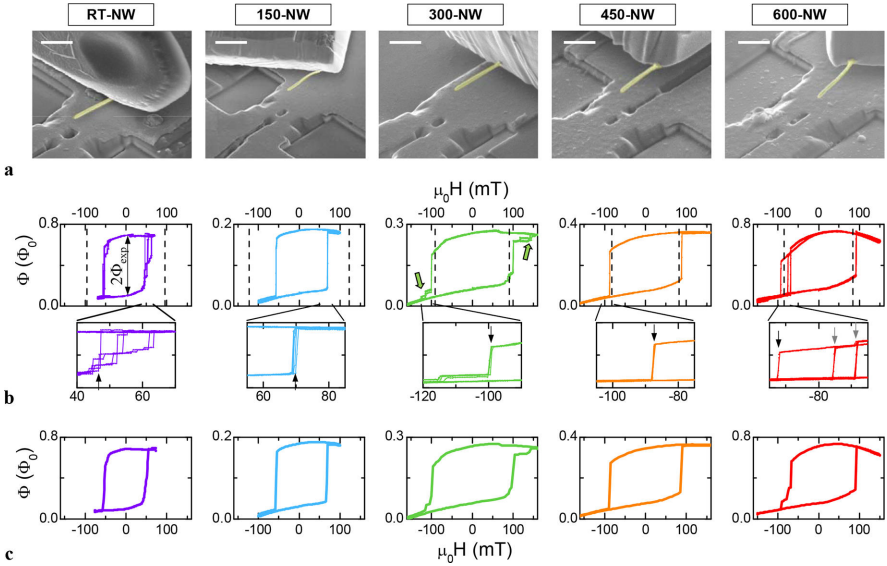

Figure 2.4: (a) SEM images of the Co nanowires (yellow) positioned above the YBCO nanoSQUIDs. Scale bars are 1 μm. (b) 5 representative hysteresis loops of each NW measured at 15 K. (c) Mean hysteresis loops at 15 K after averaging. Figure from appended publication 2.

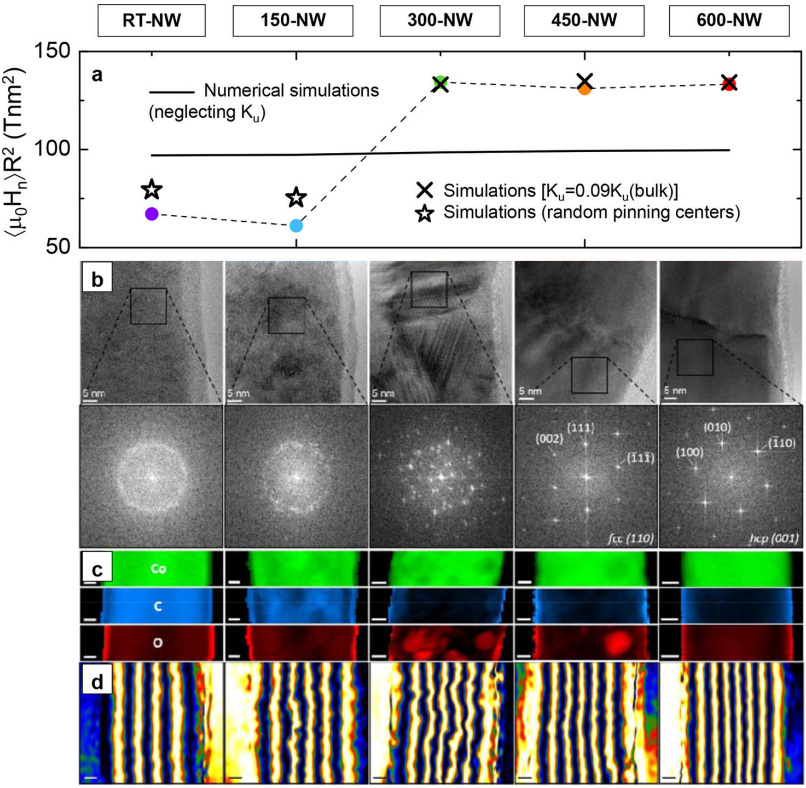

Figure 2.5: (a) $\mu_0 H_\mathrm{n}$ multiplied by the NW radius squared for all 5 wires: experimental values (colored dots), simulations with (crosses) and without magnetocrystalline anisotropy (solid line) and with random pinning centers (stars). (b) TEM images of each NW and FFT images of indicated regions. (c) STEM-EELS chemical maps for Co (green), C (blue) and O (red). (d) Electron holography images representing the magnetic induction flux. Unlabeled scale bars are 10 nm. Figure from appended publication 2.

zation of Co $M_s = 1.4 \times 10^6$ A/m, yielding 75 ± 26 atom % for the RT-NW in good agreement with the STEM-EELS value of 72 %.

For the 150- and 300-NW, the numbers of steps in the hysteresis loop are reduced and the nucleation field is increased, which in combination with the roughly linear temperature dependence of H_n indicates significant structural changes. This is also seen in TEM, where diffraction spots start to appear in the FFT images (Fig. 2.5(b)). As seen in panel (c), STEM-EELS shows the nucleation of oxygen-rich regions as well as a significant reduction of C impurities inside the 300-NW, which causes the transition from a reduced to an increased H_n upon increasing the annealing temperature, as illustrated in Fig. 2.5(a). The reduction originates from defects that act as nucleation points, whereas the increased H_n can be attributed to magnetocrystalline anisotropy of the larger Co grains. The purity of the wires, as measured by nanoSQUID magnetometry, increases to 84 ± 26 % and 96 ± 25 % for the 150- and 300-NW, respectively, compared to 78 % and 88 % obtained from STEM-EELS. In both the 150- and the 300-NW, Co oxide inclusions of different size cause the presence of an exchange bias at different temperatures in the hysteresis loops, like the one seen in Fig. 2.4(b) for the 150-NW at 15 K.

The 450- and 600-NW both exhibit increased nucleation fields due to magnetocrystalline anisotropy. Accordingly, the TEM and FFT images show crystalline regions of $\sim$ 100 nm size in both hcp and fcc configuration. Extracted purities are 106 ± 30 % for the 450-NW and 106 ± 26 % for the 600-NW as determined from the SQUID measurements. The STEM-EELS

values of 92 % and 94 % are well within the error bars of the SQUID measurements, which apparently overestimate the Co content. In both wires, the magnetization reversal takes place in a single step, however with multiple coexisting reversal paths in case of the 600-NW (cf. Fig. 2.4(b)), probably caused by the presence of few antiferromagnetic Co oxide inclusions like the one that can bee seen in the oxygen STEM-EELS map of the 450-NW in Fig. 2.5(c).

Contributions

This work was done in collaboration with M. J. Martínez-Pérez, J. Sesé and the group of J. M. de Teresa from the Aragón Materials Science Institute (Spanish National Research Council and University of Zaragoza), who performed the experiments. I fabricated and prepatterned the YBCO films, calculated the coupling factors using numerical simulations and assisted in the interpretation of the results and preparation of the manuscript.

2.1.3 Publication 3 & 4: NanoSQUID magnetometry of individual cobalt nanoparticles

In publications 3 and 4, YBCO nanoSQUIDs are used to perform magnetization-reversal experiments on single Co nanoparticles grown by FEBID.

Publication 3: NanoSQUID magnetometry of individual cobalt nanoparticles grown by focused electron beam induced deposition

The first part of the publication deals with the characterization of the 5 YBCO nanoSQUIDs that were used for the measurements. They all have critical currents $I_c = 2I_0 = 500 - 600\,\mu$A at 4.2 K, decreasing to 150-200 μA at 70 K. Upon varying the temperature, also the mutual inductance $M = \Phi/I_{mod}$ between the constriction and the SQUID changes, i.e. the amount of flux coupled into the nanoSQUID loop by a certain modulation current. The dependence of the inverse mutual inductance $1/M$, normalized to the $T = 0$ values, is shown in Fig. 2.6(a) for all 5 devices. This temperature dependence arises from the fact that $M = M_g + M_k$ is composed not only of a geometric contribution M_g but also a kinetic part M_k that reflects the additional phase gradient induced by the kinetic momentum of the Cooper pairs flowing along the constriction. Since also the London penetration depth depends on the Cooper pair density, one expects $M_k(T) = M_{k0} \cdot \lambda_L^2(T)/\lambda_{L0}^2$ with the zero temperature values M_{k0} and λ_{L0}. Thus, by combination of the measured $M(T)$ values and numerical simulations of $M(\lambda_L)$ using 3D-MLSI [113–115], we can extract $\lambda_L(T)$ for all devices, as shown in Fig. 2.6(b). The observed dependence $\lambda_L(T) = \lambda_{L0}[1-(T/T_c)^2]^{-1/3}$ matches very well with earlier results from other groups [118], which have also been added to Fig. 2.6(b). The absolute values obtained for λ_L are in the range 170-240 nm, which also confirms earlier re-

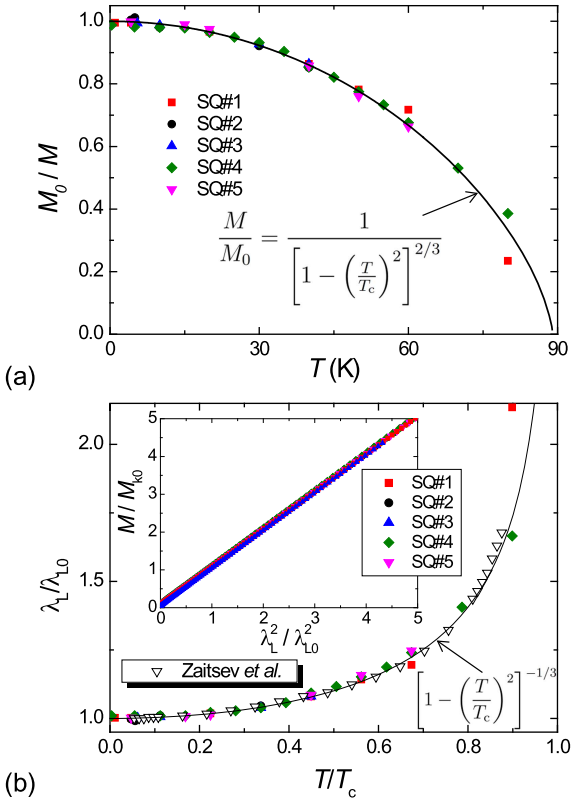

Figure 2.6: (a) Normalized temperature dependence of $1/M$ for all 5 nanoSQUIDs. (b) Normalized temperature dependence of λ_L for all 5 SQUIDs. Inset shows numerical simulations of $M(\lambda_L^2)$. Figure from appended publication 3.

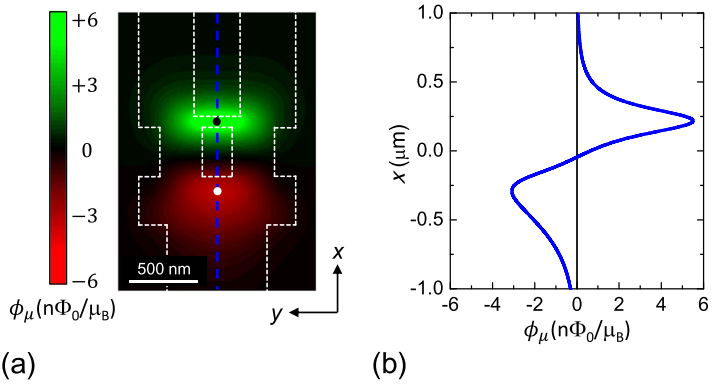

Figure 2.7: Contour plot of ϕ_μ for SQ #2 in the plane 80 nm above the YBCO film surface. (b) Linescan along the dashed blue line in (a). Figure from appended publication 3. © 2016 IOP Publishing.

sults [38, 45, 118, 119]. Another important insight is the almost negligible contribution ($< 10\,\%$) of M_g to the total mutual inductance, illustrated by the hardly visible vertical offsets in the inset of Fig. 2.6(b). The different nanoSQUIDs exhibit very low flux noise levels $\lesssim 1\,\mu\Phi_0/\mathrm{Hz}^{1/2}$ at a frequency of 100 kHz.

The coupling factor above the SQUIDs is determined via numerical simulations using the software package 3D-MLSI [113–115], taking into account the precise lateral dimensions of the nanoSQUIDs as determined from SEM imaging. Fig. 2.7(a) visualizes the calculated coupling factor 80 nm above the YBCO film (i.e. 10 nm above the Au layer) for the geometry of SQ #2 (cf. Fig. 2.8(b) for the corresponding SEM image). A linescan

along the dashed blue line is shown in panel (b), revealing maximum coupling ($5.5\,\mathrm{n}\Phi_0/\mu_\mathrm{B}$) on the constriction and good coupling ($-3.1\,\mathrm{n}\Phi_0/\mu_\mathrm{B}$) on the opposite side of the loop, whereas ϕ_μ quickly vanishes for other positions. With the flux noise levels mentioned before, all 5 nanoSQUIDs achieve spin sensitivites of a few hundred $\mu_\mathrm{B}/\mathrm{Hz}^{1/2}$. For interpretation of the magnetization measurements described in the following, the coupling factor for each SQUID is averaged over the magnetic volume of the particle, as already described in publications 1 and 2.

In the second part of the publication, magnetic hysteresis loops of FEBID-grown Co nanoparticles are traced out with the YBCO nanoSQUIDs. The particles are deposited by scanning a 5 keV, 25 pA focused electron beam over the area desired for the growth, while injecting $Co_2(CO)_8$ precursor gas into the vacuum chamber [48]. 5 particles are grown on the 5 different SQUIDs, with the particles on SQ #1, SQ #2 and SQ #3 having the shape of a spherical cap, diameters of 50-90 nm and thicknesses of 35-60 nm. They are placed on the constrictions of the nanoSQUIDs, as shown in Fig. 2.8(a) and (b) for SQ #1 and SQ #2. The particles on SQ #4 and SQ #5, however, have larger diameters of 100 and 200 nm and are therefore placed on the side opposite to the constriction, as shown for SQ #5 in Fig. 2.8(c). They are disc-shaped and have a thickness of 35 nm, which has been measured by atomic force microscopy (AFM).

Representative hysteresis loops are shown in Fig. 2.8(d)-(e), which have been measured at different temperatures with the nanoSQUIDs in FLL mode by sweeping the magnetic field perpendicularly to the grain boundary plane. The curves obtained from the particles on SQ #1, #2 and #3 show a single step upon

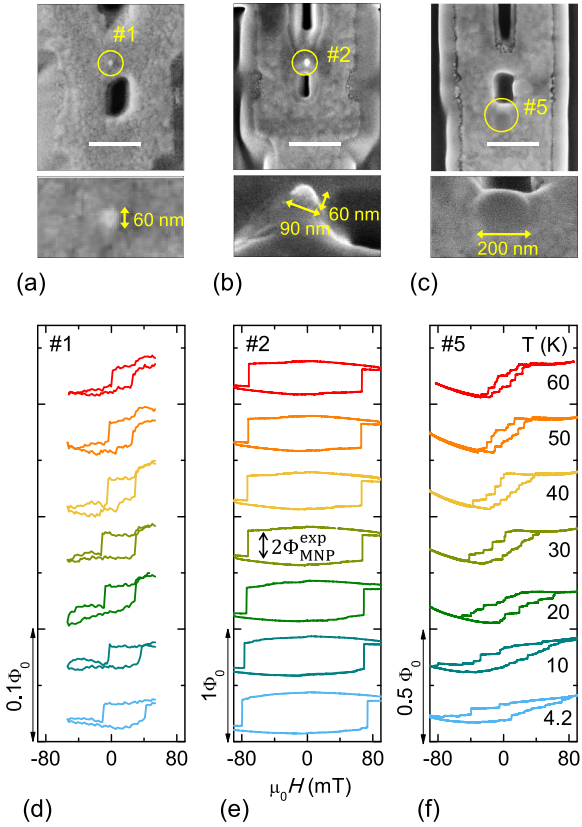

Figure 2.8: (a)-(c) SEM images of SQ #1, SQ #2 and SQ #5 and zoomed views of the corresponding Co particles. Unlabeled scale bars are 500 nm. (d)-(e) Representative magnetic hysteresis loops of the particles shown in (a)-(c), measured at different temperatures as indicated in (f). Figure from appended publication 3.

sweeping the magnetic field, indicating reversal of the magnetization. The reduction of the switching field H_{sw} upon increasing the temperature indicates a thermally assisted reversal process. The height of the energy barrier that has to be overcome to switch the magnetization can be determined from measurements of the dependence of H_{sw} on the temperature and field sweeping rate by applying the Kurkijärvi model [15]. The determined barrier heights agree with earlier results from other groups obtained on Co particles of comparable size [120]. The nanoparticles on SQ #4 and SQ #5 both show several reproducible steps in their hysteresis loops, which are analyzed in detail in publication 4. For all particles, the total magnetic moment μ_{MNP} as well as the magnetic volume V_{mag} can be determined from the flux signals $\Phi_{\mathrm{MNP}}^{\mathrm{exp}}$ detected in the fully saturated state and the coupling factor ϕ_{MNP} averaged over the magnetic volume of the particle via $\Phi_{\mathrm{MNP}}^{\mathrm{exp}} = |\phi_{\mathrm{MNP}}|\mu_{\mathrm{MNP}}$. This yields magnetic moments $\mu_{\mathrm{MNP}} = pV_{\mathrm{mag}}M_{\mathrm{s}} = (1-30)\times 10^6\,\mu_{\mathrm{B}}$ with an estimated purity $p = 60\,\%$ and the saturation magnetization of Co $M_{\mathrm{s}} = 1.4\times 10^6\,\mathrm{A/m}$. The resulting magnetic volumes are roughly a factor of 3 smaller than the geometric volumes measured by SEM imaging, which can be explained by non-ferromagnetic interface layers, like a paramagnetic layer at the interface between particle and nanoSQUID due to a reduced Co concentration in the first stage of the growth process [121] and an antiferromagnetic Co oxide layer due to surface oxidation [122].

Contributions

This work was done in collaboration with J. Sesé from the Aragón Materials Science Institute (Spanish National Research Council and University of Zaragoza), who deposited the nanoparticles and helped with the interpretation of the data. M. J. Martínez-Pérez nanopatterned the nanoSQUIDs, built the experimental setup, performed the SQUID measurements, interpreted the results and wrote most of the manuscript. D. Schwebius assisted in the SQUID measurements and D. Korinski assisted in the calculation of the coupling factors. I fabricated and prepatterned the YBCO films and assisted in the fabrication of the SQUIDs and building of the measurement setup. I also improved the simulation routines and performed the simulations for calculation of the coupling factors and the derivation of $\lambda_{\mathrm{L}}(T)$. I performed the AFM measurements and assisted in the SQUID measurements, data analysis and interpretation of results. Further, I wrote parts of the manuscript.

Publication 4: Magnetic vortex nucleation and annihilation in bi-stable ultra-small ferromagnetic particles

This publication is a follow-up on publication 3, to investigate in detail the magnetization-reversal mechanism of disc-shaped ferromagnetic nanoparticles.

For this purpose, FEBID-grown Co nanodiscs are analyzed using SQUID magnetometry as well as electron holography. Discs of different size are deposited by Co-FEBID, as already

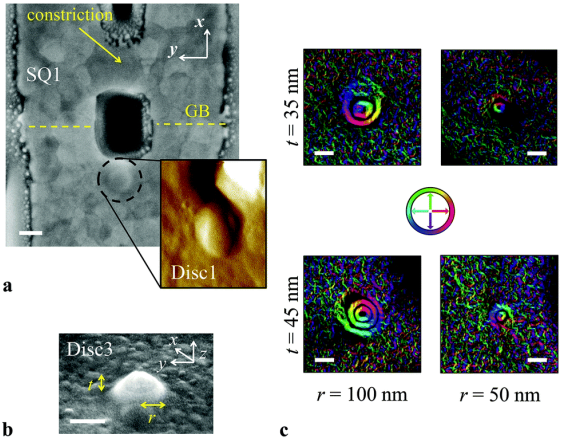

Figure 2.9: (a) SEM and AFM (inset) images of Disc1 on SQ1. The yellow dashed lines indicate the position of the grain boundary (GB). (b) SEM image of Disc3 with radius r and thickness t. (c) Electron holography images of Co nanoparticles with thicknesses and radii as denoted. Color scale indicates the direction of the magnetic flux. Scale bars are 100 nm. Figure from appended publication 4. © 2020 The Royal Society of Chemistry.

described earlier in this thesis. 3 discs (Disc1 to Disc3) are deposited directly on the surface of YBCO nanoSQUIDs to trace out magnetic hysteresis loops, whereas several other discs of different sizes are deposited on a SiN membrane for electron holography analysis. Fig. 2.9 shows a collection of samples.

Disc1 corresponds to the particle #4 of publication 3 and has radius $r = 50\,\text{nm}$ and thickness $t = 35\,\text{nm}$. Disc2 is mentioned there as the particle #5, with $r = 100\,\text{nm}$ and $t = 35\,\text{nm}$. Disc3

with $r = 65\,\mathrm{nm}$ and $t = 50\,\mathrm{nm}$ does not appear in publication 3. As can be seen in the electron holography images of Fig. 2.9(c), a flux-closure configuration of magnetic field lines is present for Co nanodiscs of different size at room temperature. This vortex state (VS) can be observed in the as-grown condition, as well as after saturating the particles by a strong perpendicular magnetic field, confirming that the VS is the ground state of the nanodiscs at room temperature.

Magnetic hysteresis loops for Disc1 to Disc3 are obtained at different temperatures by sweeping the external magnetic field perpendicularly to the grain boundary plane (along $\hat{e}_x$) while operating the SQUIDs in FLL mode. In Fig. 2.10(a), two typical hysteresis loops measured at 10 K for Disc1 and Disc3 are shown in the upper panel. The measured hysteresis loops exhibit, in contrast to those of smaller Co-FEBID particles (P#1 to P#3 from publication 3), several reproducible steps, which can be explained with the bi-stable co-existence of a vortex state (VS) and quasi-single domain (QSD) state as possible ground states. This is shown in the bottom panel of Fig. 2.10(a) and panel (b), where the numerically calculated spatially resolved magnetization of Disc1 is illustrated: At large positive magnetic field, the magnetization of the particle is saturated in the QSD state (#5). This state is preserved even when the field is reduced to zero, which is in contrast to the canonical vortex-mediated magnetization reversal behavior [123]. Upon increasing the magnetic field in the opposite direction, a VS is nucleated at H_n^- (#1 in Fig. 2.10(b)), resulting in a strong decrease of the stray field sensed by the nanoSQUID. Further increase of $-H$ leads to steps in the magnetization, probably due to the presence of pinning

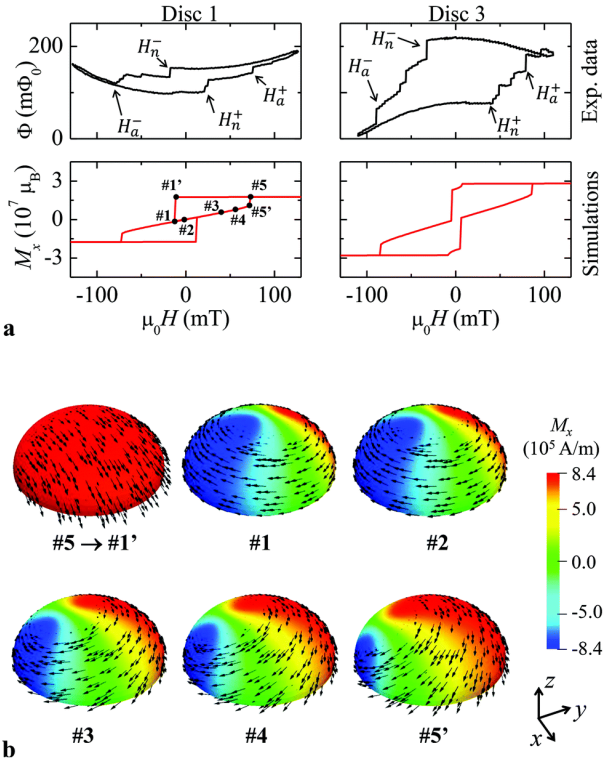

Figure 2.10: (a) (top) Magnetic hysteresis loops measured at $T = 10\,\mathrm{K}$ for Disc1 and Disc3. (bottom) Magnetization $M_x(H)$ obtained from corresponding numerical simulations. (b) Numerically simulated spatially-resolved magnetization of Disc1 at magnetic field values as indicated in bottom left panel of (a). Figure from appended publication 4. © 2020 The Royal Society of Chemistry.

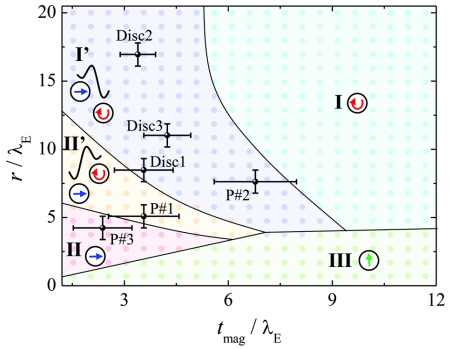

Figure 2.11: Numerically calculated stability diagram for QSD and VS in spherical-cap shaped particles. Simulations were performed with exchange length $\lambda_{ex} = 5.9\,\text{nm}$ for colored scatter grid points. Regions I to III correspond to different stability regions as discussed in the main text. Experimental data for Disc1 to Disc3 and P#1 to P#3 are shown. Figure from appended publication 4. © 2020 The Royal Society of Chemistry.

sites resulting in non-constant movement of the vortex. Finally, the vortex is annihilated at H_a^-. For higher temperatures, the number of minor steps is reduced, which can be explained by the relative reduction of the pinning strength due to increased thermal fluctuations.

Using numerical simulations [124], one can calculate the critical dimensions for QSD or VS stability for spherical-cap shaped particles. Neglecting magnetocrystalline anisotropy, this results in the stability diagram shown in Fig. 2.11. Within region I, the particle has a vortex ground state with an unstable QSD state. In regions II and III, the VS is unstable, resulting in an in-plane

QSD ground state for region II and an out-of-plane QSD ground state in region III. In the bi-stable region I', the ground state corresponds to the VS and the QSD configuration is metastable, whereas for region II' the opposite is true. For both bi-stability regions, nucleation of the VS is not possible by reducing the external magnetic field after saturating the magnetization into the QSD state.

The positions of the experimentally analyzed particles P#1 to P#3 and Disc1 to Disc3 within the stability diagram are determined by calculation of their magnetic thicknesses t_{mag} and radii r. This is done by combining the coupling factor, which is individually calculated for each particle, with the experimentally determined magnetic flux signal, as already described earlier in this thesis. P#1, P#2 and P#3 are found to be in regions II', I' and II, respectively, which matches the square-shaped hysteresis loops found experimentally (see Fig. 2.8(d) and (e)). Disc1 to Disc3 are all situated in region I' and show hysteresis loops with vortex formation and annihilation even after being in the QSD state. This can be explained by the presence of a small uniaxial anisotropy that increases the critical field of magnetization reversal in the QSD state to a value beyond the VS nucleation field. Such an anisotropy can have different origins, like for example deviations from the perfect spherical shape or a net effective magnetocrystalline anisotropy. For the simulated hysteresis loops in the bottom panel of Fig. 2.10(a), a uniaxial anisotropy constant $K_{\mathrm{u}} \sim 2\,\mathrm{kJ/m^3}$ was used, yielding a good agreement with the experimentally determined values for the nucleation and annihilation fields $H_{\mathrm{n/a}}$. Disc1 is among the smallest nanoparticles in which nucleation and annihilation of a

vortex has been observed experimentally [125–127].

The dependence of $H_{\mathrm{n/a}}$ on temperature and field sweeping rate can again be approximated using the model of Kurkijärvi [15], yielding heights for the energy barriers that have to be overcome for vortex nucleation and annihilation. The determined energy barrier heights for vortex nucleation at zero magnetic field $U_{\mathrm{n}}(H = 0)/k_{\mathrm{B}} \sim 6 \times 10^3\,\mathrm{K}$ are in good agreement with values published on permalloy nanodiscs [128], which have an exchange length comparable to that of Co-FEBID. This also explains the presence of the VS after the QSD state in the electron holography images: At room temperature, relaxation from the metastable QSD into the VS takes only a few milliseconds, whereas at the low temperatures of the SQUID measurements this process becomes immeasurably long.

Contributions

This work was done in collaboration with M. J. Martínez-Pérez and J. Sesé from the Aragón Materials Science Institute (Spanish National Research Council and University of Zaragoza), and L. A. Rodriguez and E. Snoeck from the Center for Materials Elaboration and Structural Studies in Toulouse. J. Lin assisted in the fabrication and pre-patterning of the YBCO films. I fabricated and prepatterned the YBCO films and assisted in the fabrication of the SQUIDs and building of the measurement setup. I also performed the AFM measurements and the simulations for calculation of the coupling factors. Further, I assisted in the SQUID measurements, data analysis and interpretation of the results as well as the preparation of the manuscript.

2.2 Preparatory studies for future nanoSQUIDs

In Publications 5 to 8, ideas and methods for the design and fabrication of future nanoSQUIDs are presented. Such devices can possibly overcome the limitations which are present in current nanoSQUIDs, offering new possibilities for the investigation of magnetic nanoparticles.

2.2.1 Publication 5: Three-Axis Vector Nano Superconducting Quantum Interference Device

Publication 5 describes the design, realization and performance of a three-axis vector nanoSQUID - a device that is able to detect the 3 components of a nanoparticle's vector magnetic moment $\vec{\mu}$ simultaneously and independently. Such measurements can, in contrast to the one-dimensional measurements presented in publications 1-4, provide deep insights into the anisotropic magnetic properties of the particle under investigation - something that is not possible with other methods.

The three-axis nanoSQUID consists of 3 mutually orthogonal nanoSQUIDs, as shown in Fig. 2.12. The SQUIDs are based on superconductor/normal metal/superconductor-type Nb/HfTi/Nb Josephson junctions that feature non-hysteretic current-voltage characteristics at 4.2 K, which are fabricated using electron beam lithography and chemical mechanical polishing [50]. This process offers sub-100 nm resolution [129] and

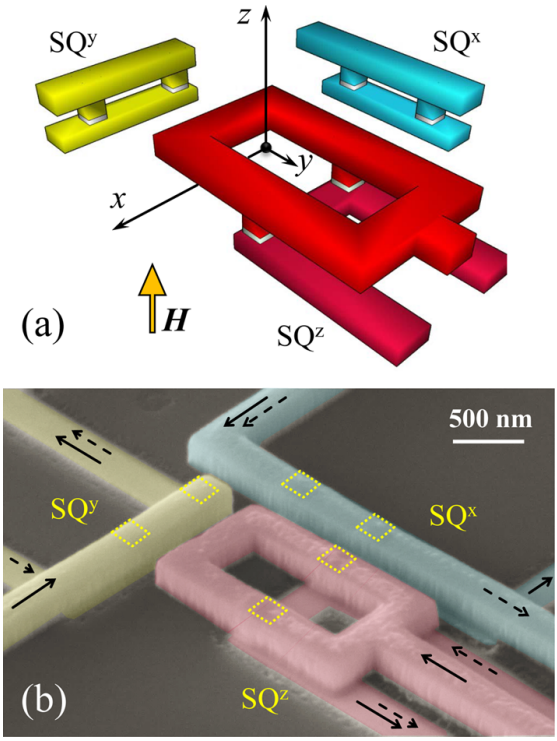

Figure 2.12: Design of the three-axis vector nanoSQUID. (a) Schematic representation. Origin of the coordinate axes indicates the position of the nanoparticle under investigation. (b) False-colored SEM image. Solid and dashed arrows indicate bias and modulation currents for all 3 SQUIDs, respectively, and the yellow dashed squares indicate the position of the junctions. Figure from appended publication 5. © 2016 American Chemical Society.

a large flexibility in the designs, since the orientation of the SQUID loop plane can be either parallel [130] or perpendicular [51] to the substrate plane. In the device presented here, two nanoSQUIDs (SQ^x and SQ^y) are fabricated in a stripline geometry with their $600 \times 90\,nm^2$ loops oriented perpendicularly to each other and to the substrate plane, for the detection of the in-plane x and y components of $\vec{\mu}$. The third SQUID SQ^z is dedicated to the detection of μ^z, which is the component parallel to the externally applied magnetic field $\vec{H} = H\hat{e}_z$. Thus, SQ^z is realized as a planar first-order parallel gradiometer, which is insensitive to a uniformly applied field in the z direction but able to detect the imbalance between its two loops. The magnetic nanoparticle under investigation must therefore be placed inside one of the $500 \times 500\,nm^2$ sized gradiometer loops, as indicated in Fig. 2.12(a) by the origin. All 3 SQUIDs can be current and flux biased independently (cf. dashed and solid arrows in Fig. 2.12(b)), allowing for FLL operation at the respective optimum working point for each nanoSQUID. All of the Josephson junctions are $150 \times 150\,nm^2$ in size, as indicated by the yellow dashed squares.

The electrical transport and noise characteristics measured at $T = 4.2\,K$ of one device are shown in Fig. 2.13. The 3 SQUIDs have very similar critical current densities $j_c \approx 800\,kA/cm^2$ and resistances, resulting in characteristic voltages around $65\,\mu V$. The inductances are all $\sim 1\,pH$. Fig. 2.13(b) shows $V(\Phi)$ for SQ^z with a maximum transfer function of $330\,\mu V/\Phi_0$. $V_\Phi = 300 - 400\,\mu V/\Phi_0$ is also found for SQ^x and SQ^y. The spectral density of flux noise is 170, 160 and $240\,n\Phi_0/Hz^{1/2}$ for SQ^x, SQ^y and SQ^z, respectively, as indicated by the dashed arrows in

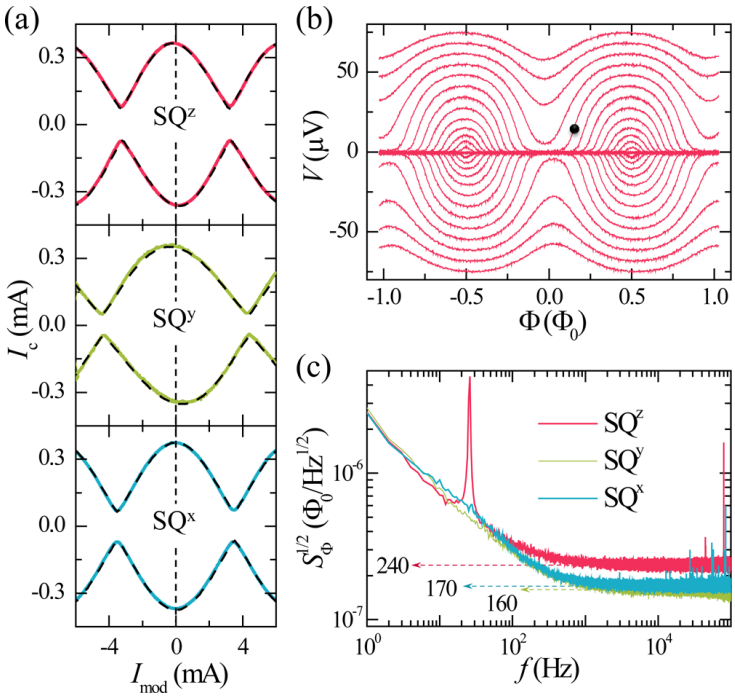

Figure 2.13: Electrical transport and noise characteristics of a three-axis vector nanoSQUID. (a) Measured (solid) and simulated (dashed) maximum critical current vs modulation current for all 3 SQUIDs. (b) $V(\Phi)$ for SQ^z. (c) Spectral density of rms flux noise for all 3 SQUIDs, measured in FLL with a SQUID series array amplifier. Figure from appended publication 5.

Fig. 2.13(c). With coupling factors of 0.28, 0.25 and 3.4 $\mathrm{n}\Phi_0/\mu_\mathrm{B}$ calculated using 3D-MLSI [113–115] as described before, the device achieves a spin sensitivity of 610, 640 and 70 $\mu_\mathrm{B}/\mathrm{Hz}^{1/2}$ for the x, y and z direction of $\vec{\mu}$. Due to the necessary placement of the particle inside the gradiometer, the coupling factor ϕ_μ^z is about an order of magnitude higher than ϕ_μ^x and ϕ_μ^y, resulting in the roughly an order of magnitude worse spin sensitivities of SQ^x and SQ^y as compared to SQ^z.

The vector magnetometer capabilities of the device are illustrated by the simulated hysteresis loops in Fig. 2.14: Upon tilting the easy axis of a magnetic nanoparticle positioned as shown in Fig. 2.12(a) from the z axis towards the y axis, the shape of the hysteresis loops detected by the different SQUIDs changes dramatically. This is true for a point-like particle coupled to an ideal vector magnetometer (black dashed line) as well as for semisphere-shaped particles with different radii coupled to a realistic device (solid lines). However, for larger particle sizes the erroneously detected signal increases, as can be seen e.g. in the top panels of Fig. 2.14(a) and (b), where in the ideal case neither SQ^x nor SQ^y should detect any signal. Instead, both of them detect signals of approximately 10 % of the maximum signal for the 50 nm particle and almost 30 % for the 200 nm one. The reason for this behavior is the non-zero coupling factors of SQ^x and SQ^y for a magnetization along $\hat{e}_z$, causing flux to be coupled into the loops and thus a signal output. The relative error flux (i.e. the total flux detected from components of $\vec{\mu}$ oriented in parallel to the SQUID loop plane normalized to the flux detected from the desired orthogonal component) depends strongly on the position of $\vec{\mu}$. In the case of the device pre-

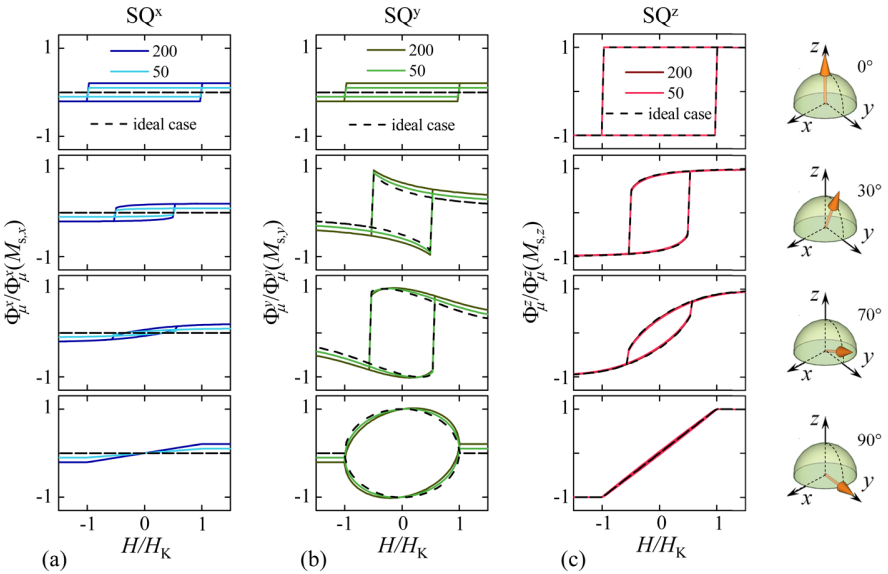

Figure 2.14: Simulated magnetic hysteresis curves of a magnetic nanoparticle with different orientations of the easy magnetization axis as recorded by (a) SQ^x, (b) SQ^y and (c) SQ^z. Easy axis is along $\hat{e}_z$ (top panels) and tilted towards the y axis by 30° (2nd row of panels), 70° (3rd row) and along $\hat{e}_y$ (bottom panels). Figure from appended publication 5.

sented here, the error flux is kept below 10 % within a distance of ~ 55 nm from the origin and below 25 % within 170 nm.

Contributions

This work was done in collaboration with J. Sesé from the Aragón Materials Science Institute (Spanish National Research Council and University of Zaragoza), and with V. Morosh and O. Kieler from the Physikalisch-Technische Bundesanstalt in Braunschweig, who fabricated the devices. M. J. Martínez-Pérez developed the design, did part of the transport measurements, performed the simulations for calculation of the coupling factors and error fluxes and wrote most of the manuscript. D. Gella performed most of the transport measurements and assisted with the simulations. R. Wölbing assisted in the design of the devices. I assisted in the transport measurements, built the setup and performed the noise measurements, and assisted in data analysis and writing the manuscript.

2.2.2 Publication 6: Josephson Junctions and SQUIDs Created by Focused Helium-Ion-Beam Irradiation of $YBa_2Cu_3O_7$

In this publication, a novel method for the creation of Josephson junctions in YBCO is investigated.

In 2015, the fabrication of JJs in YBCO by irradiation with a focused He ion beam (He-FIB) was successfully demonstrated by Cybart and co-workers [52]. Publication 6 presents recent

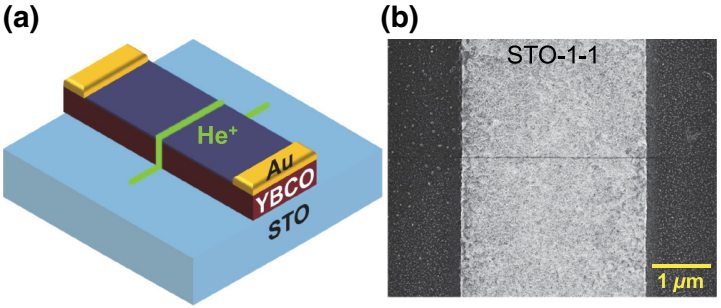

Figure 2.15: (a) Schematic illustration of the He-FIB JJ geometry. (b) SEM image of a JJ, which is visible as a thin dark line. Figure from appended publication 6. © 2019 American Physical Society.

results on such He-FIB JJs that have been obtained in Tübingen. The JJs were fabricated by scanning the He-FIB across prepatterned YBCO bridges, which were fabricated by Ar ion milling of YBCO films grown by PLD on single-crystal STO, MgO and LSAT substrates. A schematic illustration of the irradiation process is sketched in Fig. 2.15(a). Panel (b) displays an SEM image of an actual JJ.

The electronic behavior of the irradiated linescans depends strongly on the irradiation dose D, ranging from flux-flow and Josephson-like IVCs at $T = 4.2\,\mathrm{K}$ to highly resistive barriers at low temperatures, as shown in the $R(T)$ curves of Fig. 2.16. STEM analysis of the irradiated regions shows amorphous tracks for $D \gtrsim 1500\,\mathrm{ions/nm}$ with widths ranging from few nm to $\sim 170\,\mathrm{nm}$ at $D = 10^5\,\mathrm{ions/nm}$.

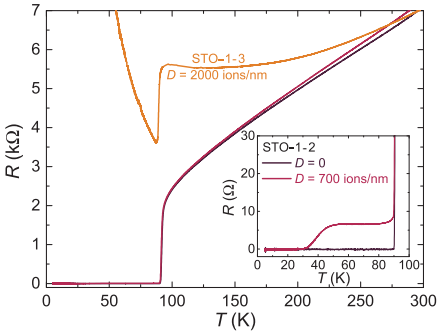

Figure 2.16: $R(T)$ dependence of a YBCO bridge before (black) and after (red) irradiation with $D = 700\,\text{ions/nm}$ and of a bridge irradiated with $D = 2000\,\text{ions/nm}$ (orange). Figure from appended publication 6. © 2019 American Physical Society.

More detailed investigation of the electrical transport properties reveals an exponential decay of the critical current density $j_c(D) \propto \exp(-D/D_0)$ over several orders of magnitude, as indicated by the dashed lines in Fig. 2.17(a). For JJs fabricated on STO and MgO substrates, $D_0 = 130\,\text{ions/nm}$ is found, whereas for JJs on LSAT, j_c decays faster with $D_0 = 38\,\text{ions/nm}$. IVCs of JJs irradiated with low dose are of flux-flow type, whereas for devices with $j_c \lesssim 2\,\text{MA/cm}^2$ the behavior can be described within the resistively and capacitively shunted junction (RCSJ) model [131, 132]. This is supported by numerical simulations based on the RCSJ model, which reproduce the measured IVCs of these devices very well. From these simulations, we are able to extract the noise-free j_c and resistance times area product

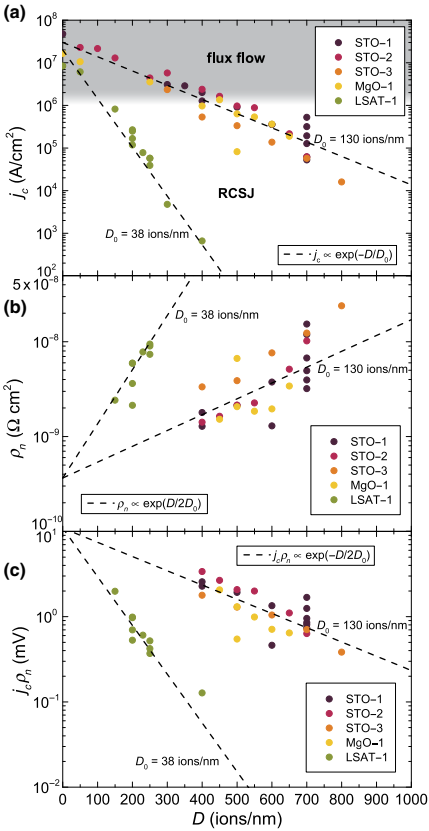

Figure 2.17: (a) $j_c(D)$, (b) $\rho_n(D)$ and (c) $j_c\rho_n(D)$ of different He-FIB JJs. Dashed lines indicate exponential scalings. Figure from appended publication 6. © 2019 American Physical Society.

ρ_n, as well as the Stewart-McCumber parameter β_C and excess current density j_e. We also find an exponential scaling $\rho_n(D) \propto \exp(D/2D_0)$, which results in a scaling of the characteristic voltage $V_c = j_c\rho_n \propto \exp(-D/2D_0)$. Further, we find $V_c \propto j_c^{1/2}$, similar to results obtained for different other JJ types in cuprate superconductors [133]. Maximum absolute values of V_c of a few mV can be reached. However, for $V_c \gtrsim 1\,\mathrm{mV}$, an excess current appears in the IVCs.

The fact that j_c can be fully suppressed with a sufficiently high dose allows for modification of the sample geometry using He-FIB irradiation. This method has been used to fabricate a dc SQUID into a YBCO bridge by combining a $300 \times 300\,\mathrm{nm}^2$ square irradiated with a dose of $4000\,\mathrm{ions/nm}^2$ and a linescan with $D = 230\,\mathrm{ions/nm}$. This device features $V_c = 414\,\mu\mathrm{V}$ and $L = 19\,\mathrm{pH}$. A transfer function $V_\Phi = 2.1\,\mathrm{mV}/\Phi_0$ is reached. The rms spectral density of flux noise scales roughly as $S_\Phi \propto 1/f$ for $1\,\mathrm{Hz} < f < 166\,\mathrm{kHz}$, which is the bandwidth limit of the measurement setup. Thus, we can only give an upper limit $S_\Phi^{1/2} \leq 500\,\mathrm{n}\Phi_0/\mathrm{Hz}^{1/2}$ for the flux noise in the thermal white noise regime.

Contributions

This publication was realized in collaboration with the group of C. J. Burkhardt at the NMI in Reutlingen, where the sample preparation for STEM was done by B. Schröppel and the STEM images were captured by M. Becker. M. Karrer did the $R(T)$ measurements, assisted in the STEM analysis, the sample fabrication and the 4.2 K measurements. F. Limberger assisted

in the STEM analysis, the $R(T)$ and the 4.2 K measurements. I adapted the fabrication process from Ref. [52] to the technologies available in Tübingen and fabricated the samples. I also developed and built the setup, performed the 4.2 K measurements and assisted in the STEM sample preparation and analysis. Further, I did the analysis and interpretation of the data, ran the RCSJ simulations and wrote the manuscript.

2.2.3 Publication 7 & 8: Vortex pinning arrays in $YBa_2Cu_3O_7$ created by focused He ion beam irradiation

Publications 7 and 8 deal with vortex pinning arrays in YBCO that have been fabricated by irradiating different point lattices in the helium ion microscope. Compared to previous methods like masked ion beam irradiation, much denser arrays can be fabricated using He-FIB irradiation. This provides the opportunity to significantly improve pinning, and thus reduce the low-frequency noise of YBCO nanoSQUIDs operated in strong magnetic fields.

Publication 7: Ultradense Tailored Vortex Pinning Arrays in Superconducting $YBa_2Cu_3O_{7-\delta}$ Thin Films Created by Focused He Ion Beam Irradiation for Fluxonics Applications

In the first part of this publication, the irradiation process in the HIM is described. During irradiation, the He ions of the beam collide with the nuclei of the atoms in the sample. In YBCO, this leads to a displacement of oxygen atoms [134, 135], which in turn results in a local reduction or suppression of T_c. If the He beam is focused on the sample surface, the irradiated area will increase with increasing depth due to scattering of the He ions after collisions, producing pinning centers of conical shape instead of the desired cylindrical shape. As a solution to this problem, the He beam has been defocused to a diameter of about 20 nm before irradiation. According to numerical simulations, this results in a cylindrical defect channel of 25 nm width up to a depth of 80 nm for 30 keV He ions.

Using a dose of 15 000 ions per lattice point, two samples with quasi-kagomé (QK) pinning arrays have been irradiated using the helium ion microscope, as shown schematically in Fig. 2.18. The quasi-kagomé lattice consists of a hexagonal lattice in which 3 neighbouring sites are not occupied [136], as shown in the HIM image in Fig. 2.18. Sample QK90 has a lattice spacing of 90 nm and a YBCO film thickness of 75 nm, whereas for sample QK70 the spacing is reduced to 70 nm at a film thickness of 50 nm.

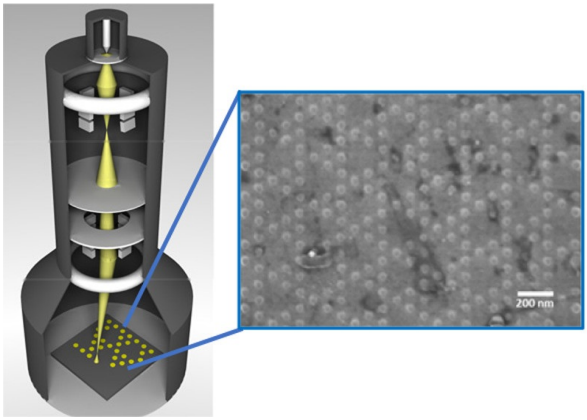

Figure 2.18: Schematic illustration of the HIM irradiation process. The HIM image in blue frame shows a test pattern with the same quasi-kagomé lattice as for sample QK90, but irradiated with a much higher dose (5×10^6 ions/point) for visualization. Figure adapted from appended publication 7.

The second part of the publication treats the electrical transport measurement data of the samples. For both samples, pronounced matching effects in the critical current density and resistivity can be observed over a wide temperature range. This can be seen in Fig. 2.19(a) at $B = 0.23\,\mathrm{T}$ for sample QK90 and in panel (b) at $B = 0.38\,\mathrm{T}$ for QK70. However, these field strengths do correspond neither to B_6, where each of the He-FIB induced pinning sites of the quasi-kagomé lattice is occupied by one vortex, nor to B_9, where the vortex lattice equals the full hexagonal lattice, resulting in minimum lattice distortion energy, after additional occupation of the 3 voids in the QK lattice. Instead, strong matching occurs at B_7 in both samples, which corresponds to one interstitial vortex in each unit cell in addition to the fully occupied QK pinning array.

This behavior can be understood with the help of molecular dynamics simulations that consider not only the vortex-vortex interaction and pinning force, but also an external driving force and thermal stochastic force [137–140]. The vortex configurations for magnetic fields B_6 to B_9 at conditions adapted to the experimental data of QK90 are shown in Fig. 2.19(c). At B_6, not all pinning sites are occupied due to strong repulsion between the vortices in the very dense array and the total energy is thus minimized by movement of some vortices into the voids. These vortices are only weakly pinned, and in turn $I_\mathrm{c}(B_6)$ is not increased. For B_7, nearly all pinning sites are occupied and typically one excess vortex is caged in the voids by the repulsive vortex-vortex force, resulting in the observation of clear matching features at this field value. For B_8 and B_9, this pinning strength (and thus I_c) is reduced again due to the caging of sev-

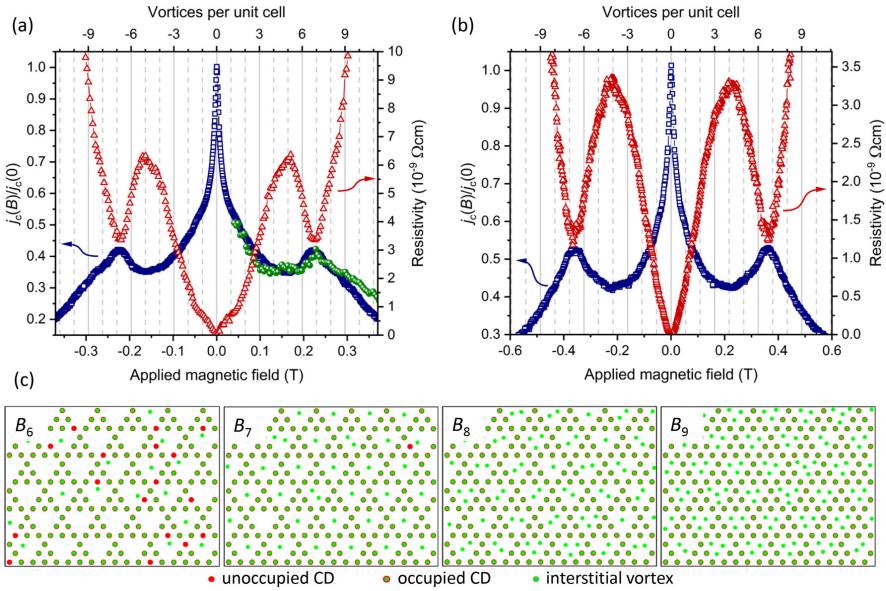

Figure 2.19: (a) Magnetic field dependence of the normalized critical current density (blue squares) at 83 K and resistivity (red triangles) at 83.5 K for sample QK90. Green dots represent results of molecular dynamics simulations. (b) Magnetic field dependence of the normalized critical current density (blue squares) at 52 K and resistivity (red triangles) at 55 K for sample QK70. (c) Simulated vortex distributions in QK90 for different magnetic field values. Figure from appended publication 7.

eral vortices that repel each other. The simulation results are in good agreement with the experimental $I_c(B)$ results, as shown by the green dots in panel (a) of Fig. 2.19.

By reducing the temperature, the balance between the pinning force from the artificial defects and vortex caging can be shifted in favor of the pinning array [141]. Fig. 2.20(a) shows the normalized critical current density j_c versus B of sample QK90 for different temperatures down to 67 K, which is far below T_c. At $T < 80$ K, a second peak at B_6 can be observed. For $T < 75$ K, the normalized critical current density at B_6 becomes larger than at B_7, which is shown in panel (b). This crossover indicates that for low temperatures the pinning at B_6 becomes more efficient than at B_7, as expected due to the increased influence of the artificial pinning centers.

Contributions

This work was done in collaboration with the groups of W. Lang at the University of Vienna where the electric transport measurements were done, V. R. Misko from the University of Antwerp and RIKEN and F. Nori from RIKEN who performed the molecular dynamics simulations, and the group of J. Pedarnig at the Johannes Kepler University Linz, where the YBCO films were fabricated. B. Aichner and I developed the HIM irradiation process. M. Karrer and I irradiated the samples and F. Limberger assisted in the irradiation. Further, I contributed in developing the original idea of irradiation using the HIM, and assisted in the interpretation of the data and writing of the manuscript.

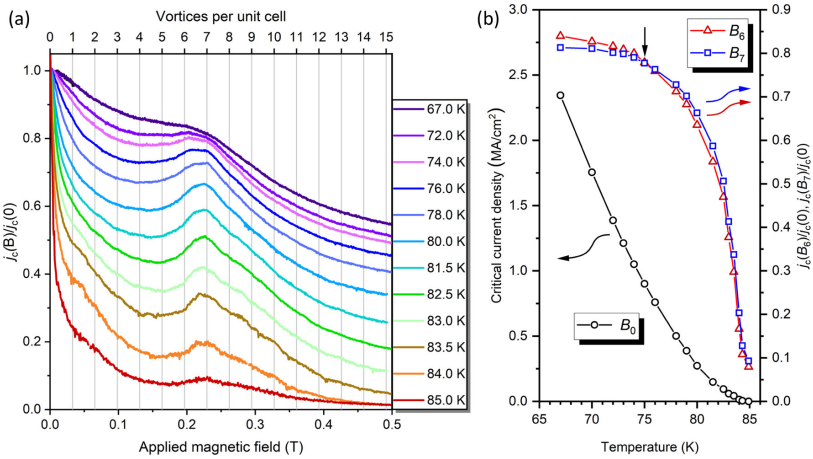

Figure 2.20: (a) Magnetic field dependence of the normalized critical current density for sample QK90 at different temperatures. (b) Temperature dependence of zero-field critical current density (black circles), and normalized critical current densities at B_6 (red triangles) and B_7 (blue squares). Figure from appended publication 7. © 2019 American Chemical Society.

Publication 8: Angular magnetic-field dependence of vortex matching in pinning lattices fabricated by focused or masked helium ion beam irradiation of superconducting $YBa_2Cu_3O_{7-\delta}$ thin films

This publication is a follow-up on publication 7, investigating in detail the dependence of matching effects on the angle at which the magnetic field is applied.

Two samples with square vortex pinning arrays in YBCO have been produced by different methods of irradiation with He ions. For sample SQ200 with a YBCO film thickness of 80 nm, the irradiation was performed using a helium ion microscope as described in publication 7. The beam was intentionally defocused to 50 nm before irradiating a square lattice with 200 nm spacing with a He ion dose of 51 000 ions per lattice point. A schematic illustration of this irradiation method is shown in Fig. 2.21(a). In panel (b), the irradiation process for sample SQ500 with a spacing of 500 nm is shown. This sample has been irradiated via masked ion beam structuring (MIBS) [91], using a collinear beam of 75 keV He ions and a Si stencil mask with holes of 180 nm diameter. The YBCO film thickness of sample SQ500 is 210 nm. Both samples had $T_c \approx 90$ K before irradiation.

Using the Stopping and Range of Ions in Matter (SRIM) software package [142], the defect densities in the defect columns of the pinning arrays can be calculated [143]. According to the simulations, both irradiation methods produce efficient pinning

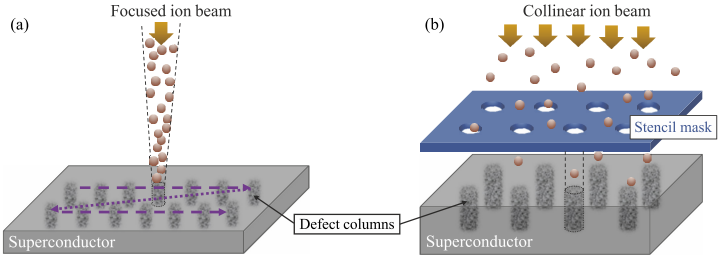

Figure 2.21: Schematic illustration of the irradiation process for (a) sample SQ200 using the helium ion microscope and (b) sample SQ500 using masked ion beam structuring. Figure from appended publication 8. © 2020 Authors.

centers by creating cylindrical columns with suppressed T_c while leaving the non-irradiated regions intact. This is also confirmed by the only minor reduction of the critical temperatures $\Delta T_c = 2.6\,\mathrm{K}$ and $4\,\mathrm{K}$ for SQ200 and SQ500, respectively.

Matching effects can be identified for both samples at the expected values of the applied magnetic field B_a. Sample SQ200 also appears in the supplemental material of publication 7, and the $I_c(B)$ and $R(B)$ data can thus be found in Fig. 1.6 on page 14 of this thesis.

For strong pinning at the artificial pinning lattice, the observed matching effects should depend only on the magnetic field component parallel to the vortex cores [95, 144]. This component scales as $B_\parallel = B_a \cos\alpha$ if the magnetic field is applied at an angle α as sketched in the inset of Fig. 2.22. As shown by the measured $R(B_\parallel)$ curves of sample SQ200 in Fig. 2.22, matching

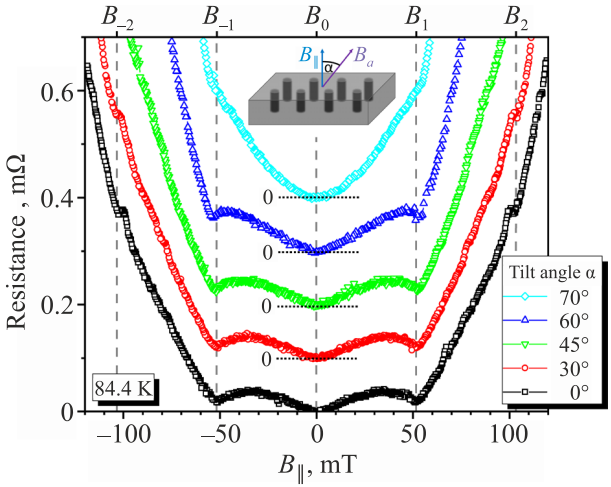

Figure 2.22: Resistance of sample SQ200 versus parallel component of the applied magnetic field as sketched in the inset. For angles $\alpha > 0$, curves are shifted vertically for clarity. Figure from appended publication 8. © 2020 Authors.

effects can be identified at the same values of $B_\parallel$ for angles up to 70°. The parallel component of the matching field is independent of the tilt angle α, indicating that the pinning at the induced defects of the artificial pinning array is much stronger than the intrinsic pinning of interstitial vortices. This is also true for sample SQ500, as can be seen in Fig. 2.23, where the anglular dependence of $B_\parallel$ for the first matching field B_1, as determined experimentally, is shown for both samples.

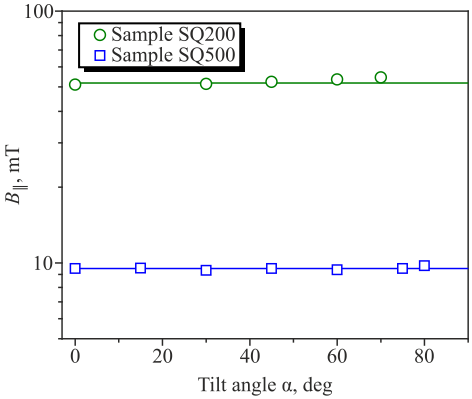

Figure 2.23: Angular dependencies of the parallel components of the first matching fields. Horizontal lines are guides to the eye. Figure from appended publication 8. © 2020 Authors.

Contributions

This work was done in collaboration with the groups of W. Lang at the University of Vienna, where the electric transport measurements and simulations of the columnar defects were done, and the group of J. Pedarnig at the Johannes Kepler University Linz, where the YBCO films were fabricated and the MIBS irradiation was done. B. Aichner and I developed the HIM irradiation process. M. Karrer assisted in the HIM irradiation. I contributed in developing the original idea of irradiation using the HIM and irradiated the sample. I also assisted in interpretation of the data and writing of the manuscript.

2.3 Review article

2.3.1 Publication 9: $YBa_2Cu_3O_7$ and Nb NanoSQUIDs for the investigation of Magnetization Reversal of Individual Magnetic Nanoparticles

This publication is a review article, in which an overview of the nanoSQUID activities within the group in Tübingen is given. This includes publications 1 to 3, 5 and 6 of this thesis as well as previous work on YBCO nanoSQUIDs [37, 38, 45] and further activities on Nb nanoSQUIDs [19, 51, 130, 145] which are not part of this thesis.

Contributions

This publication summarizes work that was done in collaboration with V. Morosh, T. Weimann and O. F. Kieler from the Physikalisch-Technische Bundesanstalt in Braunschweig, where the Nb nanoSQUIDs were fabricated, and M. J. Martínez-Pérez and J. Sesé from the Aragón Materials Science Institute (Spanish National Research Council and University of Zaragoza), where the deposition of Co nanoparticles and parts of the measurements were done. J. Lin, M. Karrer, F. Limberger and myself contributed to the ideas, sample fabrication, measurements and data analysis as specified in the contributions descriptions of publications 1 to 3, 5 and 6. J. Linek and I contributed to work on Nb nanoSQUIDs. Further, I wrote parts of the manuscript.

Chapter 3

Outlook and conclusion

Within the first part of this thesis, nanoSQUIDs based on the high-transition temperature cuprate superconductor $YBa_2Cu_3O_7$ have been used successfully for investigations of the magnetization reversal mechanisms in different magnetic nanoparticles. A precise and controlled positioning of the particles close to the SQUID loop is required to achieve sufficiently strong coupling between the magnetic moment of the particle and the nanoSQUID. This remains a challenging task, especially for smaller particles and materials that cannot be deposited by focused electron-beam-induced deposition or similar methods. This task can be approached in different ways, like for example with the use of carbon nanotubes as vehicles for individual magnetic nanoparticles [146, 147]. While precise handling and positioning of carbon nanotubes is possible with standard

nanopositioning systems, the controlled encapsulation of single nanoparticles inside the carbon nanotubes is still demanding. Another approach would be the deposition of particles from a colloidal solution into topographical trap structures on the surface by capillary forces [148]. Ultimately, the usage of a cryogenic atomic force microscope with a magnetic nanoparticle attached to the tip could enable in-situ reference measurements by retracting the particle from the SQUID.

In the second part of this thesis, very encouraging results of different studies for further improvements of the nanoSQUIDs themselves have been presented. The integration of these optimizations into the design of future nanoSQUIDs is still pending but should be pursued, because the results of measurements performed with such improved nanoSQUIDs can provide even deeper insights into the properties of magnetic nanoparticles and the appealing field of nanomagnetism.

List of acronyms

AFM atomic force microscopy

BR bias reversal

CNT carbon nanotube

dc direct current

EELS electron energy loss spectroscopy

FEBID focused electron-beam-induced deposition

FFT fast Fourier transform

FIB focused ion beam

FLL flux-locked loop

GB grain boundary

GFIS gas field ion source

HIM helium ion microscope

He-FIB focused helium ion beam

IVC current-voltage characteristic

JJ Josephson junction

LSAT lanthanum aluminate - strontium aluminium tantalate, $(LaAlO_3)_{0.3}(Sr_2AlTaO_6)_{0.7}$

MgO magnesium oxide, MgO

MIBS masked ion beam structuring

MNP magnetic nanoparticle

NW nanowire

PLD pulsed laser deposition

QSD quasi-single domain

QK quasi-kagomé

RCSJ resistively and capacitively shunted junction

rms root mean square

SEM scanning electron microscopy

SQUID superconducting quantum interference device

STEM scanning transmission electron microscopy

STO strontium titanate, $SrTiO_3$

TEM transmission electron microscopy

VS vortex state

Bibliography

[1] L. Thomas, F. Lionti, R. Ballou, D. Gatteschi, R. Sessoli, and B. Barbara, Nature **383**, 145–147 (1996).

[2] S. Piramanayagam and K. Srinivasan, J. Magn. Magn. Mater. **321**, 485–494 (2009).

[3] J. Åkerman, Science **308**, 508–510 (2005).

[4] S. Odenbach, MRS Bull. **38**, 921–924 (2013).

[5] R. C. Semelka and T. K. G. Helmberger, Radiology **218**, 27–38 (2001).

[6] A. Sarwar, A. Nemirovski, and B. Shapiro, J. Magn. Magn. Mater. **324**, 742–754 (2012).

[7] A. Jordan, R. Scholz, P. Wust, H. Fähling, and R. Felix, J. Magn. Magn. Mater. **201**, 413–419 (1999).

[8] R. Klingeler, S. Hampel, and B. Büchner, Int. J. Hyperthermia **24**, 496–505 (2008).

[9] A. P. Guimarães, *Principles of Nanomagnetism* (Springer Berlin Heidelberg, 2009).

[10] S. A. Majetich, T. Wen, and O. T. Mefford, MRS Bull. **38**, 899–903 (2013).

[11] C. P. Bean, J. Appl. Phys. **26**, 1381–1383 (1955).

[12] W. Wernsdorfer, Adv. Chem. Phys. **118**, 99–190 (2001).

[13] E. C. Stoner and E. P. Wohlfarth, Philos. Trans. Roy. Soc. London **240**, 599–642 (1948).

[14] E. H. Frei, S. Shtrikman, and D. Treves, Phys. Rev. **106**, 446–455 (1957).

[15] J. Kurkijärvi, Phys. Rev. B **6**, 832–835 (1972).

[16] M. Bode, O. Pietzsch, A. Kubetzka, and R. Wiesendanger, Phys. Rev. Lett. **92**, 067201 (2004).

[17] A. Tonomura, T. Matsuda, J. Endo, T. Arii, and K. Mihama, Phys. Rev. B **34**, 3397–3402 (1986).

[18] D. Rugar, R. Budakian, H. J. Mamin, and B. W. Chui, Nature **430**, 329–332 (2004).

[19] A. Buchter, J. Nagel, D. Rüffer, F. X. amd D. P. Weber, O. F. Kieler, T. Weimann, J. Kohlmann, A. B. Zorin, E. Russo-Averchi, R. Huber, P. Berberich, A. Fontcuberta i Morral, M. Kemmler, R. Kleiner, D. Koelle, D. Grundler, and M. Poggio, Phys. Rev. Lett. **111**, 067202 (2013).

[20] J. M. Taylor, P. Cappellaro, L. Childress, L. Jiang, D. Budker, P. R. Hemmer, A. Yacoby, R. Walsworth, and M. D. Lukin, Nat. Phys. **4**, 810–816 (2008).

[21] G. Balasubramanian, I. Y. Chan, R. Kolesov, M. Al-Hmoud, J. Tisler, C. Shin, C. Kim, A. Wojcik, P. R. Hemmer, A. Krueger, T. Hanke, A. Leitenstorfer, R. Bratschitsch, F. Jelezko, and J. Wrachtrup, Nature **455**, 648–651 (2008).

[22] J. R. Maze, P. L. Stanwix, J. S. Hodges, S. Hong, J. M. Taylor, P. Cappellaro, L. Jiang, M. V. G. Dutt, E. Togan, A. S. Zibrov, A. Yacoby, R. L. Walsworth, and M. D. Lukin, Nat. Nanotechnol. **455**, 644–647 (2008).

[23] L. Theil Kuhn, A. K. Geim, J. G. S. Lok, P. Hedegård, K. Ylänen, J. B. Jensen, E. Johnson, and P. E. Lindelof, Eur. Phys. J. D **10**, 259–263 (2000).

[24] S. Wirth and S. v. Molnár, Appl. Phys. Lett. **76**, 3283–3285 (2000).

[25] Y. Li, P. Xiong, S. von Molnár, S. Wirth, Y. Ohno, and H. Ohno, Appl. Phys. Lett. **80**, 4644–4646 (2002).

[26] W. Wernsdorfer, K. Hasselbach, D. Mailly, B. Barbara, A. Benoit, L. Thomas, and G. Suran, J. Magn. Magn. Mater. **145**, 33–39 (1995).

[27] R. Doll and M. Näbauer, Phys. Rev. Lett. **7**, 51–52 (1961).

[28] B. S. Deaver, Jr. and W. M. Fairbank, Phys. Rev. Lett. **7**, 43–46 (1961).

[29] B. D. Josephson, Adv. Phys. **14**, 419–451 (1965).

[30] W. Wernsdorfer, Supercond. Sci. Technol. **22**, 064013 (2009).

[31] J. Clarke and A. I. Braginski, eds., *The SQUID Handbook. Vol. I: Fundamentals and Technology of SQUIDs and SQUID systems* (Wiley-VCH, Weinheim, 2004).

[32] M. Ketchen, D. Awschalom, W. Gallagher, A. Kleinsasser, R. Sandstrom, J. Rozen, and B. Bumble, IEEE Trans. Magn. **25**, 1212–1215 (1989).

[33] N. C. Koshnick, M. E. Huber, J. A. Bert, C. W. Hicks, J. Large, H. Edwards, and K. A. Moler, Appl. Phys. Lett. **93**, 243101 (2008).

[34] D. L. Tilbrook, Supercond. Sci. Technol. **22**, 064003 (2009).

[35] K. Hasselbach, C. Veauvy, and D. Mailly, Physica C **332**, 140–147 (2000).

[36] V. Bouchiat, Supercond. Sci. Technol. **22**, 064002 (2009).

[37] J. Nagel, K. B. Konovalenko, M. Kemmler, M. Turad, R. Werner, E. Kleisz, S. Menzel, R. Klingeler, B. Büchner, R. Kleiner, and D. Koelle, Supercond. Sci. Technol. **24**, 015015 (2011).

[38] R. Wölbing, T. Schwarz, B. Müller, J. Nagel, M. Kemmler, R. Kleiner, and D. Koelle, Supercond. Sci. Technol. **27**, 125007 (2014).

[39] C. Granata, P. Silvestrini, B. Ruggiero, and A. Vettoliere, IEEE Trans. Appl. Supercond. **28**, 1600705 (2018).

[40] R. Meservey and P. M. Tedrow, J. Appl. Phys. **40**, 2028–2034 (1969).

[41] C. Granata and A. Vettoliere, Phys. Rep. **614**, 1–69 (2016).

[42] M. J. Martínez-Pérez and D. Koelle, Phys. Sci. Rev. **2**, 20175001 (2017).

[43] L. Hao and C. Granata, Supercond. Sci. Technol. **30**, 050301 (2017).

[44] D. Vasyukov, Y. Anahory, L. Embon, D. Halbertal, J. Cuppens, L. Ne'eman, A. Finkler, Y. Segev, Y. Myasoedov, M. L. Rappaport, M. E. Huber, and E. Zeldov, Nat. Nanotechnol. **8**, 639–644 (2013).

[45] T. Schwarz, J. Nagel, R. Wölbing, M. Kemmler, R. Kleiner, and D. Koelle, ACS Nano **7**, 844–850 (2013).

[46] J. Lin, B. Müller, J. Linek, M. Karrer, M. J. Martínez-Pérez, R. Kleiner, and D. Koelle, Nanoscale **12**, 5658–5668 (2020).

[47] J. M. De Teresa, A. Fernández-Pacheco, R. Córdoba, L. Serrano-Ramón, S. Sangiao, and M. R. Ibarra, J. Phys. D: Appl. Phys. **49**, 243003 (2016).

[48] R. Córdoba, J. Sesé, J. De Teresa, and M. Ibarra, Microelectron. Eng. **87**, 1550–1553 (2010).

[49] J. Pablo-Navarro, D. Sanz-Hernández, C. Magén, A. Fernández-Pacheco, and J. M. de Teresa, J. Phys. D: Appl. Phys. **50**, 18LT01 (2017).

[50] D. Hagedorn, O. Kieler, R. Dolata, R. Behr, F. Müller, J. Kohlmann, and J. Niemeyer, Supercond. Sci. Technol. **19**, 294–298 (2006).

[51] R. Wölbing, J. Nagel, T. Schwarz, O. Kieler, T. Weimann, J. Kohlmann, A. B. Zorin, M. Kemmler, R. Kleiner, and D. Koelle, Appl. Phys. Lett. **102**, 192601 (2013).

[52] S. A. Cybart, E. Y. Cho, J. T. Wong, B. H. Wehlin, M. K. Ma, C. Huynh, and R. C. Dynes, Nat. Nanotechnol. **10**, 598–602 (2015).

[53] B. W. Ward, J. A. Notte, and N. P. Economou, J. Vac. Sci. Technol. B **24**, 2871–2874 (2006).

[54] M. T. Postek, A. Vladár, C. Archie, and B. Ming, Meas. Sci. Technol. **22**, 024004 (2011).

[55] G. Hlawacek and A. Gölzhäuser, eds., *Helium Ion Microscopy* (Springer International Publishing, 2016).

[56] D. Emmrich, A. Beyer, A. Nadzeyka, S. Bauerdick, J. C. Meyer, J. Kotakoski, and A. Gölzhäuser, Appl. Phys. Lett. **108**, 163103 (2016).

[57] S. K. Tolpygo, B. Nadgorny, S. Shokhor, F. Tafuri, Y. Lin, A. Bourdillon, and M. Gurvitch, Physica C **209**, 211–214 (1993).

[58] A. J. Pauza, W. E. Booij, K. Herrmann, D. F. Moore, M. G. Blamire, D. A. Rudman, and L. R. Vale, J. Appl. Phys. **82**, 5612–5632 (1997).

[59] W. E. Booij, A. J. Pauza, D. F. Moore, E. J. Tarte, and M. G. Blamire, IEEE Trans. Appl. Supercond. **7**, 3025–3028 (1997).

[60] W. E. Booij, C. A. Elwell, E. J. Tarte, P. F. McBrien, F. K. D. F. Moore, M. G. Blamire, N. H. Peng, and C. Jeynes, IEEE Trans. Appl. Supercond. **9**, 2886–2889 (1999).

[61] A. E. White, K. T. Short, R. C. Dynes, A. F. J. Levi, M. Anzlowar, K. W. Baldwin, P. A. Polakos, T. A. Fulton, and L. N. Dunkleberger, Appl. Phys. Lett. **53**, 1010–1012 (1988).

[62] K. Chen, S. A. Cybart, and R. C. Dynes, Appl. Phys. Lett. **85**, 2863–2865 (2004).

[63] K. Chen, S. A. Cybart, and R. C. Dynes, IEEE Trans. Appl. Supercond. **15**, 149–152 (2005).

[64] S. S. Tinchev, Supercond. Sci. Technol. **3**, 500–503 (1990).

[65] N. Bergeal, X. Grison, J. Lesueur, G. Faini, M. Aprili, and J. P. Contour, Appl. Phys. Lett. **87**, 102502 (2005).

[66] E. Y. Cho, M. K. Ma, C. Huynh, K. Pratt, D. N. Paulson, V. N. Glyantsev, R. C. Dynes, and S. A. Cybart, Appl. Phys. Lett. **106**, 252601 (2015).

[67] E. Y. Cho, Y. W. Zhou, J. Y. Cho, and S. A. Cybart, Appl. Phys. Lett. **113**, 022604 (2018).

[68] E. Y. Cho, H. Li, J. C. LeFebvre, Y. W. Zhou, R. C. Dynes, and S. A. Cybart, Appl. Phys. Lett. **113**, 162602 (2018).

[69] H. Li, H. Cai, E. Y. Cho, S. J. McCoy, Y.-T. Wang, J. C. LeFebvre, Y. W. Zhou, and S. A. Cybart, Appl. Phys. Lett. **116**, 070601 (2020).

[70] A. T. Cortez, E. Y. Cho, H. Li, D. Cunnane, B. Karasik, and S. A. Cybart, IEEE Trans. Appl. Supercond. **29**, 1102305 (2019).

[71] J. Wang, H. Li, E. Y. Cho, J. C. LeFebvere, and S. A. Cybart, IEEE Trans. Appl. Supercond. **29**, 1600804 (2019).

[72] A. A. Abrikosov, J. Exp. Theor. Phys. **5**, 1174–1182 (1957).

[73] V. V. Moshchalkov and J. Fritzsche, *Nanostructured Superconductors* (World Scientific Publishing, Singapore, 2011).

[74] K. Matsumoto and P. Mele, Supercond. Sci. Technol. **23**, 014001 (2010).

[75] A. I. Larkin and Y. N. Ovchinnikov, J. Low Temp. Phys. **34**, 409–428 (1979).

[76] J. I. Martin, M. Velez, J. Nogues, and I. K. Schuller, Phys. Rev. Lett **79**, 1929–1932 (1997).

[77] J. E. Villegas, E. M. Gonzalez, M. I. Montero, I. K. Schuller, and J. L. Vicent, Phys. Rev. B **68**, 224504 (2003).

[78] J. E. Villegas, M. I. Montero, C.-P. Li, and I. K. Schuller, Phys. Rev. Lett. **97**, 027002 (2006).

[79] A. V. Silhanek, W. Gillijns, V. V. Moshchalkov, B. Y. Zhu, J. Moonens, and L. H. A. Leunissen, Appl. Phys. Lett. **89**, 152507 (2006).

[80] A. T. Fiory, A. F. Hebard, and S. Somekh, Appl. Phys. Lett. **32**, 73–75 (1978).

[81] A. N. Lykov, Sol. Stat. Commun. **86**, 531–533 (1993).

[82] M. Baert, V. V. Metlushko, R. Jonckheere, V. V. Moshchalkov, and Y. Bruynseraede, Phys. Rev. Lett. **74**, 3269–3272 (1995).

[83] V. V. Moshchalkov, M. Baert, V. V. Metlushko, E. Rosseel, M. J. V. Bael, K. Temst, Y. Bruynseraede, and R. Jonckheere, Phys. Rev. B **57**, 3615–3622 (1998).

[84] U. Welp, Z. L. Xiao, J. S. Jiang, V. K. Vlasko-Vlasov, S. D. Bader, G. W. Crabtree, J. Liang, H. Chik, and J. M. Xu, Phys. Rev. B **66**, 212507 (2002).

[85] M. Kemmler, C. Gürlich, A. Sterck, H. Pöhler, M. Neuhaus, M. Siegel, R., Kleiner, and D. Koelle, Phys. Rev. Lett. **97**, 147003 (2006).

[86] V. R. Misko, D. Bothner, M. Kemmler, R. Kleiner, D. Koelle, F. M. Peeters, and F. Nori, Phys. Rev. B **82**, 184512 (2010).

[87] D. Bothner, R. Seidl, V. R. Misko, R. Kleiner, D. Koelle, and M. Kemmler, Supercond. Sci. Technol. **27**, 065002 (2014).

[88] L. Civale, A. D. Marwick, T. K. Worthington, M. A. Kirk, J. R. Thompson, L. Krusin-Elbaum, Y. Sun, J. R. Clem, and F. Holtzberg, Phys. Rev. Lett. **67**, 648–651 (1991).

[89] L. Civale, Supercond. Sci. Technol. **10**, A11–A28 (1997).

[90] A. Castellanos, R. Wördenweber, G. Ockenfuss, A. v. Hart, and K. Keck, Appl. Phys. Lett. **71**, 962–964 (1997).

[91] W. Lang, M. Dineva, M. Marksteiner, T. Enzenhofer, K. Siraj, M. Peruzzi, J. D. Pedarnig, D. Bäuerle, R. Kornтner, E. Cekan, and et al., Microelectron. Eng. **83**, 1495–1498 (2006).

[92] W. Lang, H. Richter, M. Marksteiner, K. Siraj, M. Bodea, J. Pedarnig, C. Grigoropoulos, D. Bauerle, C. Hasenfuss, L. Palmetshofer, R. Kolarova, and P. Bauer, Int. J. Nanotechnol. **6**, 704–714 (2009).

[93] J. Pedarnig, K. Siraj, M. Bodea, I. Puica, W. Lang, R. Kolarova, P. Bauer, K. Haselgrübler, C. Hasenfuss, I. Beinik, and C. Teichert, Thin Solid Films **518**, 7075–7080 (2010).

[94] I. Swiecicki, C. Ulysse, T. Wolf, R. Bernard, N. Bergeal, J. Briatico, G. Faini, J. Lesueur, and J. E. Villegas, Phys. Rev. B **85**, 224502 (2012).

[95] J. Trastoy, V. Rouco, C. Ulysse, R. Bernard, A. Palau, T. Puig, G. Faini, J. Lesueur, J. Briatico, and J. E. Villegas, New J. Phys. **15**, 103022 (2013).

[96] L. Haag, G. Zechner, W. Lang, M. Dosmailov, M. Bodea, and J. Pedarnig, Physica C **503**, 75–81 (2014).

[97] G. Zechner, F. Jausner, L. T. Haag, W. Lang, M. Dosmailov, M. A. Bodea, and J. D. Pedarnig, Phys. Rev. Applied **8**, 014021 (2017).

[98] J. Eisenmenger, M. Oettinger, C. Pfahler, A. Plettl, P. Walther, and P. Ziemann, Phys. Rev. B **75**, 144514 (2007).

[99] P. Sabatino, C. Cirillo, G. Carapella, M. Trezza, and C. Attanasio, J. Appl. Phys. **108**, 053906 (2010).

[100] B. Dam, J. M. Huijbregtse, F. C. Klaassen, R. C. F. V. der Geest, G. Doornbos, J. H. Rector, A. M. Testa, S. Freisem, J. C. Martinez, B. Stäuble-Pümpin, and R. Griessen, Nature **399**, 439–442 (1999).

[101] R. Wördenweber and P. Selders, Physica C **366**, 135–146 (2002).

[102] D. D. Awschalom, J. R. Rozen, M. B. Ketchen, W. J. Gallagher, A. W. Kleinsasser, R. L. Sandstrom, and B. Bumble, Appl. Phys. Lett. **53**, 2108–2110 (1988).

[103] D. J. Van Harlingen, R. H. Koch, and J. Clarke, Appl. Phys. Lett. **41**, 197–199 (1982).

[104] E. M. Levenson-Falk, R. Vijay, N. Antler, and I. Siddiqi, Supercond. Sci. Technol. **26**, 055015 (2013).

[105] R. H. Koch, J. Clarke, W. M. Goubau, J. M. Martinis, C. M. Pegrum, and D. J. V. Harlingen, J. Low Temp. Phys. **51**, 207–224 (1983).

[106] M. Khalid, A. Setzer, M. Ziese, P. Esquinazi, D. Spemann, A. Pöppl, and E. Goering, Phys. Rev. B **81**, 214414 (2010).

[107] K. Potzger, J.Osten, A. A.Levin, A.Shalimov, G.Talut, H.Reuther, S.Arpaci, D. Bürger, H. Schmidt, T.Nestler, and D. C.Meyer, J. Magn. Magn. Mater. **323**, 1551–1562 (2011).

[108] A. Winkler, T. Mühl, S. Menzel, R. Kozhuharova-Koseva, S. Hampel, A. Leonhardt, and B. Büchner, J. Appl. Phys. **99**, 104905 (2006).

[109] A. Leonhardt, S. Hampel, C. Müller, I. Mönch, R. Koseva, M. Ritschel, D. Elefant, K. Biedermann, and B. Büchner, Chem. Vap. Deposition **12**, 380–387 (2006).

[110] T. Mühl, J. Körner, S. Philippi, C. F. Reiche, A. Leonhardt, and B. Büchner, Appl. Phys. Lett. **101**, 112401 (2012).

[111] K. Lipert, S. Bahr, F. Wolny, P. Atkinson, U. Weißker, T. Mühl, O. G. Schmidt, B. Büchner, and R. Klingeler, Appl. Phys. Lett. **97**, 212503 (2010).

[112] A. Aharoni, Phys. Stat. Sol. **16**, 3–42 (1966).

[113] M. M. Khapaev, A. Y. Kidiyarova-Shevchenko, P. Magnelind, and M. Y. Kupriyanov, IEEE Trans. Appl. Supercond. **11**, 1090–1093 (2001).

[114] M. M. Khapaev, M. Y. Kupriyanov, E. Goldobin, and M. Siegel, Supercond. Sci. Technol. **16**, 24–27 (2003).

[115] M. M. Khapaev and M. Y. Kupriyanov, Supercond. Sci. Technol. **28**, 055013 (2015).

[116] M. E. Schabes, J. Magn. Magn. Mater. **95**, 249–288 (1991).

[117] J. Pablo-Navarro, C. Magén, and J. M. de Teresa, ACS Appl. Nano Mater. **1**, 38–46 (2018).

[118] A. G. Zaitsev, R. Schneider, G. Linker, F. Ratzel, R. Smithey, P. Schweiss, J. Geerk, R. Schwab, and R. Heidinger, Rev. Sci. Instr. **73**, 335–344 (2002).

[119] L. Thiel, D. Rohner, M. Ganzhorn, P.Appel, E. Neu, B. Müller, R. Kleiner, D. Koelle, and P. Maletinsky, Nat. Nanotechnol. **11**, 677–681 (2016).

[120] W. Wernsdorfer, K. Hasselbach, A. Benoit, G. Cernicchiaro, D. Mailly, B. Barbara, and L. Thomas, J. Magn. Magn. Mater. **151**, 38–44 (1995).

[121] A. Fernández-Pacheco, J. M. De Teresa, A. Szkudlarek, R. Córdoba, M. R. Ibarra, D. Petit, L. O'Brien, H. T.

Zeng, E. R. Lewis, D. E. Read, and R. P. Cowburn, Nanotechnol. **20**, 475704 (2009).

[122] J. Pablo-Navarro, C. Magén, and J. M. de Teresa, Nanotechnol. **27**, 285302 (2016).

[123] K. Y. Guslienko, V. Novosad, Y. Otani, H. Shima, and K. Fukamichi, Phys. Rev. B **65**, 024414 (2001).

[124] T. Fischbacher, M. Franchin, G. Bordignon, and H. Fangohr, IEEE Trans. Magn. **43**, 2896–2898 (2007).

[125] M. Goiriena-Goikoetxea, K. Y. Guslienko, M. Rouco, I. Orue, E. Berganza, M. Jaafar, A. Asenjo, M. L. Fernández-Gubieda, L. Fernández Barquín, and A. García-Arribas, Nanoscale **9**, 11269–11278 (2017).

[126] J. Mejía-López, D. Altbir, P. Landeros, J. Escrig, A. H. Romero, I. V. Roshchin, C.-P. Li, M. R. Fitzsimmons, X. Batlle, and I. K. Schuller, Phys. Rev. B **81**, 184417 (2010).

[127] R. K. Dumas, K. Liu, C.-P. Li, I. V. Roshchin, and I. K. Schuller, Appl. Phys. Lett. **91**, 202501 (2007).

[128] G. A. Melkov, Y. Kobljanskyj, V. Novosad, A. N. Slavin, and K. Y. Guslienko, Phys. Rev. B **88**, 220407 (2013).

[129] V. Morosh, J. Linek, B. Müller, M. J. Martínez-Pérez, S. Wolter, T. Weimann, J. Beyer, T. Schurig, O. Kieler, A. B. Zorin, R. Kleiner, and D. Koelle, submitted to Phys. Rev. Applied .

[130] J. Nagel, O. F. Kieler, T. Weimann, R. Wölbing, J. Kohlmann, A. B. Zorin, R. Kleiner, D. Koelle, and M. Kemmler, Appl. Phys. Lett. **99**, 032506 (2011).

[131] W. C. Stewart, Appl. Phys. Lett **12**, 277–280 (1968).

[132] D. McCumber, J. Appl. Phys. **39**, 3113–3118 (1968).

[133] R. Gross, L. Alff, A. Beck, O. Froehlich, D. Koelle, and A. Marx, IEEE Trans. Appl. Supercond. **7**, 2929–2935 (1997).

[134] Z. Sefrioui, D. Arias, E. M. González, C. León, J. Santamaria, and J. L. Vicent, Phys. Rev. B **63**, 064503 (2001).

[135] S. A. Cybart, P. X. T. Yen, E. Y. Cho, J. U. Huh, V. N. Glyantsev, C. S. Yung, B. Moeckly, J. W. Beeman, and R. C. Dynes, IEEE Trans. Appl. Supercond. **24**, 1100105 (2014).

[136] D. Perez de Lara, A. Alija, E. M. Gonzalez, M. Velez, J. I. Martin, and J. L. Vicent, Phys. Rev. B **82**, 174503 (2010).

[137] V. R. Misko, S. Savel'ev, and F. Nori, Phys. Rev. Lett. **95**, 177007 (2005).

[138] V. R. Misko, S. Savel'ev, and F. Nori, Phys. Rev. B **74**, 024522 (2006).

[139] C. Reichhardt, C. J. Olson, and F. Nori, Phys. Rev. B **57**, 7937–7943 (1998).

[140] V. R. Misko and F. Nori, Phys. Rev. B **85**, 184506 (2012).

[141] I. B. Khalfin and B. Y. Shapiro, Physica C **207**, 359–365 (1993).

[142] J. F. Ziegler, M. Ziegler, and J. Biersack, Nucl. Instrum. Methods Phys. Res., Sect. B **268**, 1818–1823 (2010).

[143] K. Mletschnig and W. Lang, Microelectron. Eng. **215**, 110982 (2019).

[144] G. Zechner, K. L. Mletschnig, W. Lang, M. Dosmailov, M. A. Bodea, and J. D. Pedarnig, Supercond. Sci. Technol. **31**, 044002 (2018).

[145] J. Nagel, A. Buchter, F. Xue, O. F. Kieler, T. Weimann, J. Kohlmann, A. B. Zorin, D. Rüffer, E. Russo-Averchi, R. Huber, P. Berberich, A. Fontcuberta i Morral, D. Grundler, R. Kleiner, D. Koelle, M. Poggio, and M. Kemmler, Phys. Rev. B **88**, 064425 (2013).

[146] M. del Carmen Giménez-López, F. Moro, A. L. Torre, C. J. Gómez-García, P. D. Brown, J. van Slageren, and A. N. Khlobystov, Nat. Commun. **2**, 407 (2011).

[147] M. Gellesch, M. Dimitrakopoulou, M. Scholz, C. G. Blum, M. Schulze, J. van den Brink, S. Hampel, S. Wurmehl, and B. Büchner, Cryst. Growth Des. **13**, 2707–2710 (2013).

[148] V. Flauraud, M. Mastrangeli, G. D. Bernasconi, J. Butet, D. T. L. Alexander, E. Shahrabi, O. J. F. Martin, and J. Brugger, Nat. Nanotechnol. **12**, 73–80 (2017).

Appended publications

Publication 1

Low-Noise $YBa_2Cu_3O_7$ Nano-SQUIDs for Performing Magnetization-Reversal Measurements on Magnetic Nanoparticles

T. Schwarz,[1] R. Wölbing,[1] C. F. Reiche,[2] B. Müller,[1] M. J. Martínez-Pérez,[1] T. Mühl,[2] B. Büchner,[2] R. Kleiner,[1] and D. Koelle[1]

[1]*Physikalisches Institut-Experimentalphysik II and Center for Collective Quantum Phenomena in LISA$^+$, Universität Tübingen, Auf der Morgenstelle 14, D-72076 Tübingen, Germany*

[2]*Leibniz Institute for Solid State and Materials Research IFW Dresden, Helmholtzstrasse 20, 01069 Dresden, Germany*

(Received 1 October 2014; published 17 April 2015)

We fabricate $YBa_2Cu_3O_7$ (YBCO) direct-current nano- superconducting quantum-interference devices (nano-SQUIDs) based on grain-boundary Josephson junctions by focused-ion-beam patterning. Characterization of electric transport and noise properties at 4.2 K in a magnetically shielded environment yields a very small inductance L of a few pH for an optimized device geometry. This, in turn, results in very low values of flux noise $< 50\ n\Phi_0/Hz^{1/2}$ in the thermal white-noise limit, which yields spin sensitivities of a few $\mu_B/Hz^{1/2}$ (Φ_0 is the magnetic flux quantum, and μ_B is the Bohr magneton). We observe frequency-dependent excess noise up to 7 MHz, which can be eliminated only partially by bias reversal readout. This behavior indicates the presence of fluctuators of unknown origin, possibly related to defect-induced spins in the $SrTiO_3$ substrate. We demonstrate the potential of using YBCO nano-SQUIDs for the investigation of small spin systems, by placing a 39-nm-diameter Fe nanowire encapsulated in a carbon nanotube on top of a nonoptimized YBCO nano-SQUID and by measuring the magnetization reversal of the Fe nanowire via the change of magnetic flux coupled to the nano-SQUID. The measured flux signals upon magnetization reversal of the Fe nanowire are in very good agreement with estimated values, and the determined switching fields indicate magnetization reversal of the nanowire via curling mode.

DOI: 10.1103/PhysRevApplied.3.044011

I. INTRODUCTION

Small spin systems or magnetic nanoparticles (MNPs), like single-molecular magnets, nanowires, or nanotubes behave very differently from magnetic bulk material, which makes them very interesting, both for basic research and applications ranging from spintronics and spin-based quantum-information processing to industrial use of ferrofluidic devices and biomedical applications [1–7]. Because of their nanoscale size, MNPs have very small magnetic moments, which does not allow one to use standard magnetic characterization techniques for the investigation of their properties. In one approach, which has been pioneered by Wernsdorfer [8], MNPs are placed very close to miniaturized superconducting quantum-interference devices (SQUIDs), often referred to as micro-SQUIDs or nano-SQUIDs [9–25], and the magnetization reversal of MNPs is measured directly via the change of stray magnetic flux coupled to the micro-SQUIDs or nano-SQUIDs. Major challenges for this application are the development of SQUIDs (i) with ultralow flux noise, which can be achieved via the reduction of the inductance L of the SQUID loop and (ii) which can be operated in very large magnetic fields (up to the tesla range), without significant degradation of their noise performance.

The most common approach for the realization of direct-current (dc) nano-SQUIDs uses two constriction-type Josephson junctions (CJJs) intersecting the SQUID loop [11,12,14,16,23,26,27]. In this case, optimum coupling between a MNP and the nano-SQUID is achieved by placing the particle directly on top of one of the CJJs. The use of CJJs offers the possibility to operate the SQUIDs in strong magnetic fields. However, if conventional metallic superconductors such as Pb or Nb are used, high-field operation is limited by the upper critical field of typically 1 T for thin films [28]. Still, it has been demonstrated that by using ultrathin films, this limitation can be overcome [29]. However, with ultrathin films the SQUID inductance L is dominated by a large kinetic inductance contribution, which yields large flux noise. To date, the most successful approach is the SQUID on tip (SOT) [26]. With the so far smallest Pb SOT with 46-nm effective loop diameter and 15-nm film thickness, ultralow flux noise down to $50\ n\Phi_0/Hz^{1/2}$ at 4.2 K has been demonstrated [28] (Φ_0 is the magnetic flux quantum). The inductance for a slightly larger device (56-nm effective diameter) was estimated as $L = 5.8$ pH. The SOT technology is extremely powerful for high-resolution scanning SQUID microscopy and provides a spin sensitivity below $1\ \mu_B/Hz^{1/2}$ for certain intervals of applied magnetic field up to about 1 T (μ_B is the Bohr magneton) estimated for a pointlike MNP with 10 nm distance to the SOT. However, maintaining the optimum flux bias point in a variable

magnetic field is not possible; i.e., the flux noise and spin sensitivity strongly depend on the applied field, which makes such devices less interesting for the investigation of the magnetization reversal of MNPs.

An alternative approach is the use of $YBa_2Cu_3O_7$ (YBCO) dc nano-SQUIDs with grain-boundary Josephson junctions (GBJJs) for operation at temperature $T = 4.2$ K and below [30]. Magnetization reversal of a MNP can be detected by applying an in-plane magnetic field perpendicular to the grain boundary, i.e., without significant suppression of the GBJJ critical currents. The huge upper critical field of YBCO in the range of tens of teslas offers the possibility for operation in strong fields up to the tesla range, without using ultrathin films [31]. Hence, very low inductance devices with potentially ultralow flux noise can be realized.

Very recently, we performed an optimization study for the design of YBCO nano-SQUIDs [32]. This work is based on the calculation of the coupling factor ϕ_μ, i.e., the amount of magnetic flux coupled to the SQUID per magnetic moment of a pointlike MNP placed on top of a narrow constriction inserted into the SQUID loop. This additional constriction allows for the optimization of ϕ_μ (via constriction geometry) without affecting the junctions. In addition, we performed numerical simulations to calculate the SQUID inductance and root-mean-square (rms) spectral density of flux noise $S_{\Phi,w}^{1/2}$ in the thermal white-noise limit. This approach enabled us to predict the spin sensitivity in the thermal white-noise limit $S_{\mu,w}^{1/2} = S_{\Phi,w}^{1/2}/\phi_\mu$ for our devices as a function of all relevant device parameters. This optimization study predicts optimum performance for a YBCO film thickness $d \approx 120$ nm, which allows us to realize nano-SQUIDs with very small L of a few pH. For optimized devices, we predict $S_{\Phi,w}^{1/2}$ of several tens of $n\Phi_0/Hz^{1/2}$ and $\phi_\mu \sim 10$–$20\ n\Phi_0/\mu_B$ (for a MNP placed 10 nm above the YBCO film on top of the constriction) yielding a spin sensitivity $S_{\mu,w}^{1/2}$ of a few $\mu_B/Hz^{1/2}$.

Here, we report on the realization of optimized YBCO nano-SQUIDs based on GBJJs and on the experimental determination of their electric transport and noise properties in a magnetically shielded environment at $T = 4.2$ K. To demonstrate the suitability of our YBCO nano-SQUIDs for the detection of small spin systems, we present the measurement of the magnetization reversal (up to approximately 200 mT at $T = 4.2$ K) of an Fe nanowire with diameter $d_{Fe} = 39$ nm, which is positioned close the SQUID loop.

II. DEVICE FABRICATION AND EXPERIMENT SETUP

The fabrication of the devices is carried out according to Refs. [30,31]. A *c*-axis-oriented YBCO thin film of thickness d is grown epitaxially by pulsed laser deposition on a $SrTiO_3$ (STO) [001] bicrystal substrate with a 24° grain-boundary misorientation angle. An *in situ* evaporated Au layer of thickness d_{Au} serves as shunt resistance to provide nonhysteretic current-voltage characteristics (IVCs). SQUIDs with smallest line widths down to 50 nm are patterned by focused-ion-beam (FIB) milling with 30-keV Ga ions. The Au layer also minimizes Ga implantation into the YBCO film during FIB milling.

For characterization of the device properties, electric transport and noise measurements are performed in an electrically and magnetically shielded environment at $T = 4.2$ K, i.e., with the samples immersed into liquid He. By applying a modulation current I_{mod} across the constriction, the magnetic flux coupled to the SQUID can be modulated. This scheme allows flux biasing at the optimum working point and operation in a flux-locked loop (FLL) mode [33]. In FLL mode, a deviation from the voltage at the optimum working point (due to any flux signal), is amplified and then fed back via a feedback resistor as a feedback current through the constriction. The feedback current produces a feedback flux canceling the applied flux signal; i.e., the SQUID is always operated at its optimum working point, and the voltage across the feedback resistor (proportional to the flux signal) serves as the output signal. The readout in FLL mode is limited by the bandwidth of the feedback circuit. If the signals applied to the SQUID are small enough, one can also operate the SQUID in open-loop mode; i.e., the voltage across the SQUID is amplified without feedback, and the amplified voltage serves as the output signal. In this case, the readout is limited by the bandwidth of the voltage amplifier, which is typically larger than the FLL bandwidth. To determine the spectral density of flux noise S_Φ vs frequency f of the devices, we use a Magnicon SEL-1 SQUID electronics [34] in direct readout mode [35], which is either operated in open-loop mode (maximum bandwidth of approximately 7 MHz) or in FLL mode (maximum bandwidth of approximately 500–800 kHz). The SEL electronics allows for SQUID operation either with constant bias current (dc bias) or with a bias reversal readout scheme [maximum bias

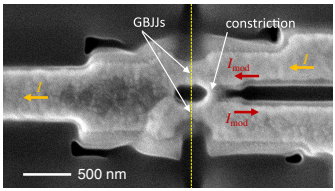

FIG. 1. SEM image of YBCO nano-SQUID-1. Vertical dashed line indicates position of the grain boundary intersecting the two SQUID arms. Horizontal arrows indicate paths for modulation current I_{mod} across the constriction and bias current I across the grain-boundary Josephson junctions.

TABLE I. Parameters of optimized SQUID-1 and -2 and of SQUID-3 used for measurements on Fe nanowire. Values for V_ϕ correspond to working points of noise measurements. Values in brackets for $S_{\Phi,w}^{1/2}$ and $S_{\mu,w}^{1/2}$ of SQUID-1 are based on the fitted noise spectrum. All devices have $d_{Au} = 70$ nm. SQUID-1 and -3 are measured at 4.2 K; SQUID-2 is measured at 5.3 K.

	d (nm)	l_c (nm)	l_J (nm)	w_c (nm)	w_{J1} (nm)	w_{J2} (nm)	β_L	L (pH)	I_c (μA)	R_N (Ω)	I_cR_N (mV)	V_Φ (mV/Φ_0)	$S_{\Phi,w}^{1/2}$ (nΦ_0/Hz$^{1/2}$)	ϕ_μ (nΦ_0/μ_B)	$S_{\mu,w}^{1/2}$ (μ_B/Hz$^{1/2}$)
SQUID-1	120	190	350	85	210	160	1.8	3.9	960	2.0	1.92	4.4	<50 (45)	13	<3.7 (3.4)
SQUID-2	120	230	370	100	180	230	0.94	6.3	311	2.5	0.78	1.7	<83	12	<6.7
SQUID-3	75	190	340	100	270	340	0.95	28	69	2.3	0.16	0.65	<1450	15	<98

reversal (BR) frequency $f_{BR} = 260$ kHz], to reduce $1/f$ noise caused by fluctuations of the critical currents $I_{0,1}$ and $I_{0,2}$ of the Josephson junctions 1 and 2, respectively [33].

Below we present the data of our best device, SQUID-1, with a $d = 120$-nm-thick YBCO film. Figure 1 shows a scanning electron microscope (SEM) image of SQUID-1. The loop size 350×190 nm^2 is given by the length l_J of the bridges straddling the grain boundary and by the length l_c of the constriction. SQUID-1 has junction widths $w_{J1} = 210$ nm and $w_{J2} = 160$ nm and a constriction width $w_c = 85$ nm. The parameters for SQUID-1 are summarized in Table I. For comparison, we also include parameters for a similar device, SQUID-2, which has the same YBCO film thickness, however, slightly larger inductance $L = 6.3$ pH, and about a factor of 2.5 smaller characteristic voltage $V_c \equiv I_cR_N$. I_c is the maximum critical current, and R_N is the asymptotic normal-state resistance of the SQUID. Details on electric transport and noise characteristics of SQUID-2 are presented in Sec. I of the Supplemental Material [36]. Those also include noise data taken from 6 to 65 K in a different setup with a temperature stability of approximately 1 mK [37]. Table I also includes parameters for SQUID-3, which is used for measurements on an Fe nanowire in a high-field setup, as discussed further below.

III. SQUID-1: ELECTRIC TRANSPORT AND NOISE

A. SQUID-1: Dc characteristics

Figure 2 shows the dc characteristics of SQUID-1. Figure 2(a) shows IVCs for $I_{mod} = 0$ and two values of I_{mod} corresponding to the maximum and minimum critical current. The IVCs are slightly hysteretic with maximum critical current $I_c = 960$ μA and $R_N = 2.0$ Ω, which yields $V_c = 1.92$ mV. The inset of Fig. 2(a) shows the modulation of the critical current $I_c(I_{mod})$. From the modulation period, we find for the magnetic flux Φ coupled to the SQUID by I_{mod} the mutual inductance $M = \Phi/I_{mod} = 0.44\Phi_0/\text{mA} = 0.91$ pH. We perform numerical simulations based on the resistively and capacitively shunted junction model to solve the coupled Langevin equations which include thermal fluctuations of the junction resistances [38]. From simulations of the $I_c(I_{mod})$ characteristics [cf. inset of Fig. 2(a)], we obtain for the screening parameter $\beta_L = 2I_0L/\Phi_0 = 1.8$ [with $I_0 = (I_{0,1} + I_{0,2})/2$], which yields a SQUID inductance $L = 3.9$ pH. We do find good agreement between the measured and simulated $I_c(I_{mod})$ characteristics if we include an inductance asymmetry $\alpha_L \equiv (L_2 - L_1)/(L_2 + L_1) = 0.20$ (L_1 and L_2

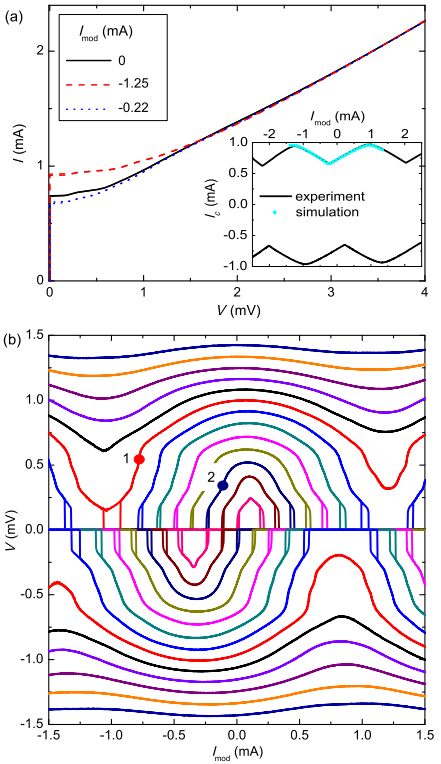

FIG. 2. SQUID-1 dc transport characteristics. (a) Measured IVCs for three different values of I_{mod}, including flux bias (I_{mod}) values which yield maximum and minimum critical current. Inset: Measured $I_c(I_{mod})$ for positive and negative current bias (solid lines) and numerical simulations (dots). (b) Measured $V(I_{mod})$ for bias currents $|I| = 0.64$–1.12 mA (in 40-μA steps). Points 1 and 2 are bias points with $V_\Phi = 12$ and 4.5 mV/Φ_0, respectively.

are the inductances of the two SQUID arms) and a critical current asymmetry $\alpha_I \equiv (I_{0,2} - I_{0,1})/(I_{0,2} + I_{0,1}) = 0.27$. These asymmetries are caused by asymmetric biasing of the SQUID and by asymmetries of the device itself.

$V(I_{\rm mod})$ is plotted in Fig. 2(b) for different bias currents. The transfer function, i.e., the maximum value of $\partial V/\partial\Phi$, in the nonhysteretic regime is $V_\Phi \approx 12$ mV/Φ_0 [at $I = 0.92$ mA; cf. point 1 in Fig. 2(b)].

B. SQUID-1: Noise data

1. Open-loop mode

Figure 3(a) shows the rms spectral density of flux noise $S_\Phi^{1/2}(f)$ of SQUID-1 measured in open-loop mode to reach the highest possible bandwidth of the readout electronics. Because of the limitation in the maximum bias current of the readout electronics, noise spectra are taken at $I = 0.72$ mA with a transfer function $V_\Phi = 4.5$ mV/Φ_0 [cf. point 2 in Fig. 2(b)]. Up to the cutoff frequency $f_{3\,\rm dB} = 7$ MHz, there is no white flux noise observable. Instead, the flux noise scales roughly as $S_\Phi \propto 1/f$, with $S_\Phi^{1/2} \approx 10\ \mu\Phi_0/{\rm Hz}^{1/2}$ at $f = 100$ Hz and $1\ \mu\Phi_0/{\rm Hz}^{1/2}$ at 10 kHz. This level of low-frequency excess noise is quite typical for YBCO GBJJ SQUIDs (also at $T = 77$ K) and has been ascribed to critical current fluctuations in the GBJJs [39]. However, due to the limitation by thermal white noise, typically between 1 and $10\ \mu\Phi_0/{\rm Hz}^{1/2}$ for low-noise YBCO SQUIDs, this f-dependent excess noise has not been observed so far up to the megahertz range. We note that for YBCO nano-SQUIDs implementing CJJs [27], a frequency-dependent $(1/f)$-like excess noise at $T = 8$ K of almost the same level as that for SQUID-1 was reported very recently and was also attributed to critical current fluctuations. For frequencies above 10 kHz, the flux noise of the YBCO nano-SQUID in Ref. [27] was limited by amplifier background noise.

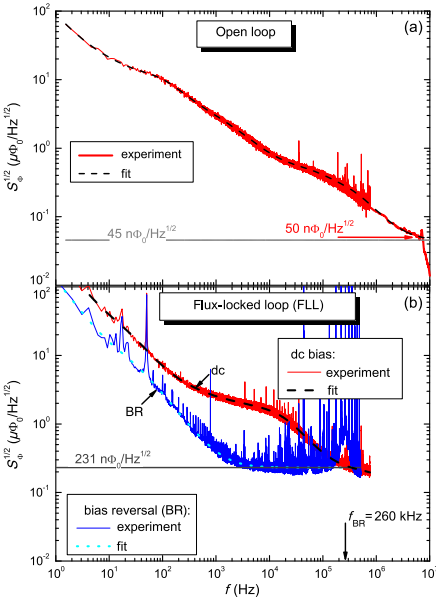

FIG. 3. Rms flux noise of SQUID-1. (a) Measured in open-loop mode at bias point 2 ($I = 0.72$ mA) in Fig. 2(b). Dashed line is a fit to the measured spectrum with white noise as indicated by the horizontal line. (b) Measured in FLL mode with dc bias and bias reversal ($|I| = 0.43$ mA, $V_\Phi = 4.4$ mV/Φ_0). Vertical arrow indicates bias reversal frequency $f_{\rm BR}$. Dashed and dotted lines are fits to the spectra; horizontal lines indicate fitted white noise.

For a more detailed analysis of the measured flux noise $S_\Phi(f)$, we apply an algorithm [40] to decompose the noise spectra into a sum of Lorentzians $F_i(f) = F_{0,i}/[1 + (f/f_{c,i})^2]$ plus a white-noise contribution F_w. The noise spectrum measured for SQUID-1 in open loop can be very well fitted by $F_{\rm op}(f) = F_{w,\rm op} + F_{s,\rm op} + \sum_{i=1}^{16} F_{{\rm op},i}(f)$, i.e., the superposition of a white-noise contribution with $F_{w,\rm op}^{1/2} = 45\ {\rm n}\Phi_0/{\rm Hz}^{1/2}$ plus a $1/f^2$ spectrum $F_{s,\rm op}$ (i.e., one or more Lorentzians with characteristic frequencies f_c well below 1 Hz) with $F_{s,\rm op}^{1/2}(1\ {\rm Hz}) = 84\ \mu\Phi_0/{\rm Hz}^{1/2}$ plus 16 Lorentzians, with $f_{c,i}$ ranging from 2.6 Hz to 2.6 MHz. For more details, see Sec. III of the Supplemental Material [36]. Hence, the decomposition of the spectrum into Lorentzians yields an estimate of the white rms flux noise $S_{\Phi,w}^{1/2} \approx 45\ {\rm n}\Phi_0/{\rm Hz}^{1/2}$ for SQUID-1. We note that this value for $S_{\Phi,w}^{1/2}$ is only a factor of 1.8 above the value, which we obtain from numerical simulations of the coupled Langevin equations [38] at $T = 4.2$ K for the parameters of SQUID-1.

Taking the measured flux noise at 7 MHz as an upper limit for $S_{\Phi,w}^{1/2}$, we still obtain a very low white rms flux noise, i.e., $S_{\Phi,w}^{1/2} < 50\ {\rm n}\Phi_0/{\rm Hz}^{1/2}$. This more conservative estimate for the white rms flux noise level is an improvement by more than an order of magnitude compared to our nonoptimized devices operated at 4.2 K and compared to the lowest value reported so far for a YBCO SQUID (at 8 K) very recently [27]. Furthermore, this value is the same as the lowest value reported for a Pb SOT operated at 4.2 K [28] and among the lowest flux noise levels ever achieved for a SQUID [9,41,42].

For the geometry of SQUID-1, we calculate [32] a coupling factor $\phi_\mu = 13.4\ {\rm n}\Phi_0/\mu_{\rm B}$ (10 nm above the YBCO film). With $S_{\Phi,w}^{1/2} < 50\ {\rm n}\Phi_0/{\rm Hz}^{1/2}$, we can determine an upper limit for the spin sensitivity (white-noise limit) of $S_{\mu,w}^{1/2} < 3.7\ \mu_B/{\rm Hz}^{1/2}$. If we take the fitted white

flux noise of 45 $n\Phi_0/Hz^{1/2}$, we obtain $S_{\mu,w}^{1/2} = 3.4\,\mu_B/Hz^{1/2}$. Hence, the achieved performance matches very well the predictions of our recent optimization study [32].

2. FLL mode: Dc bias vs bias reversal

Although the achieved low level of white flux noise for SQUID-1 is encouraging, one certainly will like to extend such a low-noise performance down to much lower frequencies. Therefore, we also perform noise measurements in FLL mode (with approximately 700-kHz bandwidth) and compare measurements with dc bias and bias reversal (with $f_{BR} = 260$ kHz). We note that the measurements in FLL mode are performed within a different cooling cycle, after SQUID-1 already shows a slight degradation in I_c [43]. Still, we are able to find a working point (at $|I| = 0.43$ mA) which yields almost the same transfer function, 4.4 mV/Φ_0, as for the measurement before degradation in open-loop mode.

Figure 3(b) shows rms flux noise spectra taken with dc bias and bias reversal. Comparing first the FLL dc bias measurement with the open-loop data, we note that the noise levels at f_{BR} coincide. For $f < f_{BR}$, the noise levels of the open-loop and FLL dc bias data are similar; however, the shape of the spectra differ, which we attribute to the above-mentioned degradation and variations between different cooling cycles. The dashed line in Fig. 3(b) is a fit to the measured spectral density of flux noise by $F_{dc}(f) = F_{w,dc} + \sum_{i=1}^{15} F_{dc,i}(f)$, i.e., the superposition of 15 Lorentzians, with $f_{c,i}$ ranging from 0.8 Hz to 6.8 MHz, plus a white-noise contribution $F_{w,dc}^{1/2} = 41\ n\Phi_0/Hz^{1/2}$, which we fix to a value similar to the white-noise level determined for the open-loop measurement. For more details, see Sec. III of the Supplemental Material [36].

Applying bias reversal, one expects a suppression of the contributions due to in-phase and out-of-phase critical current fluctuations of the GBJJs [39]. If the f-dependent excess noise below f_{BR} arises solely from I_0 fluctuations, one expects in bias reversal mode a frequency-independent noise for frequencies below the peak at f_{BR}, at a level which is given by the noise measured at f_{BR} in dc bias mode. This behavior can be observed for frequencies down to a few kilohertz, with an f-independent noise $F_{w,BR}^{1/2} = 231\ n\Phi_0/Hz^{1/2}$. For lower frequencies, however, we still find a strong f-dependent excess noise in bias reversal mode, which, hence cannot be attributed to I_0 fluctuations.

The spectral density of flux noise measured in bias reversal mode can be well approximated [cf. dotted line in Fig. 3(b)] by $F_{BR}(f) = F_{w,BR} + F_{s,BR} + \sum_{i=1}^{6} F_{BR,i}(f)$, with $F_{s,BR}^{1/2}(1\ Hz) = 128\ \mu\Phi_0/Hz^{1/2}$ and $f_{c,i}$ of the six Lorentzians ranging from 21 Hz to 5 kHz. For more details, see Sec. III of the Supplemental Material [36].

Obviously, below a few kilohertz, the low-frequency excess noise is dominated by slow fluctuators, which cannot be attributed to I_0 fluctuations. For different working points (I and I_{mod}) and also for other devices, the observation of low-f excess noise in bias reversal mode is reproducible [cf. flux noise data of SQUID-2 (from $T =$ 6 K up to 65 K) and of SQUID-3 (at $T = 4.2$ K) in Secs. I and II, respectively, of the Supplemental Material [36]].

Considering the narrow linewidths of the SQUID structures, we estimate a threshold field for trapping of Abrikosov vortices [44] to be well above 1 mT. Since the measurements are performed in a magnetically shielded environment well below 100 nT, the presence of Abrikosov vortices as the source of the observed low-f fluctuators is very unlikely.

Low-frequency excess noise, which neither arises from I_0 nor from vortex fluctuations, has been reported during the last decades for SQUIDs based on conventional superconductors like Nb, Pb, PbIn, and Al, in particular, at temperatures well below 1 K [45]. This issue has recently been revived due to the increasing interest in the development of flux qubits and SQUIDs for ultra-low-temperature applications [46]. Various models have been suggested to describe the origin of such low-f excess noise, e.g., based on the coupling of magnetic moments associated with trapped electrons [47] or surface states [48,49], although the microscopic nature of defects as sources of excess "spin noise" still remains unclear.

For YBCO SQUIDs, excess low-f spin noise has not been addressed so far. However, it seems quite likely that defects are also a source of magnetic fluctuators in SQUIDs based on cuprates or any other oxide superconductors. Such defects can be present either in the thin-film SQUID structures themselves or in the substrates onto which the thin films are grown or at the interface between the thin film and the substrate.

The emergence and modification of magnetism at interfaces and surfaces of oxides, which are diamagnetic in the bulk, is currently an intensive field of research [50–52]. For STO, oxygen-vacancy-induced magnetism has been predicted [53], and experimental studies suggest ferromagnetic ordering up to room temperature [54], e.g., for defects induced by ion irradiation of single crystalline STO [55]. Furthermore, defect-induced magnetism in oxide grain boundaries and related defects have been suggested to be the intrinsic origin of ferromagnetism in oxides [56].

Obviously, further investigations on the impact and nature of such defects in our devices are needed and will be the subject of further studies. Such studies will include detailed noise measurements (dc vs bias reversal, variable flux bias, temperature, and magnetic field) to characterize and understand the f-dependent noise sources and, hopefully, eliminate them. Furthermore, readout with bias reversal at higher frequency up to the megahertz range in FLL mode has to be implemented in order to maintain the achieved ultralow white flux noise level down to lower frequencies. And finally, for applications of our nano-SQUIDs, it will be important to avoid

degradation in time, which shall be achieved by adding a suitable passivation layer, however, without introducing f-dependent excess noise.

IV. SQUID-3: MAGNETIZATION REVERSAL OF FE NANOWIRE

As a proof of principle, we demonstrate nano-SQUID measurements on the magnetization reversal of an Fe nanowire which is encapsulated in a carbon nanotube (CNT) [57]. Such iron-filled CNTs (Fe CNTs) are of fundamental interest with respect to studies on nanomagnetism. Furthermore, they are attractive for various applications, e.g., as tips in magnetic-force microscopy [58,59]. The Fe nanowire, which contains mainly single crystalline (ferromagnetic) α-Fe, has a diameter $d_{\mathrm{Fe}} = 39$ nm and length $l_{\mathrm{Fe}} = 13.8$ μm. The CNT has a diameter of approximately 130 nm. We note that this section is not directly related to the previous section in a sense to demonstrate the ultimate sensitivity of our devices on a magnetic nanoparticle with the smallest yet still detectable signals and operation in the strongest possible magnetic fields. Rather, we want to show an example of the feasibility of using our YBCO nano-SQUIDs for practical applications. As shown within this section, we can demonstrate signal-to-noise ratios which are clearly superior to micro-Hall measurements on similar nanowires.

The Fe CNT is positioned by a Kleindiek three-axis manipulator inside a FIB SEM combination onto SQUID-3, such that the distance between the left end of the Fe nanowire and the SQUID loop is approximately 300 nm (cf. Fig. 4). We note that for optimum coupling of the stray field of the Fe nanowire into the SQUID, it is preferable to place the end of the Fe nanowire close to the edge of the SQUID loop opposite the constriction. At this location, the coupling factor is slightly smaller than directly on top of the constriction; however, it does not fall off very rapidly upon moving farther away from the loop, as it is the case near the constriction [31]. The Fe nanowire axis (its easy axis) is aligned as close as possible with the substrate plane (x-y plane), with an inclination angle $\theta \approx 4°$ and perpendicular to the grain boundary, which is oriented along the y axis. The inclination of the Fe wire axis with respect to the x axis is $<1°$. The vertical distance (along the z axis) between the nanowire axis (at its left end) and the surface of the YBCO film is approximately 300 nm.

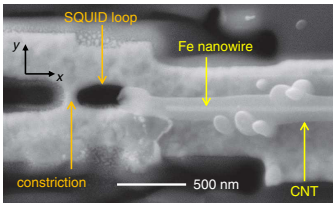

FIG. 4. SEM image of SQUID-3 with an Fe-wire-filled carbon nanotube positioned close to the SQUID loop.

The measurements on the Fe nanowire are performed with the nonoptimized SQUID-3. This device has a significantly larger inductance (due to its smaller film thickness) and much smaller characteristic voltage, resulting in a much smaller transfer function $V_\Phi = 0.65$ mV/Φ_0, as compared to SQUID-1 and -2. Magnetization-reversal measurements on the Fe CNT are performed with SQUID-3 operated in FLL dc bias mode up to $f = 190$ kHz. At this frequency, the noise is limited by the readout electronics, which yields for SQUID-3 an upper limit of the white rms flux noise $S_{\Phi,w}^{1/2} \leq 1.45$ $\mu\Phi_0/\mathrm{Hz}^{1/2}$. Below approximately 40 kHz, SQUID-3 shows f-dependent excess noise with $S_\Phi^{1/2} \approx 8$ $\mu\Phi_0/\mathrm{Hz}^{1/2}$ at $f = 100$ Hz and $S_\Phi^{1/2} \approx 20$ $\mu\Phi_0/\mathrm{Hz}^{1/2}$ at $f = 10$ Hz, with an approximately $1/f^2$ increase of S_Φ below 10 Hz. Some experimentally determined parameters of SQUID-3 are listed in Table I. Details on low-field electric transport and noise characteristics of SQUID-3 are presented in Sec. II of the Supplemental Material [36].

For magnetization-reversal measurements of the Fe nanowire on top of SQUID-3, the sample is mounted in a high-field setup, which allows us to apply magnetic fields up to $\mu_0 H = 7$ T [31]. To minimize coupling of the external magnetic field H into the SQUID, the SQUID loop (in the x-y plane) is aligned parallel to the field. To minimize coupling of the external field into the GBJJs, the grain boundary (along the y axis) is aligned perpendicular to the applied field. The alignment of the SQUID with respect to the applied field direction is performed by an Attocube system including two goniometers with perpendicular tilt axes and one rotator. In this configuration, the external field H is applied along the x axis (cf. Fig. 4), and the angle between H and the Fe nanowire axis is given by θ.

Figure 5 shows the flux signal $\Phi(H)$ detected by SQUID-3, while sweeping H, at a rate $\mu_0 \partial H/\partial t \approx 1$ mT/s. At the fields $\pm\mu_0 H_n = \pm 101$ mT, abrupt changes by $\Delta\Phi \approx 150$ mΦ_0 clearly indicate magnetization reversal of the Fe nanowire. The shape of the $\Phi(H)$ curve indicates magnetization reversal of a single-domain particle. The slope of the curve in the interval $-H_n \leq H \leq H_n$ depends strongly on the alignment of the SQUID with respect to the applied field. Hence, this slope can be attributed, at least partially, to the coupling of the external field to the SQUID loop. The hysteresis in the signals for $|H| \gtrsim 100$ mT is typically observed also for our SQUIDs measured in the high-field setup without MNPs coupled to them. Hence, this hysteresis is attributed to a spurious magnetization signal from our setup or from the above-mentioned magnetic defects close to the nano-SQUID, rather than being generated by the nanowire.

In order to convert from magnetic flux detected by the SQUID to magnetization of the Fe nanowire, we follow the

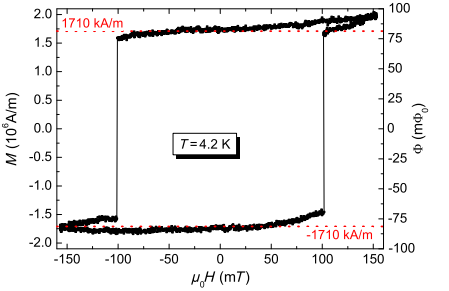

FIG. 5. Hysteresis loop $\Phi(H)$ of the Fe nanowire detected with SQUID-3 (operated in FLL dc bias mode with cutoff frequency approximately 190 kHz, at optimum working point with $V_\Phi = 0.65$ mV/Φ_0). Switching of the magnetization occurs at $\pm\mu_0 H_n = \pm 101$ mT. The residual field $\mu_0 H_{\rm res} = 4.0$ mT is subtracted. Left axis indicates corresponding magnetization $M = \Phi/\phi_M$; the dashed lines indicate the literature's value of the saturation magnetization $\pm M_s$.

approach described in Ref. [60]. We numerically calculate the coupling factor $\phi_\mu(\hat{e}_\mu, \vec{r}_p)$ for a pointlike MNP with orientation $\hat{e}_\mu$ of its magnetic moment at position $\vec{r}_p$ in the 3D space above the SQUID [32]. These simulations take explicitly into account the geometry of SQUID-3 and are based on London theory [61]. We then assume that the Fe nanowire is in its fully saturated state, with saturation magnetization M_s, with all moments oriented along the wire axis. The corresponding saturation flux coupled to the SQUID is denoted as Φ_s. The ratio Φ_s/M_s is obtained by integration of the coupling factor ϕ_μ over the volume $V_{\rm Fe}$ of the Fe wire, at its given position, determined from SEM images. This integration yields

$$\phi_M \equiv \frac{\Phi_s}{M_s} = \int_{V_{\rm Fe}} \phi_\mu(\vec{r}_p) dV = 47.6 \frac{\rm n\Phi_0}{\rm Am^{-1}}. \qquad (1)$$

From this result, we calculate $\Phi_s = M_s \phi_M = 81.4$ mΦ_0, with $M_s = 1710$ kA/m taken from the literature [62]. The comparison with the measured flux signals ± 82.5 mΦ_0 at $H = 0$ shows very good agreement. The left axis in Fig. 5 shows the magnetization axis scaled as $M = \Phi/\phi_M$ with the horizontal dotted lines indicating the literature's value $M_s = \pm 1710$ kA/m. Hence, the measured flux signals are also in quantitative agreement with the assumption that the Fe nanowire switches to a fully saturated single-domain state.

In Ref. [58], it was shown for a similar Fe CNT that the nucleation field H_n changes with θ in a way which is typical for nucleation of magnetization reversal via the curling mode [63] in ferromagnetic nanowires as opposed to uniform rotation of the magnetic moments in small enough MNPs as described by the Stoner-Wolfarth model [64]. For switching via curling mode, one obtains for $\theta = 0$ the simple relation $H_n = M_s a/2$, with a negligible increase well below 1% with $\theta = 4°$ [65]. Here, $a = 1.08(2\lambda_{\rm ex}/d_{\rm Fe})^2$, with the exchange length $\lambda_{\rm ex} = \sqrt{4\pi A/(\mu_0 M_s^2)}$ and the exchange constant A [62]. For $d_{\rm Fe} = 39$ nm and with $\lambda_{\rm ex} = 5.8$ nm [62], we obtain $a = 0.0955$, and with $M_s = 1710$ kA/m, we obtain an estimate of the nucleation field $H_n = 103$ mT, which is in very good agreement with the experimentally observed value.

Finally, we note that the SQUID measurement yields a noise amplitude of approximately 1 mΦ_0, which is 2 orders of magnitude smaller than the detected signal upon magnetization reversal. For comparison, measurements on a similar Fe nanowire by micro-Hall magnetometry yield a noise amplitude which was about 1 order of magnitude below the switching signal [58]. Hence, the use of our nano-SQUID improves the signal-to-noise ratio by about 1 order of magnitude.

V. CONCLUSIONS

In conclusion, we fabricate and investigate optimized YBCO nano-SQUIDs based on grain-boundary Josephson junctions. For our best device, an upper limit for the white flux noise level $S_\Phi^{1/2} < 50$ nΦ_0/Hz$^{1/2}$ in magnetically shielded environment can be determined, which corresponds to a spin sensitivity $S_\mu^{1/2} \equiv S_\Phi^{1/2}/\phi_\mu = 3.7\ \mu_B$/Hz$^{1/2}$ for a magnetic nanoparticle located 10 nm above the constriction in the SQUID loop. Here, the coupling factor ϕ_μ is determined by numerical simulations based on London theory, which takes the device geometry into account. An obvious drawback of YBCO grain-boundary junction nano-SQUIDs is the frequency-dependent excess noise, which extends up to the megahertz range for optimized devices with ultralow flux noise in the white-noise limit. To eliminate $1/f$ noise, a bias reversal scheme is applied, which reduces only the frequency-dependent excess noise partially. Hence, in addition to critical current fluctuations, spin noise which is possibly due to fluctuations of defect-induced magnetic moments in the $SrTiO_3$ substrate is a major issue, which has to be studied in more detail for further improvement of the nano-SQUID performance at low frequencies. Nevertheless, we demonstrate the suitability of the YBCO nano-SQUIDs as detectors for magnetic nanoparticles in moderate magnetic fields by measuring the magnetization reversal of an iron nanowire that is placed close to the SQUID loop. Switching of the magnetization is detected at $\mu_0 H \approx \pm 100$ mT, which is in very good agreement with nucleation of magnetization reversal via curling mode.

ACKNOWLEDGMENTS

T. S. acknowledges support by the Carl-Zeiss-Stiftung. M. J. M.-P. acknowledges support by the Alexander von

Humboldt Foundation. We gratefully acknowledge fruitful discussions with D. Drung (Physikalisch-Technische Bundesanstalt Berlin) and technical support by M. Turad and R. Löffler [instrument scientists of the core facility Center for Light-Matter Interaction, Sensors & Analytics (LISA$^+$)]. This work is supported by the Nachwuchswissenschaftlerprogramm of the Universität Tübingen, by the Deutsche Forschungsgemeinschaft (DFG) via Projects No. KO 1303/13-1, No. MU 1794/3-2, and No. SFB/TRR 21 C2 and by the EU-FP6-COST Action MP1201.

[1] *Molecular Magnets: Physics and Applications*, edited by Juan Bartolomé, Fernando Luis, and Julio F. Fernández (Springer, Heidelberg, 2014).

[2] Lapo Bogani and Wolfgang Wernsdorfer, Molecular spintronics using single-molecule magnets, Nat. Mater. **7**, 179 (2008).

[3] Michael N. Leuenberger and Daniel Loss, Quantum computing in molecular magnets, Nature (London) **410**, 789 (2001).

[4] S. Odenbach, Ferrofluids and their applications, MRS Bull. **38**, 921 (2013).

[5] Andreas Jordan, Regina Scholz, Peter Wust, Horst Fähling, and Roland Felix, Magnetic fluid hyperthermia (MFH): Cancer treatment with AC magnetic field induced excitation of biocompatible superparamagnetic nanoparticles, J. Magn. Magn. Mater. **201**, 413 (1999).

[6] R. C. Semelka and T. K. G. Helmberger, State of the art: Contrast agents for MR imaging of the liver, Radiology **218**, 27 (2001).

[7] R. Klingeler, S. Hampel, and B. Büchner, Carbon nanotube based biomedical agents for heating, temperature sensoring and drug delivery, International Journal of Hyperthermia **24**, 496 (2008).

[8] W. Wernsdorfer, Classical and quantum magnetization reversal studied in nanometersized particles and clusters, Adv. Chem. Phys. **118**, 99 (2001).

[9] D. D. Awschalom, J. R. Rozen, M. B. Ketchen, W. J. Gallagher, A. W. Kleinsasser, R. L. Sandstrom, and B. Bumble, Low-noise modular microsusceptometer using nearly quantum limited dc SQUIDs, Appl. Phys. Lett. **53**, 2108 (1988).

[10] M. Ketchen, D. Awschalom, W. Gallagher, A. Kleinsasser, R. Sandstrom, J. Rozen, and B. Bumble, Design, fabrication, and performance of integrated miniature SQUID susceptometers, IEEE Trans. Magn. **25**, 1212 (1989).

[11] K. Hasselbach, D. Mailly, and J. R. Kirtley, Micro-superconducting quantum interference device characteristic, J. Appl. Phys. **91**, 4432 (2002).

[12] S. K. H. Lam and D. L. Tilbrook, Development of a niobium nanosuperconducting quantum interference device for the detection of small spin populations, Appl. Phys. Lett. **82**, 1078 (2003).

[13] J.-P. Cleuziou, W. Wernsdorfer, V. Bouchiat, T. Ondarçuhu, and M. Monthioux, Carbon nanotube superconducting quantum interference device, Nat. Nanotechnol. **1**, 53 (2006).

[14] Aico G. P. Troeman, Hendrie Derking, Bert Borger, Johannes Pleikies, Dick Veldhuis, and Hans Hilgenkamp, NanoSQUIDs based on niobium constrictions, Nano Lett. **7**, 2152 (2007).

[15] Nicholas C. Koshnick, Martin E. Huber, Julie A. Bert, Clifford W. Hicks, Jeff Large, Hal Edwards, and Kathryn A. Moler, A terraced scanning super conducting quantum interference device susceptometer with submicron pickup loops, Appl. Phys. Lett. **93**, 243101 (2008).

[16] L. Hao, J. C. Macfarlane, J. C. Gallop, D. Cox, J. Beyer, D. Drung, and T. Schurig, Measurement and noise performance of nano-superconducting-quantum-interference devices fabricated by focused ion beam, Appl. Phys. Lett. **92**, 192507 (2008).

[17] C. P. Foley and H. Hilgenkamp, Why NanoSQUIDs are important: An introduction to the focus issue, Supercond. Sci. Technol. **22**, 064001 (2009).

[18] V. Bouchiat, Detection of magnetic moments using a nano-squid: Limits of resolution and sensitivity in near-field squid magnetometry, Supercond. Sci. Technol. **22**, 064002 (2009).

[19] W. Wernsdorfer, From micro- to nano-SQUIDs: Applications to nanomagnetism, Supercond. Sci. Technol. **22**, 064013 (2009).

[20] Francesco Giazotto, Joonas T. Peltonen, Matthias Meschke, and Jukka P. Pekola, Superconducting quantum interference proximity transistor, Nat. Phys. **6**, 254 (2010).

[21] M. J. Martínez-Pérez, E. Bellido, R. de Miguel, J. Sesé, A. Lostao, C. Gómez-Moreno, D. Drung, T. Schurig, D. Ruiz-Molina, and F. Luis, Alternating current magnetic susceptibility of a molecular magnet submonolayer directly patterned onto a micro superconducting quantum interference device, Appl. Phys. Lett. **99**, 032504 (2011).

[22] E. J. Romans, S. Rozhko, L. Young, A. Blois, L. Hao, D. Cox, and J. C. Gallop, Noise performance of niobium nano-SQUIDs in applied magnetic fields, IEEE Trans. Appl. Supercond. **21**, 404 (2011).

[23] R. Russo, C. Granata, E. Esposito, D. Peddis, C. Cannas, and A. Vettoliere, Nanoparticle magnetization measurements by a high sensitive nano-superconducting quantum interference device, Appl. Phys. Lett. **101**, 122601 (2012).

[24] Carmine Granata, Antonio Vettoliere, Roberto Russo, Matteo Fretto, Natascia De Leo, and Vincenzo Lacquaniti, Three-dimensional spin nanosensor based on reliable tunnel Josephson nano-junctions for nanomagnetism investigations, Appl. Phys. Lett. **103**, 102602 (2013).

[25] D. Drung, J.-H. Storm, F. Ruede, A. Kirste, M. Regin, T. Schurig, A. M. Repollés, J. Sesé, and F. Luis, Thin-film microsusceptometer with integrated nanoloop, IEEE Trans. Appl. Supercond. **24**, 1600206 (2014).

[26] Amit Finkler, Yehonathan Segev, Yuri Myasoedov, Michael L. Rappaport, Lior Ne'eman, Denis Vasyukov, Eli Zeldov, Martin E. Huber, Jens Martin, and Amir Yacoby, Self-aligned nanoscale SQUID on a tip, Nano Lett. **10**, 1046 (2010).

[27] R. Arpaia, M. Arzeo, S. Nawaz, S. Charpentier, F. Lombardi, and T. Bauch, Ultra low noise $YBa_2Cu_3O_{7-\delta}$

nano superconducting quantum interference devices implementing nanowires, Appl. Phys. Lett. **104**, 072603 (2014).
[28] Denis Vasyukov, Yonathan Anahory, Lior Embon, Dorri Halbertal, Jo Cuppens, Lior Ne'eman, Amit Finkler, Yehonathan Segev, Yuri Myasoedov, Michael L. Rappaport, Martin E. Huber, and Eli Zeldov, A scanning superconducting quantum interference device with single electron spin sensitivity, Nat. Nanotechnol. **8**, 639 (2013).
[29] Lei Chen, Wolfgang Wernsdorfer, Christos Lampropoulos, George Christou, and Irinel Chiorescu, On-chip SQUID measurements in the presence of high magnetic fields, Nanotechnology **21**, 405504 (2010).
[30] J. Nagel, K. B. Konovalenko, M. Kemmler, M. Turad, R. Werner, E. Kleisz, S. Menzel, R. Klingeler, B. Büchner, R. Kleiner, and D. Koelle, Resistively shunted $YBa_2Cu_3O_7$ grain boundary junctions and low-noise SQUIDs patterned by a focused ion beam down to 80 nm linewidth, Supercond. Sci. Technol. **24**, 015015 (2011).
[31] T. Schwarz, J. Nagel, R. Wölbing, M. Kemmler, R. Kleiner, and D. Koelle, Low-noise nano superconducting quantum interference device operating in tesla magnetic fields, ACS Nano **7**, 844 (2013).
[32] R. Wölbing, T. Schwarz, B. Müller, J. Nagel, M. Kemmler, R. Kleiner, and D. Koelle, Optimizing the spin sensitivity of grain boundary junction nanoSQUIDs–Towards detection of small spin systems with single-spin resolution, Supercond. Sci. Technol. **27**, 125007 (2014).
[33] D. Drung and M. Mück, in *The SQUID Handbook*, edited by John Clarke and Alex I. Braginski, Fundamentals and Technology of SQUIDs and SQUID Systems Vol. 1 (Wiley-VCH, Weinheim, 2004), Chap. 4, pp. 127–170.
[34] SQUID electronics SEL-1, http://www.magnicon.com.
[35] D. Drung, High-t_c and low-t_c dc SQUID electronics, Supercond. Sci. Technol. **16**, 1320 (2003).
[36] See the Supplemental Material at http://link.aps.org/supplemental/10.1103/PhysRevApplied.3.044011 for additional data and analysis of SQUID-1, -2 and -3.
[37] M. Kemmler, D. Bothner, K. Ilin, M. Siegel, R. Kleiner, and D. Koelle, Suppression of dissipation in Nb thin films with triangular antidot arrays by random removal of pinning sites, Phys. Rev. B **79**, 184509 (2009).
[38] B. Chesca, R. Kleiner, and D. Koelle, in *The SQUID Handbook*, edited by John Clarke and Alex I. Braginski, Fundamentals and Technology of SQUIDs and SQUID systems Vol. 1 (Wiley-VCH, Weinheim, 2004), Chap. 2, pp. 29–92.
[39] D. Koelle, R. Kleiner, F. Ludwig, E. Dantsker, and John Clarke, High-transition-temperature superconducting quantum interference devices, Rev. Mod. Phys. **71**, 631 (1999).
[40] E. Sassier, R. Kleiner, and D. Koelle, A spectroscopic method for excess-noise spectrum analysis (unpublished).
[41] D. J. Van Harlingen, Roger H. Koch, and John Clarke, Superconducting quantum interference device with very low magnetic flux noise energy, Appl. Phys. Lett. **41**, 197 (1982).
[42] E. M. Levenson-Falk, R. Vijay, N. Antler, and I. Siddiqi, A dispersive nanoSQUID magnetometer for ultra-low noise, high bandwidth flux detection, Supercond. Sci. Technol. **26**, 055015 (2013).
[43] From measurements on a similar device, we find an almost linear decrease in I_c with time, with an approximately 20% reduction in I_c after 40 days. This rate of degradation is typical for most of our devices. A possible explanation of this effect is outdiffusion of oxygen from the submicron GBJJs along the *a*-*b* plane of the YBCO thin film.
[44] G. Stan, S. B. Field, and J. M. Martinis, Critical Field for Complete Vortex Expulsion from Narrow Superconducting Strips, Phys. Rev. Lett. **92**, 097003 (2004).
[45] Frederick C. Wellstood, Cristian Urbina, and John Clarke, Low-frequency noise in dc superconducting quantum interference devices below 1 K, Appl. Phys. Lett. **50**, 772 (1987).
[46] D. Drung, J. Beyer, J.-H. Storm, M. Peters, and T. Schurig, Investigation of low-frequency excess flux noise in dc SQUIDs at mK temperatures, IEEE Trans. Appl. Supercond. **21**, 340 (2011).
[47] Roger H. Koch, David P. DiVincenzo, and John Clarke, Model for $1/f$ Flux Noise in SQUIDs and Qubits, Phys. Rev. Lett. **98**, 267003 (2007).
[48] Rogerio de Sousa, Dangling-bond spin relaxation and magnetic $1/f$ noise from the amorphous-semiconductor/oxide interface: Theory, Phys. Rev. B **76**, 245306 (2007).
[49] S. Sendelbach, D. Hover, A. Kittel, M. Mück, John M. Martinis, and R. McDermott, Magnetism in SQUIDs at Millikelvin Temperatures, Phys. Rev. Lett. **100**, 227006 (2008).
[50] M. Venkatesan, C. B. Fitzgerald, and J. M. D. Coey, Thin films: Unexpected magnetism in a dielectric oxide, Nature (London) **430**, 630 (2004).
[51] N. Pavlenko, T. Kopp, E. Y. Tsymbal, J. Mannhart, and G. A. Sawatzky, Oxygen vacancies at titanate interfaces: Two-dimensional magnetism and orbital reconstruction, Phys. Rev. B **86**, 064431 (2012).
[52] J. M. D. Coey, Ariando, and W. E. Pickett, Magnetism at the edge: New phenomena at oxide interfaces, MRS Bull. **38**, 1040 (2013).
[53] I. R. Shein and A. L. Ivanosvkii, First principle prediction of vacancy-induced magnetism in non-magnetic Perovskite $SrTiO_3$, Phys. Lett. A **371**, 155 (2007).
[54] M. Khalid, A. Setzer, M. Ziese, P. Esquinazi, D. Spemann, A. Pöppl, and E. Goering, Ubiquity of ferromagnetic signals in common diamagnetic oxide crystals, Phys. Rev. B **81**, 214414 (2010).
[55] K. Potzger, J. Osten, A. A. Levin, A. Shalimov, G. Talut, H. Reuther, S. Arpaci, D. Bürger, H. Schmidt, T. Nestler, and D. C. Meyer, Defect-induced ferromagnetism in crystalline $SrTiO_3$, J. Magn. Magn. Mater. **323**, 1551 (2011).
[56] Boris B. Straumal, Andrei A. Mazilkin, Svetlana G. Protasova, Ata A. Myatiev, Petr B. Straumal, Gisela Schütz, Peter A. van Aken, Eberhard Goering, and Brigitte Baretzky, Magnetization study of nanograined pure and Mn-doped ZnO films: Formation of a ferromagnetic grain-boundary foam, Phys. Rev. B **79**, 205206 (2009).
[57] A. Leonhardt, S. Hampel, C. Müller, I. Mönch, R. Koseva, M. Ritschel, D. Elefant, K. Biedermann, and B. Büchner, Synthesis, properties, and applications of ferromagnetic-filled carbon nanotubes, Chem. Vap. Deposition **12**, 380 (2006).

[58] K. Lipert, S. Bahr, F. Wolny, P. Atkinson, U. Weißker, T. Mühl, O. G. Schmidt, B. Büchner, and R. Klingeler, An individual iron nanowire-filled carbon nanotube probed by micro-Hall magnetometry, Appl. Phys. Lett. **97**, 212503 (2010).

[59] T. Mühl, J. Körner, S. Philippi, C. F. Reiche, A. Leonhardt, and B. Büchner, Magnetic force microscopy sensors providing in-plane and perpendicular sensitivity, Appl. Phys. Lett. **101**, 112401 (2012).

[60] J. Nagel, A. Buchter, F. Xue, O. F. Kieler, T. Weimann, J. Kohlmann, A. B. Zorin, D. Rüffer, E. Russo-Averchi, R. Huber, P. Berberich, A. Fontcubertai Morral, D. Grundler, R. Kleiner, D. Koelle, M. Poggio, and M. Kemmler, Nanoscale multifunctional sensor formed by a Ni nanotube and a scanning Nb nanoSQUID, Phys. Rev. B **88**, 064425 (2013).

[61] M. Khapaev, M. Kupriyanov, E. Goldobin, and M. Siegel, Current distribution simulation for superconducting multilayered structures, Supercond. Sci. Technol. **16**, 24 (2003).

[62] Manfred E. Schabes, Micromagnetic theory of non-uniform magnetization processes in magnetic recording particles, J. Magn. Magn. Mater. **95**, 249 (1991).

[63] A. Aharoni, Magnetization curling, Phys. Status Solidi **16**, 3 (1966).

[64] R. Skomski, *Simple Models of Magnetism* (Oxford University Press, New York, 2008).

[65] Amikam Aharoni, Angular dependence of nucleation by curling in a prolate spheroid, J. Appl. Phys. **82**, 1281 (1997).

Supplementary Information for Low-Noise $YBa_2Cu_3O_7$ NanoSQUIDs for Performing Magnetization-Reversal Measurements on Magnetic Nanoparticles

T. Schwarz,[1] R. Wölbing,[1] C. F. Reiche,[2] B. Müller,[1]
M. J. Martínez-Pérez,[1] T. Mühl,[2] B. Büchner,[2] R. Kleiner,[1] and D. Koelle[1]

[1] *Physikalisches Institut – Experimentalphysik II and Center for Collective Quantum Phenomena in LISA$^+$, Universität Tübingen, Auf der Morgenstelle 14, D-72076 Tübingen, Germany*

[2] *Leibniz Institute for Solid State and Materials Research IFW Dresden, Helmholtzstr. 20, 01069 Dresden, Germany*

(Dated: March 23, 2015)

I. CHARACTERIZATION OF SQUID-2

SQUID-2 was characterized in an electrically and magnetically shielded setup, with the sample mounted in vacuum (or in He gas) on a temperature-controlled cryostage. This enabled us to characterize electric transport and noise properties at variable temperature T, with a T stability of $\sim 1\,\mathrm{mK}$ [1].

Figure 1 shows data of electric transport properties and flux noise of SQUID-2, measured at $T = 5.3\,\mathrm{K}$. Figure 1(a) shows current-voltage-characteristics (IVCs) for modulation current $I_{\mathrm{mod}} = 0$ and two values of I_{mod}, corresponding to maximum and minimum critical current. The IVCs are slightly hysteretic with maximum critical current $I_c = 311\,\mu\mathrm{A}$ and normal state resistance $R_N = 2.5\,\Omega$, which yields a characteristic voltage $V_c \equiv I_c R_N = 0.78\,\mathrm{mV}$. The inset of Fig. 1(a) shows the modulation of the critical current $I_c(I_{\mathrm{mod}})$. From the modulation period, we find for the magnetic flux Φ coupled to the SQUID by I_{mod} the mutual inductance $M = \Phi/I_{\mathrm{mod}} = 0.8\,\Phi_0/\mathrm{mA} = 1.66\,\mathrm{pH}$. From resistively and capacitively shunted junction (RCSJ) simulations [2] of the $I_c(I_{\mathrm{mod}})$ characteristics [cf. inset of Fig. 1(a)] we obtain for the screening parameter $\beta_L = 2I_0L/\Phi_0 = 0.94$ (with $I_0 = I_c/2$), which yields a SQUID inductance $L = 6.3\,\mathrm{pH}$. We do find good agreement between the measured and simulated $I_c(I_{\mathrm{mod}})$ characteristics if we include an inductance asymmetry $\alpha_L \equiv (L_2 - L_1)/(L_2 + L_1) = 0.83$ (L_1 and L_2 are the inductances of the two SQUID arms) and a critical current asymmetry $\alpha_I \equiv (I_{0,2} - I_{0,1})/(I_{0,2} + I_{0,1}) = 0.30$; $I_{0,1}$ and $I_{0,2}$ are the critical currents of the Josephson junctions 1 and 2, respectively, intersecting the SQUID loop. These asymmetries are caused by asymmetric biasing of the SQUID and by asymmetries of the device itself.

$V(I_{\mathrm{mod}})$ is plotted in Fig. 1(b) for different bias currents. The transfer function, i.e. the maximum value of $\partial V/\partial\Phi$, in the non-hysteretic regime is $V_\Phi \approx 1.7\,\mathrm{mV}/\Phi_0$.

Fig. 1(c) shows the rms spectral density of flux noise $S_\Phi^{1/2}(f)$ of SQUID-2. This measurement was performed open loop (in dc bias mode) with a Nb dc SQUID (at $T = 4.2\,K$) as a voltage preamplifier, i.e. in 2-stage configuration, with a $\sim 700\,\mathrm{kHz}$ bandwidth. As for SQUID-1 (see main text), we find dominating f-dependent noise, with a noise power which scales very roughly as $S_\Phi \propto 1/f$.

Figure 2 shows rms flux noise spectra of SQUID-2 mea-

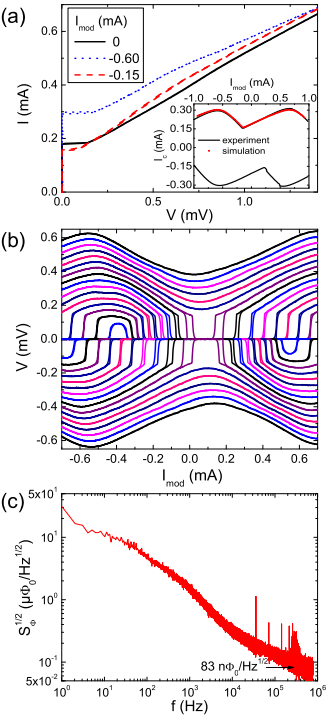

FIG. 1. Characteristics of SQUID-2 at $T = 5.3\,\mathrm{K}$. (a) IVCs for three different values of I_{mod}, including flux bias (I_{mod}) values which yield maximum and minimum critical current. Inset: measured $I_c(I_{\mathrm{mod}})$ together with numerical simulation results. (b) $V(I_{\mathrm{mod}})$ for bias currents $|I| = 175\ldots400\,\mu\mathrm{A}$ (in $15\,\mu\mathrm{A}$ steps). (c) rms spectral density of flux noise, measured open loop (dc bias) in 2-stage configuration. Arrow indicates upper limit for measured white noise at $\sim 700\,\mathrm{kHz}$.

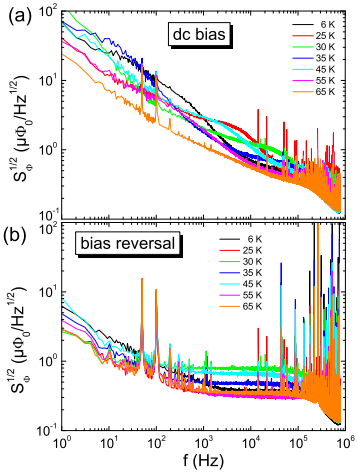

FIG. 2. rms spectral density of flux noise for SQUID-2, measured in FLL mode at different temperatures from 6 K to 65 K. (a) dc bias mode (b) bias reversal mode ($f_{\rm br} = 260\,$kHz).

sured with direct readout in flux locked loop (FLL), with $\sim 500\,$kHz bandwidth, in dc bias and bias reversal mode [3] for temperatures T ranging from 6 K to 65 K. For all data measured with dc bias [cf. Fig. 2(a)], we find f-dependent excess noise up to the cutoff frequency of the readout electronics. The flux noise S_Φ scales roughly as $1/f$, and for different T, the rms flux noise does not differ by more than about a factor of five, and does not show any systematic T-dependence.

Similar to SQUID-1 (cf. main text), in bias reversal mode [cf. Fig. 2(b)] the f-dependent excess noise above $\sim 1\,$kHz is suppressed. The remaining low-f excess flux noise observed in bias reversal mode roughly scales as $S_\Phi \propto 1/f$ for all values of T, again without any systematic T-dependence.

II. CHARACTERIZATION OF SQUID-3

Figure 3 shows electric transport and flux noise data for SQUID-3, taken in the magnetically and electrically shielded low-field setup at $T = 4.2\,$K, as described in the main text. The IVC shown in Fig. 3(a) is non-hysteretic, with $I_c = 69\,\mu$A and $R_N = 2.3\,\Omega$, which yields $V_c = 0.16\,$mV. The inset shows $I_c(I_{\rm mod})$, from which we obtain the mutual inductance $M = \Phi/I_{\rm mod} = 3.3\,\Phi_0/$mA. From the modulation depth of $I_c(I_{\rm mod})$ we determine $\beta_L = 0.95$. With the measured I_c, this yields a SQUID inductance $L = 28\,$pH. The bumps in the IVC at $V_{\rm res} \approx \pm 0.28\,$mV, can be attributed to an LC resonance. From the relation $V_{\rm res}/I_c R_N = (\frac{\pi}{2}\beta_C\beta_L)^{-1/2}$ [2] we determine the Stewart-McCumber parameter for the GBJJs as $\beta_C \approx 0.22$.

Figure 3(b) shows $V(I_{\rm mod})$ curves for different bias currents, yielding a transfer function $V_\Phi = 0.65\,{\rm mV}/\Phi_0$ at the optimum bias point, at which noise spectra have been taken ($I = 54\,\mu$A). Figure 3(c) shows the rms spectral density of flux noise $S_\Phi^{1/2}(f)$ for SQUID-3, measured in direct readout FLL mode up to $f = 100\,$kHz. For comparison, the bottom trace shows the background noise

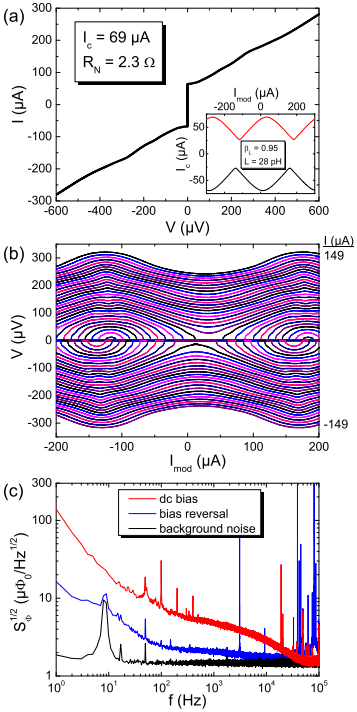

FIG. 3. Electric transport and noise characteristics of SQUID-3. (a) IVC of SQUID-3 for flux bias ($I_{\rm mod}$) which yields maximum critical current. Inset shows $I_c(I_{\rm mod})$ curves for positive and negative current bias. (b) Voltage V vs modulation current $I_{\rm mod}$ for bias currents between $I = \pm 149\,\mu$A (step width $\Delta I \approx 4\,\mu$A). (c) Rms spectral density of flux noise measured in FLL with dc bias and bias reversal mode ($f_{\rm br} = 260\,$kHz). The lower trace shows the background noise of the readout electronics.

from the readout electronics $S_\Phi^{1/2} \approx 1.45\,\mu\Phi_0/\mathrm{Hz}^{1/2}$. For $f \lesssim 40\,\mathrm{kHz}$, we find f-dependent flux noise. For larger f, the noise is limited by the electronics background noise. Hence, we can only give an upper limit of the white rms flux noise of SQUID-3 as $S_{\Phi,\mathrm{w}}^{1/2} < 1.45\,\mu\Phi_0/\mathrm{Hz}^{1/2}$. With bias reversal (at $f_{\mathrm{br}} = 81\,\mathrm{kHz}$), the f-dependent excess noise is clearly reduced. Still, we obtain with decreasing f a slight increase in rms flux noise up to $\sim 2.4\,\mu\Phi_0/\mathrm{Hz}^{1/2}$ at 100 Hz. Below 100 Hz SQUID-3 shows approximately $1/f$ noise, i.e. an increase in $S_\Phi^{1/2}$ to $\sim 16\,\mu\Phi_0/\mathrm{Hz}^{1/2}$ at 1 Hz.

III. ANALYSIS OF NOISE SPECTRA OF SQUID-1

For a more detailed analysis of the measured spectral density of equivalent flux noise power $S_\Phi(f)$ for SQUID-1, we applied an algorithm [4] to decompose the noise spectra into a sum of Lorentzians $F_i(f) = F_{0,i}/[1 + (f/f_{\mathrm{c},i})^2]$ plus a $1/f^2$ spectrum $F_{\mathrm{s}}(f) = F_{\mathrm{s}}(1\,\mathrm{Hz})/(f^2/\mathrm{Hz}^2)$ (i.e. one or more Lorentzians with characteristic frequencies f_{c} well below 1 Hz) plus a white noise contribution F_{w}. This means, the measured spectra are fitted by $F(f) = F_{\mathrm{w}} + F_{\mathrm{s}} + \sum_i F_i$.

Figure 4 shows the fit $F_{\mathrm{op}}^{1/2}(f)$ to the spectrum measured open loop (dc bias) [cf. Fig. 3(a) in the main text]. This yields an rms white noise level $F_{\mathrm{w,op}}^{1/2} = 45\,\mathrm{n}\Phi_0/\mathrm{Hz}^{1/2}$, a 1 Hz noise $F_{\mathrm{s,op}}^{1/2} = 84\,\mu\Phi_0/\mathrm{Hz}^{1/2}$ from $F_{\mathrm{s,op}}$ plus 16 Lorentzians with characteristic frequencies $f_{\mathrm{c},i}$, ranging from 2.6 Hz to 2.6 MHz, and amplitudes $F_{0,i}^{1/2}$ as listed in Tab. I(a).

For comparison of the fluctuation strengths of the different fluctuators with different $f_{\mathrm{c},i}$, in Tab. I we also list $\Delta\Phi_i = F_{0,i}^{1/2} \cdot \sqrt{2\pi f_{\mathrm{c},i}}$, which yields values in the range $\sim 30 \ldots 350\,\mu\Phi_0$.

Figure 5(a) and (b) shows the fits $F_{\mathrm{dc}}^{1/2}(f)$ and $F_{\mathrm{br}}^{1/2}(f)$ to the spectra measured in FLL with dc bias and bias reversal, respectively [cf. Fig. 3(b) in the main text]. Here, we fixed the white noise contribution in dc bias mode to $F_{\mathrm{w,dc}}^{1/2} = 41\,\mathrm{n}\Phi_0/\mathrm{Hz}^{1/2}$, i.e. a value close to the one obtained for the measurement in open loop mode. The white noise contribution in bias reversal mode is determined by the noise level achieved in dc bias mode at the bias reversal frequency f_{br}, which yields $F_{\mathrm{w,br}}^{1/2} = 231\,\mathrm{n}\Phi_0/\mathrm{Hz}^{1/2}$. The spectrum fitted to the dc bias measurement is decomposed into 15 Lorentzians, while for the bias reversal measurement, fitting with 6 Lorentzians is sufficient. The rms noise at 1 Hz for the bias reversal spectrum is by a factor ~ 1.8 lower than the one for the dc bias spectrum. Characteristic frequencies $f_{\mathrm{c},i}$, and amplitudes of the Lorentzians are listed in Tab. I(b) for the dc bias spectrum and in Tab. I(c) for the bias reversal spectrum.

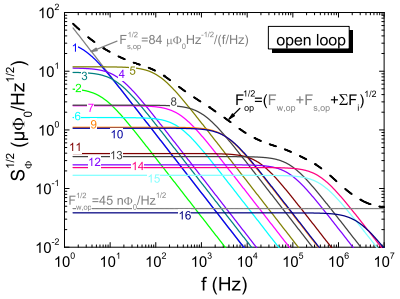

FIG. 4. Analysis of flux noise of SQUID-1: The dashed line is the fit to the noise spectrum, measured open loop (dc bias). This spectrum is the sum of the shown Lorentzians (labeled as $i = 1 \ldots 16$) plus a white noise contribution plus a $F_s \propto 1/f^2$ contribution.

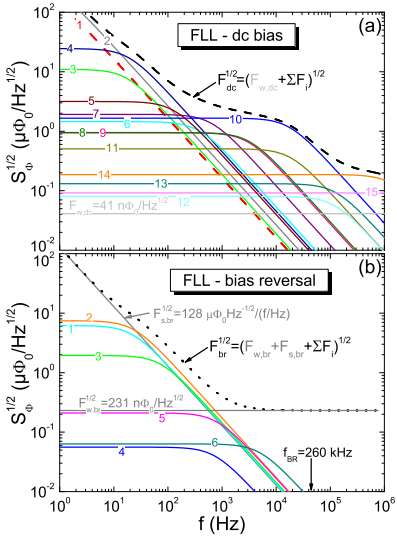

FIG. 5. Analysis of flux noise of SQUID-1: The dashed line in (a) and the dotted line in (b) are fits to the noise spectra, measured in FLL (a) with dc bias and (b) with bias reversal. Those spectra are superpositions of the shown Lorentzians [labeled as $i = 1 \ldots 11$ in (a) and $i = 1 \ldots 6$ in (b)] plus a white noise contribution plus a $F_s \propto 1/f^2$ contribution.

TABLE I. Characteristic frequencies $f_{c,i}$, rms amplitudes $F_{0,i}^{1/2}$ and flux amplitudes $\Delta\Phi_i$ of Lorentzians F_i calculated to approximate the flux noise spectra of SQUID-1, measured (a) in open loop (dc bias) [cf. Fig. 4], (b) in FLL dc bias [cf. Fig. 5(a)], and (c) in FLL bias reversal mode [cf. Fig. 5(b)].

(a) open loop

i	1	2	3	4	5	6	7	8	9	10	11	12	13	14	15	16
$f_{c,i}$ (Hz)	2.6	6.5	13	14	111	301	325	1.0 k	3.3 k	3.5 k	18 k	82 k	88 k	380 k	410 k	2.6 M
$F_{0,i}^{1/2}$ ($\mu\Phi_0/\mathrm{Hz}^{1/2}$)	33	5.1	9.6	11	12	1.6	2.6	2.6	1.1	1.1	0.40	0.25	0.35	0.23	0.17	0.038
$\Delta\Phi_i$ ($\mu\Phi_0$)	131	32	87	106	314	71	119	211	158	158	131	182	261	352	269	155

(b) FLL – dc bias

i	1	2	3	4	5	6	7	8	9	10	11	12	13	14	15
$f_{c,i}$ (Hz)	0.8	1	17	18	126	369	631	2.9 k	3.2 k	17.1 k	18.5 k	117 k	126 k	1.4 M	6.8 M
$F_{0,i}^{1/2}$ ($\mu\Phi_0/\mathrm{Hz}^{1/2}$)	206	265	11.0	24.5	3.2	1.4	1.9	0.94	0.95	1.7	0.51	0.08	0.13	0.19	0.09
$\Delta\Phi_i$ ($\mu\Phi_0$)	461	665	114	264	89	70	121	128	134	544	173	69	117	546	600

(c) FLL – bias reversal

i	1	2	3	4	5	6
$f_{c,i}$ (Hz)	21	23	74	736	794	5 k
$F_{0,i}^{1/2}$ ($\mu\Phi_0/\mathrm{Hz}^{1/2}$)	6.2	7.4	1.9	0.056	0.21	0.063
$\Delta\Phi_i$ ($\mu\Phi_0$)	72	90	42	3.8	15	11

[1] M. Kemmler, D. Bothner, K. Ilin, M. Siegel, R. Kleiner, and D. Koelle, "Suppression of dissipation in Nb thin films with triangular antidot arrays by random removal of pinning sites," Phys. Rev. B **79**, 184509 (2009).

[2] B. Chesca, R. Kleiner, and D. Koelle, "SQUID Theory," in The SQUD Handbook, Vol. 1: Fundamentals and Technology of SQUIDs and SQUID systems, edited by John Clarke and Alex I. Braginski (Wiley-VCH, Weinheim, 2004) Chap. 2, pp. 29–92.

[3] D. Drung and M. Mück, "SQUID Electronics," in The SQUD Handbook, Vol. 1: Fundamentals and Technology of SQUIDs and SQUID systems, edited by John Clarke and Alex I. Braginski (Wiley-VCH, Weinheim, 2004) Chap. 4, pp. 127–170.

[4] E. Sassier, R. Kleiner, and D. Koelle, "A spectroscopic method for excess-noise spectrum analysis," Unpublished.

Publication 2

NANO LETTERS
Cite This: Nano Lett. 2018, 18, 7674−7682
Letter
pubs.acs.org/NanoLett

NanoSQUID Magnetometry on Individual As-grown and Annealed Co Nanowires at Variable Temperature

M. J. Martínez-Pérez,*[,†,‡] J. Pablo-Navarro,[¶] B. Müller,[§] R. Kleiner,[§] C. Magén,[†,¶] D. Koelle,[§] J. M. de Teresa,[†,¶] and J. Sesé[†,¶]

[†]Instituto de Ciencia de Materiales de Aragón and Departamento de Física de la Materia Condensada, CSIC-Universidad de Zaragoza, 50009 Zaragoza, Spain

[‡]Fundación ARAID, 50018 Zaragoza, Spain

[¶]Laboratorio de Microscopías Avanzadas (LMA), Instituto de Nanociencia de Aragón (INA), Universidad de Zaragoza, 50018 Zaragoza, Spain

[§]Physikalisches Institut, Experimentalphysik II and Center for Quantum Science (CQ) in LISA[+], Universität Tübingen, 72076 Tübingen, Germany

S *Supporting Information*

ABSTRACT: Performing magnetization studies on individual nanoparticles is a highly demanding task, especially when measurements need to be carried out under large sweeping magnetic fields or variable temperature. Yet, characterization under varying ambient conditions is paramount in order to fully understand the magnetic behavior of these objects, e.g., the formation of nonuniform states or the mechanisms leading to magnetization reversal and thermal stability. This, in turn, is necessary for the integration of magnetic nanoparticles and nanowires into useful devices, e.g., spin-valves, racetrack memories, or magnetic tip probes. Here, we show that nanosuperconducting quantum interference devices based on high critical temperature superconductors are particularly well suited for this task. We have successfully characterized a number of individual Co nanowires grown through focused electron beam induced deposition and subsequently annealed at different temperatures. Magnetization measurements performed under sweeping magnetic fields (up to ∼100 mT) and variable temperature (1.4−80 K) underscore the intrinsic structural and chemical differences between these nanowires. These point to significant changes in the crystalline structure and the resulting effective magnetic anisotropy of the nanowires, and to the nucleation and subsequent vanishing of antiferromagnetic species within the nanowires annealed at different temperatures.

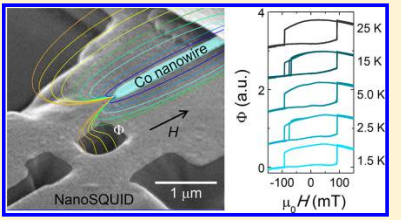

KEYWORDS: *NanoSQUID, magnetization measurements, magnetic nanowires, focused electron beam induced deposition, magnetization reversal*

Beyond well-studied two-dimensional (stripe-like) planar magnetic nanowires, the scientific community is increasingly interested in their three-dimensional (3D) counterparts.[1] Not being restricted to the plane, 3D nanowires (NWs) offer new functionalities with potential for applications such as vertical racetrack memories,[2] magnetic logic,[3] magnetic nanocantilevers for high-resolution imaging,[4] or actuators.[5] Due to their geometry, these objects also offer a richer variety of available magnetic configurations and possible domain walls with very attractive topological and dynamical properties that are appealing from a fundamental and technological point of view.[6,7]

Magnetic characterization of such small objects still poses many technological challenges in terms of spin sensitivity and operation conditions, i.e., the possibility of applying large magnetic fields and operating at broad temperature ranges. Magneto-Optical Kerr Effect (MOKE) microscopy, Hall sensors, and off-axis electron holography have been successfully applied to the study of 3D magnetic NWs.[8−11] However, MOKE does not usually offer the possibility of working under variable temperature and provides very poor sensitivity. Hall sensors, however, are noted for operating in extraordinary large magnetic field and temperature ranges but not being well-suited for ultrasensitive sensing. Electron holography is characterized by its capability to produce spatially resolved quantitative imaging of the magnetization states as a function of temperature and magnetic field,[12] even tomographic.[13] However, it has also limited sensitivity and the stability requirements impose remarkable experimental constraints. More recently, ultrasoft oscillating microcantilevers have

Received: August 16, 2018
Revised: October 28, 2018
Published: November 20, 2018

DOI: 10.1021/acs.nanolett.8b03329
Nano Lett. 2018, 18, 7674−7682

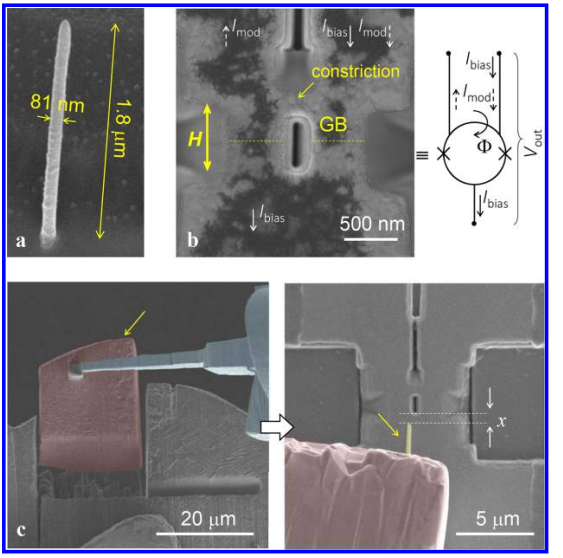

Figure 1. (a) SEM image of an as-grown Co-FEBID NW. (b) Typical nanoSQUID device and schematic of the equivalent electric circuit. The field (H) direction, the position of the grain boundary (GB), and the constriction (see Methods for more details on the constriction) are highlighted. A current (I_{mod}) flowing through the constriction couples flux (Φ) to the nanoloop serving to modulate the nanoSQUID response. I_{bias} and V_{out} are the biasing current and output voltage, respectively. (c) False colored images of the NW transport process. The micromanipulator (blue), the copper lamella (red), and the NW (yellow arrow) are highlighted. x is defined as the in-plane distance between the NW's end tip and the nanoloop edge.

been operated as force sensors to detect individual magnetic NWs.[14] The sensitivity can reach impressive values of few Bohr magnetons when using cantilevers made of, e.g., carbon nanotubes.[15] Such an approach is, however, technologically very challenging, and the results can not be interpreted straightforwardly. Alternatively, nano-Superconducting Quantum Interference Devices (nanoSQUIDs) provide a direct measure of minute fractions of the magnetic flux quantum (Φ_0).[16−19] These sensors were indeed used in the first pioneering experiments for detecting individual magnetic nanoparticles and NWs.[20,21] Being superconducting, nanoSQUIDs are usually restricted to narrow temperature and field ranges. We have beaten such limitations by using the high critical temperature and high critical field superconductor $YBa_2Cu_3O_7$ (YBCO) and grain boundary Josephson junctions.[22,23] The resulting nanoSQUIDs are fully operative upon large in-plane applied magnetic fields (up to $\mu_0 H = 1$ T) and broad temperature ranges (mK < T < 80 K).[24]

Regarding fabrication, 3D NWs can be synthesized using both chemical and physical methods. In the former case, templates such as alumina matrices,[25] carbon nanotubes,[10] or GaAs NWs[14] are required to produce vertical NWs and hollow nanotubes. Among physical methods, Focused Electron Beam Induced Deposition (FEBID) stands out as it allows depositing 3D nanoscopic objects with arbitrary shape and dimensions down to few tens of nanometers in a single step.[26] Unfortunately, Co- and Fe-FEBID magnetic deposits are often formed by nanocrystals with poor metallic content due to the presence of carbonaceous impurities. This yields degraded magnetic and transport properties compared with pure bulk materials. Recently, high-quality Co-FEBID NWs have been obtained by implementing an ex situ annealing process in high vacuum conditions.[27] Increasing the annealing temperature up to 600 °C improves the degree of crystallinity, increasing also the Co purity and saturation magnetization up to values very close to bulk crystalline Co.

Here, we present a thorough study of individual Co-FEBID NWs annealed at different temperatures by using YBCO nanoSQUID sensors. For this purpose we have first developed an extremely precise technical protocol that has allowed the growth, annealing, and subsequent integration of individual Co-FEBID NWs onto nanoSQUIDs with nanometric resolution. Thanks to the latter, we achieve excellent sample−sensor magnetic coupling. This fact, together with the high spin-sensitivity of YBCO nanoSQUIDs, allows us distinguishing minute magnetic signals produced by domain wall nucleation, pinning/depinning, or complete magnetization reversal.

As demonstrated in ref 27, NWs annealed at different temperatures undergo drastic structural and chemical changes. These changes have dramatic consequences on the magnetic response of the NWs that become only apparent when performing magnetization measurements at variable temperature. We have succeeded in observing such effects thanks to the broad operation temperature range of YBCO nanoSQUIDs. Based on the observed temperature-dependent

DOI: 10.1021/acs.nanolett.8b03329
Nano Lett. 2018, 18, 7674−7682

magnetization switching of the NWs, we have classified them into three groups. The behavior of the as-grown NW reveals the existence of many defects or impurities and, more importantly, large spin frustration. NWs annealed at 150 and 300 °C seem to be influenced by the presence of sizable antiferromagnetic crystals. These effects diminish in NWs annealed at 450 and 600 °C, which exhibit higher crystal and chemical quality and increased anisotropy.

Results. *Experimental Setup.* Three-dimensional Co-FEBID NWs are fabricated by FEBID in a dual-beam system equipped with an electron and a Ga Focused Ion Beam (FIB) column, using $Co_2(CO)_8$ precursor gas (see Methods). Fabrication parameters are chosen to maximize the resulting Co purity while preserving good spatial resolution.[28] One NW is left as-grown (see Figure 1a), whereas the rest are annealed at different temperatures in high-vacuum conditions as described in the Methods. As demonstrated in ref 28, all NWs consist of an inner magnetic Co core surrounded by a ∼5 nm-thick nonmagnetic layer. Resulting geometrical parameters of all NWs can be seen in Table 1. The as-grown NW and those annealed at 150, 300, 450, and 600 °C are denoted as RT-, 150-, 300-, 450-, and 600-NW, respectively.

Table 1. Geometrical Parameters of Each NW: Radius (R) Excluding the Nonmagnetic External Layer of ∼5 nm, Length (l), Magnetic Volume (V_{mag}), z Positions of the NW End Tip with Respect to the nanoSQUID Surface, Total Magnetic Moment (μ_{NW}), and Co Purity (p)

	R (nm)	l (μm)	V_{mag} (10^5 nm^3)	z (nm)	μ_{NW} (10^9 μ_B)	p
RT-NW	35.5	1.8	7.13	379	1.1	0.75 ± 0.26
150-NW	31.5	2.3	7.17	1050	1.0	0.84 ± 0.26
300-NW	36.5	2.2	9.21	1055	1.4	0.96 ± 0.25
450-NW	38.5	1.9	8.85	980	1.5	1.06 ± 0.30
600-NW	38.0	2.1	9.53	483	1.8	1.06 ± 0.26

A Scanning Electron Microscopy (SEM) image of a typical nanoSQUID device can be seen in Figure 1b (see Methods for details). These devices are operated in a variable temperature insert (minimum temperature ≈ 1.4 K) equipped with a rotator that allows aligning the nanoSQUID with respect to the externally applied magnetic field (indicated by a yellow arrow in Figure 1b). Field must be aligned parallel to the SQUID substrate and perpendicularly to the grain boundary's plane so that no magnetic flux is coupled both to the nanoloop and to the Josephson junctions. Magnetization measurements are performed by sweeping the external magnetic field and measuring the total flux Φ captured by the nanoSQUID loop as the NW is driven through magnetization reversal.

NWs are transported using an Omniprobe nanomanipulator installed in the dual-beam system. Here, we describe briefly the transport protocol used for the annealed NWs (see the Supporting Information for more details on the transport of RT-NW). Thin (few μm-thick) Cu lamellae where NWs have been grown and annealed are used as carriers. The nanomanipulator tip is attached to the corresponding Cu lamella by Focused Ion Beam Induced Deposition (FIBID) of Pt using $CH_3CpPt(CH_3)_3$ precursor gas (see Figure 1c, left). The carrier is then located with nanometric resolution over the sensor surface so that the corresponding NW's long axis is parallel to the externally applied magnetic field with the end tip lying close to the nanoloop (see Figure 1c, right). A second Pt-FIBID deposit is used to fix the carrier to the substrate. The nanomanipulator tip is finally released by FIB-cutting.

After the transport process, all NWs lie at equivalent positions chosen so to guarantee an optimum NW-sensor coupling (see Figure 2a). For this purpose, the NWs' end tip lies at just $x \approx 100-300$ nm from the nanoloop (see Figure 1c, right). The corresponding vertical distance z measured from the NWs' end tip to the surface of the sensor is given in Table 1.

Hysteresis Loops. Figure 2b shows representative hysteresis loops measured at 15 K for each NW (five curves are shown in each panel). Loops are square-shaped indicating that the NWs are in the quasi single-domain state (as expected due to their large aspect-ratio) and that the field is applied along the NW's easy axis. In the classical model of Stoner−Wohlfarth,[29] the magnetization reversal of a single domain particle takes place coherently, i.e., all magnetic moments reverse at unison. This is only true for very small magnetic objects (few nm). More conveniently, magnetic moments will tilt around the easy axis of the NW in a vortex-like configuration, which saves some magnetostatic energy at the cost of exchange energy (curling model).[30] This is a quite accepted mechanism for magnetization reversal in NWs that will serve us as starting point to analyze our experimental data.

Under these circumstances and, assuming a negligible contribution of the magnetocrystalline anisotropy due to the standard polycrystalline nature of the NWs, the nucleation magnetic field is given by $H_n^{cur} = \kappa M_s(\lambda_{ex}/R)^2$.[30] Here, the exchange length λ_{ex} is defined as $\sqrt{2A/\mu_0 M_s^2}$, μ_0 being the magnetic permeability constant, M_s the saturation magnetization, A the exchange stiffness, R the radius of the NW, and $\kappa = 3.39$ for an infinite cylinder. We will approximate $M_s = pM_s(\text{bulk})$ and $A = pA(\text{bulk})$, with p being the Co purity ($0 < p < 1$), $M_s(\text{bulk}) = 1.4 \times 10^6$ A/m, and $A(\text{bulk}) = 2.5 \times 10^{-11}$ J/m for pure crystalline Co. We highlight that, within this very simple model, the resulting values of H_n^{cur} are independent of p and l, depending only on the radius of the NW as $H_n^{cur} \propto 1/R^2$. Inserting the R values listed in Table 1 yields the values indicated in Figure 2b with dashed lines.

In the case of RT- and 150-NW, the curling model overestimates by far the experimentally measured nucleation fields. This is usually found in practice as, in real NWs, magnetization reversal is more likely to undergo a nucleation and propagation process. Such a process is energetically favorable and takes place at fields much lower than H_n^{cur}. In this scenario, a small reversed region is first nucleated by curling together with the corresponding domain wall.[31] Subsequently, this domain wall moves rapidly (ns−ps time scales) through the NW until the magnetization reversal is complete. Strikingly, in the case of 300-, 450-, and 600-NW, the H_n^{cur} values are slightly underestimated. This suggests some additional structural differences between the samples annealed at higher temperatures as also supported by the evident differences in the hysteresis loops.

These differences can be better seen by enlarging the field region in which magnetization switching events take place (Figure 2b, bottom panel). Inspection of these curves reveals that the switching of RT-NW takes place in several steps. This

DOI: 10.1021/acs.nanolett.8b03329
Nano Lett. 2018, 18, 7674−7682

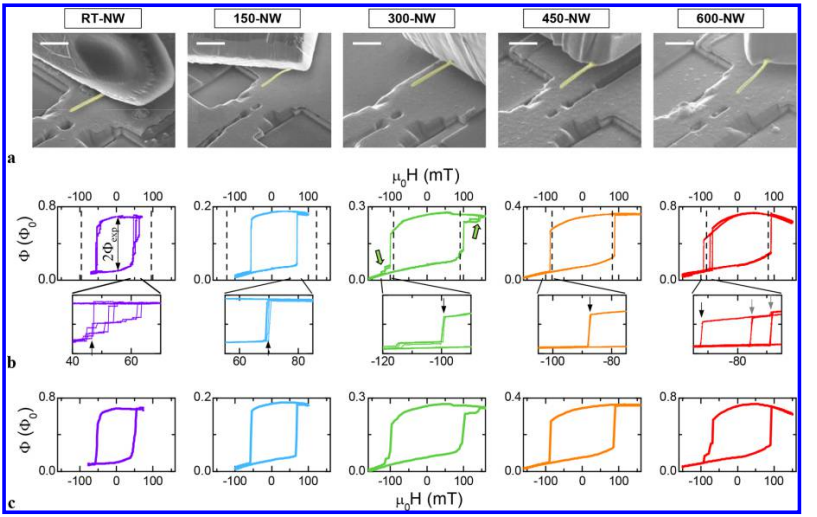

Figure 2. (a) False colored SEM images of the different YBCO nanoSQUIDs with their corresponding Co-FEBID NW (yellow). Scale bars are 1 μm. (b) Five representative hysteresis loops obtained at 15 K for each NW. Φ_{exp} is the total signal coupled to the nanoSQUID from the NW. Dashed lines correspond to the theoretical nucleation fields resulting from the curling model of magnetization reversal. Bottom panels show an enlarged view of the region where magnetization switches direction. The nucleation fields $H_n^{\pm}$ are indicated by black arrows. Gray arrows highlight the existence of distinct switching events in 600-NW, whereas green thick arrows indicate additional minor steps after the main switching event in 300-NW. (c) Mean hysteresis loops at 15 K for each NW obtained after averaging over 30−50 curves.

is typically found when magnetization reversal follows a nucleation/propagation process, as discussed previously. Starting from the quasi-single domain saturated state at large positive (negative) magnetic fields, the first step observed in the hysteresis curve when decreasing (increasing) the sweeping magnetic field stems from the nucleation of the small reversed region and the corresponding domain wall. This serves to define the experimental nucleation fields, i.e., H_n^+ and H_n^-, for increasing and decreasing magnetic fields, respectively (as an example, one value of H^+ is indicated by an arrow in Figure 2b, bottom panel). The presence of steps suggests that RT-NW is not completely homogeneous, containing structural defects, impurities, or a certain degree of surface roughness that behaves as pinning defects for the moving domain wall.

However, magnetization reversal of the rest of the NWs takes place in extremely well-defined *single* switching events (indicated by the respective arrows in Figure 2b), defining the nucleation fields $H_n^{\pm}$. This suggests that these NWs have fewer (or a different kind of) defects as compared to RT-NW. In the case of 300-NW, an additional minor step (thick green arrows) is always observed at large (positive and negative) magnetic fields, after the main switching event has taken place. Interestingly, in the case of 600-NW, and for decreasing sweeping magnetic fields only, three clearly separated switching events can be distinguished. These are highlighted by three arrows (black and gray) in Figure 2b. The latter suggests the occurrence of three different reversal paths that are undertaken stochastically.

We highlight that such peculiarities become apparent only for single shot measurements performed on individual NWs. To illustrate this, in Figure 2c we plot the hysteresis loops resulting after averaging over 30−50 curves measured at 15 K. This serves to mimic the results that one would obtain when measuring a large number of identical NWs. The same would apply to measurements where averaging large number of hysteresis loops is required to achieve a tolerable signal-to-noise ratio, i.e., typical MOKE signals. For instance, a reversal process consisting of many-step events as that of RT- or 300-NW can not be distinguished from the occurrence of distinct switching events as the case of 600-NW.

Temperature Dependence of $\langle H_n \rangle$. Differences between the NWs become even more evident when performing measurements at variable temperature. The T-dependence of $\langle H_n \rangle$ is shown in Figure 3. Here, $\langle H_n \rangle = (\langle H_n^+ \rangle - \langle H_n^- \rangle)/2$ with $\langle H_n^{\pm} \rangle$ being the mean value of $H_n^{\pm}$ after averaging over 30−50 curves measured at each temperature. In the case of RT-NW, $\langle H_n \rangle$ values decrease with increasing temperature roughly following a power-law. In the case of 150-NW, $\langle H_n \rangle$ exhibits three regimes: it increases first with increasing temperature up to $T < 30$ K; for $T > 30$ K, $\langle H_n \rangle$ decreases showing a large step at $T = 60$ K. A similar step can be also observed for 300-NW. In these two later cases, i.e., 150-NW and 300-NW, $\langle H_n \rangle$ depends almost linearly on T. Finally, in the case of 450- and 600-NW, $\langle H_n \rangle$ decreases for increasing temperature and a clear flattening is observed at low temperatures below ∼20 K.

Such decrease of the nucleation field as the temperature is increased is found when magnetization reversal follows a thermally activated process, as typical in magnetic nanoparticles. However, the remarkable differences between the T-

DOI: 10.1021/acs.nanolett.8b03329
Nano Lett. 2018, 18, 7674−7682

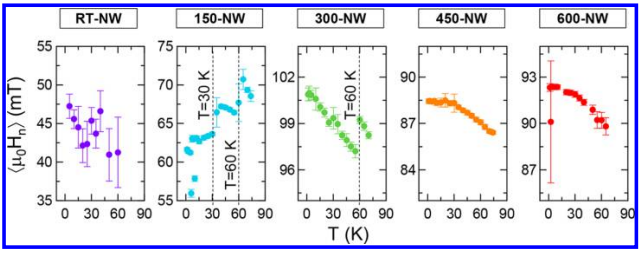

Figure 3. Temperature dependence of the averaged nucleation field for each NW. Notice that the vertical axis covers 20 mT in the case of RT- and 150-NW, and just 10 mT for 300-, 450-, and 600-NW. In the case of 150- and 300-NW, the relevant temperature ranges discussed in the text are highlighted.

dependence of the nucleation field of each NW (power-law, linear or T-independent behavior at low temperatures) point to a quite intricate scenario. We can speculate that these differences are due to structural changes going on in the NWs at intermediate annealing temperatures that lead to different nucleation mechanisms for the reversed domain.[32] This issue will be treated in detail in a separated publication.

In the case of RT-NW, the large scattering found in the $\langle H_n \rangle$ vs T values suggests that this NW might find multiple almost-equivalent paths to reverse their magnetization. This can be due to the presence of pinned Co atoms or antiferromagnetic species, e.g., CoO or Co_3O_4. These oxides are very likely to be present at the surface of the NW and even in the core. Interaction between ferromagnetic Co nanocrystals and pinned Co atoms or antiferromagnetic regions leads to spin frustration that typically exhibits a nonreproducible (spin glass-like) behavior along different measurements. In this scenario, the energy landscape and, therefore, the effective reversal path varies fairly from one hysteresis measurement to the other, leading to a quite broad distribution of nucleation fields.

Finally, the behavior of 150- and 300-NW can be tentatively explained as follows. The hysteresis loops of 150-NW measured at $T < 35$ K are slightly shifted toward positive H values (see Figure 2b). In this temperature range, the nucleation field also exhibits other counterintuitive behavior, like the fact that $\langle H_n \rangle$ increases for increasing temperatures. This is contrary to what is expected for a thermally-activated process and is usually found in exchange-biased systems.[33] It is tempting to associate such a behavior with the presence of some amount of Co_3O_4 phase being antiferromagnetic below ~35 K. CoO has a very large Neél temperature T_N close to room temperature, but Co_3O_4 exhibits $30 < T_N < 40$ K, typically.[34] At $T < T_N$, the exchange bias effect might lead to the aforementioned positive H-shift.[35] This effect disappears at $T > 35$ K. In this temperature range, $\langle H_n \rangle$ values decrease for increasing temperature, and hysteresis loops are well centered around zero field (not shown). In addition to that, a small negative H-shift is observed at $T > 60$ K for both 150- and 300-NW. A more comprehensive analysis of this behavior will be also given in a separate publication.

Effects of the Annealing Temperature on the Crystalline Structure. Regarding the internal structure of the NWs, it will be useful to focus on the experimentally measured nucleation field of each NW at fixed temperature, e.g., $T = 1.4$ K. It is important to highlight that, according to the simple curling model of magnetization reversal, the nucleation field does not depend on p but depends strongly on the radius of the NW as $\propto 1/R^2$. The same also applies to more realistic models including nucleation/propagation of magnetic domains. This can be easily seen by performing micromagnetic simulations and considering the actual geometry of each NW (see Methods). Simulations assume zero temperature and neglect any contribution of the magnetocrystalline anisotropy. In Figure 4a we plot the numerically calculated nucleation fields multiplied by R^2 (solid line). These results must be compared with $\langle H_n^{1.4} \rangle R^2$, i.e., the averaged nucleation field measured for each NW at the lowest experimental temperature ($T = 1.4$ K) multiplied by R^2 (colored dots). As expected, numerical calculations lead to an approximately flat horizontal curve. Interestingly, experimental points exhibit a striking crossover: $\langle H_n^{1.4} \rangle R^2$ corresponding to RT- and 150-NW lie well below the calculated data points, whereas values obtained for 300-, 450-, and 600-NW are much larger than expected. The behavior of RT- and 150-NW is not surprising since defects, unavoidable in real NWs, behave as localized nucleation points for reversed domains. This decreases the effective energy barriers for magnetization reversal and thus the nucleation fields. These effects can be emulated by means of numerical simulations. For this purpose, we assume that there are a number (~250) of randomly distributed pinning centers (5 nm radius spheres) having randomly fixed magnetization. In these simulations we also neglect the contribution of the magnetocrystalline anisotropy. The results can be seen in Figure 4a (open stars). Interestingly, the numerically calculated nucleation fields are largely reduced as compared to those obtained in the absence of pinning centers. As discussed previously, pinned defects serve as nucleation centers for the reversed magnetization, triggering switching.

However, the behavior of the NWs annealed at larger temperatures suggests that magnetocrystalline anisotropy, K_u, can not be neglected in these samples. This can be implemented in the numerical simulations by assuming a net uniaxial anisotropy constant $K_u = \beta K_u(\text{bulk})$ where $K_u(\text{bulk}) = 5.2 \times 10^5$ J/m^3 is that of bulk crystalline Co. As it can be seen in Figure 4a, experimental data (colored dots) can be nicely accounted for by simulation setting $\beta = 0.09$ (crosses). This behavior might originate from the crystallization of larger and larger pure Co crystals as annealing temperature increases. To prove this, High Resolution Transmission Electron Microscopy (HRTEM) imaging has been performed to monitor the structural change of the NWs with increasing annealing temperature (Figure 4b). The RT-NW shows the typical

DOI: 10.1021/acs.nanolett.8b03329
Nano Lett. 2018, 18, 7674−7682

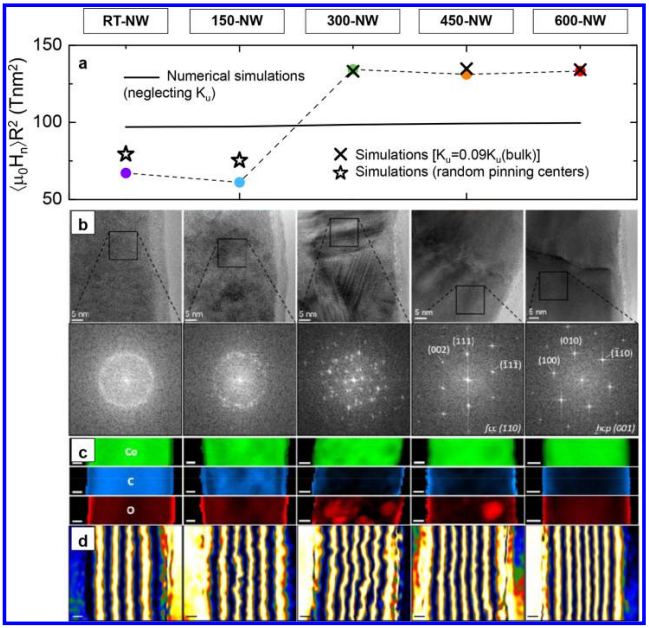

Figure 4. (a) Experimentally determined (colored dots) and numerically simulated (solid line) nucleation fields at T = 0 K multiplied by R^2 for the NWs annealed at different temperatures. (b) HRTEM images of each NW case accompanied by the corresponding FFT of a small area of the image. (c) STEM-EELS chemical maps showing the spatial distribution of Co, C, and O in green, blue, and red, respectively. (d) Magnetic induction flux representations obtained by normalizing the magnetic phase images to the diameter (maximum thickness) and calculating the cosine of 350 times the normalized magnetic phase. The undefined scale bars in all images correspond to 10 nm. Measurements shown in panels b–d were performed on NWs grown and annealed under the same experimental conditions as those used for the nanoSQUID experiments.[27]

nanocrystalline microstructure, with no texture, as the fast Fourier transform (FFT) of a small area of the image evidences a diffuse diffraction ring. For the 150-NW, some individual Bragg diffraction spots can be observed in combination with the diffuse diffraction ring, which indicates the presence of grains of larger size. In the 300-NW case, the diffuse scattering has vanished and areas with superposition of different crystals are most commonly detected. In the 450-NW, the FFT patterns reveal that larger areas exhibit a microstructure composed of single crystals. In this case, the grain size becomes similar to the NW diameter, identifying fewer regions with overlapping between different crystals. Finally, in the case of 600-NW, the nanostructure is constituted by several large crystals, whose lateral size is the NW width and separated from each other by grain boundaries expanded along the whole diameter. Examples of different crystal structures are shown in Figure 4b, where face-centered-cubic (*fcc*) and hexagonal-closest-packed (*hcp*) Co crystals have been found.

Effects of the Annealing Temperature on the Co Purity. Magnetization measurements allow us extracting information about the Co purity as well. From the total signal captured by each nanoSQUID (Φ_{exp}, see Figure 2b), it is possible to numerically estimate the total magnetic moment of the NWs (μ_{NW}). For this purpose, experimental values of Φ_{exp} must be compared with the calculated flux $\Phi_{theo} = |\phi_\mu|\mu_{NW}$, where ϕ_μ is the averaged coupling factor for each nanoSQUID across the NW volume (see Methods). The obtained values of μ_{NW} and the resulting Co purity, defined as $p = \mu_{NW}/V_{mag}M_s$(bulk), are given in Table 1. Remarkably, p increases for increasing annealing temperature in very good agreement with results obtained from Electron Energy Loss Spectroscopy (EELS) chemical analysis in Scanning Transmission Electron Microscopy (STEM) mode, as shown in Figure 4c. The average Co composition increases from 72 atom % of RT-NW up to 78% for 150-NW, 88% for 300-NW, 92% for 450-NW, and 94% for 600-NW. Accordingly, the core average net magnetic induction, obtained by off-axis electron holography experiments (see Figure 4d), increases from 0.91 T for RT-NW up to 1.22 T for 150-NW, 1.36 T for 300-NW, 1.49 T for 450-NW, and 1.61 T for 600-NW, reaching a value very close to the bulk magnetic induction of 1.76 T.

Discussion. Considering these experimental data, it is possible to provide a tentative interpretation of the results. According to our observations, samples could be divided into three groups.

RT-NW. The RT-NW exhibits clear signs of high structural disorder and an important degree of magnetic frustration leading to a spin glass-like behavior. This is evidenced by the

DOI: 10.1021/acs.nanolett.8b03329
Nano Lett. 2018, 18, 7674−7682

presence of a multiple-step magnetization reversal (Figure 2b) and the large scattering observed in the $\langle H_n \rangle$ vs T values (see Figure 3) The T-dependence of $\langle H_n \rangle$ follows the typical power law observed for thermally-assisted magnetization reversal in nanoparticles.

150- and 300-NW. Annealing the NWs seems to reduce the degree of disorder as suggested by the reduced number of steps in the hysteresis loops (Figure 2b). In addition to that, we observe a striking trend change in the T-dependence of $\langle H_n \rangle$ that becomes roughly linear (Figure 3) together with an important increase of the nucleation field (crossover shown in Figure 4a). These observations point to significant structural changes taking place in the annealed NWs having an influence on the switching mechanisms and the effective anisotropy of the NWs.

On the other side, the presence of antiferromagnetic species becomes much more evident. This is manifested by the nonsymmetric hysteresis loops observed in 150-NW below 35 K (Figure 2b) and the fact that $\langle H_n \rangle$ increases for increasing temperature (Figure 3). The latter points to the existence of substantial antiferromagnetic crystals that become paramagnetic above $T \approx 35$ K. A similar effect is observed for both 150- and 300-NW at $T > 60$ K where hysteresis loops are slightly shifted toward negative magnetic fields. Interestingly, oxygen-rich regions nucleate in the NW's core precisely for annealing temperatures between 150 and 300 °C. This is evidenced by the oxygen chemical maps obtained from EELS measurements (Figure 4c). The observed oxygen-rich regions may well correspond to relatively large (∼10 nm) Co oxide nanoparticles that would lead to the well-known phenomenon of exchange bias observed experimentally.

450- and 600-NW. Finally, NWs annealed at 450 and 600 °C behave very similar. Both exhibit a similar dependence of $\langle H_n \rangle$ on T (Figure 3) and increased values of the nucleation fields (Figure 4a), suggesting an effectively increased (magnetocrystalline) anisotropy as discussed previously. Remarkably, HRTEM images and FFT patterns provide the existence of both *hcp* and *fcc* Co crystals, forming quite large (∼100 nm) crystalline regions separated by grain boundaries (Figure 4c). Being randomly distributed, such crystalline grains might lead to a net uniaxial magnetocrystalline anisotropy that would indeed increase the resulting nucleation fields. However, the presence of antiferromagnetic species or spin frustration is still suggested by the observation of multiple coexisting reversal paths (Figure 2b). Indeed, oxygen-rich regions are still visible in the STEM-EELS chemical map shown in Figure 4c for 450-NW.

Conclusions. In summary, we have presented a detailed study of the magnetic properties of individual Co-FEBID NWs annealed at different temperatures. This has been possible thanks to the enormous spin sensitivity and broad field and temperature operation range of YBCO nanoSQUID sensors. Experimental results point clearly to an enhanced Co content and increased degree of crystallinity in NWs annealed at large temperatures (450 and 600 °C). The latter results in an increased effective magnetocrystalline anisotropy, as revealed by the exceedingly large values for the switching magnetic fields. However, antiferromagnetic species have a limited influence in these NWs. These observations agree very well with the structural and chemical characterization performed on NWs grown and annealed under the same experimental conditions.[27] Ex situ annealing magnetic FEBID nanostructures seems, therefore, to be a very promising strategy to routinely produce high-quality, pure, and crystalline nanomagnets with large spatial and lateral resolution. In addition, our measurements demonstrate the enormous convenience of using YBCO nanoSQUID sensors for the magnetic characterization of nanoscopic magnets.

Methods. *Fabrication of Co-FEBID NWs.* The working principle of FEBID is similar to chemical vapor deposition assisted by an electron beam. Co-FEBID NWs are fabricated using $Co_2(CO)_8$ precursor gas in an FEI Helios Nanolab 650 dual-beam system. The electron beam current is kept to 100 pA, leading to total deposition times of 40−60 s. RT-NW is fabricated onto a 500 nm-thick Si_3N_4 membrane covered by 10 nm of Al avoiding charge effects (see Figure 1a). The rest of the NWs are grown on TEM copper grids. The use of metallic grids is paramount to guarantee good thermalization of the NWs during the post-growth ex situ annealing treatment. These grids are previously thinned and partially cut into microscopic lamellae, which facilitates the subsequent transport steps. Annealing is carried out during 100 min in an FEI Quanta FEG-250 scanning electron microscope equipped with a heating stage (heating ramp of 50 °C/min). After annealing, the heater is turned off, and the sample is left to cool down.

NanoSQUID Sensors. NanoSQUIDs are made out of a 80 nm-thick YBCO film epitaxially grown on a $SrTiO_3$ (STO) bicrystal substrate (24° missorientation angle) and covered by 70 nm of gold. The STO grain boundary (GB) is naturally transferred to the YBCO film, and the GB in YBCO exhibits Josephson-like behavior. Due to oxygen outdiffusion from the narrow junction and the ensuing degradation, the fabrication of submicron junctions from grain boundaries in cuprates is a difficult task. We have overcome this problem through a careful FIB milling method that produces a certain amount of redeposited amorphous YBCO and STO covering the junction edges and preventing oxygen outdiffusion. Following this method, a central loop with typical dimensions 550 × 400 nm^2 is FIB patterned, intersecting the GB (indicated as a dashed yellow line in Figure 1b). This leads to minute inductances below a few tens of pH and exceptionally low values of the flux noise, ∼1 $\mu\Phi_0/\sqrt{\text{Hz}}$ at 100 kHz. The resulting devices have nonhysteretic current−voltage characteristics with typical critical currents $I_c \approx 500-800$ μA (at 4.2 K) and normal state resistances $R \approx 1$ Ω. The SQUIDs are current-biased and operated in Flux Locked Loop (FLL) mode using commercial SQUID readout electronics. FLL operation is possible thanks to the patterning of a narrow constriction (width ≈ 180 nm, typically) that allows coupling a net magnetic flux to the nanoloop (see Figure 1b). The mutual inductance between the nanoloop and the constriction is $M \approx \Phi_0/\text{mA}$.

Magnetization Measurements with NanoSQUID. Each nanoSQUID containing one individual NW is mounted in good thermal contact to a sapphire plate installed in a variable temperature insert (minimum temperature ≈ 1.4 K). This sapphire plate is mounted on a rotator that allows aligning the nanoSQUID with respect to the externally applied magnetic field with a resolution better than 0.1°. Magnetization measurements are performed by sweeping the external magnetic field at a fixed rate of $\nu = 8.3$ mT/s and measuring the output nanoSQUID voltage (V_{out}) as the NW is driven through magnetization reversal. A total number of 30−50 hysteresis loops are measured at each temperature. V_{out} is converted into units of magnetic flux threading the nanoloop $\Phi_{exp}=V_{out}M/R_f$ where R_f is the feedback resistance of the SQUID readout electronics ($R_f = 3.3$ kΩ, typically). Differ-

DOI: 10.1021/acs.nanolett.8b03329
Nano Lett. 2018, 18, 7674−7682

ences between the total captured flux (Φ_{exp}) from each NW are due to slight geometrical differences between the nanoSQUIDs, differences between the NWs' positions, and differences in the total magnetic moment of the NWs.

The reproducibility of the fabrication procedure has been checked on 300-NW. For this purpose, a different NW grown and annealed under the same experimental conditions was deposited on a different nanoSQUID. Measurements yield very similar results to those shown here (see Figure S2 in the Supporting Information).

Calculation of the Coupling Factor. In order to estimate the average coupling factor, it is necessary to know the exact position of the NW, its precise dimensions and those of the nanoSQUID. Numerical calculations are performed using the finite-element based software package 3D-MLSI:[36] A circulating current is sent around the SQUID loop in 11 current sheets,[37,38] taking into account the precise thickness and in-plane geometry of the device. The magnetic field generated inside the volume occupied by the NW is then used to calculate ϕ_μ.[23,36] To estimate the error resulting from the SEM-based measurements of the NW position, ϕ_μ was recalculated with the NW position shifted by ±100 nm, using the maximum deviations as errors for ϕ_μ ($\Delta\phi_\mu$). The calculated Co purity error given in Table 1 also includes the uncertainty in the measurement of the NW radius ($\Delta r = \pm 2$ nm) and in the experimental total signal coupled to the nanoSQUID ($\Delta\Phi_{exp} = \pm 10$ mΦ).

Microstructural, Compositional, and Magnetic Analyses by TEM. HRTEM imaging was carried out in a Titan Cube 60−300 system operated at 300 kV, equipped with an S-FEG, a CETCOR aberration corrector for a objective lens from CEOS providing subangstrom point resolution, and a 2K × 2K Ultrascan CCD camera from Gatan. STEM and EELS experiments were performed in a Titan Low-Base 60−300 system operated at 300 kV, fitted with a high-brightness field emission gun (X-FEG) and a CETCOR corrector for the condenser system, which produces an electron probe with a lateral size below 1 Å. The STEM-EELS experiments were performed using a Gatan Image Filter (GIF) Tridiem 866 ERS, with a 25 mrad convergence semiangle, an energy dispersion of 0.5 eV/pixel with a resolution of 1.5 eV, a GIF aperture of 2.5 mm, a camera length of 10 mm, a pixel time of 15 ms, and an estimated beam current of 270 pA. The magnetic induction was determined by off-axis Electron Holography in the Titan Cube 60−300 system mentioned above. These holographic experiments were performed at 300 kV by switching off the objective lens and using the Lorentz lens to form the image. The detailed experimental procedure can be found elsewhere.[28] A motorized electrostatic biprism was excited at 150−170 V to generate an interferometric pattern in an overlapping area of 400−500 nm in width, with a fringe contrast ranging from 20% to 25%. The hologram acquisition time was 5 s, and they were acquired at a remanence state after the saturation of the magnetization in the two opposite directions along the longitudinal NW axis by tilting the object by 30° and exciting the objective lens up to a magnetic field of 0.3 T. Thus, the electrostatic phase shift can be subtracted and the magnetic phase shift (φ_{MAG}) extracted. If the NW axis is set along the x axis, the magnetic induction component B_x can be obtained as $|B_x(x,y)| = (\hbar/et)[\partial\varphi_{MAG}(x,y)/\partial y]$, where $\hbar$ is the reduced Planck constant, e the electron charge, and t the total variable thickness along the NW width.[28]

Micromagnetic Simulations. Micromagnetic simulations are performed using the GPU-accelerated MUMAX^3 package.[39] We set the saturation magnetization $M_s = pM_s$(bulk) and the exchange stiffness $A = pA$(bulk) with p given in Table 1, and M_s(bulk) = 1.4×10^6 A/m and A(bulk) = 2.5×10^{-11} J/m for pure crystalline Co. However, the size of each NW is set to its actual geometrical dimensions given in Table 1. The cell size is set to $2.4 \times 2.4 \times 3.5$ nm^3, which is below the exchange length of bulk Co ($\lambda_{ex} \approx 4.5$ nm).

■ ASSOCIATED CONTENT

Supporting Information

The Supporting Information is available free of charge on the ACS Publications website at DOI: 10.1021/acs.nanolett.8b03329.

NW transport details and procedure reproducibility (PDF)

■ AUTHOR INFORMATION

Corresponding Author

*E-mail: pemar@unizar.es.

ORCID

M. J. Martínez-Pérez: 0000-0002-8125-877X

C. Magén: 0000-0002-6761-6171

J. M. de Teresa: 0000-0001-9566-0738

Notes

The authors declare no competing financial interest.

■ ACKNOWLEDGMENTS

This work was partly funded and supported by the Spanish MINECO (MAT2014-51982-C2, MAT2015-73914-JIN, MAT2015-64083-R, MAT2015-69725-REDT, MAT2017-82970-C2-1-R, and MAT2017-82970-C2-2-R), the Aragón Regional Government through projects E26, E09_17R, and E13_17R (Construyendo Europa desde Aragón), COST Action CA16218, COST Project CELINA, and the Deutsche Forschungsgemeinschaft via project KO 1301/13-2. J.P.-N. grant is funded by the Ayuda para Contratos Predoctorales para la Formación de Doctores of the Spanish MINECO (BOE 12/06/15) with the participation of the European Social Fund. B.M. gratefully acknowledges support by the German Academic Scholarship Foundation. The Research Support Services and the staff at the Advanced Microscopy Laboratory from the University of Zaragoza are acknowledged.

■ REFERENCES

(1) Fernández-Pacheco, A.; Streubel, R.; Fruchart, O.; Hertel, R.; Fischer, P.; Cowburn, R. P. Three-dimensional nanomagnetism. *Nat. Commun.* **2017**, *8*, 15756.

(2) Parkin, S. S. P.; Hayashi, M.; Thomas, L. Magnetic Domain-Wall Racetrack Memory. *Science* **2008**, *320*, 190−194.

(3) Allwood, D. A.; Xiong, G.; Faulkner, C. C.; Atkinson, D.; Petit, D.; Cowburn, R. P. Magnetic Domain-Wall Logic. *Science* **2005**, *309*, 1688−1692.

(4) Poggio, M.; Degen, C. L. Force-detected nuclear magnetic resonance: recent advances and future challenges. *Nanotechnology* **2010**, *21*, 342001.

(5) Vavassori, P.; Pancaldi, M.; Perez-Roldan, M. J.; Chuvilin, A.; Berger, A. Remote Magnetomechanical Nanoactuation. *Small* **2016**, *12*, 1013−1023.

(6) Da Col, S.; Jamet, S.; Rougemaille, N.; Locatelli, A.; Mentes, T. O.; Burgos, B. S.; Afid, R.; Darques, M.; Cagnon, L.; Toussaint, J. C.; Fruchart, O. Observation of Bloch-point domain walls in cylindrical

DOI: 10.1021/acs.nanolett.8b03329
Nano Lett. 2018, 18, 7674−7682

magnetic nanowires. *Phys. Rev. B: Condens. Matter Mater. Phys.* **2014**, *89*, 180405.
(7) Vazquez, M., Ed. *Magnetic Nano- and Microwires: Design, Synthesis, Properties and Applications*; Woodhead Publishing, 2015.
(8) Fernández-Pacheco, A.; Serrano-Ramón, L.; Michalik, J. M.; Ibarra, M. R.; De Teresa, J. M.; O'Brien, L.; Petit, D.; Lee, J.; Cowburn, R. P. Three dimensional magnetic nanowires grown by focused electron-beam induced deposition. *Sci. Rep.* **2013**, *3*, 1492.
(9) Keller, L.; Mamoori, M. K. I. A.; Pieper, J.; Gspan, C.; Stockem, I.; Schröder, C.; Barth, S.; Winkler, R.; Plank, H.; Pohlit, M.; Müller, J.; Huth, M. Direct-write of free-form building blocks for artificial magnetic 3D lattices. *Sci. Rep.* **2018**, *8*, 6160.
(10) Lipert, K.; Bahr, S.; Wolny, F.; Atkinson, P.; Weißker, U.; Mühl, T.; Schmidt, O. G.; Büchner, B.; Klingeler, R. An individual iron nanowire-filled carbon nanotube probed by micro-Hall magnetometry. *Appl. Phys. Lett.* **2010**, *97*, 212503.
(11) Pablo-Navarro, J.; Sanz-Hernández, D.; Magén, C.; Fernández-Pacheco, A.; de Teresa, J. M. Tuning shape, composition and magnetization of 3D cobalt nanowires grown by focused electron beam induced deposition (FEBID). *J. Phys. D: Appl. Phys.* **2017**, *50*, 18LT01.
(12) Rodríguez, L.; Magén, C.; Snoeck, E.; Gatel, C.; Marín, L.; Serrano-Ramón, L.; Prieto, J.; Muñoz, M.; Algarabel, P.; Morellon, L.; Teresa, J. D.; Ibarra, M. Quantitative in situ magnetization reversal studies in Lorentz microscopy and electron holography. *Ultramicroscopy* **2013**, *134*, 144−154.
(13) Wolf, D.; Rodriguez, L. A.; Béché, A.; Javon, E.; Serrano, L.; Magen, C.; Gatel, C.; Lubk, A.; Lichte, H.; Bals, S.; Tendeloo, G. V.; Fernández-Pacheco, A.; Teresa, J. M. D.; Snoeck, E. 3D Magnetic Induction Maps of Nanoscale Materials Revealed by Electron Holographic Tomography. *Chem. Mater.* **2015**, *27*, 6771−6778.
(14) Buchter, A.; et al. Reversal Mechanism of an Individual Ni Nanotube Simultaneously Studied by Torque and SQUID Magnetometry. *Phys. Rev. Lett.* **2013**, *111*, 067202.
(15) Ganzhorn, M.; Klyatskaya, S.; Ruben, M.; Wernsdorfer, W. Carbon Nanotube Nanoelectromechanical Systems as Magnetometers for Single-Molecule Magnets. *ACS Nano* **2013**, *7*, 6225−6236.
(16) Granata, C.; Vettoliere, A. Nano Superconducting Quantum Interference device: A powerful tool for nanoscale investigations. *Phys. Rep.* **2016**, *614*, 1−69.
(17) Martínez-Pérez, M. J.; Koelle, D. NanoSQUIDs: Basics & recent advances. *Phys. Sci. Rev.* **2017**, *2*, 20175001.
(18) Martínez-Pérez, M. J.; Gella, D.; Müller, B.; Morosh, V.; Wölbing, R.; Sesé, J.; Kieler, O.; Kleiner, R.; Koelle, D. Three-Axis Vector Nano Superconducting Quantum Interference Device. *ACS Nano* **2016**, *10*, 8308−8315.
(19) Vasyukov, D.; Ceccarelli, L.; Wyss, M.; Gross, B.; Schwarb, A.; Mehlin, A.; Rossi, N.; Tütüncüoglu, G.; Heimbach, F.; Zamani, R. R.; Kovács, A.; i Morral, A. F.; Grundler, D.; Poggio, M. Imaging Stray Magnetic Field of Individual Ferromagnetic Nanotubes. *Nano Lett.* **2018**, *18*, 964−970.
(20) Wernsdorfer, W.; Hasselbach, K.; Mailly, D.; Barbara, B.; Benoit, A.; Thomas, L.; Suran, G. DC-SQUID magnetization measurements of single magnetic particles. *J. Magn. Magn. Mater.* **1995**, *145*, 33−39.
(21) Wernsdorfer, W.; Hasselbach, K.; Benoit, A.; Barbara, B.; Doudin, B.; Meier, J.; Ansermet, J.-P.; Mailly, D. Measurements of magnetization switching in individual nickel nanowires. *Phys. Rev. B: Condens. Matter Mater. Phys.* **1997**, *55*, 11552−11559.
(22) Schwarz, T.; Nagel, J.; Wölbing, R.; Kemmler, M.; Kleiner, R.; Koelle, D. Low-Noise Nano Superconducting Quantum Interference Device Operating in Tesla Magnetic Fields. *ACS Nano* **2013**, *7*, 844−850.
(23) Schwarz, T.; Wölbing, R.; Reiche, C.; Müller, B.; Martínez-Pérez, M. J.; Mühl, T.; Büchner, B.; Kleiner, R.; Koelle, D. Low-Noise $YBa_2Cu_3O_7$ Nano-SQUIDs for Performing Magnetization-Reversal Measurements on Magnetic Nanoparticles. *Phys. Rev. Appl.* **2015**, *3*, 044011.
(24) Martínez-Pérez, M. J.; Müller, B.; Schwebius, D.; Korinski, D.; Kleiner, R.; Sesé, J.; Koelle, D. NanoSQUID magnetometry of individual cobalt nanoparticles grown by focused electron beam induced deposition. *Supercond. Sci. Technol.* **2017**, *30*, 024003.
(25) Vivas, L. G.; Escrig, J.; Trabada, D. G.; Badini-Confalonieri, G. A.; Vázquez, M. Magnetic anisotropy in ordered textured Co nanowires. *Appl. Phys. Lett.* **2012**, *100*, 252405.
(26) De Teresa, J. M.; Fernández-Pacheco, A.; Córdoba, R.; Serrano-Ramón, L.; Sangiao, S.; Ibarra, M. R. Review of Magnetic Nanostructures Grown by Focused Electron Beam Induced Deposition (FEBID). *J. Phys. D: Appl. Phys.* **2016**, *49*, 243003.
(27) Pablo-Navarro, J.; Magén, C.; de Teresa, J. M. Purified and Crystalline Three-Dimensional Electron-Beam-Induced Deposits: The Successful Case of Cobalt for High Performance Magnetic Nanowires. *ACS Appl. Nano Mater.* **2018**, *1*, 38−46.
(28) Pablo-Navarro, J.; Magén, C.; de Teresa, J. M. Three-dimensional core - shell ferromagnetic nanowires grown by focused electron beam induced deposition. *Nanotechnology* **2016**, *27*, 285302.
(29) Stoner, E. C.; Wohlfarth, E. P. A Mechanism of Magnetic Hysteresis in Heterogeneous Alloys. *Philos. Trans. R. Soc., A* **1948**, *240*, 599−642.
(30) Hubert, A.; Schafer, R. *Magnetic Domains*; Springer: Berlin, 1998.
(31) Paulus, P.; Luis, F.; Kröll, M.; Schmid, G.; de Jongh, L. Low-temperature study of the magnetization reversal and magnetic anisotropy of Fe, Ni, and Co nanowires. *J. Magn. Magn. Mater.* **2001**, *224*, 180−196.
(32) Stankiewicz, J.; Luis, F.; Camón, A.; Kröll, M.; Bartolomé, J.; Blau, W. Magnetization switching of Fe nanowires at very low temperatures. *J. Magn. Magn. Mater.* **2004**, *272*−*276*, 1637−1639.
(33) Nogués, J.; Sort, J.; Langlais, V.; Skumryev, V.; Suriñach, S.; Muñoz, J.; Baró, M. Exchange bias in nanostructures. *Phys. Rep.* **2005**, *422*, 65−117.
(34) He, L.; Chen, C.; Wang, N.; Zhou, W.; Guo, L. Finite size effect on Néel temperature with Co_3O_4 nanoparticles. *J. Appl. Phys.* **2007**, *102*, 103911.
(35) Tripathy, D.; Adeyeye, A. O.; Chakrabarti, K.; Singh, N. Tuning the exchange bias in large area Co/CoO nanowire arrays. *J. Appl. Phys.* **2010**, *107*, 09D705.
(36) Khapaev, M. M.; Kupriyanov, M. Y.; Goldobin, E.; Siegel, M. Current Distribution Simulation for Superconducting Multi-Layered Structures. *Supercond. Sci. Technol.* **2003**, *16*, 24−27.
(37) Nagel, J.; Konovalenko, K. B.; Kemmler, M.; Turad, M.; Werner, R.; Kleisz, E.; Menzel, S.; Klingeler, R.; Büchner, B.; Kleiner, R.; Koelle, D. Resistively shunted $YBa_2Cu_3O_7$ grain boundary junctions and low-noise SQUIDs patterned by a focused ion beam down to 80 nm linewidth. *Supercond. Sci. Technol.* **2011**, *24*, 015015.
(38) Wölbing, R.; Schwarz, T.; Müller, B.; Nagel, J.; Kemmler, M.; Kleiner, R.; Koelle, D. Optimizing the spin sensitivity of grain boundary junction nanoSQUIDs—towards detection of small spin systems with single-spin resolution. *Supercond. Sci. Technol.* **2014**, *27*, 125007.
(39) Vansteenkiste, A.; Leliaert, J.; Dvornik, M.; Helsen, M.; García-Sánchez, F.; Waeyenberge, B. V. The design and verification of MuMax3. *AIP Adv.* **2014**, *4*, 107133.

DOI: 10.1021/acs.nanolett.8b03329
Nano Lett. 2018, 18, 7674−7682

NanoSQUID Magnetometry on Individual As-grown and Annealed Co Nanowires at Variable Temperature.

M. J. Martínez-Pérez,[*,†,‡] J. Pablo-Navarro,[¶] B. Müller,[§] R. Kleiner,[§] C. Magén,[†,¶] D. Koelle,[§] J. M. de Teresa,[†,¶] and J. Sesé[†,¶]

†*Instituto de Ciencia de Materiales de Aragón and Departamento de Física de la Materia Condensada, CSIC-Universidad de Zaragoza, 50009 Zaragoza, Spain*

‡*Fundación ARAID, 50018 Zaragoza, Spain*

¶*Laboratorio de Microscopías Avanzadas (LMA), Instituto de Nanociencia de Aragón (INA), Universidad de Zaragoza, 50018 Zaragoza, Spain*

§*Physikalisches Institut – Experimentalphysik II and Center for Quantum Science (CQ) in LISA$^+$, Universität Tübingen, 72076 Tübingen, Germany*

E-mail: pemar@unizar.es

Supporting Information

NW transport

NW growth, annealing and subsequent transport to the sensor surface is a critical task that ultimately determines the success of the experiment. To begin with, the magnetic sample must be located as close as possible to the SQUID nanoloop to guarantee large magnetic coupling between them. In principle, NWs could be directly grown on the surface of the

sensor, in close vicinity to the nanoloop. However, this would end up with the NW forming a non-zero angle with respect to the SQUID substrate surface and not being parallel to the externally applied field. This is not ideal since interpretation of the results is easier if the external field is applied parallel to the anisotropy axis of the NW (NW's long axis). On the other hand, the YBCO nanoSQUID substrate can under no circumstances be subjected to the annealing process. For these two reasons, NWs must be grown and annealed on a separate substrate and later transferred to the nanoSQUID.

In order to fulfill all these requirements we have developed a transport process based on the use of an Omniprobe nanomanipulator installed in the dual-beam microscope. The transport process of RT-NW is summarized in Fig. 1. The NW (yellow) is directly grown vertically on an Al-coated 500 nm-thick Si_3N_4 palette (#1). The sample is then removed from the microscope and rotated by 90 degrees so that the NW lies horizontally. In step #2, the nanomanipulator W-tip (blue) is attached to the palette by means of a small Pt-FIBID deposit (green). After attaching, the palette is released by means of a small FIB cut. The palette containing the NW is then transferred to the nanoSQUID surface and located so that the NW's tip lies as close as possible to the nanoloop (#3). In this step it is also important to ensure that the NW axis will lie parallel to the substrate and perpendicularly to the grain boundary's plane (*i.e.*, along the externally applied magnetic field H, indicated by an orange arrow). The palette is finally attached to the substrate by Pt-FIBID (green) and the nanomanipulator tip is released by FIB-cutting.

The procedure is similar in case of the annealed NWs. However, in this case, the use of metallic palettes instead of the insulating Si_3N_4 is extremely important to guarantee proper annealing of the NWs. For this reason, we have used thinned (down to few μm-thick) copper lamellae as carriers, as explained in the main text.

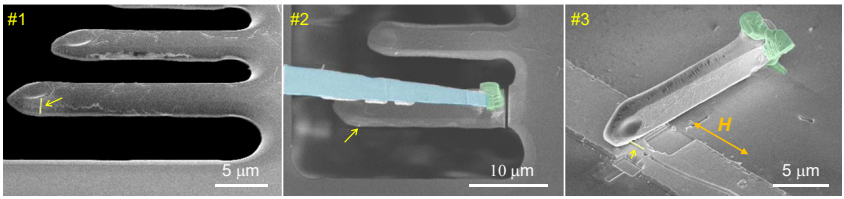

Figure 1: False colored SEM images of the complete transport process of the Co-FEBID RT-NW to a YBCO nanoSQUID. The NW (yellow) is always indicated by a yellow arrow. The nanomanipulator tip is indicated in blue whereas the Pt-FIBID deposit is in green. The externally applied magnetic field (H) direction is represented by an orange arrow.

Procedure reproducibility

The reproducibility of the NW growth and annealing procedure has been checked out for samples annealed at 300 °C. Two NWs are grown and subsequently annealed under nominally identical experimental conditions. The first NW, *i.e.*, 300-NW analyzed in the main text, has dimensions $R = 36.5$ nm and $l = 2.2$ μm whereas for the second one $R = 34.5$ nm and $l = 2.3$ μm. Both NWs are later transferred to two distinct nanoSQUIDs as shown in Fig. 2**a**. In Fig. 2**b** we show the corresponding representative hysteresis loops obtained at $T = 10$ K. 300-NW lies quite parallel to the nanoSQUID substrate whereas the second NW is slightly tilted. The latter lies at $\sim 20°$ with respect to the externally applied magnetic field yielding the evident differences in the shape of the hysteresis loops. However, as highlighted by vertical dashed lines, the main switching events take place at very similar magnetic fields. This is true even for the smaller steps (dash-dotted lines) observable at larger magnetic fields $|H|$, proving the reproducibility of the growing and annealing processes.

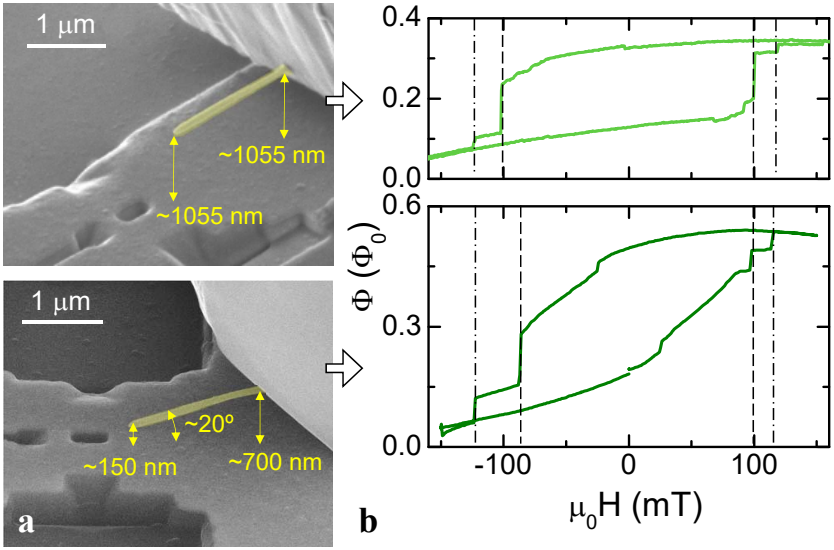

Figure 2: **a**: NWs annealed at 300 °C deposited over two different nanoSQUIDs (300-NW analyzed in the main text is shown in the top panel). **b**: Hysteresis loops corresponding to the NWs shown in **a**.

Publication 3

Reproduced with permission from
M. J. Martínez-Pérez *et al.*, Supercond. Sci. Technol. **30**, 024003 (2017).

IOP Publishing Superconductor Science and Technology
Supercond. Sci. Technol. 30 (2017) 024003 (10pp) doi:10.1088/0953-2048/30/2/024003

NanoSQUID magnetometry of individual cobalt nanoparticles grown by focused electron beam induced deposition

M J Martínez-Pérez[1], B Müller[1], D Schwebius[1], D Korinski[1], R Kleiner[1], J Sesé[2] and D Koelle[1]

[1] Physikalisches Institut—Experimentalphysik II and Center for Quantum Science (CQ) in LISA$^+$, Universität Tübingen, Auf der Morgenstelle 14, D-72076 Tübingen, Germany
[2] Laboratorio de Microscopías Avanzadas (LMA), Instituto de Nanociencia de Aragón (INA), Universidad de Zaragoza, E-50018 Zaragoza, Spain

E-mail: pemar@unizar.es

Received 27 September 2016, revised 28 October 2016
Accepted for publication 1 November 2016
Published 1 December 2016

Abstract

We demonstrate the operation of low-noise nano superconducting quantum interference devices (SQUIDs) based on the high critical field and high critical temperature superconductor $YBa_2Cu_3O_7$ (YBCO) as ultra-sensitive magnetometers for single magnetic nanoparticles (MNPs). The nanoSQUIDs exploit the Josephson behavior of YBCO grain boundaries and have been patterned by focused ion beam milling. This allows us to precisely define the lateral dimensions of the SQUIDs so as to achieve large magnetic coupling between the nanoloop and individual MNPs. By means of focused electron beam induced deposition, cobalt MNPs with a typical size of several tens of nm have been grown directly on the surface of the sensors with nanometric spatial resolution. Remarkably, the nanoSQUIDs are operative over extremely broad ranges of applied magnetic field ($-1\,\mathrm{T} < \mu_0 H < 1\,\mathrm{T}$) and temperature ($0.3\,\mathrm{K} < T < 80\,\mathrm{K}$). All these features together have allowed us to perform magnetization measurements under different ambient conditions and to detect the magnetization reversal of individual Co MNPs with magnetic moments $(1–30) \times 10^6\ \mu_B$. Depending on the dimensions and shape of the particles we have distinguished between two different magnetic states yielding different reversal mechanisms. The magnetization reversal is thermally activated over an energy barrier, which has been quantified for the (quasi) single-domain particles. Our measurements serve to show not only the high sensitivity achievable with YBCO nanoSQUIDs, but also demonstrate that these sensors are exceptional magnetometers for the investigation of the properties of individual nanomagnets.

Keywords: nanoSQUID, magnetic nanoparticles, nanoparticle patterning, single particle detection, magnetization measurements

(Some figures may appear in colour only in the online journal)

1. Introduction

Magnetic nanoparticles (MNPs) are targeted by the scientific community and industry. After recognizing the large number of size and shape-dependent properties of MNPs, a huge range of potential applications became immediately evident. Just to mention a few, these properties include magnetic anisotropy (memory) [1, 2], phase transitions [3], magnetocaloric effects [4] or resonance frequencies [5]. Very different industrial sectors have already benefited from the use of MNPs starting from electronics and information technologies up to medical diagnostics and cancer therapy [6]. In addition, fundamental research on MNPs might also find applications in solid-state quantum information technologies [7] and molecular spintronics [8]. In this regard, developing tools for magnetic characterization of small amounts of MNPs

or, if possible, individual ones, represents an important step towards the realization and fine-tuning of the properties of MNPs for different applications.

Experiments on individual MNPs were pioneered by Wernsdorfer and collaborators (for reviews see e.g., [9, 10]). Among a vast number of studies, this group succeeded in demonstrating experimentally, e.g., magnetization reversal as described by the Néel–Brown [11–13] and Stoner–Wohlfarth model [14, 15] or the occurrence of macroscopic quantum tunneling of the vector magnetic moment [16]. The magnetometers used for this goal were microscopic superconducting quantum interference devices (SQUIDs) based on niobium thin films. Since then, SQUID sensors have been further miniaturized to the nanosocopic scale, boosting enormously their sensitivity and noise performance [17, 18]. However, the realization of routine magnetization measurements and the investigation of interesting physics using nanoSQUIDs is still quite limited [17, 18].

Among other reasons, this is mainly due to (i) restrictions imposed on the SQUID operation ranges of applied magnetic field $\boldsymbol{H}$ and temperature T, which are often much smaller than what is usually required for comprehensive characterization of magnetic materials and (ii) the difficulty of positioning individual MNPs with high spatial precision close to the nanoSQUID loop, which is crucial to achieve the sensitivity required to detect the tiny magnetic moment of MNPs.

We have overcome the first mentioned challenge by using recently developed ultra-sensitive nanoSQUID sensors based on the high critical field and high critical temperature (T_c) superconductor $YBa_2Cu_3O_7$ (YBCO) and submicron grain boundary (GB) Josephson junctions [19–21]. This approach allows sensor operation at remarkably large in-plane applied magnetic fields (up to one Tesla) and a large range of temperatures (300 mK–80 K). Regarding the second issue, cobalt MNPs have been directly grown at precise positions by focused electron beam induced deposition (FEBID) [22]. Being polycrystalline, FEBID-Co is a soft magnetic material with negligible volume-averaged magnetocrystalline anisotropy. The equilibrium magnetic state of these MNPs will, therefore, result from the competition between the exchange and magnetotstatic (shape) energies [23]. The use of FEBID allows us to control not only the particle location with nanometric resolution, but also its size and shape. This gives access to investigating the boundary between single-domain MNPs (dominated by the minimization of the exchange energy) and more complicate spin configurations of topological origin (dominated by the minimization of the magnetostatic energy) [24, 25].

Here, we present nanoSQUID magnetization measurements on five different FEBID-Co MNPs by using a set of five nanoSQUIDs SQ $\#i$ containing MNPs labeled as $\#i$, with $i = 1$–5, respectively. NanoSQUID fabrication, operation and electrical characterization is presented in section 2 along with the calculation of their corresponding position-dependent magnetic coupling and spin sensitivity. MNP growth is described in section 3, followed by the description of the magnetization measurements in section 4. Within this section the total magnetic moment per particle is estimated and the temperature and angular dependence of the switching magnetic fields is analyzed in detail. Section 5 is left for conclusions.

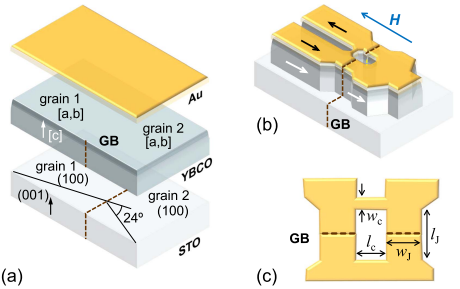

Figure 1. YBCO nanoSQUID fabrication: (a) scheme of the thin-film deposition process: a 120 nm thick YBCO film is grown epitaxially on a STO bicrystal substrate leading to the natural formation of a grain boundary (GB; dashed line). The YBCO is covered with a 70 nm thick Au layer. (b) Final layout of the device after FIB patterning. White and black arrows indicate direction of bias and modulation current, respectively. An external magnetic field $\boldsymbol{H}$ (blue arrow) can be applied in the plane of the SQUID loop. (c) Schematic top view of the SQUID loop, indicating the relavant geometric parameters.

2. NanoSQUID characterization

2.1. NanoSQUID fabrication

The fabrication of the devices is summarized in figure 1 and briefly described in the following (see [20] for further details). A 120 nm thick YBCO film is grown epitaxially by pulsed laser deposition on a $SrTiO_3$ (STO) bicrystal substrate, leading to the natural formation of a GB indicated by the dashed line in figure 1(a). The GB with 24° misorientation angle acts as a Josephson barrier exhibiting a remarkably large critical current density $j_0 \sim 10^5$ A cm^{-2} at 4.2 K, typically. Subsequently, a 70 nm thick Au film is deposited *in situ* by electron beam evaporation, which provides resistive shunting to the Josephson junctions and protects the YBCO layer during patterning by focused ion beam (FIB) milling. In this step, two bridges typically $w_J \sim 300$ nm wide and $l_J \sim 300$ nm long straddling the GB are formed to define the Josephson junctions intersecting the SQUID loop (see figure 1(b)). For SQUID operation, a bias current I_b flows across the junctions (white arrows in figure 1(b)). In addition, a typically $w_c = 100$–200 nm wide and $l_c = 200$ nm long constriction is also patterned into the SQUID nanoloop; this provides the position with largest coupling for MNPs (see section 2.4). Via a modulation current I_{mod} (black arrows in figure 1(b)) flowing through the constriction, the SQUID can be flux biased at its optimum working point, which also allows SQUID readout in flux locked loop (FLL) mode [26]. The relevant geometric parameters for the SQUID loop are

indicated in figure 1(c), and corresponding values for l_J, w_J, l_c and w_c for all five YBCO nanoSQUIDs are given in table 1.

Using FIB patterning, the lateral dimensions of the YBCO nanoSQUIDs can be controlled down to ∼50 nm, providing a flexible and convenient way of tuning the size and geometry of the nanoloop. This in turn determines its main parameters, [27] such as (i) the maximum critical current I_0 of the Josephson junctions, (ii) the total inductance L with a geometric and kinetic contribution, the latter depending also on the film thickness, and (iii) the dimensions of the constriction, which determine the strength of maximum coupling of a MNP to the SQUID loop [27].

2.2. Measurement setup and high field operation

Sensors are mounted in good thermal contact to the copper cold finger of a ^{3}He refrigerator operative at 300 mK $< T <$ 300 K. The refrigerator is introduced in a ^{4}He cryostat hosting a vector magnet operating at a maximum sweeping rate of $\nu = 4.5$ mT s^{-1}. The vector magnet allows to carefully align the externally applied magnetic field $\boldsymbol{H}$ in the substrate (SQUID loop) plane and perpendicularly to the plane formed by the GB junctions (blue arrow in figure 1(b)). In this configuration, magnetic flux is coupled neither to the nanoSQUID loop nor to the Josephson junctions, allowing to operate the devices up to ∼1 T as demonstrated in [20]. To verify this, we have characterized a large number of bare nanoSQUIDs operating them in both open loop and FLL mode while sweeping H. While the nanoSQUIDs are fully operative up to very large magnetic fields, we have observed the presence of abrupt changes in their response at $\mu_0 H \sim 1$ T. This behavior is still under investigation and is attributed to the entrance of Abrikosov vortices, probably stabilized at one or both sides of the constriction. Measurements presented here have been obtained, however, at $\mu_0 H < 0.15$ T where these effects play no role.

2.3. Electrical characterization

All devices presented here exhibited values of the maximum total critical current $I_c = 2I_0 \sim 500$–$600\ \mu$A at 4.2 K, decreasing to $I_c \sim 150$–$200\ \mu$A at 70 K. The response of the nanoSQUIDs at constant I_b can be modulated via I_{mod}, allowing us to experimentally observe the Φ_0-periodic response of the output voltage V versus magnetic flux Φ in the SQUID loop (Φ_0 is the magnetic flux quantum). From these measurements (see, e.g., [20]) it is possible to determine the modulation currrent $I_{mod,0}$ which is required to induce $1\Phi_0$. This yields the mutual inductance $M \equiv \Phi/I_{mod}$ between the constriction and the SQUID. The experimental determination of M is paramount in order to quantify the flux $\Phi = V_{out} M/R_f$ coupled to the SQUID. Here, V_{out} is the output voltage and R_f is the feedback resistance of the SQUID readout electronics operated in FLL mode ($R_f = 3.3$ kΩ, typically).

Figure 2(a) shows the measured T dependence of $1/M$ for all five SQUIDs. Here, M is normalized to the extrapolated zero temperature value $M_0 \equiv M(T = 0)$ for each SQUID SQ #i (values for M_0 are listed in table 1). The data are well approximated by $M/M_0 = (1 - t^2)^{-2/3}$, with the reduced temperature $t \equiv T/T_c$ and $T_c = 89$ K, which we will explain in the following.

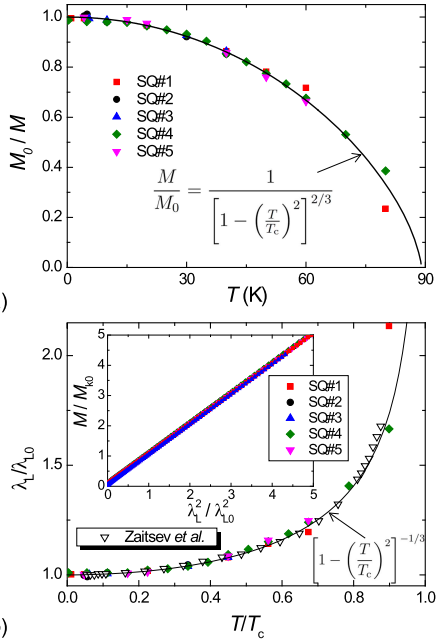

Figure 2. Temperature dependence of the mutual inductance M and London penetration depth λ_L of all five YBCO nanoSQUIDs at $H = 0$: (a) measured T dependence of $1/M$ (symbols) normalized to $1/M_0$ (see table 1). Solid line is a fit to the data with $T_c = 89$ K. (b) T dependence of λ_L extracted from data shown in (a) and numerical simulations of $M(\lambda_L^2)$ as shown in the inset. For comparison, the main graph includes data from Zaitsev *et al* [28], with $\lambda_{L0} = 210$ nm and $T_c = 92$ K .

Generally, M contains both a geometric and a kinetic contibution, $M = M_g + M_k$. M_g reflects the magnetic field produced by I_{mod}, which is captured by the SQUID loop. The kinetic part M_k reflects the contribution to the phase gradient of the superconductor wave function that is induced by the kinetic momentum of the Cooper pairs flowing along the constriction. M_k is expected to be T-dependent through the Cooper pair density $n_s(T)/n_s(0) = \lambda_{L0}^2/\lambda_L^2(T)$, [29] with the London penetration depth λ_L and $\lambda_{L0} \equiv \lambda_L(T = 0)$. Hence, one expects $M_k = M_{k0}\lambda_L^2(T)/\lambda_{L0}^2$. Generally, M_g can also be T-dependent, as the current density distribution across the constriction may vary with $\lambda_L(T)$. However, as the constriction width w_c is of the order of λ_{L0} (see table 1 and determination of λ_{L0} values below), already for the lowest temperatures we can assume a rather homogeneous current density distribution across the constriction, which will not change with T.

Table 1. Parameters for all five SQUIDs SQ #i: geometric parameters of the SQUID layout (w_J, l_J, w_c and l_c) and to $T = 0$ extrapolated values for mutual inductances M_0, M_g, M_{k0} and London penetration depth λ_{L0}.

	w_J (nm)	l_J (nm)	w_c (nm)	l_c (nm)	M_0 Φ_0 mA^{-1}	M_g Φ_0 mA^{-1}	M_{k0} Φ_0 mA^{-1}	λ_{L0} (nm)
SQ #1	380	330	500	220	0.29	0.02	0.27	243
SQ #2	270	255	80	265	1.17	0.08	1.09	166
SQ #3	350	270	260	180	0.58	0.02	0.56	241
SQ #4	330	300	220	250	0.44	0.04	0.40	171
SQ #5	360	270	190	190	0.48	0.03	0.45	179

In order to quantify the T-dependence of M and its relation to $\lambda_L(T)$, we performed numerical simulations of $M(\lambda_L)$ for the geometry of all five nanoSQUIDs, based on the London equations using the software package 3D-MLSI [30]. The comparison of the measured values for $M(T)$ with the simulation results $M(\lambda_L)$ allows us to extract $\lambda_L(T)$ and λ_{L0} for all five devices.

We note that the value of λ_{L0} extracted from the simulations crucially depends on the value for the constriction width w_c. Here, the largest uncertainty comes from the unknown value of the width of the damaged regions at the constriction edges due to FIB milling, which effectively reduces w_c by some value δw_c. This effect is strongest for SQ #2 with the smallest w_c. Taking $\delta w_c = 20$ nm, reduces the extracted value for λ_{L0} by 15% for SQ #2.

The inset of figure 2 shows M/M_{k0} versus $(\lambda_L/\lambda_{L0})^2$. Here, the data points for all five devices follow nicely the quadratic scaling with λ_L, with almost invisible vertical shifts due to the small offset given by M_g/M_{k0}. Values for M_g and M_{k0} are listed in table 1. We clearly see that $M_0 = M_g + M_{k0}$ is dominated by the kinetic contribution ($M_g \sim (7 \pm 3)\%$ of M_{k0}).

$\lambda_L(T)$ is displayed in figure 2(b), where we normalized λ_L to λ_{L0} and T to $T_c = 89$ K. The T-dependence of λ_L is roughly given by $\lambda_L(T) = \lambda_L(0)[1 - t^2]^{1/3}$, leading to the observed T-dependence of M, since $M_g \ll M_k$. Thus, due to the dominant kinetic contribution of M in our devices, the measured T dependence of $1/M$ (figure 2(a)) closely reflects the T dependence of n_s.

We note that the values for λ_{L0} vary from ~170 to ~240 nm for the five devices presented here. Those values are significantly above the values $\lambda_{L0} \sim 150$ nm in the a–b plane for YBCO single crystals. [31]. However, they are consistent with results by Zaitsev *et al* [28] obtained from microwave measurements of the absolute London penetration depth for epitaxially grown YBCO films and with results which we obtained earlier for our YBCO nanoSQUIDs [20, 27] and thin films [32]. For comparison, we included in figure 2(b) results of one representative sample from [28], which shows a $\lambda_L(T)$ dependence that is very consistent with what we find for our devices presented here.

Finally, we have characterized the noise response of the devices in FLL mode obtaining very low values of the root-mean-square (rms) spectral density of flux noise $S_\Phi^{1/2}$. Figure 3 shows data for SQ #1 and SQ #2 at $H = 0$ and $T = 4.2$ K. The former exhibits the typical $S_\Phi \propto 1/f$ contribution, which dominates up to ~1 kHz where it starts to saturate reaching just $S_\Phi^{1/2} \sim 500$ nΦ_0 Hz$^{-1/2}$ at 100 kHz. SQ # 2, on the other hand, exhibits also a $1/f$ contribution plus a broad peak at ~200 Hz. The noise in the white region is larger, in this case giving $S_\Phi^{1/2} \sim 1.2$ $\mu\Phi_0$ Hz$^{-1/2}$ at 100 kHz. Both the presence of peaks in the noise spectra and excess $1/f$ contributions are typically found in these devices [21, 33]. These effects have been attributed to I_0 fluctuations in the GB junctions and to the existence of ubiquitous magnetic fluctuators either at the STO/YBCO interface or in the GB junctions [21].

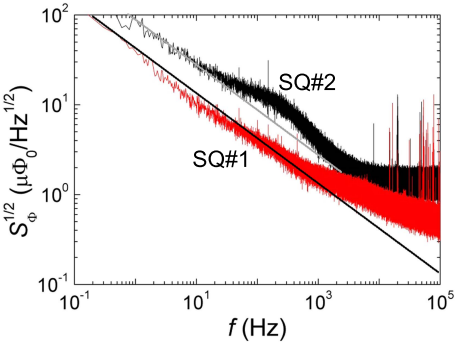

Figure 3. Rms spectral density of flux noise measured in FLL at 4.2 K and $H = 0$ for devices SQ #1 and SQ #2. Solid lines indicate the $1/f$ contributions.

Operation in external magnetc fields and at variable temperature has been investigated experimentally by measuring the noise of SQ #1 at -100 mT $< \mu_0 H < 400$ mT and 0.3 K $< T <$ 50 K. Similarly to the spectra shown in figure 3, the flux noise is dominated by a large $1/f$ contribution exhibiting the presence of peaks at frequencies that depend on both T and H. Although no systematic T- or H-dependence has been found, [21] we can state that noise spectra are only weakly affected by the application of external magnetic fields or by the operation at higher temperatures. As a matter of fact, $S_\Phi^{1/2}$ values at 100 kHz do not change by more than a factor 4–5.

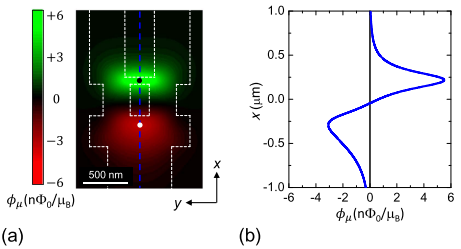

Figure 4. (a) $\phi_\mu(x, y)$ contour plot of a typical nanoSQUID, 10 nm above the surface of the 70 nm thick Au layer, for $\hat{\boldsymbol{e}}_\mu \parallel \hat{\boldsymbol{e}}_x$. White dashed lines indicate the contour of the chosen nanoSQUID geometry with an 80 nm wide constriction. Black and white dots indicate the positions of maximum coupling, i.e., $\phi_\mu = 5.5$ and $-3.1\ n\Phi_0/\mu_B$, respectively. The blue dashed line indicates the position of the line scan shown in (b). (b) $\phi_\mu(x)$ along the dashed line in (a). Note that the x-axis (vertical axis) in (a) and (b) coincide.

2.4. Calculation of coupling and spin sensitivity

In order to estimate the regions of maximum coupling for MNPs above the surface of the sensors, we performed numerical simulations based on the London equations to calculate the coupling factor $\phi_\mu(\boldsymbol{r}, \hat{\boldsymbol{e}}_\mu)$. This quantity expresses the amount of magnetic flux coupled into the nanoSQUID loop per magnetic moment of a point-like MNP with its magnetic moment $\boldsymbol{\mu} = \mu\hat{\boldsymbol{e}}_\mu$ oriented along $\hat{\boldsymbol{e}}_\mu$ and located at position $\boldsymbol{r}$. ϕ_μ was calculated using 3D-MLSI [30] to obtain the magnetic field $\boldsymbol{B}_J(\boldsymbol{r})$ at position $\boldsymbol{r}$ induced by a current J circulating in a two-dimensional sheet around the SQUID hole, taking into account the lateral geometry of the SQUID. As shown in [19] and [27], $\phi_\mu(\boldsymbol{r}, \hat{\boldsymbol{e}}_\mu)$ can then be obtained via

$$\phi_\mu(\boldsymbol{r}, \hat{\boldsymbol{e}}_\mu) = -\hat{\boldsymbol{e}}_\mu \cdot \boldsymbol{B}_J(\boldsymbol{r})/J. \quad (1)$$

This calculation was done for 11 current sheets spread equally across the film thickness as described in [27]. The resulting coupling factors were averaged for each position $\boldsymbol{r}$, resulting in position-resolved maps $\phi_\mu(x, y)$ in the plane parallel to the SQUID loop plane, as shown in figure 4(a). Figure 4(b) shows a line-scan $\phi_\mu(x)$ calculated along the dashed line in figure 4(a). Results plotted in figure 4 have been calculated for a vertical distance $z = 80$ nm above the YBCO surface, i.e., 10 nm above the Au surface, for a device with geometry similar to SQ # 2. In these calculations we have assumed $\hat{\boldsymbol{e}}_\mu$ parallel to the externally applied magnetic field H (along the x direction). Note that ϕ_μ reverses it sign upon going from the constriction to the opposite side of the SQUID loop. This is simply related to the direction of the flux lines coupled to the nanoloop and makes no difference for the measurements performed here. As λ_{L0} varies from $\sim$170 to 250 nm for our devices, we have performed simulations of ϕ_μ for variable λ_{L0}. In contrast to the scaling of $M(\lambda_L)$, we find only a very weak dependence of $\phi_\mu(\lambda_L)$. Hence, for the calculations of ϕ_μ presented below, we fixed λ_L to 250 nm to be consistent with our earlier work [27].

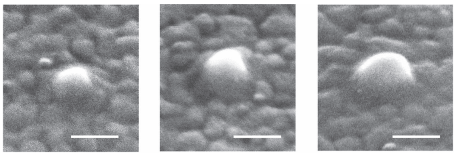

Figure 5. SEM images of three typical cobalt nanoparticles deposited by FEBID on top of a YBCO/Au bilayer. Scale bar is 100 nm.

Regions of maximum $|\phi_\mu|$ are found at the constriction ($\phi_\mu = 5.5\ n\Phi_0/\mu_B$, at the position of the black dot in figure 4(a)) and at the opposite side of the nanoSQUID loop ($\phi_\mu = -3.1\ n\Phi_0/\mu_B$, at the position of the white dot in figure 4(a)); μ_B is the Bohr magneton. A particle located at the constriction is better coupled as this is the region with smallest linewidth of the SQUID. Accordingly, more flux lines can be captured through the nanoloop.

Experimental values of $S_\Phi^{1/2}$ and the calculated ϕ_μ allow estimating the expected spin sensitivity. This is the figure of merit of nanoSQUID sensors, defined as

$$S_\mu^{1/2} = S_\Phi^{1/2}/|\phi_\mu|. \quad (2)$$

For a point-like particle on top of the constriction of SQ #2 at $z = 80$ nm, we obtain $S_\mu^{1/2} \sim 220\ \mu_B\ Hz^{-1/2}$ at 100 kHz. This means that 220 μ_B fluctuating at 100 kHz can be detected in a 1 Hz bandwidth.

3. Co MNP growth

Polycrystalline cobalt MNPs have been grown by FEBID in a dual-beam system from FEI (models Helios 600 and 650). The focused electron beam is used to take SEM images of the nanoSQUID and spot the precise location where the Co MNP is desired to be grown. The precursor gas $Co_2(CO)_8$ is supplied locally with a gas injection system that approaches a needle to a distance $\sim$150 μm from the site of interest. The base pressure of the chamber is 2×10^{-6} mbar, and increases to $\sim 1.5 \times 10^{-5}$ mbar when the precursor valve is open. The electron beam is scanned on the selected area using a small current (25 pA) to ensure a good spatial resolution, and with low voltage (5 kV) to produce a material with moderate purity $\sim$60 at%; a higher purity of 90% is possible, but then the sample is very prone to oxidation in ambient conditions [34].

Three FEBID-Co nanoparticles grown on top of a YBCO/Au bilayer are displayed in figure 5, showing a high degree of control over the geometrical volume V_{geo} of the particles. These particles have been obtained by scanning the electron beam on a 10 nm diameter circle leading to the formation of a spherical cap-like MNP with geometrical diameter d_{geo} and thickness (height) t_{geo}. From left to right in

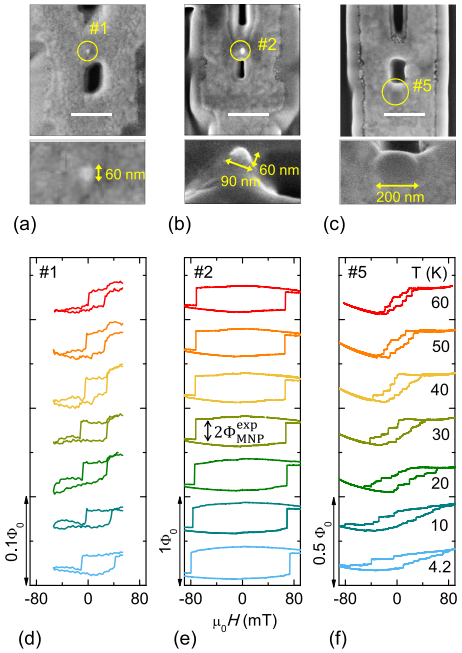

Figure 6. (a)–(c) SEM images of devices SQ #1, SQ #2 and SQ #5, respectively (upper panels); scale bars correspond to 500 nm. Co MNPs are highlighted by circles and shown in zoomed view in the bottom panels (tilted images in (b) and (c)). (d)–(f) Representative hysteresis curves $\Phi(H)$ measured for MNP #1, #2 and #5, respectively, at different temperatures as indicated in (f). The field sweep rate was $\nu = 4.5$ mT s^{-1} in (d) and $\nu = 0.45$ mT s^{-1} in (e) and (f). Curves are vertically shifted for clarity. The vertical axes are in units of magnetic flux coupled to the nanoSQUID; notice the different scales.

figure 5, these MNPs have d_{geo}/t_{geo} ~65/30, ~85/40 and ~115/60 nm nm^{-1}. Still, the likely presence of a magnetically dead/paramagnetic layer does not allow the precise determination of the real magnetic volume V_{mag} of the Co particles from SEM images. The dead layer might arise at the first stage of the growth process due to a likely lower concentration of Co [23]. Partial oxidation at the surface of the particle might also lead to a thin antiferromagnetic CoO_x layer [34]. In section 4.1 V_{mag} will be estimated by combining the calculated coupling between the MNP and the SQUID nanoloop and the experimentally measured magnetic flux.

FEBID-Co nanoparticles have been grown as described above at the precise positions where ϕ_μ is maximum. SEM images of three representative samples, SQ #1, SQ #2 and SQ #5, are shown in figures 6(a)–(c), respectively.

Particles #1, #2 and #3 are similar to those shown in figure 5. Their estimated geometrical dimensions correspond to $d_{geo}/t_{geo} \sim 60/40$, ~90/60 and ~50/35 nm nm^{-1}, respectively. Their geometrical volume is then obtained as that of a spherical cap, i.e., $V_{geo} = \frac{\pi}{6} t_{geo}(\frac{3}{4} d_{geo}^2 + t_{geo}^2)$. Particle #1 is placed above the 500 nm wide constriction of SQ #1 (figure 6(a)), whereas particle #2 lies on top of the much narrower 80 nm wide constriction of SQ #2 (figure 6(b)), and particle #3 sits on SQ #3 with intermediate constriction width $w_c = 260$ nm. This entails clear differences between their respective coupling factors, being largest for particle #2, as will be discussed in section 4.1.

Particles #4 and #5 are, on the other hand, disc-shaped. They were grown by scanning the electron beam on 100 and 200 nm diameter circles, respectively. Their geometrical thickness is $t_{geo} \sim 35$ nm, as determined by atomic force microscopy performed directly on the surface of the sensors. From these measurements we also conclude that the surface of the MNPs is very smooth (5 nm roughness). In this case, $V_{geo} = \frac{\pi}{4} t_{geo} d_{geo}^2$ has been calculated as that of a cylinder.

We highlight that the larger discs #4 and #5, have been deposited close to the edge of the nanoloop opposite to the constriction. The reason is that this region provides a smoother Au surface, less affected by FIB milling effects at the edges. As shown in figure 4, this region still offers large values of ϕ_μ. Together with their larger volumes, this provides reasonable magnetic signals as we will see in the following.

4. Magnetization measurements

Magnetization hysteresis loops of Co MNPs, i.e. change of magnetic flux Φ coupled to the nanoSQUID versus applied magnetic field H, of the different samples have been obtained by sweeping H at different temperatures while operating the nanoSQUIDs in FLL mode. Except for the measurements presented in section 4.3, H was always applied perpendicular to the GB plane. Some representative measurements performed with SQ #1, SQ #2 and SQ #5, are shown in figures 6(d)–(f) respectively. These curves have been obtained at the same temperatures as indicated in figure 6(f). All particles exhibit hysteretic behavior. The magnetic signal of each particle saturates at different values of the external magnetic field in the range 40 mT $< \mu_0 H <$ 80 mT. When sweeping back the magnetic field from the fully saturated state, abrupt steps indicate the onset of an irreversible process of magnetization reversal. In all cases, the observed switching fields depend on temperature, suggesting the occurrence of a thermally activated magnetization reversal process.

However, clear differences are observed in measurements on different samples. Hysteresis curves corresponding to #1, #2 and #3 are square shaped, suggesting that particles remain in the (quasi) single-domain state while H is swept. This does not necessarily mean that particles are uniformly magnetized. Non-uniformities are likely to appear at the edges so to reduce the total magnetostatic energy [35, 36].

In contrast to this, measurements obtained with #4 and #5 exhibit a number of reproducible steps, suggesting that magnetization reversal is assisted by the formation of more complicated multi-domain magnetic states. Owing to the

Table 2. Experimentally measured Φ_{MNP}^{exp} (with an rms noise amplitude $\sim 1 m\Phi_0$), geometric MNP parameters d_{geo}, t_{geo} and V_{geo} (determined from SEM images with an estimated error ± 10 nm in d_{geo} and t_{geo}), calculated values of $|\phi_{MNP}|$ (for $\Phi_{MNP}^{theo} = \Phi_{MNP}^{exp}$), magnetic MNP parameters V_{mag} and t_{mag} (determined from Φ_{MNP}^{exp} and ϕ_{MNP}), and estimated magnetic moment μ_{MNP} for each particle.

	Φ_{MNP}^{exp} ($m\Phi_0$)	d_{geo} (nm)	t_{geo} (nm)	V_{geo} ($\times 10^{-16}$cm^3)	$\lvert\phi_{MNP}\rvert$ ($n\Phi_0/\mu_B$)	V_{mag} ($\times 10^{-16}$cm^3)	t_{mag} (nm)	μ_{MNP} ($\times 10^6 \mu_B$)
#1	10	60	40	0.9 ± 0.2	3.0 ± 0.2	0.4 ± 0.1	21 ± 6	3.3 ± 0.9
#2	110	90	60	3.0 ± 0.5	4.9 ± 0.6	2.4 ± 0.5	52 ± 8	23 ± 6
#3	5.5	50	35	0.6 ± 0.2	3.9 ± 0.3	0.15 ± 0.04	14 ± 5	1.4 ± 0.4
#4	24	100	35	2.7 ± 0.5	3.0 ± 0.2	0.9 ± 0.2	11 ± 3	8.0 ± 2.0
#5	80	200	35	11 ± 2	2.7 ± 0.2	3.2 ± 0.6	10 ± 2	30 ± 7

circular shape of the particles, flux-closure magnetic states such as vortices might be stabilized at equilibrium or nucleate when sweeping the magnetic field [24, 25]. These measurements will be analyzed in more detail elsewhere.

4.1. Magnetic flux signals

The maximum experimentally detected magnetic flux $\pm\Phi_{MNP}^{exp}$ coupled by a fully saturated Co MNP to the nanoSQUID depends on the position, size and saturation magnetization M_s of the MNP and on the specific geometry of the nanoSQUID through the magnetic coupling. This can be appreciated in figures 6(d)–(f) by observing the differences in Φ_{MNP}^{exp} for different samples or in table 2, where the values of Φ_{MNP}^{exp} are summarized. Φ_{MNP}^{exp} can be compared with the expected signal calculated as $\Phi_{MNP}^{theo} = |\phi_{MNP}| V M_s$. Here, V is the volume of the particle, $M_s = p M_s^{Co}$ where $p = (60 \pm 10)$at% is the expected concentration of Co atoms, and $M_s^{Co} = 1.4 \times 10^6$ A m^{-1} is the saturation magnetization of cobalt [37]. ϕ_{MNP} is the averaged coupling factor for each nanoSQUID across the particle volume, given by

$$\phi_{MNP} = \frac{\int_V \phi_\mu(\mathbf{r})\,dV}{V}. \quad (3)$$

In all cases, taking $V = V_{geo}$ in the above formula yields values of Φ_{MNP}^{theo} larger than the experimental ones. This fact suggests an effective magnetic volume V_{mag} smaller than V_{geo} estimated from the SEM images and the AFM measurements. $V_{mag} < V_{geo}$ is reasonable considering that the FEBID process might lead to an effectively dead magnetic layer as discussed in section 3. We have estimated V_{mag} as the volume required in order to obtain $\Phi_{MNP}^{theo} = \Phi_{MNP}^{exp}$. The magnetic thickness t_{mag} is then calculated by assuming $d_{mag} = d_{geo}$. Estimated values are given in table 2 together with the measured d_{geo}, t_{geo} and V_{geo}. The table also provides the total resulting estimated magnetic moment per particle $\mu_{MNP} = V_{mag} M_s$ and the values of ϕ_{MNP} calculated by averaging across $V = V_{mag}$.

In case of particle #2 a volume averaged magnetic coupling of $\phi_{MNP} = 4.9$ $n\Phi_0/\mu_B$ has been calculated. This value results when integrating over the magnetic volume of MNP #2 assuming it lies on top of the Au layer, i.e., at $z = 70$ nm. We note that due to FIB-induced rounding of the nanoSQUID patterned edges, the Au thickness and hence z may vary across the constriction. This effect becomes especially important in nanoSQUID #2 with the smallest constriction width ($w_c \sim 80$ nm) where the particle is deposited very close to the edge (see bottom panel of figure 6(b)). In this case, assuming a reasonable value of, e.g., $z = 35$ nm would yield $\phi_{MNP} = 7.3$ $n\Phi_0/\mu_B$ obtained upon integration over $V_{mag} = (1.6 \pm 0.3) \times 10^{-16}$ cm^3. This translates into an estimated magnetic thickness of $t_{mag} = 40 \pm 7$ and $\mu_{MNP} = (15 \pm 4) \times 10^6$ μ_B.

As it can be seen, the effective magnetic volume of each particle is smaller than the geometrical one by a factor ~ 3 on average. Put another way, the dead magnetic layer amounts to 20–25 nm roughly. Alternatively, Φ_{MNP}^{theo} and Φ_{MNP}^{exp} could agree if we assume that these particles have a much lower amount of Co atoms. In this case, the Co purity can be estimated by assuming $V = V_{geo}$, leading to just $p \sim 20$ at%. We consider this latter scenario as unrealistic, as such a low Co concentration would yield a purely paramagnetic material [22, 38].

We note the high signal-to-noise ratio of our hysteresis loop measurements (the rms noise amplitude of Φ_{MNP}^{exp} amounts to $\lesssim 1 m\Phi_0$). This is due to the high spatial resolution achieved with FEBID growth of the MNPs directly on top of the FIB-patterned constrictions in the nanoSQUIDs. For SQ #2 with only 80 nm constriction width, the largest value of the averaged coupling factor is achieved. In this case, MNPs having a total magnetic moment of just $\sim 10^5$ μ_B would still provide a measurable signal.

4.2. Temperature dependence

The T dependence of the switching magnetic field H_{sw} is analyzed in the following. H_{sw} is defined as $H_{sw} = (H_{sw}^+ + H_{sw}^-)/2$ where $H_{sw}^{+(-)}$ is that at which irreversible jumps are observed in the hysteresis curves when sweeping up (down) the field. Except for these jumps occurring at H_{sw}^+ and H_{sw}^-, the nanoSQUID output signal vs H is reversible. $H_{sw}(T)$ values for particles #1 and #2 are plotted in figure 7 showing that H_{sw} decreases with increasing T. As mentioned above, this behavior is typical for a single-domain particle if its magnetization reversal is assisted by thermal fluctuations. Such fluctuations allow the magnetization to overcome the energy barrier U_0 created by the magnetic anisotropy. Being an stochastic process, H_{sw} should depend on both the temperature T and the field sweeping rate ν. This is further confirmed by the fact that H_{sw} increases with increasing ν, as shown in the inset of figure 7 where data were

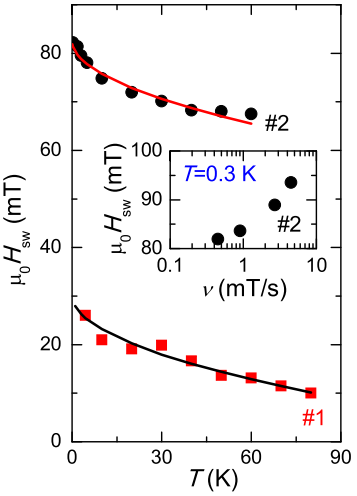

Figure 7. Temperature dependence of H_{sw} for particle #1 ($\nu = 4.5$ mT s^{-1}) and #2 ($\nu = 0.45$ mT s^{-1}). Solid lines are fits to the Kurkijärvi model, equation (4), for a thermally activated process over an energy barrier. The inset shows H_{sw} versus field sweeping rate at 0.3 K for particle #2.

taken at $T = 0.3$ K. Within the Néel–Brown model of magnetization reversal, [12, 13] the mean switching field can be obtained from the model of Kurkijärvi [39–41]

$$\mu_0 H_{sw} = \mu_0 H_{sw}^0 \left\{ 1 - \left[\frac{k_B T}{U_0} \ln\left(\frac{cT}{\nu} \right) \right]^{1/\alpha} \right\}, \qquad (4)$$

where $c = H_{sw}^0 k_B / \tau_0 \alpha U_0 \varepsilon^{\alpha-1}$. H_{sw}^0 is the switching field at $T = 0$, $\varepsilon = 1 - H_{sw}/H_{sw}^0$, τ_0 is an attempt time, k_B is the Boltzmann constant and α varies usually between 1 and 2 [25]. Experimental data are fitted by equation (4) as shown by the solid lines in figure 7 where best fits are found for $\alpha = 2$. For both particles, $\tau_0 = 10^{-10}$ s has been used, although it influences only marginally the fits. We found $U_0/k_B = 3.8 \times 10^3$ K and $\mu_0 H_{sw}^0 = 30$ mT for particle #1 and $U_0/k_B = 3.2 \times 10^4$ K and $\mu_0 H_{sw}^0 = 83$ mT for particle #2. This is of the same order of magnitude as $U_0/k_B = 6.8 \times 10^3$ K and 2.7×10^4 K, obtained by Wernsdorfer *et al* [42] for elliptical polycrystalline cobalt particles with dimensions $80 \times 50 \times 30$ and $150 \times 80 \times 30$ nm^3, respectively.

The energy barrier can be translated into a phenomenological activation volume $V_{act} = U_0/\mu_0 H_{sw}^0 M_s$. Calculated values for particle #1 and #2 yield $V_{act} \sim 2$ and 6×10^{-18} cm^3, respectively. These values are just ~6% and 3% of V_{mag} for each particle, respectively, suggesting that magnetization reversal is triggered by a nucleation process followed by propagation of domain walls. According to this picture, magnetization reversal initiates within a small region of volume $\sim V_{act}$. This is followed by a rapid (ps–ns) propagation of the reversed magnetization through the whole volume of the particle. This process cannot be distinguished from pure coherent magnetization reversal by only inspecting the hysteresis curves as both mechanisms, i.e., nucleation and propagation, take place within the experimental field step-size.

4.3. Angular dependence

In order to gain a deeper insight into the mechanisms leading to magnetization reversal, we performed magnetization measurements by rotating the externally applied magnetic field by an angle θ in the plane of the nanoSQUID loop (substrate plane). Results are shown in figure 8(a) where few representative $\Phi(H)$ hysteresis curves are shown for different values of θ. Notice that the hysteresis sense is inverted between the interval $-90° < \theta < 90°$ to $90° < \theta < 270°$.

Some of the magnetization curves also reveal the existence of intermediate smaller steps, the height of which increases at angles close to $\theta = \pm 90°$. These steps appear typically when magnetization reversal is triggered by a nucleation process as suggested in the previous section. They arise due to the formation and annhilation of metastable multi-domain magnetic states or due to defects present in the MNP behaving as pinning sites where domain walls remain immobilized up to larger applied magnetic fields [42, 43]. The height of each step is related to the total volume of the reversed domain.

The angular dependence of the switching fields is summarized in figure 8(b) where we plot values of $H_{sw}(\theta)$ at which the first (dots) and last (stars) step is observed (see vertical dashed lines in figure 8(a)). Experimental data exhibit a clear two fold symmetry along $\theta \sim 8°$ having a small fourfold symmetric contribution at $\theta \sim 98°$. This symmetry is highlighted by the black and blue solid lines serving as a guide to the eye. Such a behavior could reflect the angular dependence of the shape anisotropy (second order) of the particle. In addition, magnetization non-uniformities might arise especially at the edges of the particle as a consequence of its shape and edge roughness. Such non-uniformities behave as nucleation sites for magnetization reversal and might lead to an effective anisotropy of higher degree. [35, 36] A more complete description of the three-dimensional properties of particle #2 would be possible only by performing magnetization measurements covering any direction in space and is far from the scope of this work.

5. Conclusions

A comprehensive characterization of a number of individual cobalt MNPs has been presented. For this purpose, five different particles having different sizes and aspect ratios have been grown directly on the surface of five ultra-sensitive YBCO-nanoSQUID sensors. The sensors are based on the use of GB Josephson junctions and have been patterned by FIB milling. MNPs have been grown by means of FEBID achieving nanometric resolution and, therefore, remarkably large magnetic couplings to the nanoSQUID.

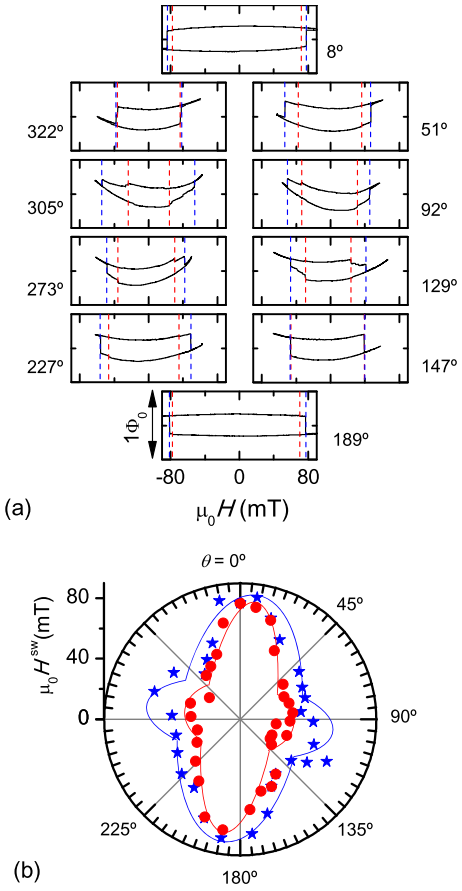

Figure 8. Angular dependence of magnetization reversal for MNP #2 obtained by rotating H within the substrate plane at $T = 4.2$ K. (a) $\Phi(H)$ Hysteresis curves obtained at different values of θ indicated at each panel. Red (blue) lines indicate the position of the first (last) switching step. The height of each graph corresponds to 1 Φ_0. (b) $H_{sw}(\theta)$ polar plot. For each value of θ, the magnitude of the corresponding switching field is represented by the distance from dots (stars) to the origin. Dots: first step; stars: last step. The red and blue lines are guides to the eye highlighting the fourfold symmetry.

The magnetic volume of each MNP has been estimated from the total magnetic signal sensed by the nanoSQUID and the calculated position-dependent magnetic coupling. A sizable reduction (by a factor ~3) of the effective magnetic volume as compared to the geometric one is observed and ascribed to surface oxidation and non-uniform Co concentration in the particle. The resulting estimated magnetic moments lie within (1–30) $\times$ 10^6 μ_B.

Moreover, we have demonstrated that magnetization measurements at magnetic fields $\mu_0|H| \leqslant 0.15$ T applied at any direction in the plane of the nanoloop and temperatures $0.3\ \text{K} < T < 80\ \text{K}$ are feasible. Based on these studies, we have distinguished between (quasi) single-domain particles, in which magnetization reversal takes place non-coherently, possibly triggered by a nucleation process, and more complicated topological magnetic states that will be analyzed elsewhere. Additionally, the energy barriers involved in the reversal process of particle #1 and #2 have been quantified. Our results demonstrate that YBCO nanoSQUID sensors are outstanding magnetometers well-suited to perform magnetization studies on individual nanomagnets.

Acknowledgments

We are grateful to J M de Teresa for fruitful discussions. MJ MP acknowledges support by the Alexander von Humboldt Foundation. This work is supported by the Nachwuchswissenschaftlerprogramm of the Universität Tübingen, by the Deutsche Forschungsgemeinschaft (DFG) via Project SFB/TRR 21 C2 and by the EU-FP6-COST Action MP1201.

References

[1] Bødker F, Mørup S and Linderoth S 1994 Surface effects in metallic iron nanoparticles *Phys. Rev. Lett.* **72** 282–5
[2] Luis F, Torres J M, García L M, Bartolomé J, Stankiewicz J, Petroff F, Fettar F, Maurice J-L and Vaurès A 2002 Enhancement of the magnetic anisotropy of nanometer-sized Co clusters: influence of the surface and of interparticle interactions *Phys. Rev.* B **65** 094409
[3] Landau D P 1976 Finite-size behavior of the simple-cubic ising lattice *Phys. Rev.* B **14** 255–62
[4] Evangelisti M and Brechin E K 2010 Recipes for enhanced molecular cooling *Dalton Trans.* **39** 4672–6
[5] Guslienko K Yu, Ivanov B A, Novosad V, Otani Y, Shima H and Fukamichi K 2002 Eigenfrequencies of vortex state excitations in magnetic submicron-size disks *J. Appl. Phys.* **91** 8037–9
[6] 2013 Special issue on magnetic nanoparticles *MRS Bull.* **38** (11https://www.cambridge.org/core/journals/mrs-bulletin/issue/A6F657BE9AE287B7E21FE4906F933B85
[7] Leuenberger M N and Loss D 2001 Quantum computing in molecular magnets *Nature* **410** 789–93
[8] Bogani L and Wernsdorfer W 2008 Molecular spintronics using single-molecule magnets *Nat. Mater.* **7** 179–86
[9] Wernsdorfer W 2001 Classical and quantum magnetization reversal studied in nanometersized particles and clusters *Adv. Chem. Phys.* **118** 99–190
[10] Wernsdorfer W 2009 From micro- to nano-SQUIDs: applications to nanomagnetism *Supercond. Sci. Technol.* **22** 064013
[11] Wernsdorfer W, Bonet Orozco E, Hasselbach K, Benoit A, Barbara B, Demoncy N, Loiseau A, Pascard H and Mailly D 1997 Experimental evidence of the Néel–Brown model of magnetization reversal *Phys. Rev. Lett.* **78** 1791–4
[12] Néel L 1949 Théorie du traînage magnétique des ferromagnétiques en grains fins avec application aux terres cuites *Ann. Géophys.* **5** 99–136

[13] Brown W F 1963 Thermal fluctuations of a single-domain particle *Phys. Rev.* **130** 1677–86
[14] Bonet E, Wernsdorfer W, Barbara B, Benoît A, Mailly D and Thiaville A 1999 Three-dimensional magnetization reversal measurements in nanoparticles *Phys. Rev. Lett.* **83** 4188–91
[15] Stoner E C and Wohlfarth E P 1948 A mechanism of magnetic hysteresis in heterogeneous alloys *Phil. Trans. R. Soc.* A **240** 599–642
[16] Wernsdorfer W, Bonet Orozco E, Hasselbach K, Benoit A, Mailly D, Kubo O, Nakano H and Barbara B 1997 Macroscopic quantum tunneling of magnetization of single ferrimagnetic nanoparticles of barium ferrite *Phys. Rev. Lett.* **79** 4014–7
[17] Granata C and Vettoliere A 2016 Nano superconducting quantum interference device: a powerful tool for nanoscale investigations *Phys. Rep.* **614** 1–69
[18] Martínez-Pérez M J and Koelle D 2016 NanoSQUIDs: Basics & recent advances *Phys. Sci. Rev.* in press, arXiv:1609.06182 [cond-mat.supr-con]
[19] Nagel J *et al* 2011 Resistively shunted $YBa_2Cu_3O_7$ grain boundary junctions and low-noise SQUIDs patterned by a focused ion beam down to 80 nm linewidth *Supercond. Sci. Technol.* **24** 015015
[20] Schwarz T, Nagel J, Wölbing R, Kemmler M, Kleiner R and Koelle D 2013 Low-noise nano superconducting quantum interference device operating in tesla magnetic fields *ACS Nano* **7** 844–50
[21] Schwarz T, Wölbing R, Reiche C F, Müller B, Martínez-Pérez M J, Mühl T, Büchner B, Kleiner R and Koelle D 2015 Low-noise $YBa_2Cu_3O_7$ nano-SQUIDs for performing magnetization-reversal measurements on magnetic nanoparticles *Phys. Rev. Appl.* **3** 044011
[22] De Teresa J M, Fernández-Pacheco A, Córdoba R, Serrano-Ramón L, Sangiao S and Ibarra M R 2016 Review of magnetic nanostructures grown by focused electron beam induced deposition (FEBID) *J. Phys. D: Appl. Phys.* **49** 243003
[23] Fernández-Pacheco A *et al* 2009 Magnetization reversal in individual cobalt micro-and nanowires grown by focused-electron-beam-induced-deposition *Nanotechnology* **20** 475704
[24] Guslienko K Yu 2008 Magnetic vortex state stability, reversal and dynamics in restricted geometries *J. Nanosci. Nanotechnol.* **8** 2745–60
[25] Fruchart O and Thiaville A 2005 Magnetism in reduced dimensions *C. R. Phys.* **6** 921–33
[26] Drung D 2003 High-T_c and low-T_c dc SQUID electronics *Supercond. Sci. Technol.* **16** 1320–36
[27] Wölbing R, Schwarz T, Müller B, Nagel J, Kemmler M, Kleiner R and Koelle D 2014 Optimizing the spin sensitivity of grain boundary junction nanoSQUIDs—towards detection of small spin systems with single-spin resolution *Supercond. Sci. Technol.* **27** 125007
[28] Zaitsev A G, Schneider R, Linker G, Ratzel F, Smithey R, Schweiss P, Geerk J, Schwab R and Heidinger R 2002 Microwave measurements of the absolute London penetration depth in double-sided $YBa_2Cu_3O_{7-x}$ thin films on sapphire *Rev. Sci. Instrum.* **73** 335–44
[29] Tinkham M 1996 *Introduction to Superconductivity* (New York: McGraw-Hill) ch 3
[30] Khapaev M M, Kupriyanov M Y, Goldobin E and Siegel M 2003 Current distribution simulation for superconducting multi-layered structures *Supercond. Sci. Technol.* **16** 24–7
[31] Buckel W and Kleiner R 2004 *Superconductivity, Fundamentals and Applications* 2nd edn (Weinheim: Wiley-VCH)
[32] Thiel L, Rohner D, Ganzhorn M, Appel P, Neu E, Müller B, Kleiner R, Koelle D and Maletinsky P 2016 Quantitative nanoscale vortex imaging using a cryogenic quantum magnetometer *Nat. Nanotechnol.* **11** 677–81
[33] Koelle D, Kleiner R, Ludwig F, Dantsker E and Clarke John 1999 High-transition-temperature superconducting quantum interference devices *Rev. Mod. Phys.* **71** 631–86
[34] Pablo-Navarro J, Magén C and de Teresa J M 2016 Three-dimensional core–shell ferromagnetic nanowires grown by focused electron beam induced deposition *Nanotechnology* **27** 285302
[35] Cowburn R P 2000 Property variation with shape in magnetic nanoelements *J. Phys. D: Appl. Phys.* **33** R1–6
[36] Han X F, Grimsditch M, Meersschaut J, Hoffmann A, Ji Y, Sort J, Nogués J, Divan R, Pearson J E and Keavney D J 2007 Magnetic instability regions in patterned structures: influence of element shape on magnetization reversal dynamics *Phys. Rev. Lett.* **98** 147202
[37] Grimsditch M, Fullerton E E and Stamps R L 1997 Exchange and anisotropy effects on spin waves in epitaxial Co films *Phys. Rev.* B **56** 2617–22
[38] Gabureac M, Bernau L, Utke I and Boero G 2010 Granular CoC nano-Hall sensors by focused-beam-induced deposition *Nanotechnology* **21** 115503
[39] Kurkijärvi J 1972 Intrinsic fluctuations in a superconducting ring closed with a Josephson junction *Phys. Rev.* B **6** 832–5
[40] Garg A 1995 Escape-field distribution for escape from a metastable potential well subject to a steadily increasing bias field *Phys. Rev.* B **51** 15592–5
[41] Gunther L and Barbara B 1994 Quantum tunneling across a domain-wall junction *Phys. Rev.* B **49** 3926–33
[42] Wernsdorfer W, Hasselbach K, Benoit A, Cernicchiaro G, Mailly D, Barbara B and Thomas L 1995 Measurement of the dynamics of the magnetization reversal in individual single-domain Co particles *J. Magn. Magn. Mater.* **151** 38–44
[43] Wernsdorfer W, Hasselbach K, Mailly D, Barbara B, Benoit A, Thomas L and Suran G 1995 DC-SQUID magnetization measurements of single magnetic particles *J. Magn. Magn. Mater.* **145** 33–9

Publication 4

Nanoscale

ROYAL SOCIETY OF CHEMISTRY

PAPER

View Article Online
View Journal | View Issue

Cite this: *Nanoscale*, 2020, **12**, 2587

Magnetic vortex nucleation and annihilation in bi-stable ultra-small ferromagnetic particles

M. J. Martínez-Pérez, *[a,b] B. Müller,[c] J. Lin,[c] L. A. Rodriguez,[d,e] E. Snoeck,[f] R. Kleiner,[c] J. Sesé [a,g] and D. Koelle [c]

Received 5th October 2019,
Accepted 3rd January 2020

DOI: 10.1039/c9nr08557b

rsc.li/nanoscale

Vortex-mediated magnetization reversal in *individual ultra-small* (~100 nm) ferromagnetic particles at low temperatures is studied by nanoSQUID magnetometry. At zero applied bias field, the flux-closure magnetic state (vortex) and the quasi uniform configuration are bi-stable. This stems from the extremely small size of the nanoparticles that lies very close to the limit of single-domain formation. The analysis of the temperature-dependent (from 0.3 to 70 K) hysteresis of the magnetization allows us to infer the nature of the ground state magnetization configuration. The latter corresponds to a vortex state as also confirmed by electron holography experiments. Based on the simultaneous analysis of the vortex nucleation and annihilation data, we estimate the magnitude of the energy barriers separating the quasi single-domain and the vortex state and their field dependence. For this purpose, we use a modified power-law scaling of the energy barriers as a function of the applied bias field. These studies are essential to test the thermal and temporal stability of flux-closure states stabilized in ultra-small ferromagnets.

Mesoscopic magnetic objects exhibit a number of possible (meta)stable magnetization configurations, *e.g.*, single-domain or non-homogeneous states including domain walls or flux-closure states like the archetypal magnetic vortex.[1] The latter is relevant for a number of applications going from electronics[2] and information technologies[3] up to cancer therapy.[4] Attempts are being made in order to reduce the size of magnetic units hosting vortices below the 100 nm range to favour their use in spintronic nanodevices and biomedical applications.[5,6]

Flat magnetic discs having radii in the few hundreds of nanometers to several micrometers range are prominent examples of bi-stability.[7,8] Their ground state configuration usually corresponds to a flux-closure vortex state (VS).[9] However, the quasi-single domain (QSD) state is metastable in ultra-small discs with radius $r \lesssim 100$ nm and thickness $t \sim 10$ nm.[7,10] If the size of the nanodisc is further reduced reaching $r \lesssim 50$ nm and t of few nm the QSD state becomes the ground state whereas the vortex is metastable at zero field. The transition probability between these states is governed by the height of the energy barriers between them, the temperature and the waiting time.[11,12] Energy barriers have been extensively studied both theoretically and experimentally in the case of uniformly magnetized particles reversing their magnetization *M via*, *e.g.*, coherent rotation, curling or domain wall nucleation and motion.[8,13–16] However, there are no theories allowing to compute the magnitude of energy barriers and their dependence on the applied bias field H in the case of nonuniform magnetization reversal. This is a problem of utmost importance as it determines ultimately the thermal and temporal stability of a given magnetic configuration.

In this work, we will focus on the energy barriers for vortex nucleation (U_n) and annihilation (U_a) in ultra-small ferromagnetic nanoparticles. Such problem has been analyzed theoretically in ref. 10 where U_n was calculated within the so-called rigid vortex model (at zero bias field). The latter usually results in energy barriers substantially larger than those found experimentally.[17,18] The rigid vortex model was extended in ref. 6 to account for small radius nanodots, where the vortex core occupies an important fraction of the total volume of the particle. Most experimental studies assume that, around the critical fields H_n^0 and H_a^0, the energy barriers follow a power-law scaling as a function of the bias field: $U_{a/n} = U_{a/n}^0(1 - H/H_{a/n}^0)^\alpha$. This is usually accepted for QSD particles, where the theory of coherent magnetization reversal predicts $1 < \alpha < 2$, approaching 2 when the field is applied along the easy axis of

[a]*Instituto de Ciencia de Materiales de Aragón and Departamento de Física de la Materia Condensada, CSIC-Universidad de Zaragoza, 50009 Zaragoza, Spain. E-mail: pemar@unizar.es*
[b]*Fundación ARAID, Avda. de Ranillas, 50018 Zaragoza, Spain*
[c]*Physikalisches Institut – Experimentalphysik II and Center for Quantum Science (CQ) in LISA⁺, Universität Tübingen, Auf der Morgenstelle 14, D-72076 Tübingen, Germany*
[d]*Departamento de Física, Universidad del Valle, A.A. 25360, Cali, Colombia*
[e]*Center of Excellence on Novel Materials - CENM, Universidad del Valle, A.A. 25360, Cali, Colombia*
[f]*CEMES-CNRS 29, rue Jeanne Marvig, B.P. 94347, F-31055 Toulouse Cedex, France*
[g]*Laboratorio de Microscopías Avanzadas (LMA), Instituto de Nanociencia de Aragón (INA), Universidad de Zaragoza, 50018 Zaragoza, Spain*

the particle.[13] In practice, $\alpha < 2$ is typically found in processes involving domain wall nucleation and propagation.[19]

Thermal and temporal stability in magnetic vortices stabilized in large (micron-sized) ferromagnetic discs has been studied in the past. For example, *individual* permalloy discs with radii $r \sim 250$–500 nm and thicknesses $t \sim 40$–50 nm were studied experimentally in ref. 20 and 21 by means of Hall and torque magnetometry, respectively. In the former, the temperature dependence of the hysteresis curves at low temperatures was interpreted as a signature of thermal activation over an energy barrier for both vortex nucleation and annihilation. In the latter work, measurements performed at different sweeping rates at room temperature yielded an equivalent explanation for vortex annihilation whereas signatures of supercooling were found for vortex nucleation. Regarding the field-dependence of the energy barriers, $\alpha = 1$ was assumed in the former work whereas $\alpha = 3/2$ was used in the latter. These studies yielded values in the range $U_n^0/k_B \sim 10^3$–10^4 K and $U_a^0/k_B \sim 10^4$–10^5 K. Other experimental works have focused on large arrays of permalloy discs. The vortex annihilation process was investigated at temperatures close to room temperature in ref. 17 using an array of relatively large discs with $r \sim 1$ μm and $t \sim 32$ nm. Fitting together the temperature and field sweeping rate-dependence of the magnetic susceptibility, different values of $1 < \alpha < 2.5$ yielded energy barriers for vortex annihilation in the range $2 \times 10^5 < U_a^0/k_B < 5 \times 10^6$ K. Kakazei *et al.* measured the slow decay of the magnetization of a saturated dot array at magnetic fields close to the vortex nucleation field.[22] The energy barrier for vortex nucleation was approximated as $U_n = U_n^0 + a(H/H_n^0 - 1)^\alpha$ with $3.6 < \alpha < 4$. From these measurements, $U_n^0/k_B \sim 10^4$ K was estimated for discs having $r \sim 250$ nm and $t \sim 40$ nm. Melkov *et al.* estimated the relaxation rate to the VS by measuring the dot occupation number through ferromagnetic resonance in smaller discs with $r \sim 150$ nm and $t \sim 14$ nm.[18] From the relaxation rate, an energy barrier for vortex nucleation at zero field $U_n(H = 0)/k_B \sim 10^3$ K was found. Interestingly, the latter also enabled the experimental estimation of the field dependence of $U_n(H)$.

Here, we study the vortex mediated magnetization reversal in *individual ultra-small* soft-magnetic particles having radii of ~50 nm (t of few tens of nm). Cobalt nanoparticles grown by means of Focused Electron Beam Induced Deposition (FEBID) of Co have been used for this purpose. Our particles are substantially smaller than those analyzed in the abovementioned works. For this reason, they yield bi-stability of both the VS and the QSD configuration at zero applied field with the VS being the ground state. To demonstrate this, the stabilization of flux closure magnetic structures at room temperature has been verified by electron holography. Magnetization measurements have been performed by directly growing individual cobalt nanoparticles on the surface of different nano-Superconducting Quantum Interference Devices (nanoSQUIDs).[23,24] NanoSQUIDs based on low temperature superconductors have proved to be very efficient for the study of nanoscopic magnetic objects.[8,25] Our devices, on the other hand, are made of the high critical temperature and high critical field superconductor $YBa_2Cu_3O_7$ (YBCO), patterned by focused ion beam milling and based on submicron grain boundary Josephson junctions.[26,27] By measuring the magnetic flux (Φ) captured by the SQUID nanoloop while sweeping the external magnetic field, we are able to distinguish the nucleation and annihilation of a flux-closure (vortex) state. Such process has been observed at different temperatures allowing us to infer the magnitude of the energy barriers separating the QSD and the VS and their field-dependence. For this purpose, we fit simultaneously the temperature-dependent critical fields for vortex nucleation and annihilation over a broad temperature range between 300 mK up to 70 K.

1. NanoSQUID characteristics and measurement setup

Three nanoSQUID sensors (labeled SQ1, SQ2 and SQ3) were fabricated as described in ref. 15. A Scanning Electron Microscope (SEM) image of SQ1 can be seen in Fig. 1a after deposition of the cobalt nanoparticle. The nanoSQUIDs exhibit non-hysteretic current–voltage characteristics within the whole range of temperatures studied here ($0.3 \text{ K} < T < 70$ K). These devices reach maximum critical currents of $I_c \sim 550$–950 μA at low temperatures, decreasing to ~100–150 μA at 70 K. SQUIDs are operated in flux locked loop mode thanks to the possibility of coupling magnetic flux to the nanoloop through a constriction patterned nearby (indicated in Fig. 1a top). The mutual inductance between this constriction and the nanoSQUID loop is measured experimentally giving $M = 0.44\Phi_0$/mA, $0.48\Phi_0$/mA and $0.65\Phi_0$/mA for SQ1, SQ2 and SQ3,

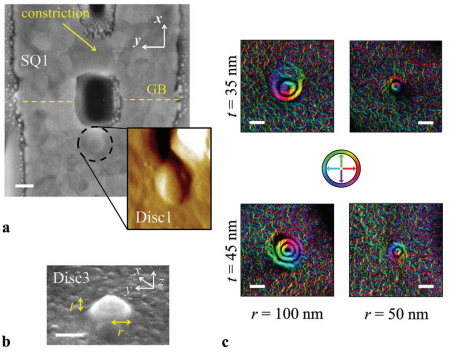

Fig. 1 (a) SEM image of Disc1 deposited on SQ1. The dashed circle highlights the position of the nanoparticle whereas dashed lines indicate the grain boundary (GB). The inset shows the corresponding AFM image of the particle. (b) SEM image of Disc3 approximated to a semi-sphere with semi-axis (r, r, t). (c) Electron holography images of few representative cobalt nanoparticles showing the presence of flux-closure ground states. The color scale in the middle represents the direction of the magnetic flux. Scale bar is 100 nm in all panels.

respectively (Φ_0 is the magnetic flux quantum). The temperature-dependence of M is also characterized experimentally for each device as described in ref. 15. These values allow us to convert the nanoSQUID output voltage into units of magnetic flux.

SQ1 and SQ2 are mounted in a ^{3}He refrigerator with base temperature of 0.3 K operated together with a split-coil superconducting vector magnet. SQ3 is mounted on a variable temperature insert with minimum temperature of 1.4 K operated with a superconducting magnet. This insert also includes a rotator coupled to the sample holder. These two approaches, *i.e.*, vector magnet and rotator, allow us to align the externally applied magnetic field parallel to the nanoSQUID substrate surface and perpendicular to the grain boundary's plane (x direction in Fig. 1a) with resolution better than 0.1°. Under such circumstances, the coupling of the external field to both, the nanoloop and the Josephson junctions, is minimized. As demonstrated in ref. 15 and 28, the devices are fully operative in external magnetic fields up to 1 T and temperatures up to 80 K.

2. Nanoparticle growth and electron holography measurements

The fabrication of polycrystalline cobalt nanoparticles is described in ref. 15 and briefly summarized here. We use a dual-beam system from FEI (model Helios 600). The working principle of FEBID is similar to chemical vapour deposition assisted by an electron beam. The latter allows imaging the region of interest prior to deposition. In this way, the final structure can be located at precise positions with a resolution of about ~10 nm. The precursor gas $Co_2(CO)_8$ is supplied close to the region of interest using a gas injection needle so that the $Co_2(CO)_8$ molecules decompose as the electron beam is scanned over the surface of the sample. An amorphous material containing carbon, oxygen and nanometric crystals of cobalt is obtained. The resulting cobalt purity (60 ± 10 at%) is determined *in situ* by energy dispersive X-ray spectroscopy and depends directly on the current used during deposition. The latter is kept at 25 pA to guarantee good spatial resolution. As it can be seen in Fig. 1b, the resulting particles are semi-spherical with semi-axis (r, r, t). As demonstrated in ref. 15, the effective magnetic thickness (t_{mag}) is lower than the geometrical thickness t. This is due to the formation of a ~20–25 nm-thick dead/paramagnetic cobalt layer in the first stage of the growth process as well as surface oxidation. t_{mag} can be estimated by nanoSQUID magnetometry. For this purpose we combine the measured nanoSQUID signal when the particle is in the saturated state and numerical simulations of the coupling factor between the nanoparticle and the SQUID nanoloop. We refer the reader to ref. 15 and 27 for more details about the calculation of the coupling factor.

To confirm the stabilization of flux-closure states we perform electron holography experiments using the dedicated Hitachi HF-3300 (I2TEM-Hitachi) transmission electron microscope. Electron holography is a high-sensitivity magnetic imaging technique that provides qualitative and quantitative magnetic information of isolated ferromagnetic nanostructures with nanometric resolution by retrieving the phase shift of the electron-beam plane wave after it passes through the sample and around it.[29–31] The spatial variation of the electron phase shift is given by the Aharonov–Bohm phase shift.[32] It is proportional to the sum of the 3D electrostatic potential, plus the magnetic vector potential parallel to the electron beam direction (z), respectively called the "electric phase shift" and the "magnetic phase shift". The later is proportional the projection of the in-plane component of the magnetic induction B_x and B_y. Subtracting the electric phase shift part from the total phase shift image allows mapping the local in-plane magnetization by imaging the projection of the magnetic flux lines.

For these experiments, we grow different cobalt nanoparticles with 50 nm < r < 250 nm and 10 nm < t < 45 nm. Particles are located around the perimeter of rectangular holes made on a 50 nm-thick SiN membrane. In Fig. 1c, we display magnetic flux line images for representative nanoparticles with $t \geq 35$ nm. Thinner nanoparticles produced noisy images or no magnetic signal due to the too weak magnetic induction of such thin material that electron holography cannot resolve. A circulation configuration of the magnetic lines around the nanoparticle center indicates a VS of the magnetization. This remanent state was observed both in as-prepared condition (magnetization state created during the FEBID deposition) and after saturating the nanoparticle with a strong perpendicular magnetic field (along z-direction). Therefore, electron holography experiments confirm that the VS is the ground state of the nanoparticles.

Finally, three cobalt nanoparticles (labeled Disc1, Disc2 and Disc3) have been deposited directly on the surface of the three YBCO nanoSQUIDs (SQ1, SQ2 and SQ3). Disc3 (Fig. 1b) is deposited at the constriction where the coupling to the nanoSQUID is maximized[15] whereas Disc1 and Disc2 are deposited on the opposite side of the nanoloop. A SEM and an Atomic Force Microscopy (AFM) image corresponding to Disc1 can be seen in Fig. 1a. We highlight that Disc1 is fabricated under the same growth conditions and is, therefore, nominally identical to the particle shown in the upper right panel of Fig. 1c. The external magnetic field is applied along the x direction. r and t are estimated from the SEM and AFM measurements whereas t_{mag} is estimated from the nanoSQUID measurements as described in ref. 15. The resulting values are given in Table 1.[33]

Table 1 Particle radius (r) and thickness (t) determined from the SEM and AFM images and estimated effective magnetic thickness (t_{mag})

	r (±5 nm)	t (±5 nm)	t_{mag} (nm)
Disc1	50	35	21 ± 5
Disc2	100	35	20 ± 3
Disc3	65	50	25 ± 4

3. Magnetization measurements and numerical simulations

Hysteresis curves $\Phi(H)$ are obtained by sweeping the external bias magnetic field H and measuring the flux Φ threading the SQUID nanoloop. Two typical hysteresis curves obtained at T = 10 K for Disc1 and Disc3 can be seen in Fig. 2a (top panels). Here, we plot the magnetic flux coupled to the nanoSQUIDs in units of the flux quantum Φ_0. The apparent curvature (positive for Disc1 and negative for Disc3) is still under investigation. A similar phenomenon is observed in all devices studied so far and is attributed to the non-perfect alignment of the external magnetic field with respect to the Josephson junctions' plane.

We now analyze in more detail the hysteresis loop of Disc1. At large positive (negative) magnetic fields the stray field produced by the particle is maximum (minimum). This can be understood as the nanoparticle is in the QSD state, with most spins pointing along the external magnetic field (x direction) and, therefore, coupling the maximum (minimum) amount of flux to the nanoSQUID. As the magnitude of the external magnetic field $+H$ ($-H$) is reduced to zero, the hysteresis curve does not exhibit any step indicating that the QSD state is preserved at remanence. As the magnitude of the magnetic field is increased in the opposite direction, *i.e.*, $-H$ ($+H$), a flux closure (vortex) state is nucleated at H_n^- (H_n^+) as evidenced by the abrupt decrease of the stray field created by the nanoparticle. If the field $-H$ ($+H$) is further increased, the vortex will move perpendicularly to the external field[34] up to its final annihilation at H_a^- (H_a^+). The presence of a few minor steps subsequent to vortex nucleation can be attributed to the nucleation of intermediate states or, most likely, the presence of pinning sites that distort the vortex path. This interpretation is supported by the reduction of minor steps at larger temperatures (*cf.* section 4 and Fig. 4). A similar behavior is found in the case of Disc2 (see Fig. 6f in ref. 15 label #5) and Disc3, although the presence of intermediate steps is much more severe.

We highlight the differences between the hysteresis loops shown here and the canonical vortex-mediated magnetization reversal hysteresis loop.[34] In the latter, coercivity approaches zero with a large initial magnetic susceptibility at H = 0. This indicates that the particle is in the VS with the QSD state being prohibited. Usually, hysteretic lobes are found at high magnetic fields stemming from the vortex annihilation and nucleation. In contrast, our nanoparticles remain in the QSD state when sweeping the field through zero. This is a signature of bi-stability of the QSD and VS configurations at zero field and is a consequence of the exceptionally small size of these particles.

The critical dimensions for QSD or VS stabilization in semi-spherical particles can be calculated numerically. We use for this purpose the finite element micromagnetic simulation package Nmag,[35] which allows to solve the Landau–Lifshitz–Gilbert equation for the specific geometry under study. The use of a finite-element discretisation method is particularly important here due to the small size of the nanoparticles. In the simulations, we neglect any contribution from magneto-crystalline anisotropy due to the polycrystalline nature of Co-FEBID. We set different initial micromagnetic configurations at zero applied field, *i.e.*, in-plane and out-of-plane saturated states and a flux-closure vortex state. We then let the system relax and calculate the total energy of each resulting state. By varying the particle dimensions, we obtain the distinct stability regions plotted in Fig. 3 (shaded). These are similar to numerical and analytical results obtained for cylindrical discs.[36] Within region I, the VS is the ground state of the particle with the QSD configuration being unstable. Regions II and III correspond to an in-plane and out-of-plane QSD ground state, respectively (with the VS being unstable). Interestingly, I′ and II′ are regions of bi-stability. I′ corresponds to a vortex ground state and a metastable QSD configuration whereas the opposite occurs in region II′. Within the bi-stability regions, decreasing the bias field after saturating the magnetization does not promote the nucleation of a VS.[5] As a matter of fact, numerical simulations predict a square-shaped hysteresis loop for particles lying on regions I′ and II′.

For comparison, in Fig. 3 we plot the measured radius r and effective magnetic thickness t_{mag} corresponding to three

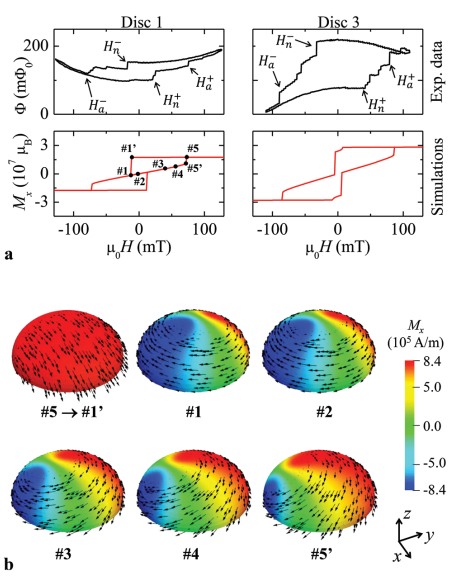

Fig. 2 Hysteresis loops of Co particles. (a) (top) Typical experimental hysteresis loops $\Phi(H)$ measured at T = 10 K and (bottom) numerical simulations $M_x(H)$ for Disc1 and Disc3. Top panels also show the definitions for the nucleation and annihilation fields. (b) Numerically simulated spatially-resolved magnetization for Disc1 at selected applied fields as indicated in panel a (bottom left). Color coding represents the magnetization along x (direction of the applied field) whereas arrows indicate the magnetization direction.

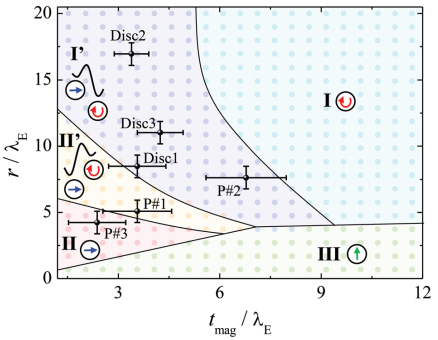

Fig. 3 Numerically calculated stability diagram for QSD and VS stabilization in semi-spherical particles (with an exchange length $\lambda_E \sim 5.9$ nm for Co-FEBID). Colored scatter indicate the points where the simulations were performed. These allow us to differentiate five stability regions (shaded). I and I′ are characterized by a vortex ground state (red curled arrow), II and II′ correspond to an in-plane ground state (blue horizontal arrow) and III corresponds to an out-of-plane ground state (green vertical arrow). Metastable configurations are also indicated schematically within each region. Solid lines are a guide to the eye. Experimental data corresponding to Disc1, Disc2, Disc3, P#1, P#2 and P#3 are shown. Particles studied by electron holography are not shown as their effective magnetic thicknesses cannot be determined.

Co-FEBID nanoparticles studied in ref. 15, *i.e.*, P#1, P#2 and P#3, and the nanoparticles studied here, *i.e.*, Disc1, Disc2 and Disc3. We highlight that P#1, P#2 and P#3 exhibited square-shaped hysteresis loops. Accordingly, these particles lye in regions II′, I′ and II, respectively. Notably, Disc1, Disc2 and Disc3 are all found in the bi-stability region I′. However, within this region, it is theoretically not possible to nucleate a VS by decreasing the bias field after saturating the magnetization. This is particularly striking in case of Disc1 that lies very close to the boundary with region II′. To the best of our knowledge, Disc1 is among the smallest nanoparticles in which a vortex has been observed to be nucleated and annihilated experimentally.[6,37,38]

Numerical simulations and experiments can come to an agreement by breaking the rotational symmetry of the nanoparticles. In this way, the experimentally measured hysteresis loops, *cf.* Fig. 2a (top panels), can be reproduced numerically by introducing a small uniaxial anisotropy parameter K_u (along the *x*-direction). The latter can have many different origins. For example, deviations from the perfect spherical shape yielding a preferred magnetization axis from magnetostatic origin. Another possibility is the existence of a net effective magnetocrystalline anisotropy (from the bulk or the substrate/surface interfaces) or magnetoelastic anisotropy. Numerical simulations are performed setting the saturation magnetization and exchange stiffness constant to $M_s = 0.6 \times 1.4$ MA m^{-1} and $A = 0.6 \times 25$ pJ m^{-1},[39] respectively. Here, the factor 0.6 reflects the reduced purity of FEBID cobalt.[40] For the anisotropy constant we choose $K_u \sim 2$ kJ m^{-3} as a reasonable value. This is estimated as $K_u = U_0/V_{mag}$ using the energy barriers (U_0) and magnetic volumes (V_{mag}) determined in ref. 15 for P#1 and P#2. To mimic the particular shape of the nanoparticles we use a semi-sphere with semi-axis (r, r, t_s). The resulting numerically calculated magnetization averaged along the *x*-direction M_x is shown in Fig. 2a (bottom panels) using $t_s = 36$ nm for Disc1 and $t_s = 27$ nm for Disc2. This simple model captures the main characteristic of the vortex-assisted magnetization reversal measured experimentally. Including few nm-sized pinned regions in the simulated nanoparticles yields the appearance of several steps ensuing vortex nucleation. These steps are similar to those observed experimentally but come at the cost of including too many degrees of freedom in the model.

4. Temperature-dependence of the vortex critical fields

In order to investigate the energy barriers involved in the processes of vortex nucleation and annihilation, we perform magnetization measurements at variable temperature. A total number of 30–50 hysteresis loops are measured at each temperature. Some representative loops obtained at given temperatures can be seen in Fig. 4 for Disc1 and Disc3. Data corresponding to Disc2 are shown in Fig. 6f from ref. 15 (with the label #5). In case of Disc1, the presence of minor steps subsequent to vortex nucleation is reduced as temperature is increased. These steps are attributed to the pinning and depin-

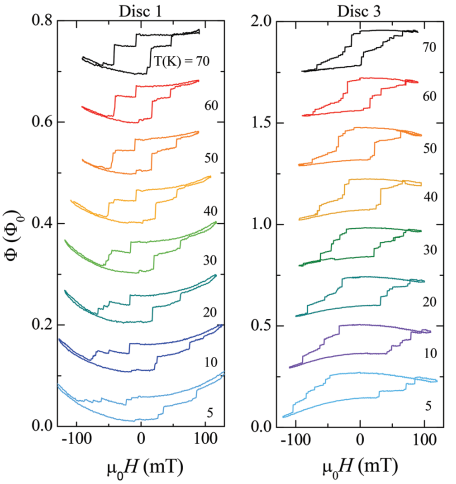

Fig. 4 Typical experimental hysteresis loops obtained at different temperatures for Disc1 and Disc3. Curves are vertically offset for clarity.

ning of the vortex core as it moves through the nanoparticle driven by the magnetic bias field. Material defects, ubiquitous in Co-FEBID nanoparticles,[15,16] lose their pinning capacity at larger temperatures yielding the observed reduction of minor steps. We also observe that both $|H_n^{\pm}|$ and $|H_a^{\pm}|$ decrease as temperature is increased for all three nanoparticles. This is typically found for thermally assisted activation processes over an energy barrier. This can be better seen by analyzing the temperature dependence of the mean nucleation and annihilation fields defined as

$$H_n(T) = (\langle H_n^- \rangle - \langle H_n^+ \rangle)/2,$$
$$H_a(T) = (\langle H_a^+ \rangle - \langle H_a^- \rangle)/2. \quad (1)$$

Here, $\langle H_n^{\pm} \rangle$ and $\langle H_a^{\pm} \rangle$ are obtained after averaging the experimentally measured values of $H_n^{\pm}$ and $H_a^{\pm}$, respectively, over 30–50 hysteresis curves at each temperature. The resulting $H_{n/a}(T)$ curves for Disc1 and Disc3 can be seen in Fig. 5.

These data can be interpreted within the Néel-Brown model of magnetization reversal.[41,42] Here, we assume that an energy barrier exist for vortex nucleation (U_n) and annihilation (U_a). Near the vortex nucleation/annihilation critical fields, we approximate the field-dependence of these energy barriers as

$$U_{n/a} = U_0 \left(1 - \frac{H - H_{off}}{H^0_{n/a} - H_{off}}\right)^{\alpha}. \quad (2)$$

With our definition, U_0 is the energy barrier at the offset field $H = H_{off}$ such that $U_a(H_{off}) = U_n(H_{off}) = U_0$ (see Fig. 6b, point #3). $H^0_{a/n}$ is the nucleation/annihilation field at $T = 0$ K and α is a generalized exponent.

The temperature and field sweeping rate-dependence of $H_{a/n}$ can be obtained from the model of Kurkijärvi[43–45] giving

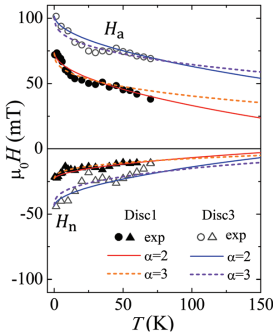

Fig. 5 Temperature dependence of the mean nucleation and annihilation fields calculated as defined in the text for Disc1 and Disc3. Dots are the experimental data. Lines are the fits to eqn (3) using the parameters shown in Table 2.

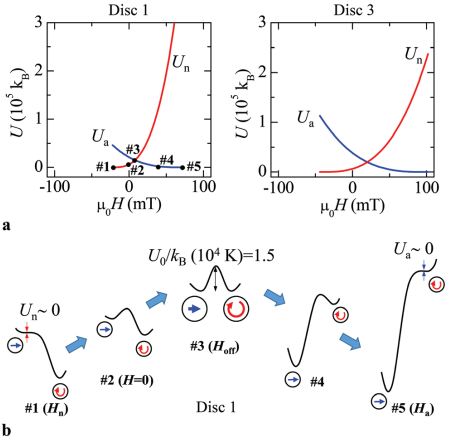

Fig. 6 (a) Field dependence of the energy barriers for vortex nucleation and annihilation calculated with eqn (2) and fitting parameters from Table 2 with α = 3 (solid lines). (b) Schematic representation of the energy landscape corresponding to Disc1 for different values of the magnetic field as indicated in panel a (left). Notice that these are the same field values at which spatially resolved maps of the magnetization are shown in Fig. 2b.

$$\mu_0 H_{n/a} = \mu_0 H_{off} + \mu_0 \left(H^0_{n/a} - H_{off}\right) \times \left\{1 - \left[\frac{k_B T}{U_0} \ln\left(\frac{\pm cT}{\nu}\right)\right]^{1/\alpha}\right\}, \quad (3)$$

where $\tau_0 = 10^{-10}$ s is an attempt time, k_B is the Boltzmann constant and ν is the magnetic field sweeping rate (ν = 4.5 mT s^{-1} and 8.3 mT s^{-1} for Disc1 and Disc3, respectively). Additionally, $c = (H^0_{n/a} - H_{off})k_B/\tau_0 \alpha U_0 \varepsilon^{\alpha-1}$ with $\varepsilon = 1 - H_{n/a}/H^0_{n/a}$.

The experimentally measured $H_a(T)$ and $H_n(T)$ curves are fitted simultaneously by eqn (3). The generalized exponent α can be, in principle, different for the processes of vortex nucleation and annihilation. In order to keep a low number of fitting parameters, we assume a single α value and we fix $H^0_{n/a}$ to the experimental fields measured at the minimum temperatures (given in Table 2). In this way, the only fitting parameters are H_{off}, U_0 and α. Simultaneous fitting is only possible for $\alpha \geq 2$. The resulting parameters obtained for α = 2 and α = 3 (solid

Table 2 Fitting parameters for Disc1 and Disc3

	$\mu_0 H^0_n$ (mT)	$\mu_0 H^0_a$ (mT)	$\mu_0 H_{off}$ (mT)	U_0/k_B ($\times 10^4$ K)	α
Disc1	−23	74	5	0.6	2
	−23	74	8	1.5	3
Disc3	−44	102	20	0.9	2
	−44	102	20	2.0	3

and dashed lines in Fig. 5, respectively) are summarized in Table 2.

The obtained energy barriers are in good agreement with values given in the literature for small size nanodiscs of permalloy, having an exchange length $\left(\lambda_E = \sqrt{2A/\mu_0 M_S^2} \sim 5\,\text{nm}\right)$ similar to that of Co-FEBID ($\lambda_E \sim 5.9$ nm). For example, Melkov *et al.* estimated $U_n(H = 0)/k_B \sim 4.7 \times 10^3$ K for permalloy discs with $r = 150$ nm and $t = 14$ nm.[18] The latter compares well with $U_n(H = 0)/k_B \sim 6 \times 10^3$ K obtained for Disc1 and $U_n(H = 0)/k_B \sim 6.5 \times 10^3$ K obtained for Disc3.

From these fitting parameters it is also possible to infer the nature of the ground state magnetization configuration at zero applied bias field (*cf.* point #2 in Fig. 6b). Positive H_{off} values indicate a vortex ground state in both particles at $H = 0$. This is confirmed by the electron holography experiments performed at room temperature, where flux-closure states were observed. The fact that nanoSQUID and electron holography measurements yield QSD and VS at zero bias field, respectively, is due to the different temperatures at which these experiments are performed. At room temperature, particles need only few milliseconds to relax towards the vortex ground state. However, this process becomes immeasurably long at low temperatures and the particle remains trapped in the QSD metastable state.

5. Field-dependence of the energy barriers

We can now calculate the field-dependence of the energy barriers for vortex nucleation and annihilation. For this purpose, we insert the fitting parameters corresponding to $\alpha = 3$ (*cf.* Table 2) into eqn (2) and plot the resulting $U_a(H)$ and $U_n(H)$ curves in Fig. 6a (solid lines). We highlight that eqn (2) is a good approximation only for field values close to the critical fields. However, this representation will help us to understand the processes of vortex nucleation and annihilation.

Let us focus on the results obtained for Disc1, assuming that the particle resides at $T = 0$ K. In order to facilitate understanding of the process, in Fig. 2b we plot a few space-resolved magnetization maps at selected field values numbered in panel a (bottom left). At large positive magnetic fields the cobalt nanoparticle is in the ground QSD state (#5 in Fig. 2b). If we decrease the field reaching the nucleation field (#1′), the energy barrier for vortex nucleation U_n becomes zero and the magnetic vortex nucleates (#1). This situation is schematically depicted in Fig. 6b point #1. If we now increase again the magnetic field, the vortex core will move along the y direction as shown in the series #1 → #2 → #3 in Fig. 2b. This translates into an increase of U_n while U_a decreases steadily up to the point at which the QSD and VS are degenerate [$U_0 = U_n(H_{off}) = U_a(H_{off}) = 1.5 \times 10^4 k_B$ K, *cf.* point #3 in Fig. 6b]. If we continue increasing the magnetic field, the particle will remain "trapped" in the metastable VS [*e.g.*, #4 in Fig. 2b and 6b]. Once the annihilation field is reached at #5′, the energy barrier for vortex annihilation U_a will equal zero so that the transition into the QSD state will take place (#5). The situation changes slightly at larger temperatures. Under these circumstances, the nanoparticle might gain enough thermal energy to overcome the energy barrier at field values prior to H_a. The same happens with the waiting time. If we repeat the measurements sweeping the external magnetic field at a much slower rate, the particle will have a larger probability of escaping the metastable VS before #5 is reached.

6. Conclusions

We have studied the occurrence of field-driven vortex nucleation and annihilation in *individual ultra-small* ferromagnetic particles by YBCO nanoSQUID magnetometry. The high sensitivity and broad operating field and temperature range of YBCO nanoSQUIDs has been key for this purpose. Based on the simultaneous analysis of the vortex nucleation and annihilation fields as a function of temperature, we demonstrate that particles are bi-stable at zero applied field, with the VS being the ground state. This has been also verified by electron holography experiments performed at room temperature. Interestingly, particles lie very close to the limit of QSD formation, being among the smallest nanoparticles in which a vortex has been observed to be nucleated and annihilated experimentally.[6,37,38]

YBCO nanoSQUID measurements also enable us to estimate the magnitude of the energy barriers separating the QSD and the VS and their field dependence. The latter has been approximated by a modified power-law around the critical field with generalized exponent $\alpha \geq 2$. This contrasts with most semiempirical models in which $\alpha = 3/2$, evidencing the need to further develop the theory of vortex energy barriers. In addition, details on the microscopic configuration prior to the field-driven vortex nucleation and annihilation processes remain obscure. This topic is of utmost importance in order to understand the thermal and temporal stability of noncollinear and other nontrivial spin textures, *e.g.*, vortices or skyrmions, confined in ultra-small ferromagnets. Controlling and manipulating magnetic units below the 100 nm range is paramount for their integration into nanoscopic spintronic and magnonic devices.[2,3,46]

Conflicts of interest

There are no conflicts to declare.

Acknowledgements

This work was partly funded through the Spanish MINECO (MAT2015-73914-JIN and MAT2015-64083-R), the Aragón Regional Government through project E09_17R (*Construyendo Europa desde Aragón*), the European Union Seventh Framework Program under Grant Agreement 312483-ESTEEM2 (Integrated Infrastructure Initiative–I3) and the COST action NANOCOHYBRI (Grant No. CA 16218). B. M. acknowledges funding by the German Academic Scholarship Foundation,

and J. Lin acknowledges funding by the Chinese Research Council (CRC). E. S. acknowledges the French National Research Agency under the "*Investissement d'Avenir*" program reference no. ANR-10-EQPX-38-01. We acknowledge K. Guslienko for fruitful discussions and the use of Servicio General de Apoyo a la Investigación-SAI, Universidad de Zaragoza.

References

1 O. Fruchart and A. Thiaville, *C. R. Phys.*, 2005, **6**, 921–933.
2 V. S. Pribiag, I. N. Krivorotov, G. D. Fuchs, P. M. Braganca, O. Ozatay, J. C. Sankey, D. C. Ralph and R. A. Buhrman, *Nat. Phys.*, 2007, **3**, 498–503.
3 S. Wintz, V. Tiberkevich, M. Weigand, J. Raabe, J. Lindner, A. Erbe, A. Slavin and J. Fassbender, *Nat. Nanotechnol.*, 2016, **11**, 948–953.
4 D.-H. Kim, E. A. Rozhkova, I. V. Ulasov, S. D. Bader, T. Rajh, M. S. Lesniak and V. Novosad, *Nat. Mater.*, 2009, **9**, 165–171.
5 R. V. Verba, D. Navas, A. Hierro-Rodriguez, S. A. Bunyaev, B. A. Ivanov, K. Y. Guslienko and G. N. Kakazei, *Phys. Rev. Appl.*, 2018, **10**, 031002.
6 M. Goiriena-Goikoetxea, K. Y. Guslienko, M. Rouco, I. Orue, E. Berganza, M. Jaafar, A. Asenjo, M. L. Fernández-Gubieda, L. Fernández Barquín and A. García-Arribas, *Nanoscale*, 2017, **9**, 11269–11278.
7 K. L. Metlov and K. Y. Guslienko, *J. Magn. Magn. Mater.*, 2002, **242–245**, 1015–1017.
8 W. Wernsdorfer, K. Hasselbach, D. Mailly, B. Barbara, A. Benoit, L. Thomas and G. Suran, *J. Magn. Magn. Mater.*, 1995, **145**, 33–39.
9 T. Shinjo, T. Okuno, R. Hassdorf, K. Shigeto and T. Ono, *Science*, 2000, **289**, 930–932.
10 H. F. Ding, A. K. Schmid, D. Li, K. Y. Guslienko and S. D. Bader, *Phys. Rev. Lett.*, 2005, **94**, 157202.
11 J. Li, J. Shi and S. Tehrani, *Appl. Phys. Lett.*, 2001, **79**, 3821–3823.
12 H. Shima, V. Novosad, Y. Otani, K. Fukamichi, N. Kikuchi, O. Kitakamai and Y. Shimada, *J. Appl. Phys.*, 2002, **92**, 1473–1476.
13 R. H. Victora, *Phys. Rev. Lett.*, 1989, **63**, 457–460.
14 W. Wernsdorfer, B. Doudin, D. Mailly, K. Hasselbach, A. Benoit, J. Meier, J. P. Ansermet and B. Barbara, *Phys. Rev. Lett.*, 1996, **77**, 1873–1876.
15 M. J. Martínez-Pérez, B. Müller, D. Schwebius, D. Korinski, R. Kleiner, J. Sesé and D. Koelle, *Supercond. Sci. Technol.*, 2017, **30**, 024003.
16 M. J. Martínez-Pérez, J. Pablo-Navarro, B. Müller, R. Kleiner, C. Magén, D. Koelle, J. M. de Teresa and J. Sesé, *Nano Lett.*, 2018, **18**, 7674–7682.
17 J. A. J. Burgess, D. C. Fortin, J. E. Losby, D. Grombacher, J. P. Davis and M. R. Freeman, *Phys. Rev. B: Condens. Matter Mater. Phys.*, 2010, **82**, 144403.
18 G. A. Melkov, Y. Kobljanskyj, V. Novosad, A. N. Slavin and K. Y. Guslienko, *Phys. Rev. B: Condens. Matter Mater. Phys.*, 2013, **88**, 220407.
19 J. Ferré, Dynamics of the magnetization reversal: from continuous to patterned ferromagnetic films, in *Spin Dynamics in Confined Magnetic Structures*, Springer, Heidelberg, 2001.
20 G. Mihajlović, M. S. Patrick, J. E. Pearson, V. Novosad, S. D. Bader, M. Field, G. J. Sullivan and A. Hoffmann, *Appl. Phys. Lett.*, 2010, **96**, 112501.
21 J. P. Davis, D. Vick, J. A. J. Burgess, D. C. Fortin, P. Li, V. Sauer, W. K. Hiebert and M. R. Freeman, *New J. Phys.*, 2010, **12**, 093033.
22 G. N. Kakazei, M. Ilyn, O. Chubykalo-Fesenko, J. Gonzalez, A. A. Serga, A. V. Chumak, P. A. Beck, B. Laegel, B. Hillebrands and K. Y. Guslienko, *Appl. Phys. Lett.*, 2011, **99**, 052512.
23 C. Granata and A. Vettoliere, *Phys. Rep.*, 2016, **614**, 1–69.
24 M. J. Martínez-Pérez and D. Koelle, *Phys. Sci. Rev.*, 2017, **2**, 20175001.
25 L. Embon, Y. Anahory, Ž. Jelić, E. O. Lachman, Y. Myasoedov, M. E. Huber, G. P. Mikitik, A. V. Silhanek, M. V. Milošević, A. Gurevich and E. Zeldov, *Nat. Commun.*, 2017, **8**, 85.
26 T. Schwarz, R. Wölbing, C. F. Reiche, B. Müller, M. J. Martínez-Pérez, T. Mühl, B. Büchner, R. Kleiner and D. Koelle, *Phys. Rev. Appl.*, 2015, **3**, 044011.
27 J. Nagel, K. B. Konovalenko, M. Kemmler, M. Turad, R. Werner, E. Kleisz, S. Menzel, R. Klingeler, B. Büchner, R. Kleiner and D. Koelle, *Supercond. Sci. Technol.*, 2011, **24**, 015015.
28 T. Schwarz, J. Nagel, R. Wölbing, M. Kemmler, R. Kleiner and D. Koelle, *ACS Nano*, 2013, **7**, 844–850.
29 D. Reyes, N. Biziere, B. Warot-Fonrose, T. Wade and C. Gatel, *Nano Lett.*, 2016, **16**, 1230–1236.
30 L. A. Rodríguez, C. Bran, D. Reyes, E. Berganza, M. Vázquez, C. Gatel, E. Snoeck and A. Asenjo, *ACS Nano*, 2016, **10**, 9669–9678.
31 E. Snoeck, R. E. Dunin-Borkowski, F. Dumestre, P. Renaud, C. Amiens, B. Chaudret and P. Zurcher, *Appl. Phys. Lett.*, 2003, **82**, 88–90.
32 Y. Aharonov and D. Bohm, *Phys. Rev.*, 1959, **115**, 485–491.
33 Disc1 and Disc2 correspond to particles #4 and #5 in ref. 10, respectively. There, the estimation of t_{mag} was done assuming that the particles are cylindrical yielding lower values of the magnetic thickness, *i.e.*, 11 and 10 nm, respectively.
34 K. Y. Guslienko, V. Novosad, Y. Otani, H. Shima and K. Fukamichi, *Phys. Rev. B: Condens. Matter Mater. Phys.*, 2001, **65**, 024414.
35 T. Fischbacher, M. Franchin, G. Bordignon and H. Fangohr, *IEEE Trans. Magn.*, 2007, **43**, 2896–2898.
36 K. L. Metlov and Y. Lee, *Appl. Phys. Lett.*, 2008, **92**, 112506.
37 J. Mejía-López, D. Altbir, P. Landeros, J. Escrig, A. H. Romero, I. V. Roshchin, C.-P. Li, M. R. Fitzsimmons,

X. Batlle and I. K. Schuller, *Phys. Rev. B: Condens. Matter Mater. Phys.*, 2010, **81**, 184417.
38 R. K. Dumas, K. Liu, C.-P. Li, I. V. Roshchin and I. K. Schuller, *Appl. Phys. Lett.*, 2007, **91**, 202501.
39 M. Grimsditch, E. E. Fullerton and R. L. Stamps, *Phys. Rev. B: Condens. Matter Mater. Phys.*, 1997, **56**, 2617–2622.
40 D. Wolf, L. A. Rodriguez, A. Béché, E. Javon, L. Serrano, C. Magen, C. Gatel, A. Lubk, H. Lichte, S. Bals, G. V. Tendeloo, A. Fernández-Pacheco, J. M. D. Teresa and E. Snoeck, *Chem. Mater.*, 2015, **27**, 6771–6778.
41 L. Néel, *Ann. Geophys.*, 1949, **5**, 99–136.
42 W. F. Brown, *Phys. Rev.*, 1963, **130**, 1677–1686.
43 J. Kurkijärvi, *Phys. Rev. B: Solid State*, 1972, **6**, 832–835.
44 A. Garg, *Phys. Rev. B: Condens. Matter Mater. Phys.*, 1995, **51**, 15592–15595.
45 L. Gunther and B. Barbara, *Phys. Rev. B: Condens. Matter Mater. Phys.*, 1994, **49**, 3926–3933.
46 K. Schultheiss, R. Verba, F. Wehrmann, K. Wagner, L. Körber, T. Hula, T. Hache, A. Kákay, A. A. Awad, V. Tiberkevich, A. N. Slavin, J. Fassbender and H. Schultheiss, *Phys. Rev. Lett.*, 2019, **122**, 097202.

Publication 5

ACSNANO
www.acsnano.org
ARTICLE

Three-Axis Vector Nano Superconducting Quantum Interference Device

María José Martínez-Pérez,*[,†] Diego Gella,[†] Benedikt Müller,[†] Viacheslav Morosh,[‡] Roman Wölbing,[†] Javier Sesé,[§] Oliver Kieler,[‡] Reinhold Kleiner,[†] and Dieter Koelle[†]

[†]Physikalisches Institut−Experimentalphysik II and Center for Quantum Science (CQ) in LISA⁺, Universität Tübingen, Auf der Morgenstelle 14, D-72076 Tübingen, Germany

[‡]Fachbereich Quantenelektronik, Physikalisch-Technische Bundesanstalt, Bundesallee 100, D-38116 Braunschweig, Germany

[§]Laboratorio de Microscopías Avanzadas (LMA), Instituto de Nanociencia de Aragón (INA), Universidad de Zaragoza, E-50018 Zaragoza, Spain

ABSTRACT: **We present the design, realization, and performance of a three-axis vector nano superconducting quantum interference device (nanoSQUID). It consists of three mutually orthogonal SQUID nanoloops that allow distinguishing the three components of the vector magnetic moment of individual nanoparticles placed at a specific position. The device is based on Nb/HfTi/Nb Josephson junctions and exhibits line widths of ∼250 nm and inner loop areas of 600 × 90 and 500 × 500 nm². Operation at temperature T = 4.2 K under external magnetic fields perpendicular to the substrate plane up to ∼50 mT is demonstrated. The experimental flux noise below ∼250 $n\Phi_0/\sqrt{Hz}$ in the white noise limit and the reduced dimensions lead to a total calculated spin sensitivity of ∼630 $\mu_B/\sqrt{Hz}$ and ∼70 $\mu_B/\sqrt{Hz}$ for the in-plane and out-of-plane components of the vector magnetic moment, respectively. The potential of the device for studying three-dimensional properties of individual nanomagnets is discussed.**

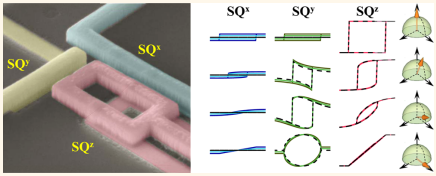

KEYWORDS: *nanoSQUID, superconductivity, nanofabrication, magnetic particle detection, three-axis magnetometry*

Gaining access to the magnetic properties of individual magnetic nanoparticles (MNPs) poses enormous technological challenges. As a reward, one does not have to cope with troublesome interparticle interactions or size-dependent dispersion effects, which facilitates enormously the interpretation of experimental results. Moreover, single-particle measurements give direct access to anisotropy properties of MNPs, which are hidden for measurements on ensembles of particles with a randomly distributed orientation.[1,2]

So far, different techniques have been developed and successfully applied to the investigation of individual MNPs or small local field sources in general. Most of these approaches rely on sensing the local stray magnetic field created by the sample under study, by using, for example, micro- or nanoSQUIDs,[3−26] micro-Hall magnetometers,[27,28] magnetic sensors based on nitrogen-vacancy centers in diamond,[29−31] or magnetic force microscopes.[5,13,32−34] Other probes, *e.g.*, cantilever and torque magnetometers,[5,13,32,35,36] are sensitive to the Lorentz force exerted by the external magnetic field on the whole MNP.

For all magnetometers mentioned above, information on just one vector component of the magnetic moment $\boldsymbol{\mu}$ of an MNP can be extracted. Yet, studies on the static and dynamic properties of individual MNPs would benefit enormously from the ability to distinguish simultaneously the three orthogonal components of $\boldsymbol{\mu}$. This is so since real nanomagnets are three-dimensional objects, usually well described by an easy axis of the magnetization, but often exhibiting additional hard/intermediate axes or higher order anisotropy terms. Magnetization reversal of real MNPs also occurs in a three-dimensional space, as described by the classical theories of uniform (Stoner−Wohlfarth)[37,38] and nonuniform spin rotation.[39] More complex dynamic mechanisms are also observed experimentally including the formation and evolution of topological magnetic states[13] and the nucleation and propagation of reversed domains.[5]

To date, few examples can be found in the literature in which three-axial detection of small magnetic signals has been achieved. This was done by combining planar and vertical microHall probes[40] or assembling together three single-axis SQUID microloops.[41,42] Further downsizing of these devices, which can significantly improve their sensitivity, is however still

Received: April 1, 2016
Accepted: June 22, 2016
Published: June 22, 2016

DOI: 10.1021/acsnano.6b02218
ACS Nano 2016, 10, 8308−8315

awaiting. This is mainly due to technical limitations in the fabrication of nanoscopic three-dimensional architectures.

Very recently, an encouraging step toward this direction has been achieved by fabricating a double-loop nanoSQUID, patterned on the apex of a nanopipet.[43] This device allowed distinguishing between the out-of-plane and in-plane components of the captured magnetic flux with ∼100 nm resolution, but only upon applying different external magnetic fields.

Here we present an ultrasensitive three-axis vector nanoSQUID, fabricated on a planar substrate and operating at temperature T = 4.2 K. The device is based on Nb/HfTi/Nb trilayer Josephson junctions.[44] This technology involves electron beam lithography and chemical−mechanical polishing, which offers a very high degree of flexibility in realizing complex nanoSQUID layouts. It allows the fabrication of planar gradiometers or stripline nanoSQUIDs, with sub-100 nm resolution, in which the loop lies parallel or perpendicular to the substrate plane.[11,45] Thanks to this flexibility, we have succeeded in fabricating three close-lying orthogonal nanoSQUID loops, allowing the simultaneous detection of the three vector components of $\boldsymbol{\mu}$ (μ_x, μ_y, μ_z) of an MNP placed at a specific position $\mathbf{r}_{NP}$. All three nanoSQUIDs operate independently, and their voltage (V)-to-flux (Φ) transfer function can be linearized by means of applying on-chip modulation currents I_{mod} for flux-locked loop (FLL) operation.[46] Additionally, moderate magnetic fields up to $\mu_0 H \approx 50$ mT can be applied perpendicular to the substrate plane, without degrading SQUID performance. These nanoSQUIDs exhibit a measured flux noise below 250 $n\Phi_0/\sqrt{Hz}$ in the white noise regime (above a few 100 Hz). The latter leads to spin sensitivities of ∼610, 650, and 70 $\mu_B/\sqrt{Hz}$ for the μ_x, μ_y, and μ_z components, respectively, of an MNP located at $\mathbf{r}_{NP}$ = (0,0,0) (Φ_0 is the magnetic flux quantum and μ_B is the Bohr magneton). As we demonstrate here, our device represents a valuable tool in the investigation of single MNPs, providing information on, for example, their three-dimensional anisotropy and the occurrence of coherent or nonuniform magnetic configurations.

RESULTS AND DISCUSSION

Sample Fabrication and Layout. A scheme of the three-axis nanoSQUID is shown in Figure 1a. Two perpendicular stripline nanoloops, SQ^x and SQ^y, are devoted to measure the x and y components of $\boldsymbol{\mu}$, respectively. The z component of the magnetic moment is sensed by a third planar first-order gradiometer, SQ^z, designed to be insensitive to uniform magnetic fields applied along $\hat{\mathbf{e}}_z$ but sensitive to the imbalance produced by a small magnetic signal in one of the two SQUID loops. Strictly speaking, the device reveals the three components of $\boldsymbol{\mu}$ only if the magnetic moment is placed at the intersection between the three nanoloop axes. In practice, this position approaches $\mathbf{r}_{NP}$ = (0,0,0), as indicated by a black dot in Figure 1a. We note that z = 0 corresponds to the interface of the upper Nb layer and the SiO_2 layer, which separates top and bottom Nb. Later on we will demonstrate that this constraint is actually flexible enough to realize three-axis magnetic detection of MNPs with finite volume, even if these are not positioned with extreme accuracy.

Figure 1b shows a false-colored scanning electron microscopy (SEM) image of a typical device. The junction barriers are made of normal metallic HfTi layers with thickness $d_{HfTi} \approx 22$ nm. The bottom and top Nb layers are, respectively, 160 and

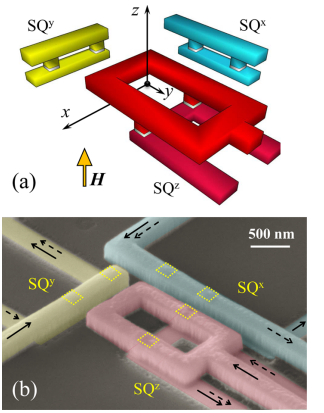

Figure 1. (a) Schematic representation of the three-axis vector nanoSQUID consisting of three mutually orthogonal nanoloops. SQ^x, SQ^y, and SQ^z are used to detect the μ_x, μ_y, and μ_z components, respectively, of the magnetic moment $\boldsymbol{\mu}$ of an MNP. The external magnetic field H is applied along $\hat{\mathbf{e}}_z$. (b) False-colored SEM image of a typical device. Yellow dashed squares indicate the position of the Josephson junctions. Black solid and dashed arrows indicate the direction of bias currents I_b and modulation currents I_{mod}, respectively.

200 nm thick and are separated by a 90 nm thick SiO_2 layer. Nb wirings are 250 nm wide, and the Josephson junctions are square-shaped with area 150 × 150 nm^2. The inner loop area of SQ^x and SQ^y corresponds to 600 × 90 nm^2, whereas SQ^z consists of two parallel-connected loops with an inner area of 500 × 500 nm^2. This configuration allows the application of moderate homogeneous magnetic fields along $\hat{\mathbf{e}}_z$ that do not couple any flux either to the nanoloops of SQ^x and SQ^y or to the junctions in the (x−y)-plane of all three nanoSQUIDs.

The bias currents I_b and modulation currents I_{mod} flow as indicated in Figure 1b by black solid and dashed arrows, respectively. The latter are used to couple flux to each nanoSQUID individually, so to linearize their flux-to-voltage transfer function in FLL operation.

Electric Transport and Noise Data. The Nb/HfTi/Nb junctions have typical critical current densities $j_c \approx 550$−850 kA/cm^2 at T = 4.2 K and resistance times junction area $\rho_n \approx 9$ $m\Omega\,\mu m^2$. As a result, large characteristic voltages up to $V_c = j_c\rho_n \approx 60$ μV can be obtained. These junctions are intrinsically shunted, providing, therefore, nonhysteretic current−voltage characteristics.[11,45]

Electric transport data of a typical device are shown in Figure 2. From the period of the maximum critical current $I_c(I_{mod})$ shown in panel (a) we can deduce the mutual inductance $M^i \equiv \Phi^i/I^i_{mod}$ between SQ^i and its corresponding modulation line (i = x, y, z). Asymmetries observed in these data for positive and negative bias current arise from the asymmetric distribution of I_b (see black solid arrows in Figure 1b). The strongest asymmetry is found for SQ^y, which is attributed to the sharp corner in the bottom Nb strip right below one of the two Josephson junctions (see Figure 1b, upper right junction of SQ^y). Numerically calculated curves based on the resistively

DOI: 10.1021/acsnano.6b02218
ACS Nano 2016, 10, 8308−8315

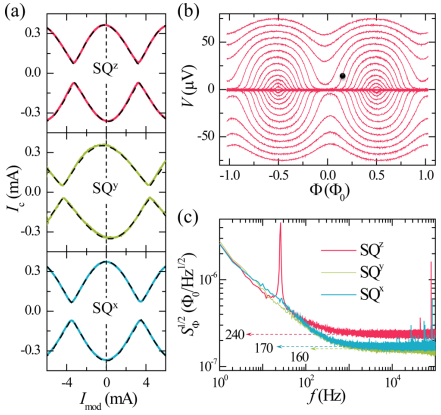

Figure 2. Transport and noise characteristics of device A2. (a) Measured (colored solid line) and simulated (black dashed line) modulation of the maximum critical current of the three nanoSQUIDs. (b) $V(\Phi)$ measured for SQ^z with $I_b = -466$ to 471 μA (in ~33.5 μA steps). The black dot indicates the optimum working point with $V_\Phi \approx 330\ \mu V/\Phi_0$ obtained for $I_b = 337\ \mu$A. (c) Spectral density of rms flux noise measured for all three nanoSQUIDs in FLL mode with an series array amplifier. Dashed arrows indicate the white noise values of $\sqrt{S_\Phi}$ in units of $n\Phi_0/\sqrt{Hz}$.

and capacitively shunted junction (RCSJ) model, including thermal noise, are fitted to these experimental data in order to estimate $\beta_L \equiv 2I_0L/\Phi_0$ and $I_c \equiv 2I_0$ (black dashed lines in Figure 2a). Here, I_0 is the average critical current of the two junctions intersecting the nanoloop, and L is its inductance. Asymmetric biasing is included in the model through an inductance asymmetry $\alpha_L \equiv (L_2 - L_1)/(L_1 + L_2)$, where L_1 and L_2 are the inductances of the two SQUID arms. On the other hand, the maximum transfer coefficient $V_\Phi \equiv \partial V/|\partial\Phi|_{max}$ can be experimentally determined by coupling Φ *via* I_{mod} and measuring the resulting $V(\Phi)$ for different I_b as shown in Figure 2b. Following this approach, we have characterized a number of devices, obtaining very low dispersion. A few examples are provided in Table 1, which gives evidence of the high quality and reproducibility of the fabrication process.

Finally, cross-talking between the three nanoSQUIDs can be quantified by the mutual inductances $M^{ij} = \Phi^i/I^j_{mod}$ $(i \neq j)$, *i.e.*, the flux Φ^i coupled to SQ^i by the modulation current I^j_{mod} in SQ^j. If the three orthogonal SQUIDs are operated in FLL, a signal Φ^j detected by SQ^j will be compensated by the feedback current $I^j_{mod} = \Phi^j/M^j$. This will also couple the (cross-talk) flux $\Phi^{ij} = \Phi^jM^{ij}/M^j$ to SQ^i. As M^{ij} is typically 2 orders of magnitude below M^j, this effect is negligible in most cases (see Methods section). Moreover, it can be avoided by operating the devices in open-loop readout.

The operation of the sensor upon externally applied magnetic fields $\mathbf{H} = H\hat{\mathbf{e}}_z$ was investigated as well. For this purpose, the output voltage response of all three nanoSQUIDs operating in FLL mode was recorded upon sweeping H for a number of devices. Under optimum conditions, a negligible flux is coupled to SQ^x and SQ^y, whereas, due to imperfect balancing, SQ^z couples ~5 $m\Phi_0/mT$. This imbalance results mainly from the asymmetric Nb wiring surrounding SQ^z and the intrinsic errors associated with the fabrication. All sensors are fully operative up to ~50 mT, where abrupt changes in the response of the device are observed. This behavior is attributed to the entrance of Abrikosov vortices in the Nb wires close to the nanoSQUIDs, as observed in similar devices.[11,32]

Figure 2c shows the spectral density of rms flux noise $\sqrt{S_\Phi}$ obtained with each nanoSQUID operating in FLL mode after low-temperature amplification using a commercial SQUID series array amplifier (SSA). The peak observed at $f = 26$ Hz for SQ^z is attributed to mechanical vibrations. Ubiquitous $1/f$ noise dominates $\sqrt{S_\Phi}$ for $f \lesssim 100$ Hz in all three spectra. Remarkably low values are obtained in the white region, yielding $\sqrt{S_\Phi} \approx 170$, 160, and 240 $n\Phi_0/\sqrt{Hz}$ for SQ^x, SQ^y, and SQ^z, respectively.

The flux noise can be translated into the spin sensitivity $\sqrt{S_\mu} \equiv \sqrt{S_\Phi}/\phi_\mu$, which is the figure of merit of nanoSQUID sensors. Here, the coupling factor $\phi_\mu \equiv \Phi_\mu/\mu$ is the magnetic flux Φ_μ per magnetic moment $\mu = |\boldsymbol{\mu}|$, which is coupled to the SQUID from an MNP with magnetic moment $\boldsymbol{\mu} = \mu\hat{\mathbf{e}}_\mu$ placed at position $\mathbf{r}$. The coupling factor can be calculated as $\phi_\mu(\hat{\mathbf{e}}_\mu\mathbf{r}) = \hat{\mathbf{e}}_\mu\cdot\mathbf{b}(\mathbf{r})$, where $\mathbf{b}(\mathbf{r}) \equiv \mathbf{B}_J/J$ is the normalized magnetic field created at position $\mathbf{r}$ by a supercurrent J circulating in the nanoloop.[47,48] We note that ϕ_μ depends on both the particle position $\mathbf{r}$ (relative to the nanoloop) and the orientation $\hat{\mathbf{e}}_\mu$ of its magnetic moment. We simulate $\mathbf{b}(\mathbf{r})$ by solving the London equations for the specific geometry of each nanoSQUID (see Methods section). For a particle at position $\mathbf{r}_{NP} = (0,0,0)$ (see

Table 1. Parameters Extracted from Simulations Based on the RCSJ Model and Experimentally Measured $1/M^i$ and V_Φ for Three Different Devices (A2, D5, and C3)

		$1/M^i$	I_0	V_c	β_L	L	α_L	V_Φ
		(mA/Φ_0)	(μA)	(μV)		(pH)		($\mu V/\Phi_0$)
A2	SQ^x	7.0	187	67	0.20	1.0	0	340
	SQ^y	8.8	176	62	0.14	0.8	0.60	390
	SQ^z	6.5	183	66	0.22	1.2	0.25	330
D5	SQ^x	7.7	136	57	0.14	1.1	0	250
	SQ^y	9.0	136	59	0.12	0.9	0.75	260
	SQ^z	5.7	145	58	0.16	1.1	0.35	240
C3	SQ^x	8.0	120	55	0.20	1.7	0	120
	SQ^y	9.1	128	54	0.32	2.6	0.40	110
	SQ^z	5.8	134	57	0.18	1.4	0.28	170

DOI: 10.1021/acsnano.6b02218
ACS Nano 2016, 10, 8308–8315

Figure 1a) we obtain for SQ^i spin sensitivities $\sqrt{S_\mu^i} \approx 610$, 650, and 70 $\mu_B/\sqrt{\text{Hz}}$ for $i = x, y, z$, respectively. The spin sensitivity for SQ^z is much better than for SQ^x and SQ^y, because $\mathbf{r}_{NP}$ is much closer to SQ^z than to SQ^x and SQ^y.

Analysis of Vector Magnetometer Performance. In the following we analyze the capability of this device to distinguish between the three components of $\boldsymbol{\mu}$. For this purpose we write the normalized field $\mathbf{b}^i = (b_x^i, b_y^i, b_z^i)$ created by each SQUID SQ^i as $\mathbf{b}^i = b_i^i\hat{\mathbf{e}}_i + b_\perp^i\hat{\mathbf{e}}_{\perp i}$; that is, we split this into a component along the i direction and a component perpendicular to that, with $b_{\perp i}^i = \sqrt{(b_j^i)^2 + (b_k^i)^2}$ $(i \neq j \neq k)$. Ideally, for each of the three SQUIDs SQ^i, $b_i^i = |\mathbf{b}^i| \equiv b^i$, *i.e.*, $b_{\perp i}^i = 0$. In that case, each SQUID SQ^i is sensitive to the component μ_i only, and one can reconstruct the magnitude μ and orientation $\hat{\mathbf{e}}_\mu$ from the signals detected by the three orthogonal SQUIDs.

To quantify the deviation from that ideal case, we define the relative error flux $\partial\Phi_\mu^i \equiv \Phi_{\mu,\perp i}^i/\Phi_{\mu,\|i}^i$ made by nanoSQUID SQ^i. Here, $\Phi_{\mu,\|i}^i \equiv \mu\hat{\mathbf{e}}_i\cdot\mathbf{b}^i = \mu b_i^i$ relates to the ideal case in which the moment $\boldsymbol{\mu}$ is oriented along $\hat{\mathbf{e}}_i$. In contrast, $\Phi_{\mu,\perp i}^i \equiv \mu\hat{\mathbf{e}}_{\perp i}\cdot\mathbf{b}^i = \mu b_{\perp i}^i$ corresponds to the worst case, when the moment is oriented along $\hat{\mathbf{e}}_{\perp i}$, which yields the maximum error. Hence, the relative error flux is given by

$$\partial\Phi_\mu^i \equiv \frac{\Phi_{\mu,\perp i}^i}{\Phi_{\mu,\|i}^i} = \frac{\sqrt{(b_j^i)^2 + (b_k^i)^2}}{b_i^i} \text{ (with } i \neq j \neq k)$$

This definition assures that $\partial\Phi_\mu^i$ does not depend on the orientation $\hat{\mathbf{e}}_\mu$ of the magnetic moment of the particle, but only on its position $\mathbf{r}_{NP}$.

The relative error flux for our device is first calculated at $\mathbf{r}_{NP} = (0,0,0)$, giving $\partial\Phi_\mu^x = \partial\Phi_\mu^y \approx 7\%$ and $\partial\Phi_\mu^z \approx 4\%$. Much better results can be obtained for SQ^x and SQ^y at $\mathbf{r}_{NP} = (0,0,-0.035)$ μm, giving $\partial\Phi_\mu^x = \partial\Phi_\mu^y \approx 0.11\%$ and $\partial\Phi_\mu^z \approx 6\%$. We note that this region becomes accessible after drilling a hole in the SiO_2 layer, which is feasible by means of, for example, focused ion beam milling.

We determine now deviations on the particle position that still lead to a tolerable level of error. For this purpose $\partial\Phi_\mu^i$ is calculated in the x–z-plane (at $y = 0$) as indicated in Figure 3a, b, and c. The results obtained for SQ^x, SQ^y, and SQ^z are shown in d, e, and f. The white line in these color plots corresponds to $\partial\Phi_\mu^i = 25\%$. As seen, SQ^y imposes more severe restrictions on the particle position. More specifically, $\partial\Phi_\mu^y \approx 10\%$ is obtained at $z = 0$ and $x \approx \pm 55$ nm, whereas 25% results at $x \approx \pm 170$ nm. Due to the symmetry of the problem, the behavior of SQ^x and SQ^y is interchanged if one considers the y–z-plane.

We finish by showing how this device can indeed serve to provide full insight on the three-dimensional properties of MNPs of finite size and the mechanisms that lead to the magnetization reversal. It will be instructive to start this discussion by focusing on the flux coupled by a point-like MNP to an ideal three-axis magnetometer; that is, we assume $\partial\Phi_\mu^i = 0$ for $i = x, y, z$. We consider for simplicity that the particle exhibits uniaxial anisotropy along a given direction $\hat{\mathbf{e}}_K$, so that magnetic states pointing along $\pm\hat{\mathbf{e}}_K$ are separated by an energy barrier. In that case, the particle will exhibit a typical hysteretic behavior when sweeping the external magnetic field $\mathbf{H} = H\hat{\mathbf{e}}_z$. This behavior will lead, however, to very different signals seen by each nanoSQUID, and those signals can strongly depend on the orientation of the easy axis with respect to the applied field direction. This is represented in Figure 4, where the flux Φ_μ^i

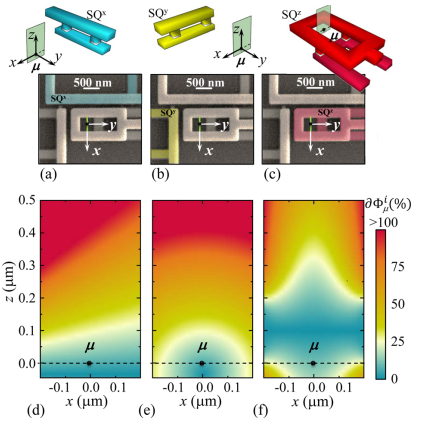

Figure 3. (a–c) SEM images of the device with SQ^x (a), SQ^y (b), and SQ^z (c) highlighted in false colors. The green line indicates the x–z-plane at $y = 0$ (shown schematically on top) for which the relative error $\partial\Phi_\mu^i$ obtained for SQ^x, SQ^y, and SQ^z is calculated in (d), (e), and (f), respectively. The device works as a three-axis vector magnetometer when $\boldsymbol{\mu}$ is placed in regions with a small $\partial\Phi_\mu^i$. Dashed lines correspond to $z = 0$ (interface between SiO_2 and top Nb layer).

coupled to SQ^i is plotted *vs* H for $i = x$ (a), y (b), z (c) (dashed black lines). The different panels correspond to different orientations of the easy axis, from $\hat{\mathbf{e}}_K = \hat{\mathbf{e}}_z$ (top) to $\hat{\mathbf{e}}_K = \hat{\mathbf{e}}_y$ (bottom), as sketched on the right side of Figure 4.

Let us first consider the case in which the easy axis points along the externally applied magnetic field, *i.e.*, $\hat{\mathbf{e}}_K = \hat{\mathbf{e}}_z$. As it can be seen, no flux is coupled to SQ^x and SQ^y, as $\boldsymbol{\mu}$ always lies parallel to $\hat{\mathbf{e}}_z$ whereas SQ^z senses the maximum amount of flux possible. In the latter case, abrupt steps correspond to the switching of $\boldsymbol{\mu}$ between the $\pm\mu\hat{\mathbf{e}}_z$ states, which leads to a typical square-shaped hysteresis curve. The situation changes dramatically if one assumes that the easy axis points perpendicular to $\mathbf{H} = H\hat{\mathbf{e}}_z$. Under these circumstances, the particle's magnetic moment tilts progressively as the external magnetic field is swept so that no abrupt steps are observed in the hysteresis curves. This is exemplified in the bottom panels of Figure 4, which result when $\hat{\mathbf{e}}_K = \hat{\mathbf{e}}_y$. As it can be seen, Φ_μ^x remains zero during the whole sweep, whereas $\Phi_\mu^y = 0$ is obtained only when the particle is saturated along $\hat{\mathbf{e}}_z$, leading to the maximum flux coupled by SQ^z. Remarkably, Φ_μ^y reaches a maximum (minimum) at $H = 0$ when $\boldsymbol{\mu} = +\mu\hat{\mathbf{e}}_y$ ($\boldsymbol{\mu} = -\mu\hat{\mathbf{e}}_y$), whereas Φ_μ^z accounts for the progressive tilting of $\boldsymbol{\mu}$ as H is swept. Intermediate situations result when the easy axis points along different directions in space, as exemplified in the middle panels.

Interestingly, a very similar behavior is observed when simulating a real experiment in which an extended MNP is measured using the three-axis nanoSQUID described here. To illustrate this, we have computed numerically Φ_μ^i when semispheres with radius $R = 50$ and 200 nm centered at position $\mathbf{r}_{NP} = (0,0,0)$ are considered (see Methods section). As it can be seen in Figure 4 (solid lines) finite $\partial\Phi_\mu^i \neq 0$ and the particle's volume does not noticeably affect the flux coupled to

DOI: 10.1021/acsnano.6b02218
ACS Nano 2016, 10, 8308–8315

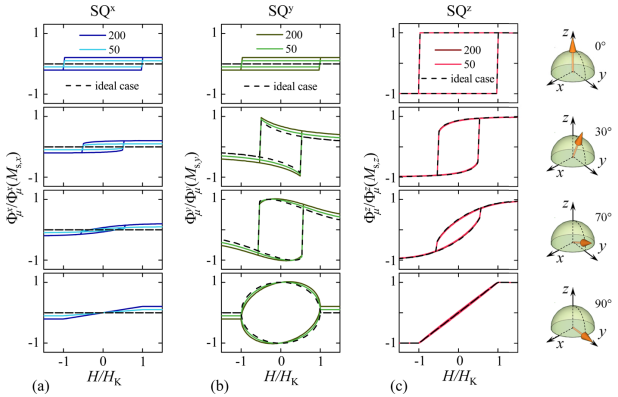

Figure 4. Simulated magnetic hysteresis curves of a nanoparticle with magnetic moment $\boldsymbol{\mu}$ located at $\mathbf{r}_{NP}$ = (0,0,0) as in Figure 3. The moment $\boldsymbol{\mu}$ couples magnetic flux $\boldsymbol{\Phi}^x_\mu$, $\boldsymbol{\Phi}^y_\mu$, and $\boldsymbol{\Phi}^z_\mu$ to SQ^x (a), SQ^y (b), and SQ^z (c), respectively. H = $H\hat{\mathbf{e}}_z$ with the particle's easy axis $\hat{\mathbf{e}}_K$ lying at 0°, 30°, 70°, and 90° (sketched on the right side of each panel). $\boldsymbol{\Phi}^j_\mu$ is normalized to the maximum possible flux in (a), (b), and (c) that is coupled when the particle is saturated along $\hat{\mathbf{e}}_x$ [$\boldsymbol{\Phi}^x_\mu(M_{s,x})$], $\hat{\mathbf{e}}_y$ [$\boldsymbol{\Phi}^y_\mu(M_{s,y})$], and $\hat{\mathbf{e}}_z$ [$\boldsymbol{\Phi}^z_\mu(M_{s,z})$], respectively ($M_s$ is the saturation magnetization). H is normalized to the anisotropy field H_K. Black dashed lines correspond to an "ideal" case in which a point-like particle is coupled to an ideal three-axis magnetometer ($\partial\boldsymbol{\Phi}^j_\mu$ = 0), whereas colored solid lines correspond to a "realistic"' situation in which semispheres of radius R = 50 and 200 nm are measured with the device presented here. MNPs are assumed to follow the Stoner−Wohlfarth model of magnetization reversal. Different values of R lead to a noticeably different behavior in (a) and (b), whereas all curves collapse into one in (c). This stems from the fact that larger particles occupy regions with larger $\partial\boldsymbol{\Phi}^x_\mu$ and $\partial\boldsymbol{\Phi}^y_\mu$, as shown in Figure 3d and e.

SQ^z, whereas it slightly changes the flux coupled to SQ^x and SQ^y. This behavior can be easily understood, as the spatial extension of relatively large particles still remains in the region confined below the white line in Figure 3f, whereas they occupy zones with larger $\partial\boldsymbol{\Phi}^x_\mu$ and $\partial\boldsymbol{\Phi}^y_\mu$ in panels d and e. Still, our simulations demonstrate the operation of the device as a three-axis vector magnetometer even if relatively large MNPs are investigated. The inspection of the hysteresis curves recorded simultaneously with all three nanoSQUIDs, together with the knowledge of the particle volume, allows extracting full information on the particle's anisotropy in a real experiment.

CONCLUSIONS

We have successfully fabricated three close-lying orthogonal nanoSQUIDs leading to the nanoscopic version of a three-axis vector magnetometer. All three nanoSQUIDs can be operated simultaneously in open- or flux-locked loop mode to sense the stray magnetic field produced by an individual MNP located at position $\mathbf{r}_{NP}$. The device operates at T = 4.2 K and is insensitive to the application of external magnetic fields perpendicular to the substrate plane (along $\hat{\mathbf{e}}_z$) up to ∼50 mT. The latter can be used to induce the magnetization reversal of the MNP under study. The limiting operation field can be increased in the future by improving the design. This implies reducing the line widths so to increase the critical field for vortex entry and improving the balancing of the gradiometric nanoSQUID.

We have demonstrated the ability of this device to distinguish between the three orthogonal components of the vector magnetic moment by calculating the spatial dependence of the total relative error flux. The latter yields values below 10% for particles located at $|r_{NP}| \leq 55$ nm. For r_{NP} = (0,0,0) we obtain a total spin sensitivity ∼610, 650, and 70 $\mu_B/\sqrt{\text{Hz}}$ for the x, y, and z components of $\boldsymbol{\mu}$, respectively. Finally, a model case has been described in which the three-axis vector nanoSQUID can be used to obtain full insight into the three-dimensional anisotropy of an extended MNP with diameter ∼100−400 nm. For this purpose, the signal captured by each nanoSQUID is used to reconstruct the magnitude and orientation of the magnetic moment during the magnetization reversal.

METHODS

Sample Fabrication. The fabrication combines electron-beam lithography (EBL) and chemical−mechanical polishing (CMP).[44] A Si wafer with a 300 nm thick thermally oxidized layer is used as a substrate. An Al_2O_3 etch stop layer is first deposited by RF sputtering. Then, the SNS trilayer consisting of Nb/$Hf_{50\ wt\ \%}Ti_{50\ wt\ \%}$/Nb is sputtered *in situ*. The next step serves to define the SNS Josephson junctions by means of an Al etching mask defined by EBL and lift-off. The pattern is transferred to the Nb/HfTi/Nb trilayer through reactive ion etching (RIE) in a SF_6 plasma and Ar ion beam acting on the counter Nb and HfTi layers, respectively. The bottom Nb layer is directly patterned using a negative EBL resist mask and SF_6-based RIE. In the following step, a 600 nm thick layer of insulating SiO_2 is deposited through plasma-enhanced chemical vapor deposition and subsequently polished through CMP. This process guarantees good wafer smoothing and electric contact to the Nb counter electrodes. In the last step, the wiring Nb layer is sputtered and patterned using an EBL Al etching mask and SF_6-based RIE.

Measurement of Electric Transport Properties and Noise. Current bias is performed by means of battery-powered low-noise current sources, and the output voltage is amplified at room temperature. Each single nanoSQUID can be operated in flux-locked loop mode simultaneously, by using commercial three-channel SQUID readout electronics. Additionally, the output signal can be amplified at low temperatures using commercial SQUID series array amplifiers. High-field measurements are performed in a cryostat hosting a vector magnet, whereas noise measurements are performed in a magnetically and high-frequency shielded environment. All measurements described

DOI: 10.1021/acsnano.6b02218
ACS Nano 2016, 10, 8308−8315

Table 2. Calculated Flux Signals Φ^i_μ and Cross-Talk Signals Φ^{ij} for Two Different Values of R and Parameters Used for Calculating Cross-Talk Signals: Average $\overline{M}^i$ (from Values in Table 1) and M^{ij} Measured for Device D5

					R = 50 nm				R = 200 nm			
	$\overline{M}^i$	M^{ij}			Φ^i_μ	Φ^{ij}			Φ^i_μ	Φ^{ij}		
	(Φ_0/A)	(Φ_0/A)			(mΦ_0)	(mΦ_0)			(mΦ_0)	(mΦ_0)		
j		x	y	z		x	y	z		x	y	z
SQ^x	132		0.49	1.2	10		0.044	1.4	600		2.6	72
SQ^y	112	1.5		0.82	10	0.11		0.98	600	6.8		49
SQ^z	167	1.4	6.1		200	0.11	0.55		10^4	6.4	33	

here were performed with the devices immersed in liquid ^{4}He, at T = 4.2 K.

Numerical Simulations. Fitting of the $I_c(I_{mod})$ experimental data is based on the RCSJ model.[49] The response of the SQUID is described by two coupled Langevin equations: $i/2 + j = \beta_c\ddot{\delta}_1 + \dot{\delta}_1 + \sin\delta_1 + i_{N1}$ and $i/2 - j = \beta_c\ddot{\delta}_2 + \dot{\delta}_2 + \sin\delta_2 + i_{N2}$. Here, $\delta_k(t)$ is the phase difference for the two junctions (k = 1, 2) and i and j are respectively the bias and circulating currents normalized to I_0. Nyquist noise is included through two independent normalized current noise sources i_{Nk}. Additionally, $j\beta_L = (\delta_2 - \delta_1)/\pi - 2\varphi_{ext} + \alpha_L\beta_L i/2$, where φ_{ext} is the external flux normalized to Φ_0. Finally, $\beta_L \equiv 2I_0L/\Phi_0$, $\beta_c \equiv 2\pi I_0R^2C/\Phi_0$, $\alpha_L \equiv (L_2 - L_1)/(L_1 + L_2)$, and R and C are the resistance and capacitance of the SQUID, respectively. In the model, the total inductance of the loop $L = L_1 + L_2$ accounts for both the geometrical and the kinetic contributions. The total dc voltage across the SQUID (V) is calculated as the time average $V = \frac{1}{2}\langle U_1 + U_2\rangle$, where $U_k(t) = \frac{\Phi_0}{2\pi}\dot{\delta}_k(t)$. We emphasize here that the magnitude of β_c does not affect the modulation of $I_c(I_{mod})$ and, therefore, our estimation of β_L and I_c. In all fittings β_c = 0.5 has been assumed for convenience, as in Chesca *et al.*[49]

For the estimation of the spin sensitivity and the relative error flux one needs to calculate the spatial distribution of $\mathbf{B}^i_j$ created by each SQ^i_j. For this purpose we have used the numerical simulation software 3D-MLSI,[50] which is based on a finite element method to solve the London equations in a superconductor with a given geometry, film thickness, and London penetration depth (λ_L = 90 nm). $\mathbf{b}^x(\mathbf{r}) = \mathbf{B}^x_j/J$ and $\mathbf{b}^y(\mathbf{r}) = \mathbf{B}^y_j/J$ with J being the supercurrent in the nanoloop. For SQ^z one needs to consider two circular currents $\pm J$ flowing around each nanoloop. The resulting normalized magnetic field is, in this case, $\mathbf{b}^z(\mathbf{r}) = \mathbf{B}^z_j/2J$.

For the simulation of the hysteresis curves we consider first an ideal point-like MNP with magnetic moment $\boldsymbol{\mu}$ described by the polar coordinates $\hat{\mathbf{e}}_\mu = (1,\theta,\varphi)$ and characterized by one second-order anisotropy term. If both $\boldsymbol{H}$ and the easy axis lie in the y–z-plane, the problem is reduced to the minimization of $e = \sin^2\phi - 2h\cos(\phi + \Psi)$ in two dimensions (φ = 90°). Here $e = E/U$ is the total energy normalized to the anisotropy barrier height, $h = H/H_K$ is the field normalized to the anisotropy field, Ψ is the angle between $\mathbf{H}$ and the easy axis, and $\phi = \theta - \Psi$ is the angle between $\boldsymbol{\mu}$ and the easy axis. Solutions of $\partial e/\partial\phi = \partial e^2/\partial^2\phi = 0$ for Ψ = 0°, 30°, 70°, and 90° yield the values of

$$\frac{\Phi^i_\mu}{\Phi^i_\mu(M_{s,i})} = \frac{\hat{\mathbf{e}}_\mu\mathbf{b}^i(\mathbf{r}_{NP})}{\hat{\mathbf{e}}_i\mathbf{b}^i(\mathbf{r}_{NP})}$$

plotted in Figure 4. Notice that, in this case, $\partial\Phi^i_\mu = 0$ so that $\mathbf{b}^i(\mathbf{r}_{NP}) = \hat{\mathbf{e}}_i b^i$, leading to $\Phi^x_\mu/\Phi^x_\mu(M_{s,x}) = 0$, $\Phi^y_\mu/\Phi^y_\mu(M_{s,y}) = \sin\theta$, and $\Phi^z_\mu/\Phi^z_\mu(M_{s,z}) = \cos\theta$.

For the simulation of extended particles we assume that all magnetic moments lie parallel to each other during the magnetization reversal. In this way, the exchange energy can be neglected and the expression for e given above is still valid (Stoner–Wohlfarth model). Here, the second-order anisotropy term might also account for the shape anisotropy introduced by the magnetostatic energy. In this case one needs to integrate over the volume (V_{NP}) of the whole MNP, leading to

$$\frac{\Phi^i_\mu}{\Phi^i_\mu(M_{s,i})} = \frac{\int_{V_{NP}}\hat{\mathbf{e}}_\mu\mathbf{b}^i(\mathbf{r})\,dV}{\int_{V_{NP}}\hat{\mathbf{e}}_i\mathbf{b}^i(\mathbf{r})\,dV}$$

Assuming, for example, a semisphere made of hcp cobalt (μ = 1.7 μ_B/atom and density 8.9 g/cm^3), one obtains $\Phi^x_\mu(M_{s,x}) = \Phi^y_\mu(M_{s,y}) \approx 10$ mΦ_0 and $\Phi^z_\mu(M_{s,z}) \approx 200$ mΦ_0 for R = 50 nm and $\Phi^x_\mu(M_{s,x}) = \Phi^y_\mu(M_{s,y}) \approx 0.6\ \Phi_0$ and $\Phi^z_\mu(M_{s,z}) \approx 10\ \Phi_0$ for R = 200 nm. For these specific examples, we can compare the flux signals Φ^i_μ quoted above with the corresponding cross-talk signals $\Phi^{ij} = \Phi^i_\mu M^{ij}/M^i$ appearing in FLL operation. For the calculation of Φ^{ij}, we used the experimentally determined values for M^{ij} of device D5 and the average values $\overline{M}^i$ obtained from the measured values of all three devices A2, D5, and C3 (from Table 1). These values are listed in Table 2 together with Φ^i_μ and Φ^{ij}. We find that the cross-talk in FLL operation is on the percent level or even below, except for Φ^{xz} and Φ^{yz}, where it is around 10%.

AUTHOR INFORMATION

Corresponding Author

*E-mail: mariajose.martinez@uni-tuebingen.de.

Notes

The authors declare no competing financial interest.

ACKNOWLEDGMENTS

M.J.M.-P. acknowledges support by the Alexander von Humboldt Foundation. D.G. acknowledges support by the EU-FP6-COST Action MP1201. This work is supported by the Nachwuchswissenschaftlerprogramm of the Universität Tübingen, by the Deutsche Forschungsgemeinschaft (DFG) via Projects KO 1303/13-1, KI 698/3-1, and SFB/TRR 21 C2, and by the EU-FP6-COST Action MP1201.

REFERENCES

(1) Martínez-Pérez, M. J.; de Miguel, R.; Carbonera, C.; Martínez-Júlvez, M.; Lostao, A.; Piquer, C.; Gómez-Moreno, C.; Bartolomé, J.; Luis, F. Size-Dependent Properties of Magnetoferritin. *Nanotechnology* **2010**, *21*, 465707.

(2) Silva, N. J. O.; Amaral, V. S.; Carlos, L. D. Relevance of Magnetic Moment Distribution and Scaling Law Methods to Study the Magnetic Behavior of Antiferromagnetic Nanoparticles: Application to Ferritin. *Phys. Rev. B: Condens. Matter Mater. Phys.* **2005**, *71*, 184408.

(3) Granata, C.; Vettoliere, A. Nano Superconducting Quantum Interference Device: A Powerful Tool for Nanoscale Investigations. *Phys. Rep.* **2016**, *614*, 1–69.

(4) Schwarz, T.; Wölbing, R.; Reiche, C. F.; Müller, B.; Martínez-Pérez, M. J.; Mühl, T.; Büchner, B.; Kleiner, R.; Koelle, D. Low-Noise $YBa_2Cu_3O_7$ Nano-SQUIDs for Performing Magnetization-Reversal Measurements on Magnetic Nanoparticles. *Phys. Rev. Appl.* **2015**, *3*, 044011.

(5) Buchter, A.; Wölbing, R.; Wyss, M.; Kieler, O. F.; Weimann, T.; Kohlmann, J.; Zorin, A. B.; Rüffer, D.; Matteini, F.; Tütüncüoglu, G.; et al. Magnetization Reversal of an Individual Exchange-Biased Permalloy Nanotube. *Phys. Rev. B: Condens. Matter Mater. Phys.* **2015**, *92*, 214432.

DOI: 10.1021/acsnano.6b02218
ACS Nano 2016, 10, 8308–8315

(6) Shibata, Y.; Nomura, S.; Kashiwaya, H.; Kashiwaya, S.; Ishiguro, R.; Takayanagi, H. Imaging of Current Density Distributions with a Nb Weak-Link Scanning Nano-SQUID Microscope. *Sci. Rep.* **2015**, *5*, 15097.
(7) Schmelz, M.; Matsui, Y.; Stolz, R.; Zakosarenko, V.; Schönau, T.; Anders, S.; Linzen, S.; Itozaki, H.; Meyer, H.-G. Investigation of All Niobium Nano-SQUIDs Based on Sub-Micrometer Cross-Type Josephson Junctions. *Supercond. Sci. Technol.* **2015**, *28*, 015004.
(8) Vasyukov, D.; Anahory, Y.; Embon, L.; Halbertal, D.; Cuppens, J.; Neeman, L.; Finkler, A.; Segev, Y.; Myasoedov, Y.; Rappaport, M. L.; et al. A Scanning Superconducting Quantum Interference Device with Single Electron Spin Sensitivity. *Nat. Nanotechnol.* **2013**, *8*, 639.
(9) Arpaia, R.; Arzeo, M.; Nawaz, S.; Charpentier, S.; Lombardi, F.; Bauch, T. Ultra Low Noise $YBa_2Cu_3O_{7-\delta}$ Nano Superconducting Quantum Interference Devices Implementing Nanowires. *Appl. Phys. Lett.* **2014**, *104*, 072603.
(10) Hazra, D.; Kirtley, J. R.; Hasselbach, K. Nano-Superconducting Quantum Interference Devices with Suspended Junctions. *Appl. Phys. Lett.* **2014**, *104*, 152603.
(11) Wölbing, R.; Nagel, J.; Schwarz, T.; Kieler, O.; Weimann, T.; Kohlmann, J.; Zorin, A. B.; Kemmler, M.; Kleiner, R.; Koelle, D. Nb Nano Superconducting Quantum Interference Devices with High Spin Sensitivity for Operation in Magnetic Fields up to 0.5T. *Appl. Phys. Lett.* **2013**, *102*, 192601.
(12) Levenson-Falk, E. M.; Vijay, R.; Antler, N.; Siddiqi, I. A Dispersive NanoSQUID Magnetometer for Ultra-Low Noise, High Bandwidth Flux Detection. *Supercond. Sci. Technol.* **2013**, *26*, 055015.
(13) Buchter, A.; Nagel, J.; Rüffer, D.; Xue, F.; Weber, D. P.; Kieler, O. F.; Weimann, T.; Kohlmann, J.; Zorin, A. B.; Russo-Averchi, E.; et al. Reversal Mechanism of an Individual Ni Nanotube Simultaneously Studied by Torque and SQUID Magnetometry. *Phys. Rev. Lett.* **2013**, *111*, 067202.
(14) Bellido, E.; González-Monje, P.; Repollés, A.; Jenkins, M.; Sesé, J.; Drung, D.; Schurig, T.; Awaga, K.; Luis, F.; Ruiz-Molina, D. Mn_{12} Single Molecule Magnets Deposited on μ-SQUID Sensors: the Role of Interphases and Structural Modifications. *Nanoscale* **2013**, *5*, 12565−12573.
(15) Granata, C.; Vettoliere, A.; Russo, R.; Fretto, M.; De Leo, N.; Lacquaniti, V. Three-Dimensional Spin Nanosensor Based on Reliable Tunnel Josephson Nano-Junctions for Nanomagnetism Investigations. *Appl. Phys. Lett.* **2013**, *103*, 102602.
(16) Martínez-Pérez, M. J.; Bellido, E.; de Miguel, R.; Sesé, J.; Lostao, A.; Gómez-Moreno, C.; Drung, D.; Schurig, T.; Ruiz-Molina, D.; Luis, F. Alternating Current Magnetic Susceptibility of a Molecular Magnet Submonolayer Directly Patterned onto a Micro Superconducting Quantum Interference Device. *Appl. Phys. Lett.* **2011**, *99*, 032504.
(17) Hao, L.; Aßmann, C.; Gallop, J. C.; Cox, D.; Ruede, F.; Kazakova, O.; Josephs-Franks, P.; Drung, D.; Schurig, T. Detection of Single Magnetic Nanobead with a Nano-Superconducting Quantum Interference Device. *Appl. Phys. Lett.* **2011**, *98*, 092504.
(18) Kirtley, J. R. Fundamental Studies of Superconductors Using Scanning Magnetic Imaging. *Rep. Prog. Phys.* **2010**, *73*, 126501.
(19) Giazotto, F.; Peltonen, J. T.; Meschke, M.; Pekola, J. P. Superconducting Quantum Interference Proximity Transistor. *Nat. Phys.* **2010**, *6*, 254−259.
(20) Vohralik, P. F.; Lam, S. K. H. NanoSQUID Detection of Magnetization from Ferritin Nanoparticles. *Supercond. Sci. Technol.* **2009**, *22*, 064007.
(21) Huber, M. E.; Koshnick, N. C.; Bluhm, H.; Archuleta, L. J.; Azua, T.; Björnsson, P. G.; Gardner, B. W.; Halloran, S. T.; Lucero, E. A.; Moler, K. A. Gradiometric Micro-SQUID Susceptometer for Scanning Measurements of Mesoscopic Samples. *Rev. Sci. Instrum.* **2008**, *79*, 053704.
(22) Hao, L.; Macfarlane, J. C.; Gallop, J. C.; Cox, D.; Beyer, J.; Drung, D.; Schurig, T. Measurement and Noise Performance of Nano-Superconducting-Quantum-Interference Devices Fabricated by Focused Ion Beam. *Appl. Phys. Lett.* **2008**, *92*, 192507.
(23) Wernsdorfer, W. Classical and Quantum Magnetization Reversal Studied in Nanometersized Particles and Clusters. *Adv. Chem. Phys.* **2001**, *118*, 99−190.
(24) Jamet, M.; Wernsdorfer, W.; Thirion, C.; Mailly, D.; Dupuis, V.; Mélinon, P.; Pérez, A. Magnetic Anisotropy of a Single Cobalt Nanocluster. *Phys. Rev. Lett.* **2001**, *86*, 4676−4679.
(25) Wernsdorfer, W.; Hasselbach, K.; Mailly, D.; Barbara, B.; Benoit, A.; Thomas, L.; Suran, G. Dc-SQUID Magnetization Measurements of Single Magnetic Particles. *J. Magn. Magn. Mater.* **1995**, *145*, 33−39.
(26) Awschalom, D. D.; Smyth, J. F.; Grinstein, G.; DiVincenzo, D. P.; Loss, D. Macroscopic Quantum Tunneling in Magnetic Proteins. *Phys. Rev. Lett.* **1992**, *68*, 3092−3095.
(27) Lipert, K.; Bahr, S.; Wolny, F.; Atkinson, P.; Weißker, U.; Mühl, T.; Schmidt, O. G.; Büchner, B.; Klingeler, R. An Individual Iron Nanowire-Filled Carbon Nanotube Probed by Micro-Hall Magnetometry. *Appl. Phys. Lett.* **2010**, *97*, 212503.
(28) Kent, A. D.; von Molnár, S.; Gider, S.; Awschalom, D. D. Properties and Measurement of Scanning Tunneling Microscope Fabricated Ferromagnetic Particle Arrays. *J. Appl. Phys.* **1994**, *76*, 6656−6660.
(29) Thiel, L.; Rohner, D.; Ganzhorn, M.; Appel, P.; Neu, E.; Müller, B.; Kleiner, R.; Koelle, D.; Maletinsky, P. Quantitative Nanoscale Vortex Imaging Using a Cryogenic Quantum Magnetometer. *Nat. Nanotechnol.* **2016**, DOI: 10.1038/nnano.2016.63.
(30) Schäfer-Nolte, E.; Schlipf, L.; Ternes, M.; Reinhard, F.; Kern, K.; Wrachtrup, J. Tracking Temperature-Dependent Relaxation Times of Ferritin Nanomagnets with a Wideband Quantum Spectrometer. *Phys. Rev. Lett.* **2014**, *113*, 217204.
(31) Rondin, L.; Tetienne, J. P.; Rohart, S.; Thiaville, A.; Hingant, T.; Spinicelli, P.; Roch, J. F.; Jacques, V. Stray-Field Imaging of Magnetic Vortices With a Single Diamond Spin. *Nat. Commun.* **2013**, *4*, 2279.
(32) Nagel, J.; Buchter, A.; Xue, F.; Kieler, O. F.; Weimann, T.; Kohlmann, J.; Zorin, A. B.; Rüffer, D.; Russo-Averchi, E.; Huber, R.; et al. Nanoscale Multifunctional Sensor Formed by a Ni Nanotube and a Scanning Nb NanoSQUID. *Phys. Rev. B: Condens. Matter Mater. Phys.* **2013**, *88*, 064425.
(33) Rugar, D.; Budakian, R.; Mamin, H. J.; Chui, B. W. Single Spin Detection by Magnetic Resonance Force Microscopy. *Nature* **2004**, *430*, 329−332.
(34) Shinjo, T.; Okuno, T.; Hassdorf, R.; Shigeto, K.; Ono, T. Magnetic Vortex Core Observation in Circular Dots of Permalloy. *Science* **2000**, *289*, 930−932.
(35) Ganzhorn, M.; Klyatskaya, S.; Ruben, M.; Wernsdorfer, W. Carbon Nanotube Nanoelectromechanical Systems as Magnetometers for Single-Molecule Magnets. *ACS Nano* **2013**, *7*, 6225−6236.
(36) Stipe, B. C.; Mamin, H. J.; Stowe, T. D.; Kenny, T. W.; Rugar, D. Magnetic Dissipation and Fluctuations in Individual Nanomagnets Measured by Ultrasensitive Cantilever Magnetometry. *Phys. Rev. Lett.* **2001**, *86*, 2874−2877.
(37) Thiaville, A. Coherent Rotation of Magnetization in Three Dimensions: A Geometrical Approach. *Phys. Rev. B: Condens. Matter Mater. Phys.* **2000**, *61*, 12221−12232.
(38) Stoner, E. C.; Wohlfarth, E. P. A Mechanism of Magnetic Hysteresis in Heterogeneous Alloys. *Philos. Trans. R. Soc., A* **1948**, *240*, 599−642.
(39) Aharoni, A. Magnetization Curling. *Phys. Status Solidi B* **1966**, *16*, 3−42.
(40) Schott, C.; Waser, J.-M.; Popovic, R. S. Single-Chip 3-D Silicon Hall Sensor. *Sens. Actuators, A* **2000**, *82*, 167−173.
(41) Miyajima, S.; Okamoto, T.; Matsumoto, H.; Huy, H.; Hayashi, M.; Maezawa, M.; Hidaka, M.; Ishida, T. Vector Pickup System Customized for Scanning SQUID Microscopy. *IEEE Trans. Appl. Supercond.* **2015**, *25*, 1600704.
(42) Ketchen, M.; Kirtley, J.; Bhushan, M. Miniature Vector Magnetometer for Scanning SQUID Microscopy. *IEEE Trans. Appl. Supercond.* **1997**, *7*, 3139−3142.
(43) Anahory, Y.; Reiner, J.; Embon, L.; Halbertal, D.; Yakovenko, A.; Myasoedov, Y.; Rappaport, M. L.; Huber, M. E.; Zeldov, E. Three-

DOI: 10.1021/acsnano.6b02218
ACS Nano 2016, 10, 8308−8315

Junction SQUID-on-Tip with Tunable In-Plane and Out-of-Plane Magnetic Field Sensitivity. *Nano Lett.* **2014**, *14*, 6481−6487.
(44) Hagedorn, D.; Kieler, O.; Dolata, R.; Behr, R.; Müller, F.; Kohlmann, J.; Niemeyer, J. Modified Fabrication of Planar Sub-μm Superconductor-Normal Metal-Superconductor Josephson Junctions for Use in a Josephson Arbitrary Waveform Synthesizer. *Supercond. Sci. Technol.* **2006**, *19*, 294−298.
(45) Nagel, J.; Kieler, O. F.; Weimann, T.; Wölbing, R.; Kohlmann, J.; Zorin, A. B.; Kleiner, R.; Koelle, D.; Kemmler, M. Superconducting Quantum Interference Devices with Submicron Nb/HfTi/Nb Junctions for Investigation of Small Magnetic Particles. *Appl. Phys. Lett.* **2011**, *99*, 032506.
(46) Drung, D. High-T_c and Low-T_c Dc SQUID Electronics. *Supercond. Sci. Technol.* **2003**, *16*, 1320−1336.
(47) Wölbing, R.; Schwarz, T.; Müller, B.; Nagel, J.; Kemmler, M.; Kleiner, R.; Koelle, D. Optimizing the Spin Sensitivity of Grain Boundary Junction NanoSQUIDs - Towards Detection of Small Spin Systems with Single-Spin Resolution. *Supercond. Sci. Technol.* **2014**, *27*, 125007.
(48) Nagel, J.; Konovalenko, K. B.; Kemmler, M.; Turad, M.; Werner, R.; Kleisz, E.; Menzel, S.; Klingeler, R.; Büchner, B.; Kleiner, R.; et al. Resistively Shunted $YBa_2Cu_3O_7$ Grain Boundary Junctions and Low-Noise SQUIDs Patterned by a Focused Ion Beam Down to 80 nm Linewidth. *Supercond. Sci. Technol.* **2011**, *24*, 015015.
(49) Chesca, B.; Kleiner, R.; Koelle, D. In *The SQUID Handbook*; Clarke, J., Braginski, A. I., Eds.; Wiley-VCH: Weinheim, 2004; Vol. *1*; Chapter 2, pp 29−92.
(50) Khapaev, M. M.; Kupriyanov, M. Y.; Goldobin, E.; Siegel, M. Current Distribution Simulation for Superconducting Multi-Layered Structures. *Supercond. Sci. Technol.* **2003**, *16*, 24.

DOI: 10.1021/acsnano.6b02218
ACS Nano 2016, 10, 8308−8315

Publication 6

Josephson Junctions and SQUIDs Created by Focused Helium-Ion-Beam Irradiation of $YBa_2Cu_3O_7$

B. Müller,[1,*] M. Karrer,[1] F. Limberger,[1] M. Becker,[1,2] B. Schröppel,[2] C.J. Burkhardt,[2] R. Kleiner,[1] E. Goldobin,[1] and D. Koelle[1]

[1] *Physikalisches Institut – Experimentalphysik II and Center for Quantum Science (CQ) in LISA+, University of Tübingen, Auf der Morgenstelle 14, Tübingen 72076, Germany*

[2] *NMI Natural and Medical Sciences Institute at the University of Tübingen, Markwiesenstraße 55, Reutlingen 72770, Germany*

(Received 25 January 2019; published 25 April 2019)

By scanning with a 30-keV focused He ion beam (He-FIB) across $YBa_2Cu_3O_7$ (YBCO) thin-film microbridges, we create Josephson barriers with critical current density j_c adjustable by irradiation dose D. The dependence $j_c(D)$ yields an exponential decay. At 4.2 K, a transition from flux-flow to Josephson behavior occurs when j_c decreases below approximately 2 MA/cm^2. The Josephson junctions exhibit current-voltage characteristics (IVCs) that are well described by the resistively and capacitively shunted junction model, without excess current for characteristic voltages $V_c \lesssim 1$ mV. Devices on MgO and LSAT substrates show nonhysteretic IVCs, while devices on $SrTiO_3$ show a small hysteresis. For all junctions, an approximate scaling $V_c \propto j_c^{1/2}$ is found. He-FIB irradiation with a high dose produces barriers with $j_c = 0$ and high resistances of 10 kΩ to 1 GΩ. This provides the possibility to write highly resistive walls or areas into YBCO using a He-FIB. Transmission electron microscopy reveals an amorphous phase within the walls, whereas for lower doses the YBCO stays crystalline. We have also "drawn" superconducting quantum-interference devices (SQUIDs) by using a He-FIB for the definition of the SQUID hole and the junctions. The SQUIDs show high performance, with flux noise $< 500\ n\Phi_0/Hz^{1/2}$ in the thermal white-noise limit for a device with 19 pH inductance.

DOI: 10.1103/PhysRevApplied.11.044082

I. INTRODUCTION

Josephson junctions (JJs), i.e., weak links between two superconducting electrodes [1], are key elements in superconducting electronic circuits and are used both for basic studies of superconductivity and for many applications [2,3]. For conventional metallic superconductors, a mature trilayer thin-film technology based on Nb electrodes, separated by insulating or normal conducting barriers, has been well established for decades. This technology offers fabrication of JJs on a wafer scale with a small spread of characteristic parameters, such as critical current density j_0 and normal resistance times area ρ_n, even with lateral JJ size well below 1 μm [4,5].

For the high-transition temperature (high-T_c) cuprate superconductors, JJ technology is much less mature. Because of the complex nature of these materials, and in particular their small coherence length associated with strong sensitivity to defects on the atomic scale, a reliable trilayer JJ technology does not exist so far. On the other hand, the peculiar properties of cuprate superconductors, such as high T_c, large upper critical field, large energy gap, and d-wave symmetry of the superconducting order parameter, can provide major advantages, if JJ devices and circuits can be realized with sufficient control over JJ parameters. Promising examples are, e.g., in the field of terahertz generation [6], self-biased rapid single flux quantum circuits [7], or magnetometry based on superconducting quantum-interference devices (SQUIDs) [8,9].

Apart from intrinsic JJs in stacks of $Bi_2Sr_2CaCu_2O_{8+\delta}$ single crystals, used for terahertz generation [6], most developed cuprate JJs are based on epitaxially grown $YBa_2Cu_3O_{7-\delta}$ (YBCO) thin films with $T_c \approx 90$ K that also offer operation with cryocoolers or liquid nitrogen; a large variety of JJ types have been developed and their properties have been investigated [10–13].

Until recently, the most reliable, simple, and most frequently used high-T_c JJs have been YBCO grain-boundary (GB) JJs [11]. They are usually fabricated by the epitaxial growth of YBCO films on (rather expensive) bicrystal substrates from only a few materials. The GBJJs can be placed only along the single GB line, which not only imposes topological limitations, but also limits the complexity of feasible circuits. The more advanced biepitaxial

*benedikt.mueller@uni-tuebingen.de

technique allows one to fabricate so-called tilt-twist GBs [12]. Such GBJJs can be distributed all over the chip and one can even fabricate 0-π JJs [14]. Still, GBJJs suffer from hardly controllable inhomogeneity along the GB line, which makes the properties of the JJs not very reproducible and causes a substantial spread in JJ parameters. Alternative approaches to create Josephson barriers in cuprates are based on local irradiation of thin films with a high-energy focused electron beam [15–18] or on irradiation with high-energy ions (protons [18], neon [19,20], oxygen [21,22]) through a lithographically defined mask with a nanogap. The local irradiation drives the material from the superconducting to the normal conducting or even insulating state. So far, this approach has been hampered by the fact that it was not possible to create ultrathin Josephson barriers that would provide JJs with high characteristic voltage $V_c = j_0\rho_n$ and current-voltage characteristics (IVCs) without excess current that are well described by the resistively and capacitively shunted junction (RCSJ) model [23,24]. This is an important prerequisite for many applications. For reviews on various approaches to modify the properties of cuprate superconductors by local irradiation, see, e.g., Refs. [25,26] and references therein.

With the recent development of helium ion microscopy (HIM) [27], a sharply focused He ion beam with an approximately 0.5-nm diameter can be used to irradiate and modify cuprate superconductors on the nanoscale. This approach has been successfully used by Cybart and co-workers to fabricate JJs using focused helium-ion-beam (He-FIB) irradiation of YBCO thin films, and they demonstrated that the barriers in such He-FIB JJs can be changed continuously from conducting to insulating by varying the irradiation dose [28]. Moreover, the same group demonstrated already the integration of He-FIB JJs into SQUID devices [29], and the feasibility to use high-dose irradiation for nanoscale patterning (without removing material) in YBCO devices [30,31]. For a short review on this approach, also including irradiation with a focused Ne ion beam, see Ref. [32]. First attempts to extend this technique to the fabrication of JJs in other cuprate materials have been reported [33], and the creation of JJs in MgB_2 thin films by He-FIB irradiation has been demonstrated very recently [34].

Here, we report on the realization of He-FIB JJs in YBCO thin films on different substrates. We focus on the analysis of the electric-transport properties at 4.2 K of such JJs, complemented by numerical simulations based on the RCSJ model and on the dependence of the JJ properties on irradiation dose. We also present results on scanning transmission electron microscopy analysis of the local structural modification of the YBCO films, which can be made highly resistive by He-FIB irradiation with a high dose. The latter feature has been used to fabricate SQUIDs, by combination of medium-dose irradiation to produce two JJs with high-dose irradiation to produce the SQUID loop, and we demonstrate dc SQUID operation, including low-noise performance.

II. DEVICE FABRICATION

We fabricate epitaxially grown *c*-axis-oriented YBCO thin films of thickness *d* by pulsed laser deposition (PLD) on various single-crystal (001)-oriented $SrTiO_3$ (STO), MgO, and $(LaAlO_3)_{0.3}(Sr_2AlTaO_6)_{0.7}$ (LSAT) substrates (10×10 mm^2). The crystalline quality of the YBCO films is characterized by x-ray diffraction to determine the full width at half maximum (FWHM) of the rocking curve of the YBCO (005) peak and to extract *d* via Laue oscillations at the YBCO (001) Bragg peak. YBCO films on STO substrates are covered *in situ* by an epitaxially grown STO cap layer with a thickness of 10 unit cells (3.9 nm). For details on the PLD growth of our YBCO films on STO substrates, as well as their structural and electric-transport properties, see Refs. [35,36].

For electrical contacts on STO and MgO chips, we photolithographically define a resist mask, covering the central area of the chips, remove an approximately 10-nm-thick surface layer (including the STO cap layer) by Ar ion milling, and *in situ* deposit a Au film by magnetron sputtering, followed by a lift-off process. For electrical contacts on LSAT chips, we deposit in-situ, after the PLD process, a Au film onto the YBCO by in-situ electron beam evaporation after the PLD process. Subsequently, we photolithographically define a resist mask, covering the outer area of the chips, and remove the Au film on the central area of the chip by Ar ion milling.

Afterward, we use photolithography and Ar ion milling to prepattern 156 YBCO microbridges of width $w \approx 4$ μm (and length ≈ 200 μm) on each chip for He ion irradiation and electric-transport measurements in a four-point configuration. Table I gives an overview of the five chips, with some basic properties of their YBCO microbridges, which have been used for fabricating devices via He-FIB irradiation. A specific bridge on one of the chips is labeled by the chip name, followed by *-n* for bridge number *n*, e.g., STO-1-4 corresponds to bridge number 4 on the chip STO-1.

TABLE I. Properties of studied chips with YBCO thin film microbridges used for fabricating He-FIB-irradiated devices. To calculate the effective penetration depth $\lambda_{\rm eff} = \lambda_L^2/d$, we assume a London penetration depth $\lambda_L = 250$ nm.

Chip (substrate)	T_c (K)	FWHM (deg)	d (nm)	w (μm)	$\lambda_{\rm eff}$ (μm)
STO-1	89	0.11	50	3.2	1.25
STO-2	89	0.15	29	4.0	2.16
STO-3	91	0.08	46	3.8	1.36
MgO-1	89	0.17	53	4.1	1.18
LSAT-1	86	0.07	50	4.4	1.25

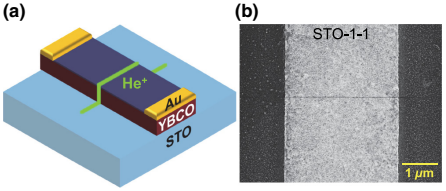

FIG. 1. (a) Schematic illustration of the He-FIB JJ geometry. (b) SEM image of a JJ (visible as thin dark line) fabricated with $D = 600$ ions/nm.

After prepatterning the YBCO microbridges, focused He-ion-beam irradiation is done in a Zeiss Orion NanoFab He/Ne ion microscope (HIM) with 30-keV He^+ ions. A beam current of 200 fA is used, and the beam is focused to a nominal diameter of 0.5 nm. A dwell time of 1 μs is used to irradiate line patterns with a dwell point spacing of 0.25 nm, which corresponds to a single linescan dose $D_{SL} = 5$ ions/nm. To obtain a certain line dose $D = Nd_{SL}$, a single linescan is repeated N times. To irradiate an area, adjacent linescans are offset by $\Delta = 0.25$ nm. In that case, a line dose of, e.g., $D = 100$ ions/nm corresponds to an area dose of $D_A \equiv D/\Delta = 400$ ions/nm^2 or 4×10^{16} ions/cm^2.

Figure 1(a) schematically illustrates the sample geometry and irradiation process for a single JJ. A scanning electron microscopy (SEM) image of STO-1-1 fabricated with $D = 600$ ions/nm is shown in Fig. 1(b). The irradiated linescan appears as a dark line in the SEM image due to He-FIB-induced carbon deposition from residual gas inside the He ion microscope chamber.

III. YBCO BRIDGES WITH HE-FIB-INDUCED BARRIERS AND JOSEPHSON JUNCTIONS

In this section, we present results obtained from devices fabricated on the chips listed in Table I.

A. Resistance vs temperature

Figure 2 shows measurements of the resistance R (at constant bias current $I_b = 1$ μA) vs temperature T of two YBCO microbridges. The $R(T)$ curve of STO-1-2, measured before He ion irradiation, shows a decrease of the resistance by about a factor of 3 from 300 to 100 K, with resistivity $\rho(100\,\mathrm{K}) \approx 190\,\mu\,\Omega$cm, followed by a sharp transition to $R < 1\,\Omega$ at $T_c = 89$ K. After irradiation with $D = 700$ ions/nm (and thus producing a JJ), the $R(T)$ curve of STO-1-2 shows an additional footlike structure with a plateau at $R = 6.6\,\Omega$ between approximately 40 K and T_c (see inset). This foot structure is due to thermally activated phase slippage [37] causing a finite voltage

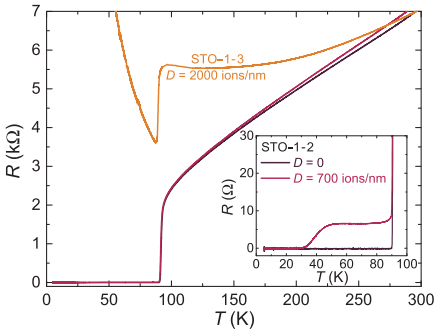

FIG. 2. $R(T)$ dependence of YBCO bridge STO-1-2 before and after irradiation and of STO-1-3 after irradiation. The inset shows an enlargement of the resistive transitions of STO-1-2.

drop across the JJ when (upon increasing T) the thermal energy k_BT approaches the Josephson coupling energy $E_J = I_0\Phi_0/(2\pi)$. Here, I_0 is the noise-free critical current of the JJ (which decreases with increasing T) and Φ_0 is the magnetic flux quantum. Accordingly, the plateau reflects the situation when the measurable critical current I_c drops below the bias current I_b, causing the JJ to reach its normal state resistance R_n. He-FIB irradiation with a high dose fully suppresses I_c. This is shown in Fig. 2 for sample STO-1-3, which has been irradiated with $D = 2000$ ions/nm. At $T = 4.2$ K, the resistance is $> 20\,\mathrm{k}\Omega$.

B. Transmission electron microscopy analysis

By the combination of atomic force microscopy and scanning near-field optical microscopy, it has been shown by Gozar *et al.* [33] that He-FIB irradiation with doses above 10^{18} ions/cm^2 induces amorphous tracks in $La_{1.84}Sr_{0.16}CuO_4$ thin films with a substantial lateral width of approximately 500 nm. In contrast to this, He-FIB produced JJs in YBCO films have been reported to show IVCs well described by the RCSJ model, indicating much less lateral damage [28]. However, no results have been reported on microstructural changes induced by a He-FIB in YBCO films so far.

To image possible structural modifications induced by He-FIB irradiation in our YBCO films, we use scanning transmission electron microscopy (STEM). For the STEM studies, we irradiate the YBCO bridge STO-1-4 with a series of 14 parallel lines using increasing doses from $D = 50$ to 10^5 ions/nm, with well-defined spacing (200 nm in most cases) between adjacent lines. Subsequently, we prepare a cross-sectional TEM lamella containing all irradiated lines, by *in situ* lift-out using a Ga-FIB microscope together with a micromanipulator. Figures 3(a)–3(d)

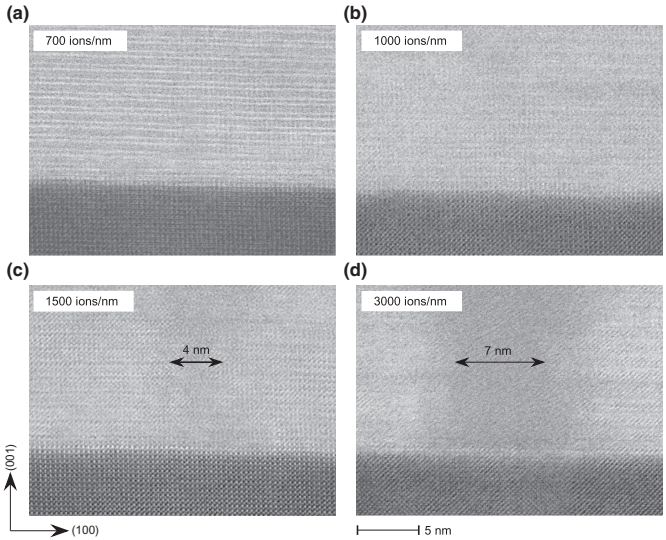

FIG. 3. Cross-section STEM images of the YBCO/STO interface (top/bottom, respectively) at the location of He-FIB irradiation with increasing dose D from (a) to (d). Arrows indicate the widths of amorphous regions.

show cross-section STEM images, viewed along the [010] zone axis, of four regions of the bottom part of the YBCO film at the YBCO/STO interface that are irradiated with $D = 700$, 1000, 1500, and 3000 ions/nm, respectively. The areas that are irradiated with $D \geq 3000$ ions/nm can be easily located in the STEM images due to significant changes in the microstructure of the YBCO films. As we know the exact spacing between the different areas irradiated along the lamella, we can also easily localize in the STEM images the areas that have been irradiated with lower D. For $D = 700$ and 1000 ions/nm [cf. Figs. 3(a) and 3(b)], we cannot identify any change in the structure of the irradiated sections. For $D = 1500$ ions/nm, an amorphous track of width $w_a \approx 4$ nm appears [cf. Fig. 3(c)], increasing to $w_a \approx 7$ nm for $D = 3000$ ions/nm [cf. Fig. 3(d)]. We note that with further increasing D, the amorphous track width w_a increases roughly linearly up to approximately 170 nm for the highest dose $D = 10^5$ ions/nm that we investigate.

Our STEM analysis indicates that medium doses do not induce significant structural damage of the YBCO crystal lattice, which is consistent with the assumption that the He-FIB easily moves oxygen ions from the Cu-O chains to interstitial sites [30], thereby altering the local electric-transport properties of YBCO on the nanometer scale without destroying the crystal lattice as a whole. Hence, He-FIB irradiation with a medium dose seems to be a very promising approach for creating JJs in YBCO. Moreover, we find that irradiation with larger doses of some 1000 ions/nm induces amorphous, and hence presumably highly resistive, regions, but still with a relatively small lateral extension of only a few nanometers.

C. Transport characteristics of He-FIB-induced Josephson junctions

In the following, we present electric-transport characteristics of approximately 50 YBCO brides that are irradiated with doses up to $D = 800$ ions/nm to produce JJs. We measure IVCs, i.e., current I vs voltage V, and the modulation of the critical current I_c in an externally applied magnetic field B (perpendicular to the substrate plane) in an electrically and magnetically shielded environment, with the samples at $T = 4.2$ K immersed in liquid He.

For all devices exhibiting IVCs that can be described by the RCSJ model, we perform numerical simulations, including thermal noise, to determine their noise-free critical current I_0, normal resistance R_n, and capacitance C. From these simulations, we determine the Stewart-McCumber parameter $\beta_C \equiv 2\pi I_0 R_n^2 C/\Phi_0$ and also the amount of excess current I_e, if present.

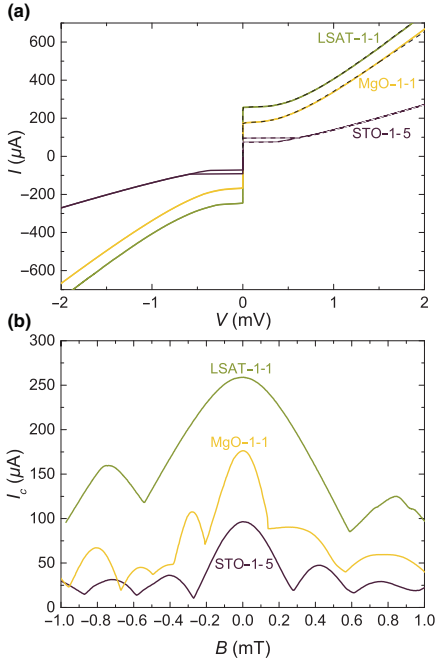

FIG. 4. Electric-transport characteristics of He-FIB JJs fabricated on different substrates: (a) IVCs showing experimental data (solid lines) and numerical simulation results for $I > 0$ (dashed lines) and (b) $I_c(B)$ patterns.

Figure 4 shows a representative set of IVCs [Fig. 4(a)] and $I_c(B)$ patterns [Fig. 4(b)] for JJs on different substrate materials. Irradiation doses and characteristic JJ parameters are given in Table II. As shown by the simulated curves [dashed lines in Fig. 4(a)], the IVCs can be well described by the RCSJ model and do not show any excess current. Only the JJ on STO shows a hysteresis in the IVC, with a JJ capacitance $C = 0.17\,\mathrm{pF}$ and $\beta_C = 2.77$ obtained from simulations. Data regarding β_C for all JJs are presented and discussed at the end of this section.

The $I_c(B)$ patterns shown in Fig. 4(b) exhibit clear modulation of the critical current with applied magnetic field; however, they significantly deviate from the Fraunhofer-like shape expected for homogeneous JJs in the short junction limit $w \lesssim 4\lambda_J$, where

$$\lambda_J = \sqrt{\frac{\Phi_0}{2\pi\,\mu_0 d_{\mathrm{eff}} j_0}} \tag{1}$$

is the Josephson penetration depth with the effective JJ inductance $\mu_0 d_{\mathrm{eff}}$. Our YBCO films grown on STO have a London penetration depth $\lambda_L \approx 250$ nm [38–41]. Therefore, the devices discussed here are clearly in the thin-film limit $d \ll \lambda_L$ and, hence, the effective penetration depth $\lambda_{\mathrm{eff}} = \lambda_L^2/d$ (see Table I) should be used to determine $d_{\mathrm{eff}} = 2\lambda_{\mathrm{eff}}$ in Eq. (1). Thus, we obtain the values of λ_J listed in Table II and see that all JJs are in the long JJ limit ($w > 4\lambda_J$).

Moreover, since $\lambda_J \ll \lambda_{\mathrm{eff}}$, these JJs are in the nonlocal regime [42–46]. In this regime, the $I_c(B)$ patterns can be calculated analytically [42,46] only in the narrow JJ limit, i.e., for $w < \lambda_{\mathrm{eff}}$ and $w < \lambda_J^{\mathrm{NL}}$, where $\lambda_J^{\mathrm{NL}} = \lambda_J^2/d$ is a nonlocal Josephson length [42]; see Table II. In our case, the above conditions are not really satisfied. Thus, our JJs are in the intermediate regime, where the exact shape of $I_c(B)$ is not known. However, we can roughly estimate the value of the penetration field B_{c1} [defined as a continuation of the first lobe of the $I_c(B)$ dependence down to $I_c = 0$] using (i) the local long JJ model and (ii) the narrow nonlocal JJ model [42] and compare them with experimentally measured values of B_{c1}^{ex}, given in Table II. The local long JJ model yields $B_{c1}^{\mathrm{LO}} = \Phi_0/(\pi d_{\mathrm{eff}}\lambda_J)$, whereas for a nonlocal narrow JJ [42], $B_{c1}^{\mathrm{NL}} = \Phi_0/(0.715w^2)$ (independent of j_0). By comparing these values with the experimental ones (see Table II), we see that B_{c1}^{ex} for STO-1-5 and MgO-1-1 are better described by the nonlocal theory, while B_{c1}^{ex} for LSAT-1-1 is closer to a local long JJ.

A detailed study of the $I_c(B)$ patterns of our He-FIB-induced JJs is out of the scope of the work presented here. Typically, our JJs on MgO have more irregular $I_c(B)$ patterns than those on STO and LSAT [cf. Fig. 4(b)]. This result indicates more inhomogeneous barrier properties of He-FIB-induced JJs on MgO and may either be attributed to the much larger lattice mismatch between MgO and YBCO and correspondingly poorer crystalline quality of

TABLE II. Irradiation doses and device parameters of JJs shown in Fig. 4.

	D (ions/nm)	I_0 (μA)	R_n (Ω)	V_c (μV)	C (pF)	β_C	λ_J (μm)	λ_J^{NL} (μm)	B_{c1}^{ex} (mT)	B_{c1}^{LO} (mT)	B_{c1}^{NL} (mT)
STO-1-5	700	99	7.44	737	0.17	2.77	0.42	1.8	0.31	0.63	0.28
MgO-1-1	500	178	3.07	546	0.15	0.77	0.37	2.6	0.25	0.75	0.17
LSAT-1-1	200	260	2.69	699	0.15	0.83	0.30	3.5	0.76	0.88	0.15

YBCO films or stronger charging of the MgO substrates that is observed during the He-FIB process.

In the following, we analyze the scaling of characteristic JJ properties j_c, ρ_n, and $j_c\rho_n$ with irradiation dose D. Note that devices irradiated with the lowest doses do not show JJ behavior. Therefore, we denote here all critical current densities as j_c. For all devices showing RCSJ behavior, however, the values given here refer to the noise-free values of j_0 obtained from numerical simulations.

Figure 5(a) summarizes $j_c(D)$ for all investigated devices. We attribute the significant scatter (cf. e.g., the data points for 700 ions/nm on STO-1) to instabilities in the fabrication process that we have not yet optimized. For instance, slight variations in the He-FIB focus spot size and beam current both affect the barrier properties. In spite of this scatter, we clearly find an exponential decay $j_c(D) \approx j_{c,0}\exp(-D/D_0)$, with $j_{c,0} = 3 \times 10^7$ A/cm^2 and with $D_0 = 38$ ions/nm for LSAT-1 and $D_0 = 130$ ions/nm for the other chips. The reason for the much stronger decay of $j_c(D)$ on LSAT compared to the devices on STO or MgO has not been clarified yet. Clearly, we do not find a correlation of D_0 with YBCO film thickness or crystalline quality (cf. FWHM values in Table I).

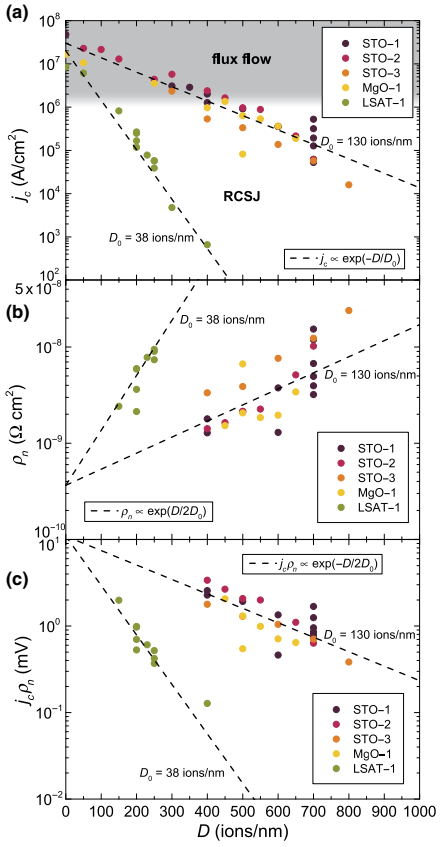

FIG. 5. Dependence of device parameters on He ion line dose D for various samples on different substrates: (a) $j_c(D)$, (b) $\rho_n(D)$, and (c) $j_c\rho_n(D)$. The dashed lines indicate the approximate scaling behavior as discussed in the text.

For $j_c \lesssim 2$ MA/cm^2, the IVCs show RCSJ-like behavior, whereas devices with higher critical current densities yield flux-flow-type IVCs, as indicated by the gray area in Fig. 5(a). Altogether, the range of variation of j_c covers 5 orders of magnitude. We note that an exponentially decaying behavior of j_c is well known from cuprate grain boundaries, where j_c decays exponentially with the grain-boundary misorientation angle Θ [11,47,48]. In a theoretical analysis of cuprate grain-boundary JJs, Graser *et al.* [48] related the exponential decay of $j_c(\Theta)$ to charging of the interface near defects induced by the structural distortions at the grain boundary. For the He-FIB-induced JJ barriers, the locally induced defect structure is not known yet, and it remains to be clarified whether a similar charging mechanism is responsible for the exponential decay of $j_c(D)$. A simple explanation of the exponential decay of j_c with increasing D would be a linear increase of the JJ barrier thickness. As stated in Sec. B, the STEM analysis yields a roughly linear increase of the amorphous track width with increasing D for doses above 1000 ions/nm. However, for lower doses, the STEM data do not allow us to make a statement on the width of the induced defect regions and their scaling with D.

Our analysis of the IVCs of He-FIB JJs produced with variable doses also yields a systematic scaling of the resistance times area product $\rho_n \equiv R_n wd \approx \rho_{n,0}\exp(D/2D_0)$ with $\rho_{n,0} = 0.37\,\text{n}\Omega\,\text{cm}^2$; i.e., ρ_n increases exponentially with D as shown in Fig. 5(b). Interestingly, the stronger decay of $j_c(D)$ for JJs on LSAT comes along with a correspondingly stronger increase in $\rho_n(D)$; i.e., we can use the same values of D_0 for the scaling of $\rho_n(D)$ as used for the scaling of $j_c(D)$. Accordingly, the characteristic voltage $V_c = j_c\rho_n$ also shows an exponential scaling $V_c \approx V_{c,0}\exp(-D/2D_0)$ with $V_{c,0} = j_{c,0}\,\rho_{n,0} = 11$ mV, as shown in Fig. 5(c). We note here that Figs. 5(b) and 5(c) contain only data points that correspond to RCSJ-type IVCs.

The fact that our analysis of the scaling of characteristic JJ properties (j_c, ρ_n, and V_c) with D can be described by the same values of D_0 indicates a universal scaling of V_c with either j_c or ρ_n independent of substrate material. This result is shown in Fig. 6, where we display $V_c(j_c)$ and $V_c(\rho_n)$ for all investigated JJs. Despite the

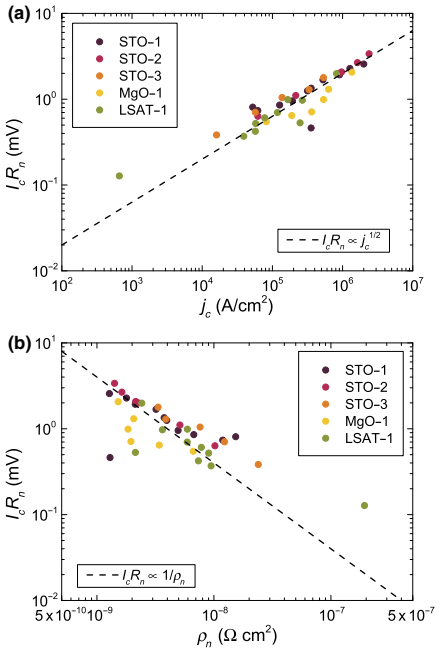

FIG. 6. Characteristic voltage I_cR_n for He-FIB JJs with RCSJ-like IVCs on different substrates (a) vs critical current density j_c and (b) vs resistance times area ρ_n. Dashed lines indicate $I_cR_n \propto \sqrt{j_c}$ in (a) and $I_cR_n \propto 1/\rho_n$ in (b) as discussed in the text.

significant scatter in the data, a clear trend is visible, which can be described by $I_cR_n \approx V_{c,1}(j_c/j_{c,1})^{1/2}$ [dashed line in Fig. 6(a)], with $V_{c,1} = 2$ mV and $j_{c,1} = 10^6$ A/cm^2 and by $I_cR_n \approx V_{c,1}(\rho_{n,1}/\rho_n)$ [dashed line in Fig. 6(b)] with $\rho_{n,1} = 2\,\text{n}\Omega\,\text{cm}^2$. We note that an approximate scaling $I_cR_n \propto \sqrt{j_c}$ and $I_cR_n \propto 1/\rho_n$ has also been observed for many cuprate grain-boundary JJs and other JJ types in cuprate superconductors, albeit with a slightly larger $V_{c,1}$ for the same $j_{c,1}$ and $\rho_{c,1}$ [10]. However, we should also note that the existence or absence of a universal scaling of I_cR_n vs j_c or ρ_n for all cuprate JJs and the origin of such a scaling has been discussed controversially in the literature; see, e.g., Refs. [10,11,16]. At least, for oxygen-depleted grain boundaries [11], there seems to be consensus on the same scaling as we see in our He-FIB JJs. This result is probably not surprising, because the He-FIB irradiation induces such an oxygen depletion [28].

So, obviously, for achieving large values of V_c, one should use doses that are as small as possible to obtain large values of j_c, but still provide JJs with RCSJ-type IVCs. Moreover, for fabricating SQUIDs (cf. Sec. IV), one wants to have nonhysteretic IVCs, i.e., $\beta_C \lesssim 1$. To address these issues, we determine from RCSJ simulations the dependencies of β_C and of the excess current densities j_e of our He-FIB JJs on j_c.

Figure 7(a) shows $\beta_C(j_c)$. We clearly find a significant difference for devices on STO as compared to those on LSAT or MgO. While for devices on LSAT and MgO the values of β_C are essentially independent of j_c and yield values between approximately 0.5 and 1, for devices on STO, β_C is always above 1 (up to approximately 4) and decays with increasing j_c. This result reflects the fact that we observe hysteretic IVCs at 4.2 K for all JJs on STO substrates and nonhysteretic IVCs for all JJs on MgO and LSAT. We attribute this behavior to a significant stray capacitance contribution caused by the large permittivity of STO at low T [49]. However, a more detailed analysis of this behavior would require a systematic variation of the JJ width, which we do not perform for the present study. For YBCO grain-boundary JJs, the capacitance C per area A has been found to vary roughly [11] within 10^{-6} to 10^{-4} F/cm^2, with a significant increase with increasing j_c from roughly 10^3 to 10^6 A/cm^2. In contrast, for our He-FIB JJs, we find for most devices C/A to scatter within the range from 5×10^{-5} to 2×10^{-4} F/cm^2 with no clear dependence on j_c in the range from 2×10^4 to 2×10^6 A/cm^2 (not shown).

Figure 7(b) shows the normalized excess current density j_e/j_c vs j_c. For the largest values of j_c, we do find excess currents that decay with decreasing j_c and finally disappear at $j_c \approx 2 \times 10^5$ A/cm^2. This behavior seems to be independent of the substrate material. The appearance of excess currents has also been reported for cuprate grain-boundary JJs and electron-beam damaged JJs with large current densities [11,16]. Such JJs are often modeled as superconductor–normal-metal–superconductor (*S–N–S*) JJs. For He-FIB JJs in YBCO films, Cybart *et al.* [28] reported on the transition from *S–N–S*-type to superconductor-insulator-superconductor-(*S–I–S*) type JJs upon increasing the irradiation dose. Our results are consistent with this observation; a more detailed analysis, however, requires transport measurements at variable temperature, which we have not performed so far in detail.

To conclude this section, we can state that for obtaining devices that do not exhibit excess currents, one should not exceed $j_c \approx 10^5$ A/cm^2. For devices on STO, however, such low j_c values come with values of β_C clearly above 1, i.e., with hysteretic IVCs. The $I_c(B)$ patterns of devices on MgO, on the other hand, show the strongest deviations from a Fraunhofer-like behavior. Hence, at the current state it seems that, among the substrate materials investigated here, He-FIB JJ devices on LSAT are most promising for applications.

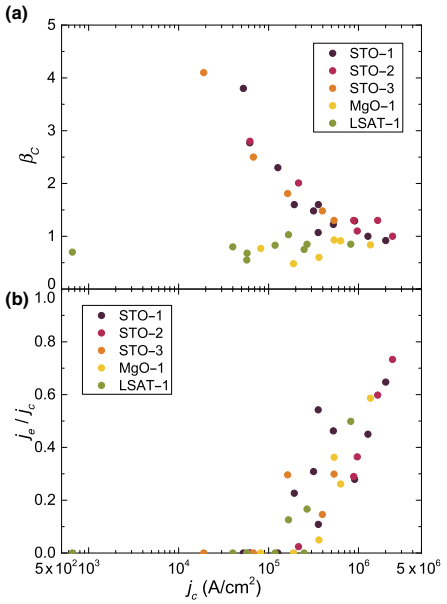

FIG. 7. (a) Stewart-McCumber parameter $\beta_C(j_c)$ and (b) normalized excess current $j_e/j_c(j_c)$ for He-FIB JJs on different substrates.

IV. HE-FIB-INDUCED DC SQUIDS

By irradiation with high He ion doses (typically for $D \gtrsim 1000$ ions/nm), j_c can be fully suppressed, as shown in Fig. 2, and the He-FIB-induced barriers can be made highly resistive (reaching even gigaohm resistances at 4.2 K for $D \gtrsim 5000$ ions/nm). This technique offers the possibility to define the sample geometry—ultimately on the nanometer scale—via direct-write lithography, without removing material by milling [30,31].

The combination of He-FIB irradiation with medium and high doses provides a simple way of fabricating dc SQUIDs from photolithographically prepatterned YBCO thin-film bridges on single-crystal substrates, with tailored JJ properties and SQUID inductance. We use this approach to fabricate simple micro- and nano-SQUIDs on STO, MgO, and LSAT substrates by first scanning over a square-shaped area at the center of the prepatterned YBCO bridge to define the SQUID "hole" (i.e., a highly resistive, magnetically transparent area) and a subsequent linescan across the whole width of the bridge using a medium dose to produce the JJs. A SEM image of such a SQUID is shown in the inset of Fig. 8(a) for a device fabricated on STO-1 with a 1×1-μm^2 hole (irradiated with $D_A = 4000$ ions/nm^2). Again, the locations of the JJs (irradiated with $D = 700$ ions/nm) and the SQUID hole are visible via the He-FIB-induced carbon deposition.

Since the hysteresis in the IVCs severely limits the performance of SQUIDs on STO substrates, the electric-transport and noise data shown in the following are measured on a device fabricated on LSAT-1. On the LSAT substrate, however, SEM imaging is only possible in poor quality due to charging of the substrate. For the device on LSAT, the SQUID hole is defined as a 300×300-nm^2 square, irradiated with $D_A = 4000$ ions/nm^2. The JJs are fabricated by a linescan with $D = 230$ ions/nm and have a width of approximately 2 μm each.

Figure 8(a) shows the IVCs for different applied magnetic flux to yield maximum (black) and minimum (red) positive critical current, exhibiting neither hysteresis nor excess current. From RCSJ simulations, we determine a mean per-junction critical current $I_0 = 43.6$ μA and normal state resistance $R_n = 9.50\,\Omega$ ($V_c = 414$ μV) and $\beta_C = 0.74$. The dependence of the critical current $I_{c,s}$ of the SQUID on the magnetic field is shown in Fig. 8(b) as solid lines, together with the numerically simulated dependence, based on the RCSJ model [50] (symbols). From the simulations, we extract the screening parameter $\beta_L \equiv 2I_cL/\Phi_0 = 0.79$, inductance $L = 19$ pH, and asymmetry parameters [50] for the critical current $\alpha_I = 0.145$ and inductance $\alpha_L = -0.15$. Figure 8(c) shows the voltage-flux dependence of the SQUID for a range of bias currents $I_b \approx \pm 110$ μA in steps of 4 μA. The dark dot near the center on the curve for $I_b = -85$ μA indicates the working point with a transfer function $V_\Phi = 2.1\,\mathrm{mV}/\Phi_0$, which is used for the noise measurement shown in Fig. 9.

To determine the spectral density of flux noise S_Φ vs frequency f of the SQUID, we use Magnicon SEL-1 SQUID electronics [51] in direct readout mode [52]. Figure 9 shows the measured rms spectral density of flux noise $S_\Phi^{1/2}(f)$ of the SQUID (red), together with the background noise of the readout electronics (black). The noise spectrum is dominated by frequency-dependent excess noise, scaling roughly as $S_\Phi \propto 1/f$ ($1/f$ noise), with a small bump (at approximately 10 kHz). This excess noise extends all the way up to the cutoff frequency $f_{el} = 166$ kHz of our readout electronics (limited by the sampling rate of the analog-to-digital converter), where it almost reaches the noise floor of the readout electronics. For YBCO SQUIDs, one typically finds a strong $1/f$ noise contribution due to I_c fluctuations in the JJs [8]. This result is also probably the case for the SQUID presented here. To further clarify this, one should operate the SQUIDs in current-bias reversal mode [53], which eliminates the excess noise contribution from I_c fluctuations. We have already successfully demonstrated this approach for YBCO nano-SQUIDs based on grain-boundary JJs [54]; however, for the simple SQUID layout without a suitable

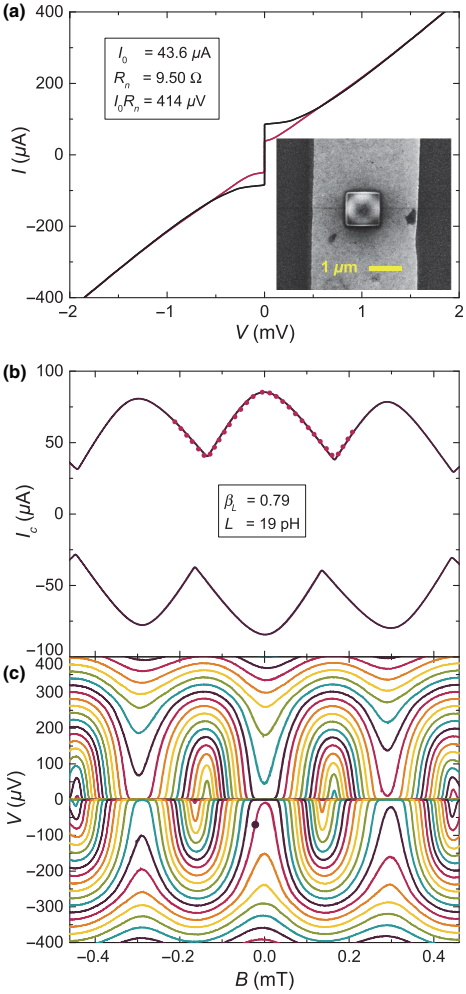

FIG. 8. Electric-transport characteristics of a He-FIB dc SQUID fabricated on LSAT-1-2. (a) IVCs for applied flux yielding maximum (black) and minimum (red) positive critical current. The inset shows a SEM image of a similar SQUID fabricated on STO-1. (b) Critical current vs magnetic field: experimental data (solid lines) and numerical simulation (symbols). (c) Voltage-flux dependence for bias currents I_b within approximately $\pm 110\,\mu$A in steps of $4\,\mu$A. The dark dot near the center indicates the working point for noise measurement.

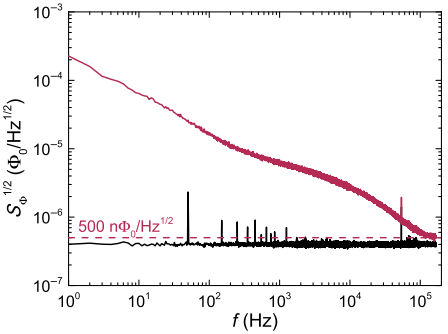

FIG. 9. Noise characteristics of a He-FIB dc SQUID fabricated on LSAT-1-2, with flux noise spectra of the SQUID (red) and electronics background (black). The dashed line indicates the upper limit for thermal white noise $S_{\Phi,w}^{1/2} = 500\,\mathrm{n}\Phi_0/\mathrm{Hz}^{1/2}$ of the SQUID.

on-chip flux coupling structure, as used in this work, it is not possible to use this approach. At least, from the noise data shown in Fig. 9, we can give an upper limit for the thermal white noise $S_{\Phi,w}^{1/2} \lesssim 500\,\mathrm{n}\Phi_0/\mathrm{Hz}^{1/2}$, which is impressively low for a $L \approx 20\,\mathrm{pH}$ SQUID.

V. CONCLUSIONS

We demonstrate the fabrication of YBCO Josephson junctions and dc SQUIDs by using a focused He ion beam, which locally modifies epitaxially grown YBCO thin films and allows us to "write" Josephson barriers and insulating areas with high spatial resolution. The analysis of the electric-transport properties at 4.2 K of our He-FIB-induced structures confirms and extends earlier results obtained by Cybart and co-workers [28–30].

We study in detail the dependence of characteristic JJ properties on the irradiation dose for devices on STO, MgO, and LSAT substrates. Upon increasing the irradiation dose, we find a transition from flux-flow to RCSJ-like behavior with some excess current contribution that vanishes upon further increasing the dose. Moreover, we find an exponential decay of the critical current density j_0 with increasing dose. For currently unclear reasons, this decay is much faster for devices on LSAT as compared to devices on STO and MgO. Another major difference regarding JJ behavior on different substrates is the observation of hysteretic IVCs for devices on STO, while devices on LSAT and MgO show no hysteresis. We attribute the hysteresis in the IVCs to a stray capacitance contribution from the STO substrates. The analysis of the characteristic voltage V_c of the fabricated JJs yields an approximate scaling $V_c \propto \sqrt{j_0}$.

Altogether, He-FIB JJs offer new perspectives for creating Josephson devices, because of the possibility to control the JJ properties by irradiation dose, even on the same substrate, and to place the JJs at virtually arbitrary positions. This flexibility obviously offers an enormous advantage for creating advanced devices, in particular employing multi-JJ configurations. Our detailed analysis of the JJ properties can be helpful for designing optimized devices for applications.

Moreover, irradiation with a high dose drives the material to be highly resistive. In this regime, our STEM analysis shows the creation of amorphous tracks in the YBCO films, which for not-too-high doses still have a lateral extension down to only a few nanometers. This observation indicates that He-FIB irradiation is a promising tool for nanopatterning (without removal of material) of YBCO films with ultrahigh resolution. We use this feature to produce dc SQUIDs by patterning both the JJs and the SQUID loop by He-FIB irradiation. For a device on LSAT, we demonstrate very low flux noise in the thermal white-noise regime. The observed low-frequency excess noise still has to be investigated in detail in further studies. Although we have not yet pushed to the ultimate limit of miniaturization, we envisage that He-FIB irradiation should be ideally suited for the realization of ultralow-noise nano-SQUIDs [55,56] due to the high spatial resolution of helium ion microscopy.

ACKNOWLEDGMENTS

B.M. acknowledges funding by the German Academic Scholarship Foundation. We gratefully acknowledge fruitful discussions with S. Cybart, V.G. Kogan, R.G. Mints, and R. Menditto and technical support by M. Turad and R. Löffler (LISA$^+$), W. Nisch and C. Warres (NMI), and C. Back. This work is supported by the COST action NANOCOHYBRI (Grant No. CA16218).

[1] K. K. Likharev, Superconducting weak links, Rev. Mod. Phys. **51**, 101 (1979).

[2] A. Barone and G. Paternò, *Physics and Applications of the Josephson Effect* (John Wiley & Sons, New York, 1982).

[3] R. Kleiner and W. Buckel, *Superconductivity*, 3rd ed., (Wiley-VCH, Weinheim, 2016).

[4] M. Bhushan and E. M. Macedo, Nb/AlO_x/Nb trilayer process for the fabrication of submicron Josephson junctions and low-noise dc SQUIDs, Appl. Phys. Lett. **58**, 1323 (1991).

[5] D. Hagedorn, O. Kieler, R. Dolata, R. Behr, F. Müller, J. Kohlmann, and J. Niemeyer, Modified fabrication of planar sub-μm superconductor-normal metal-superconductor Josephson junctions for use in a Josephson arbitrary waveform synthesizer, Supercond. Sci. Technol. **19**, 294 (2006).

[6] U. Welp, K. Kadowaki, and R. Kleiner, Superconducting emitters of THz radiation, Nat. Photon. **7**, 702 (2013).

[7] T. Ortlepp, Ariando Amd O. Mielke, C. J. M. Verwijs, K. F. K. Foo, H. Rogalla, F. H. Uhlmann, and H. Hilgenkamp, Flip-flopping fractional flux quanta, Science **312**, 1495 (2006).

[8] D. Koelle, R. Kleiner, F. Ludwig, E. Dantsker, John Clarke, High-transition-temperature superconducting quantum interference devices, Rev. Mod. Phys. **71**, 631 (1999).

[9] M. I. Faley, J. Dammers, Y. V. Maslennikov, J. F. Schneiderman, D. Winkler, V. P. Koshelets, N. J. Shah, and R. E. Dunin-Borkowski, High-T_c SQUID biomagnetometers, Supercond. Sci. Technol. **30**, 083001 (2017).

[10] R. Gross, L. Alff, A. Beck, O. M. Froehlich, D. Koelle, and A. Marx, Physics and technology of high temperature superconducting Josephson junctions, IEEE Trans. Appl. Supercond. **7**, 2929 (1997).

[11] H. Hilgenkamp and J. Mannhart, Grain boundaries in high-T_c superconductors, Rev. Mod. Phys. **74**, 485 (2002).

[12] F. Tafuri and J. R. Kirtley, Weak links in high critical temperature superconductors, Rep. Prog. Phys. **68**, 2573 (2005).

[13] F. Tafuri, D. Massarotti, L. Galletti, D. Stornaiuolo, D. Montemurro, L. Longobardi, P. Lucignano, G. Rotoli, G. P. Pepe, A. Tagliacozzo, and F. Lombardi, Recent achievements on the physics of high-T_C superconductor Josephson junctions: Background, perspectives and inspiration, J. Supercond. Nov. Magn. **26**, 21 (2013).

[14] K. Cedergren, J. R. Kirtley, T. Bauch, G. Rotoli, A. Troeman, H. Hilgenkamp, F. Tafuri, and F. Lombardi, Interplay between Static and Dynamic Properties of Semifluxons in $YBa_2Cu_3O_{7-\delta}$ 0-π Josephson Junctions, Phys. Rev. Lett. **104**, 177003 (2010).

[15] S. K. Tolpygo, B. Nadgorny, S. Shokhor, F. Tafuri, Y. Lin, A. Bourdillon, and M. Gurvitch, Electron beam writing in fabricating planar high-T_c Josephson junctions, Phys. C **209**, 211 (1993).

[16] A. J. Pauza, W. E. Booij, K. Herrmann, D. F. Moore, M. G. Blamire, D. A. Rudman, and L. R. Vale, Electron-beam damaged high-temperature superconductor Josephson junctions, J. Appl. Phys. **82**, 5612 (1997).

[17] W. E. Booij, A. J. Pauza, D. F. Moore, E. J. Tarte, and M. G. Blamire, Electrodynamics of closely coupled $YBa_2Cu_3O_{7-\delta}$ junctions, IEEE Trans. Appl. Supercond. **7**, 3025 (1997).

[18] W. E. Booij, C. A. Elwell, E. J. Tarte, P. F. McBrien, F. Kahlmann, D. F. Moore, M. G. Blamire, N. H. Peng, and C. Jeynes, Electrical properties of electron and ion beam irradiated $YBa_2Cu_3O_{7-\delta}$, IEEE Trans. Appl. Supercond. **9**, 2886 (1999).

[19] K. Chen, S. A. Cybart, and R. C. Dynes, Planar thin film $YBa_2Cu_3O_{7-\delta}$ Josephson junction pairs and arrays via nanolithography and ion damage, Appl. Phys. Lett. **85**, 2863 (2004).

[20] K. Chen, S. A. Cybart, and R. C. Dynes, Study of closely spaced $YBa_2Cu_3O_{7-\delta}$ Josephson junction pairs, IEEE Trans. Appl. Supercond. **15**, 149 (2005).

[21] S. S. Tinchev, Investigation of RF SQUIDs made from epitaxial YBCO films, Supercond. Sci. Technol. **3**, 500 (1990).

[22] N. Bergeal, X. Grison, J. Lesueur, G. Faini, M. Aprili, and J. P. Contour, High-quality planar high-T_c Josephson junctions, Appl. Phys. Lett. **87**, 102502 (2005).

[23] W. C. Stewart, Current-voltage characteristics of Josephson junctions, Appl. Phys. Lett. **12**, 277 (1968).

[24] D. E. McCumber, Effect of ac impedance of dc voltage-current characteristics of Josephson junctions, J. Appl. Phys. **39**, 3113 (1968).

[25] S. A. Cybart, P. X. T. Yen, E. Y. Cho, J. U. Huh, V. N. Glyantsev, C. S. Yung, B. Moeckly, J. W. Beeman, and R. C. Dynes, Comparison of Y–Ba–Cu–O films irradiated with helium and neon ions for the fabrication of Josephson devices, IEEE Trans. Appl. Supercond. **24**, 1100105 (2014).

[26] W. Lang, and J. D. Pedarnig, in *Nanoscience and Enigneering in Superconductivity*, edited by V. Moshchalkov, R. Wördenweber, and W. Lang (Springer Verlag, Berlin Heidelberg, 2010) Chap. 3, p. 81.

[27] G. Hlawacek and A. Gölzhäuser, eds., *Helium Ion Microscopy* (Springer International Publishing, Cham, Switzerland, 2016).

[28] S. A. Cybart, E. Y. Cho, J. T. Wong, B. H. Wehlin, M. K. Ma, C. Huynh, and R. C. Dynes, Nano Josephson superconducting tunnel junctions in $YBa_2Cu_3O_{7-\delta}$ directly patterned with a focused helium ion beam, Nat. Nano **10**, 598 (2015).

[29] E. Y. Cho, M. K. Ma, C. Huynh, K. Pratt, D. N. Paulson, V. N. Glyantsev, R. C. Dynes, and S. A. Cybart, $YBa_2Cu_3O_{7-\delta}$ superconducting quantum interference devices with metallic to insulating barriers written with a focused helium ion beam, Appl. Phys. Lett. **106**, 252601 (2015).

[30] E. Y. Cho, Y. W. Zhou, J. Y. Cho, and S. A. Cybart, Superconducting nano Josephson junctions patterned with a focused helium ion beam, Appl. Phys. Lett. **113**, 022604 (2018).

[31] E. Y. Cho, H. Li, J. C. LeFebvre, Y. W. Zhou, R. C. Dynes, and S. A. Cybart, Direct-coupled micro-magnetometer with Y-Ba-Cu-O nano-slit SQUID fabricated with a focused helium ion beam, Appl. Phys. Lett. **113**, 162602 (2018).

[32] S. Cybart, R. Bali, G. Hlawacek, F. Röder, and J. Fassbender, in *Helium Ion Microscopy*, edited by G. Hlawacek and A. Gölzhäuser (Springer International Publishing, Cham, Switzerland, 2016) Chap. 17, p. 415.

[33] A. Gozar, N. E. Litombe, Jennifer E. Hoffman, and I. Bozovic, Optical nanoscopy of high T_c cuprate nanoconstriction devices patterned by helium ion beams, Nano Lett. **17**, 1582 (2017).

[34] L. Kasaei, T. Melbourne, V. Manichev, L. C. Feldman, T. Gustafsson, Ke Chen, X. X. Xi, and B. A. Davidson, MgB_2 Josephson junctions produced by focused helium ion beam irradiation, AIP Adv. **8**, 075020 (2018).

[35] R. Werner, C. Raisch, A. Ruosi, B. A. Davidson, P. Nagel, M. Merz, S. Schuppler, M. Glaser, J. Fujii, T. Chassé, R. Kleiner, and D. Koelle, $YBa_2Cu_3O_7/La_{0.7}Ca_{0.3}MnO_3$ bilayers: Interface coupling and electric transport properties, Phys. Rev. B **82**, 224509 (2010).

[36] T. Schwarz, J. Nagel, R. Wölbing, M. Kemmler, R. Kleiner, and D. Koelle, Low-noise nano superconducting quantum interference device operating in tesla magnetic fields, ACS Nano **7**, 844 (2013).

[37] R. Gross, P. Chaudhari, D. Dimos, A. Gupta, and G. Koren, Thermally Acitvated Phase Slippage in High-T_c Grain-boundary Josephson Junctions, Phys. Rev. Lett. **64**, 228 (1990).

[38] R. Wölbing, T. Schwarz, B. Müller, J. Nagel, M. Kemmler, R. Kleiner, and D. Koelle, Optimizing the spin sensitivity of grain boundary junction nanoSQUIDs – Towards detection of small spin systems with single-spin resolution, Supercond. Sci. Technol. **27**, 125007 (2014).

[39] L. Thiel, D. Rohner, M. Ganzhorn, P. Appel, E. Neu, B. Müller, R. Kleiner, D. Koelle, and P. Maletinsky, Quantitative nanoscale vortex imaging using a cryogenic quantum magnetometer, Nat. Nanotechnol. **11**, 677 (2016).

[40] M. J. Martínez-Pérez, B. Müller, D. Schwebius, D. Korinski, R. Kleiner, J. Sesé, and D. Koelle, NanoSQUID magnetometry of individual cobalt nanoparticles grown by focused electron beam induced deposition, Supercond. Sci. Technol. **30**, 024003 (2017).

[41] D. Rohner, L. Thiel, B. Müller, M. Kasperczyk, R. Kleiner, D. Koelle, and P. Maletinsky, Real-space probing of the local magnetic response of thin-film superconductors using single spin magnetometry, Sensors **18**, 3790 (2018).

[42] M. Moshe, V. G. Kogan, and R. G. Mints, Edge-type Josephson junctions in narrow thin-film strips, Phys. Rev. B **78**, 020510 (2008).

[43] A. A. Abdumalikov Jr., G. L. Alfimov, and A. S. Malishevskii, Nonlocal electrodynamics of Josephson vortices in superconducting circuits, Supercond. Sci. Technol. **22**, 023001 (2009).

[44] John R. Clem, Josephson junctions in thin and narrow rectangular superconducting strips, Phys. Rev. B **81**, 144515 (2010).

[45] A. A. Boris, A. Rydh, T. Golod, H. Motzkau, A. M. Klushin, and V. M. Krasnov, Evidence for Nonlocal Electrodynamics in Planar Josephson Junctions, Phys. Rev. Lett. **111**, 117002 (2013).

[46] V. G. Kogan and R. G. Mints, Manipulating Josephson junctions in thin-films by nearby vortices, Phys. C **502**, 58 (2014).

[47] R. Gross and B. Mayer, Transport processes and noise in $YBa_2Cu_3O_{7-\delta}$ grain boundary junctions, Phys. C **180**, 235 (1991).

[48] S. Graser, P. J. Hirschfeld, T. Kopp, R. Gutser, B. M. Andersen, and J. Mannhart, How grain boundaries limit supercurrents in high-temperature superconductors, Nature Phys. **6**, 609 (2010).

[49] A. Beck, A. Stenzel, O. M. Froehlich, R. Gerber, R. Gerdemann, L. Alff, B. Mayer, R. Gross, A. Marx, J. C. Villegier, and H. Moriceau, Fabrication and superconducting transport properties of bicrystal grain boundary Josephson junctions on different substrates, IEEE Trans. Appl. Supercond. **5**, 2192 (1995).

[50] B. Chesca, R. Kleiner, and D. Koelle, in *The SQUD Handbook*, Vol. 1: Fundamentals and Technology of SQUIDs and SQUID systems, edited by John Clarke and Alex I. Braginski (Wiley-VCH, Weinheim, 2004) Chap. 2, p. 29.

[51] SQUID electronics SEL-1 from Magnicon GmbH, Lemsahler Landstr. 171, D-22397 Hamburg, Germany; http://www.magnicon.com.

[52] D. Drung, High-T_c and low-T_c dc SQUID electronics, Supercond. Sci. Technol. **16**, 1320 (2003).

[53] D. Drung, and M. Mück, in *The SQUD Handbook, Vol. 1: Fundamentals and Technology of SQUIDs and SQUID systems*, edited by John Clarke and Alex I. Braginski, (Wiley-VCH Weinheim, 2004) Chap. 4, p. 127.

[54] T. Schwarz, R. Wölbing, C. F. Reiche, B. Müller, M. J. Martínez-Pérez, T. Mühl, B. Büchner, R. Kleiner, and D. Koelle, Low-noise $YBa_2Cu_3O_7$ Nano-SQUIDs for Performing Magnetization-reversal Measurements on Magnetic Nanoparticles, Phys. Rev. Appl. **3**, 044011 (2015).

[55] C. Granata and A. Vettoliere, Nano superconducting quantum interference device: A powerful tool for nanoscale investigations, Phys. Rep. **614**, 1 (2016).

[56] M. J. Martínez-Pérez and D. Koelle, NanoSQUDs: Basics & recent advances, Phys. Sci. Rev. **2**, 20175001 (2017).

Publication 7

ACS APPLIED NANO MATERIALS
Cite This: ACS Appl. Nano Mater. 2019, 2, 5108−5115
Article
www.acsanm.org

Ultradense Tailored Vortex Pinning Arrays in Superconducting $YBa_2Cu_3O_{7-\delta}$ Thin Films Created by Focused He Ion Beam Irradiation for Fluxonics Applications

Bernd Aichner,[†] Benedikt Müller,[‡] Max Karrer,[‡] Vyacheslav R. Misko,[§,∥,⊥] Fabienne Limberger,[‡] Kristijan L. Mletschnig,[†] Meirzhan Dosmailov,[#] Johannes D. Pedarnig,[#] Franco Nori,[∥,%] Reinhold Kleiner,[‡] Dieter Koelle,[‡] and Wolfgang Lang*[,†]

[†]Faculty of Physics, University of Vienna, Wien, Austria
[‡]Physikalisches Institut and Center for Quantum Science (CQ) in LISA[+], Universität Tübingen, Tübingen, Germany
[§]Department of Physics, Universiteit Antwerpen, Antwerpen, Belgium
[∥]Theoretical Quantum Physics Laboratory, RIKEN Cluster for Pioneering Research, Wako-shi, Saitama, Japan
[⊥]μFlow group, Department of Chemical Engineering, Vrije Universiteit Brussel, Brussels, Belgium
[#]Institute of Applied Physics, Johannes Kepler University Linz, Linz, Austria
[%]Physics Department, University of Michigan, Ann Arbor, Michigan 48109, United States

Supporting Information

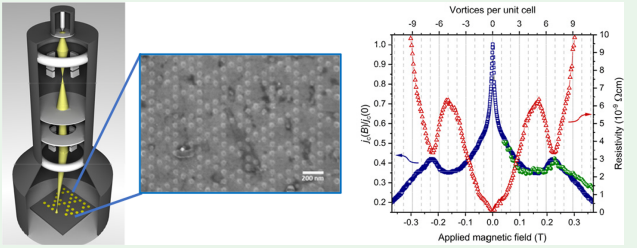

ABSTRACT: Magnetic fields penetrate a type II superconductor as magnetic flux quanta, called vortices. In a clean superconductor they arrange in a hexagonal lattice, while by addition of periodic artificial pinning centers many other arrangements can be realized. Using the focused beam of a helium ion microscope, we have fabricated periodic patterns of dense pinning centers with spacings as small as 70 nm in thin films of the cuprate superconductor $YBa_2Cu_3O_{7-\delta}$. In these ultradense kagomé-like patterns, the voids lead to magnetic caging of vortices, resulting in unconventional commensurability effects that manifest themselves as peaks in the critical current and minima in the resistance versus applied magnetic field up to ∼0.4 T. The various vortex patterns at different magnetic fields are analyzed by molecular dynamics simulations of vortex motion, and the magnetic field dependence of the critical current is confirmed. These findings open the way for a controlled manipulation of vortices in cuprate superconductors by artificial sub-100 nm pinning landscapes.

KEYWORDS: *helium ion microscope, cuprate superconductor, vortex pinning lattice, commensurability effects, critical current*

1. INTRODUCTION

Superconductivity is one of the most intriguing phenomena in condensed matter physics, and in particular the cuprate superconductors pose a challenge to the understanding of their electron-pairing mechanism. Still, their high transition temperature T_c and their possible high operating temperature in the accessible range of reliable and easy-to-handle cryocooler technology make the cuprate superconductors primary candidates for emerging technologies. However, all superconductors are only marginally suitable for technical applications in their pure and clean form. It is by the introduction of controlled defects that superconductors can be tailored for many important properties, e.g., by enhancing their ability to carry a lossless current, which requires to impede the dissipative motion of magnetic flux quanta, also called Abrikosov vortices or fluxons.[1]

Received: May 28, 2019
Accepted: July 10, 2019
Published: July 10, 2019

DOI: 10.1021/acsanm.9b01006
ACS Appl. Nano Mater. 2019, 2, 5108−5115

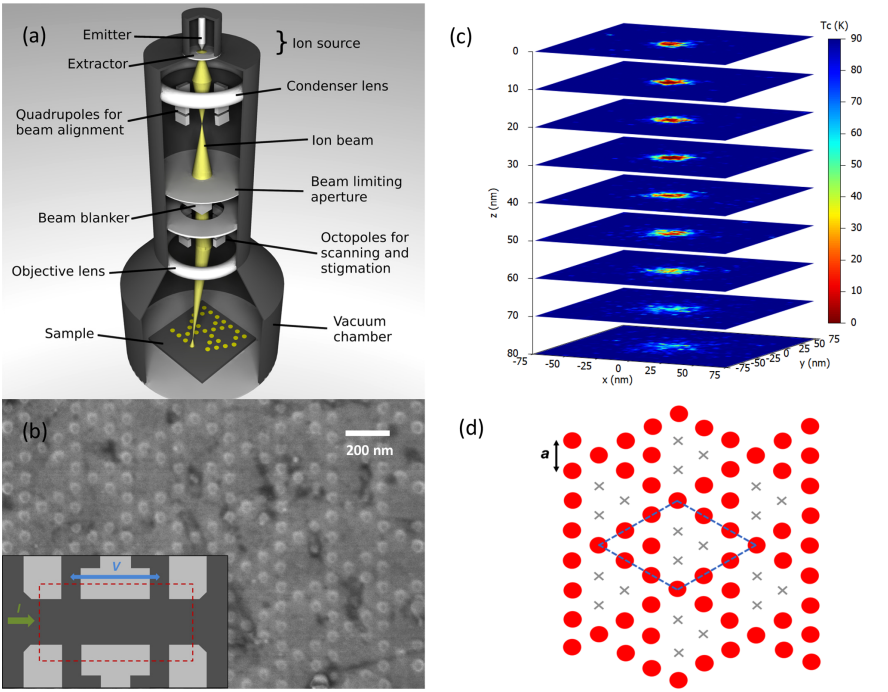

Figure 1. (a) Schematic drawing of direct modification of the local superconducting properties in a HIM. (b) HIM image of a quasi-kagomé test pattern of HIM-induced defects in a YBCO film, irradiated with a fully focused beam and with 5×10^6 ions/spot, i.e., with a 333 times larger number than in (c). The lattice spacing is a = 90 nm. Inset: sketch of the YBCO thin film samples (dark gray), the 200 μm × 100 μm rectangular irradiated area (red broken lines), direction of the applied current I, and the voltage probes V. (c) Simulation of defect-induced spatial distribution of T_c of a YBCO film (within sheets at various depths z from the surface z = 0), upon irradiating one spot with a defocused 30 keV He^+ ion beam with a Gaussian normal distributed fluence of 20 nm fwhm diameter. The number of impacting ions (15000) is the same as in the experiments (per spot) and corresponds to an average fluence of 4.8×10^{15} cm^{-2}. (d) Sketch of the pinning lattice with lattice spacing a: red disks represent irradiated spots, the blue dashed lines indicate the unit cell of the quasi-kagomé tiling, and gray crosses mark those sites that were removed from the hexagonal lattice to form the quasi-kagomé tiling.

Whereas such enhanced vortex pinning in conventional metallic superconductors, typically used for medical applications and high-field magnets, has been achieved by metallurgical techniques, the brittle nature of cuprate high-T_c superconductors (HTSCs) requires different concepts. A successful approach is to create columnar amorphous regions with diameters of a few times the superconducting coherence length by irradiation with swift heavy ions.[2]

In contrast to these extended defects, point defects can be created by inclusion of tiny nonsuperconducting particles[3] or by electron, proton, and light ion irradiation of HTSCs. For energies up to few megaelectronvolts the incident particles collide with a nucleus and displace it, eventually creating a collision cascade for high enough recoil energies. Several studies[4−6] have revealed that irradiation with He^+ ions of moderate energy is well suitable to tailor the superconducting properties in thin films of the prototypical HTSC $YBa_2Cu_3O_{7-\delta}$ (YBCO) by displacing mainly oxygen atoms, leading to a controllable reduction or even complete suppression of T_c. Arrays of cylindrical defect channels (CDs) that are populated with point defects provide a landscape in which superconductivity is locally suppressed. Recently, it has been demonstrated[7−14] that such pinning potential landscapes allow one to accommodate vortices in a commensurate arrangement, leading to peaks in the critical current and minima of the resistance at well-defined matching magnetic fields.

In the field of vortex commensurability effects, a large body of research has been established for metallic superconductors, typically using an array of holes (antidots) or blind holes with about 1 μm spacings.[15] Considerably narrower spacings have been achieved for thin Nb films grown on porous substrates.[16,17] However, in these superconductors, the Ginzburg−Landau coherence length at zero temperature is on the order of $\xi(0) \sim 10$ nm and the London penetration depth on the order of $\lambda_L(0) \sim 100$ nm, the latter setting the

DOI: 10.1021/acsanm.9b01006
ACS Appl. Nano Mater. 2019, 2, 5108−5115

range of magnetic interaction between vortices. Commensurability effects could be explored only at temperatures T very close to T_c, taking advantage of the fact that $\lambda_L(T) = \lambda_L(0)[T_c/(T_c - T)]^{1/2}$ increases substantially when approaching T_c. But choosing a rather high operation temperature is not feasible for practical applications since it is on the expense of a reduced superconducting gap, weaker pinning potential, and enhanced thermodynamic fluctuations.

On the other hand, thin films of YBCO have an in-plane $\lambda_{L,ab}(0) \sim 250$ nm,[18−21] and edge and screw dislocations, as one important type of intrinsic defects in YBCO films, have typical distances of about 300 nm.[22] Still, commensurability effects could be demonstrated close to T_c in YBCO perforated with a square array of holes with 1 μm lattice spacing.[23] But since intrinsic defects compete with the artificially created pinning landscape, it is important to fabricate and investigate pinning arrays with lattice spacings significantly below these two characteristic lengths. Here, we report on the electrical transport properties of ultradense unconventional pinning arrays in YBCO thin films with spacings down to 70 nm, fabricated with a helium ion microscope, and we demonstrate pronounced commensurability effects at strong magnetic fields well above 100 mT which persist down to at least ∼50 K, i.e., far below T_c.

2. RESULTS AND DISCUSSION

2.1. Irradiation in the Helium Ion Microscope. The ZEISS ORION NanoFab[24] is a novel multifunctional platform combining focused ion beam sources for neon and helium ions and a scanning helium ion microscope (HIM) with a spatial resolution better than 0.5 nm and unprecedented depth of focus.[25−27] The HIM consists of a gas-field He^+ ion source that emits ions from an ultrasharp tip, electrostatic ion optics to focus and trim the beam, and a deflection system to raster the beam over the sample stage as it is outlined in Figure 1a. The advantage of using a He beam over the conventional Ga focused ion beam technique is its higher spatial resolution (fabrication of nanopores down to 1.3 nm has been demonstrated[28]) and the prevention of contamination of the HTSC by Ga ions. As a first application in YBCO, the fabrication of Josephson junctions and superconducting quantum interference devices has been demonstrated via forming thin barriers of insulating material with the focused ion beam across prepatterned microbridges.[29−32]

However, for the fabrication of vortex pinning defects, the HIM in its original operation mode is less suitable. On the one hand, it is known that the diameter of defects suitable for vortex pinning must not be smaller than the superconducting coherence length, which is $\xi_{ab}(0) \simeq 1.2$ nm in YBCO.[33] On the other hand, the inherent deflection of the ion trajectories by scattering at the target atoms when traversing the material will cause a blurring of the focus with increasing depth. In this situation the fluence of the He^+ ions decreases strongly from the surface to the back of the YBCO film. To achieve a high enough ion fluence for suppression of T_c throughout the entire film thickness, the intensity of the focused ion beam must then be set to such a high value that amorphization of the YBCO crystal lattice[7,32] and mechanical destruction near the sample's surface result. This is illustrated in Figure 1b which was recorded in the HIM after irradiation of a test pattern with an optimally focused He^+ ion beam with a much larger number of ions/spot than normally used in our experiments. Around the impact point of the focused ion beam the YBCO structure is completely destroyed and blisters with about 50 nm diameter bulge out of the surface, while under the regular conditions for fabrication of pinning lattices, the irradiated areas are invisible in both the HIM and with scanning electron microscopy.

To avoid these shortcomings and irradiate a well-defined area, our approach uses an intentionally defocused ion beam. This is achieved by first adjusting the HIM settings to highest resolution and afterward changing the working distance (beam focus plane) by 8 μm. The aperture angle of the ion beam is $\pm 0.07°$; hence, the ion beam hits the sample surface almost orthogonally with a nearly Gaussian fluence profile[28] with a full width at half-maximum (fwhm) of about 20 nm.

The resulting three-dimensional shape of CDs with suppressed T_c is inferred from simulations of ion−matter interaction and collision cascades with the program SRIM[34] and calibrated to experimental data of T_c suppression as a function of defect density. Details of such calculations are reported elsewhere.[35] A defocused 30 keV He^+ beam of 20 nm fwhm diameter creates well-defined cylindrical channels with diameters ∼25 nm in a YBCO film within which T_c is suppressed or reduced up to a depth of 80 nm, as evidenced in Figure 1c. In thicker YBCO films, however, the collision cascades are prone to substantial straggling which leads to blurring of the profile and insufficient reduction of T_c due to a lower defect density as it has been observed in heavy-ion-irradiated YBCO single crystals.[36]

2.2. Vortex Commensurability Effects in Quasi-Kagomé Vortex Pinning Arrays. As a proof-of-concept experiment we have fabricated a square array of columnar defect cylinders with a defocused ion beam of fwhm = 50 nm and with a lattice spacing (nearest-neighbor distance) a = 200 nm in a 80 nm thick YBCO film and measured the critical current $I_c(B_a)$ in the superconducting state and the magneto-resistance $R(B_a)$ in the voltage state as a function of the applied magnetic field B_a. The parameters were chosen similarly to previous experiments performed with masked ion beam irradiation.[10−13] Consistently, a clear peak of $I_c(B_a)$ corresponding to a minimum of $R(B_a)$ is found when each CD is filled by one vortex, and a tiny feature can be noticed for filling of each CD by two vortices (see the Supporting Information).

Pinning lattices can be designed not only with common hexagonal[37] or square tilings[15] but also as more complex periodic or even quasi-periodic tilings that exhibit a number of unusual phenomena. Some examples of such arrays have been studied theoretically[38−41] and experimentally in metallic superconductors with holes[42−44] and magnetic dots,[45−48] like Penrose,[42,43] honeycomb,[16,49] and kagomé[50] lattices and artificial vortex ice arrangements in geometrically frustrated pinning lattices.[51−53] In HTSCs, such studies have been scarce[54] due to the much more demanding nanopatterning.

The particular advantage of irradiation in the HIM over other nanopatterning techniques is the higher spatial resolution and the ability to easily produce any desired pattern. We demonstrate this by the fabrication of quasi-kagomé pinning lattices with ultrasmall lattice spacing a = 90 nm (sample QK90) and 70 nm (sample QK70). The quasi-kagomé lattice is formed from a hexagonal lattice, where three neighboring sites are not occupied,[48] as sketched in Figure 1d. The quasi-kagomé lattice consists of vertex triangles with six sites per unit cell and large voids. It provides a unique platform to investigate the competition between pinning potentials and elastic energy of the vortex lattice. The quasi-kagomé lattice is a more extreme variant of the genuine kagomé tiling, which is formed

DOI: 10.1021/acsanm.9b01006
ACS Appl. Nano Mater. 2019, 2, 5108−5115

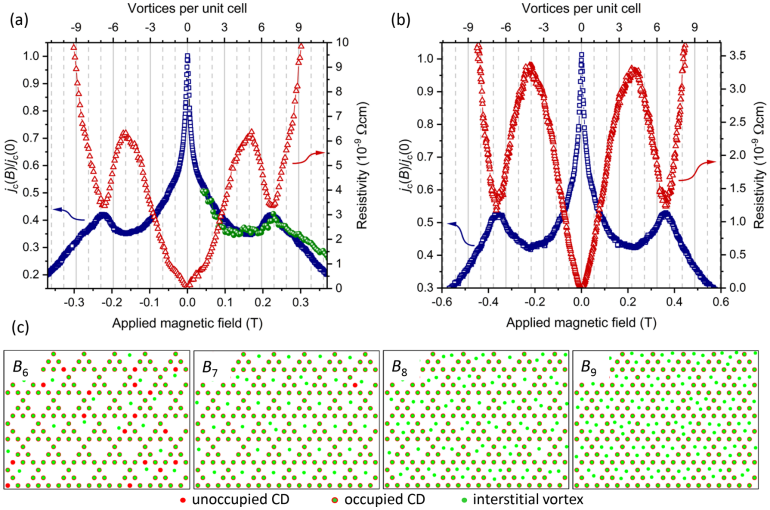

Figure 2. (a) Magnetic field dependence of the normalized critical current at 83 K (blue squares) and resistivity at 83.5 K (red triangles) of a 75 nm thick YBCO film, irradiated with a quasi-kagomé pattern of beam spots (20 nm fwhm) in a HIM (sample QK90). The upper horizontal scale indicates the matching fields B_k, calculated from eq 1, for a filling of the unit cell with k vortices. The peak in the critical current and the minimum in the resistivity correspond to $k = 7$. The green bullets represent the results from molecular dynamics simulations. Only the positive branch of the mirror symmetric results is shown for clarity. (b) Normalized critical current at 52 K (blue squares) and resistivity at 55 K (red triangles) for sample QK70. (c) Simulation of vortex arrangements in the quasi-kagomé lattice of sample QK90 for several applied magnetic fields that correspond to various commensurability conditions as labeled in the graphs. Red circles represent artificial pinning centers and green dots the vortices.

from the hexagonal lattice by eliminating every other site from every other row.

In periodic pinning lattices commensurability effects are expected to occur at applied magnetic fields that fulfill the matching condition

$$B_k = \frac{k\Phi_0}{A} \tag{1}$$

where k is the number of pinning sites (or vortices) in the unit cell of area A and $\Phi_0 = h/(2e)$ is the magnetic flux quantum.

The electrical transport properties of the YBCO films patterned with the quasi-kagomé pinning lattice show intriguing features. Those can be attributed to the fact that HIM nanopatterning enables the realization of ultradense pinning arrays. Accordingly, pronounced vortex commensurability effects in the critical current density $j_c(B_a)$ and the magnetoresistivity $\rho(B_a)$ appear at very high matching fields, at $B_a = 0.23$ T for sample QK90 and at $B_a = 0.38$ T for sample QK70, as shown in Figures 2a and 2b, respectively. The observed effects are well reproducible after storing the samples at room temperature for several weeks.

In the case of strong interactions between vortices and the pinning potential of the CDs, significant vortex commensurability effects are expected at B_6, when each CD is filled with one vortex. Conversely, with strong vortex−vortex interactions and marginal influence of the pinning landscape, the elastic energy of the vortex ensemble should favor a hexagonal lattice, and the voids are expected to be filled with three interstitial vortices, leading to commensurability signatures at B_9. The former, for instance, was observed in a quasi-kagomé lattice of magnetic Ni dots embedded in a Nb superconducting film.[48]

Surprisingly, none of these features are found here; instead, a prominent matching peak in $j_c(B_a)$ and a corresponding minimum in $\rho(B_a)$ appear at B_7, as can be seen in Figure 2a,b. Presumably, all CDs are occupied by vortices, and one interstitial vortex per unit cell is "caged" inside the voids of the lattice due to repulsion forces from the trapped vortices. On the other hand, the absence of a matching feature at B_1 indicates that the six closely packed sites of the kagomé triangle do not merge into a single pinning site. This confirms that despite the rather narrow distance of CDs they act as separate pinning potentials.

Molecular dynamics simulations shed more light on the vortex distribution in the quasi-kagomé lattice. A rectangular cell with periodic boundary conditions is used for the calculations. The vortex−vortex interaction, the pinning force on the vortices at the CDs, an external driving force, and a thermal stochastic force are taken into account, as detailed elsewhere for previous simulations.[39,40,55,56] The ground state of the static vortex arrangement (zero driving force) is obtained by starting the simulation at some elevated "temperature" and gradually decreasing it to zero, thus performing a simulated thermal annealing. Note that this corresponds to magnetic-field-cooled experiments. However, since in our measurements no hysteresis was observed between

DOI: 10.1021/acsanm.9b01006
ACS Appl. Nano Mater. 2019, 2, 5108−5115

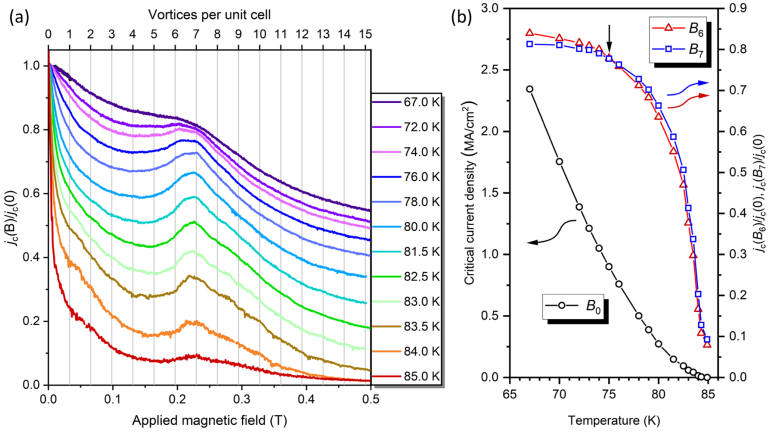

Figure 3. (a) Normalized critical current density of sample QK90 as a function of the applied magnetic field at various temperatures. The branches at reversed polarity of the magnetic field are mirror symmetric and are not shown. The upper horizontal scale displays the commensurability fields for k vortices in the unit cell of the quasi-kagomé pattern. (b) Temperature variation of the critical current density at $B_a = 0$ (black circles) and the normalized critical current densities at B_6 (red triangles) and B_7 (blue squares). At lower temperatures, starting from the crossover at 75 K marked by the arrow, the critical current at the B_6 commensurability field exceeds the critical current at B_7.

up- and down-ramping of the magnetic field, these results are equally valid for magnetic-field-ramped experiments.

In the simulations, the critical current density j_c is determined to be the minimum current density that depins the vortices; in the experiments the common electric field criterion of 10 μV/cm is used. The simulated values for the critical current density are then scaled to the experimental results (for sample QK90) at $B_a = 50$ mT.

The results of the simulations of static vortex configurations at different magnetic fields B_k and for temperatures adapted to the experimental situation are displayed in Figure 2c. For B_6, where the average density of vortices matches the density of CDs, most of the pinning centers are filled with vortices, but several empty pins and, in turn, interstitial vortices can be noticed. This is explained by the strong repulsion between the vortices located on the closely packed pinning sites such that some of these vortices can depin and move in the voids, thus minimizing the energy. For B_7 almost all pins are filled, and typically one excess vortex sits in the centers of the voids of the quasi-kagomé lattice. If the magnetic field is further increased, all pins are occupied, and the voids host two (B_8) or three (B_9) vortices with minor fluctuations ± 1 in this number. In the latter case, the hexagonal vortex lattice is mostly recovered. Note that an experimental visualization of the vortex arrangements in ultradense pinning lattices is challenging. Because $\lambda_{L,ab}(T) \gg a$ in our samples, the magnetic fields of the vortices overlap strongly and magnetic force microscopy might not provide enough contrast.

A simulation of the critical current density $j_c(B_a)$ is displayed in Figure 2a. Indeed, there is no peak in $j_c(B_a)$ visible at B_6, and peaks of $j_c(B_a)$ at B_8 and B_9 are hardly noticeable, whereas a pronounced peak at B_7 is found, in excellent agreement with the experimental results. This unconventional commensurability effect can be explained by the competition of the elastic vortex lattice energy, which favors a hexagonal lattice and the semiregular quasi-kagomé pinning potential. At B_6 filling of all CDs with vortices would lead to a maximized pinning force density, but the repulsion between the trapped vortices leads to a significant number of vacancies at the pinning sites and, in turn, mobile interstitial vortices in the kagomé voids that reduce j_c. On the other hand, for B_9, the elastic energy of the vortex lattice is minimized, but pinning is not so efficient due to the larger number of interstitial vortices. Thus, a commensurate arrangement in which all pinning sites are occupied and one interstitial vortex is caged in the center of the voids appears to be the most stable structure at temperatures near T_c.

The balance between the pinning forces at the CDs and the vortex caging potential can be tuned with temperature. While both increase at lower temperature, the pinning forces at the artificial defect lattice increase more rapidly.[57] To study this behavior on our samples, we performed electric transport measurements at variable T. Figure 3a shows normalized j_c vs B_a curves for sample QK90 at 67 K $\leq T \leq$ 85 K. We find that at temperatures $T <$ 80 K a second peak of j_c around B_6 emerges, coalescing with the peak at B_7 into a broader feature with $j_c(B_6) > j_c(B_7)$ at even lower temperatures. This is a formidable demonstration of how the vortices "crystallize" into the quasi-kagomé lattice at lower temperatures when the artificial pinning landscape becomes dominant. Figure 3b displays the critical current density j_c at $B = 0$, calculated from the sample's cross section. However, it has to be cautioned that the irradiated sample contains many CDs, and hence a significant volume in the sample does not contribute to the supercurrent, making a comparison to pristine YBCO films inappropriate. The normalized $j_c(B_6)/j_c(0)$ and $j_c(B_7)/j_c(0)$ curves reveal the crossover at $T = 75$ K, where pinning at a matching field of six vortices/unit cell becomes more efficient.

Our findings may be compared to somewhat related simulation results. For a honeycomb pinning lattice it has

DOI: 10.1021/acsanm.9b01006
ACS Appl. Nano Mater. 2019, 2, 5108−5115

been demonstrated[41] that j_c of a commensurable vortex arrangement with an additional caged vortex can be larger than that with the pinning sites occupied only. However, this only applies to shallow pinning potentials, whereas the situation is reversed for strong pinning, in excellent accordance with our observation of the crossover to $j_c(B_6) > j_c(B_7)$ at lower temperatures. Note, however, that one caged vortex in a honeycomb lattice restores the ideal hexagonal vortex lattice, while in our quasi-kagomé lattice one interstitial vortex is still associated with elastic energy of the vortex lattice. Thus, additional simulations with varying pinning potentials in the quasi-kagomé lattice are envisaged.

3. CONCLUSIONS

In summary, we have demonstrated the fabrication of periodic arrays of pinning centers in thin YBCO films with ultranarrow lattice spacings down to 70 nm by irradiation with the defocused beam of a HIM. This technique opens the route to create large arrays of pinning sites with user-defined positions and with a resolution superior to the lithographic techniques. As an example of a complex pinning landscape, the quasi-kagomé pinning lattice exhibits an unconventional commensurability effect, when all pins are occupied by vortices and one interstitial vortex is magnetically caged in each void of the lattice. It has been suggested that such caged vortices can be more easily manipulated along predetermined paths,[58] and hence, our findings can pave the way toward "Fluxonic" applications[59−61] of cuprate superconductors.

4. MATERIALS AND METHODS

Superconducting Film Growth. Thin films of $YBa_2Cu_3O_{7-\delta}$ are grown epitaxially on (100) MgO single-crystal substrates by pulsed-laser deposition using 248 nm KrF excimer laser radiation at a fluence of 3.2 J/cm^2. The thicknesses of the films are $t_z = 75 \pm 5$ nm (sample QK90) and $t_z = 50 \pm 5$ nm (sample QK70) as determined by atomic force microscopy. Bridges with dimensions 240 × 60 μm^2 are lithographically patterned for the electrical transport measurements. Two longitudinal voltage probes with a distance of 100 μm are applied on side arms of the bridges. The as-prepared samples had critical temperatures $T_c \sim 90$ K and transition widths $\Delta T_c \sim 1$ K.

Ion Beam Irradiation. The prepatterned YBCO microbridges are introduced into the Zeiss Orion NanoFab He ion microscope and with low ion fluence the proper alignment of the sample surface to the focus plane of the ion optics is checked. Controlled defocus is achieved by changing the working distance by 8 μm from the focus plane, resulting in irradiation spots of about 20 nm diameter. Every point of the lattice, defined by a deflection list loaded into the Nano Patterning and Visualization Engine (NPVE), is irradiated with 30 keV He^+ ions with a dwell time of 1.2 ms (0.83 ms) and a beam current of 2.0 pA (2.9 pA) for sample QK90 (QK70), corresponding to 15000 He^+ ions/point. The average fluence hitting the sample's surface in the focus spot of about 20 nm fwhm is 4.8×10^{15} cm^{-2}. The irradiated area is approximately 200 μm × 100 μm.

Electrical Transport Measurements. The electrical measurements are performed in a closed-cycle cryocooler mounted between the pole pieces of an electromagnet. A Cernox resistor[62] together with a LakeShore 336 temperature controller is used for in-field temperature control to a stability of about 1 mK. The magnetic field, oriented perpendicular to the sample surface, is tuned by a programmable constant current source and measured with a LakeShore 475 gaussmeter with a resolution of 0.1 μT, a zero offset <10 μT, and a reading accuracy <0.1%. The resistivity measurements are performed with a current of 0.8 mA, generated by a Keithley 6221 constant-current source in both polarities to exclude thermoelectric signals, and the voltage is measured with a Keithley 2182A nanovoltmeter. The critical current is determined from isothermal current−voltage (I−V) measurements with a voltage criterion of 100 nV, corresponding to 10 μV/cm. The I−V curves do not exhibit features that could be used to discriminate between the depinning of the vortices trapped in the CDs and the interstitial vortices, respectively.

Numerical Simulations. The simulations are performed in a 2D (in the xy-plane) simulation cell with periodic boundary conditions that models an infinite superconducting film characterized by the penetration depth λ, which is set to $\lambda_{1,ab}(T)$ at finite T. The cell is chosen large enough to avoid finite-size effects. Simulated annealing calculations are performed by numerically integrating the overdamped equations of motion:[39,40,55] $\eta \mathbf{v}_i = \mathbf{f}_i = \mathbf{f}_i^{vv} + \mathbf{f}_i^{vp} + \mathbf{f}_i^{T} + \mathbf{f}_i^{d}$. Here $\mathbf{f}_i$ is the total force per unit length acting on vortex i, $\mathbf{f}_i^{vv}$ and $\mathbf{f}_i^{vp}$ are the forces due to vortex−vortex and vortex−pin interactions, respectively, $\mathbf{f}_i^{T}$ is the thermal stochastic force, and $\mathbf{f}_i^{d}$ is the driving force; η is the viscosity, which is set to unity. The force due to the vortex−vortex interaction is $\mathbf{f}_i^{vv} = \sum_j^{N_v} f_0 K_1(|\mathbf{r}_i - \mathbf{r}_j|/\lambda)\hat{\mathbf{r}}_{ij}$ where N_v is the number of vortices, K_1 is a modified Bessel function, $\hat{\mathbf{r}}_{ij} = (\mathbf{r}_i - \mathbf{r}_j)/|\mathbf{r}_i - \mathbf{r}_j|$, and $f_0 = \Phi_0^2/8\pi^2\lambda^3$. The pinning force is $\mathbf{f}_i^{vp} = \sum_k^{N_p} f_p \cdot (|\mathbf{r}_i - \mathbf{r}_k^{(p)}|/r_p)\Theta[(r_p - |\mathbf{r}_i - \mathbf{r}_k^{(p)}|)/\lambda]\hat{\mathbf{r}}_{ik}^{(p)}$ where N_p is the number of pinning sites, f_p (expressed in f_0) is the maximum pinning force of each short-range parabolic potential well located at $\mathbf{r}_k^{(p)}$, r_p is the range of the pinning potential, Θ is the Heaviside step function, and $\hat{\mathbf{r}}_{ik}^{(p)} = (\mathbf{r}_i - \mathbf{r}_k^{(p)})/|\mathbf{r}_i - \mathbf{r}_k^{(p)}|$. All the lengths (fields) are expressed in units of λ (Φ_0/λ^2). The ground state of a system of moving vortices is obtained by simulating field-cooled experiments. In this approximation of deep short-range (δ-like) potential wells, the critical current can be defined as follows[39,40,43,44,55] (giving essentially the same results as those obtained using the threshold criterion in dynamical simulations[39,40]): $j_c(\Phi) = j_0 N_v^{(p)}(\Phi)/N_v(\Phi)$, where j_0 is a constant, and study the dimensionless value $J_c = j_c/j_0$.

■ ASSOCIATED CONTENT

Ⓢ Supporting Information

The Supporting Information is available free of charge on the ACS Publications website at DOI: 10.1021/acsanm.9b01006.

Critical current and resistance data of a square array of vortex pinning centers fabricated by irradiation in the helium ion microscope (PDF)

■ AUTHOR INFORMATION

Corresponding Author

*E-mail: wolfgang.lang@univie.ac.at.

ORCID

Vyacheslav R. Misko: 0000-0002-5290-412X
Meirzhan Dosmailov: 0000-0003-3672-0619
Johannes D. Pedarnig: 0000-0002-7842-3922
Wolfgang Lang: 0000-0001-8722-2674

Present Address

M.D.: Al-Farabi Kazakh National University, Almaty, Kazakhstan.

Notes

The authors declare no competing financial interest.

■ ACKNOWLEDGMENTS

The authors thank John Notte and Jason Huang for enlightening discussions on helium ion microscopy and for initial test irradiations in the HIM at Carl Zeiss Ion Microscopy Innovation Center in Peabody, USA, and Georg Zechner for experimental support. B.M. acknowledges funding by the German Academic Scholarship Foundation. V.R.M. and F.N. acknowledge support by the Research Foundation-

DOI: 10.1021/acsanm.9b01006
ACS Appl. Nano Mater. 2019, 2, 5108−5115

Flanders (FWO-Vl) and Japan Society for the Promotion of Science (JSPS) (JSPS-FWO Grant VS.059.18N). F.N. is supported in part by the MURI Center for Dynamic Magneto-Optics via the Air Force Office of Scientifc Research (AFOSR) (FA9550-14-1-0040), Army Research Office (ARO) (Grant 73315PH), Asian Office of Aerospace Research and Development (AOARD) (Grant FA2386-18-1-4045), Japan Science and Technology Agency (JST) (the Q-LEAP program and CREST Grant JPMJCR1676), Japan Society for the Promotion of Science (JSPS) (JSPS-RFBR Grant 17-52-50023), RIKEN-AIST Challenge Research Fund. Research was conducted within the framework of the COST Action CA16218 (NANOCOHYBRI) of the European Cooperation in Science and Technology.

REFERENCES

(1) Kleiner, R.; Buckel, W. *Superconductivity*, 3rd ed.; Wiley-VCH: Weinheim, 2016.
(2) Civale, L. Vortex pinning and creep in high-temperature superconductors with columnar defects. *Supercond. Sci. Technol.* **1997**, *10*, A11−A28.
(3) Haugan, T.; Barnes, P. N.; Wheeler, R.; Meisenkothen, F.; Sumption, M. Addition of nanoparticle dispersions to enhance flux pinning of the $YBa_2Cu_3O_{7-\delta}$ superconductor. *Nature* **2004**, *430*, 867.
(4) Sefrioui, Z.; Arias, D.; González, E. M.; Léon, C.; Santamaria, J.; Vicent, J. L. Vortex liquid entanglement in irradiated $YBa_2Cu_3O_{7-\delta}$ thin films. *Phys. Rev. B: Condens. Matter Mater. Phys.* **2001**, *63*, 064503.
(5) Lang, W.; Enzenhofer, T.; Peruzzi, M.; Pedarnig, J. D.; Bäuerle, D.; Horner, C.; Cekan, E.; Platzgummer, E.; Loeschner, H. Tailoring the transport properties of $YBa_2Cu_3O_{7-\delta}$ thin films by light-ion irradiation. *Inst. Phys. Conf. Ser.* **2004**, *181*, 1549−1555.
(6) Cybart, S. A.; Yen, P. X. T.; Cho, E. Y.; Huh, J. U.; Glyantsev, V. N.; Yung, C. S.; Moeckly, B.; Beeman, J. W.; Dynes, R. C. Comparison of Y−Ba−Cu−O Films Irradiated With Helium and Neon Ions for the Fabrication of Josephson Devices. *IEEE Trans. Appl. Supercond.* **2014**, *24*, 1−5.
(7) Lang, W.; Dineva, M.; Marksteiner, M.; Enzenhofer, T.; Siraj, K.; Peruzzi, M.; Pedarnig, J. D.; Bäuerle, D.; Korntner, R.; Cekan, E.; Platzgummer, E.; Loeschner, H. Ion-beam direct-structuring of high-temperature superconductors. *Microelectron. Eng.* **2006**, *83*, 1495−1498.
(8) Lang, W.; Richter, H.; Marksteiner, M.; Siraj, K.; Bodea, M. A.; Pedarnig, J. D.; Grigoropoulos, C.; Bäuerle, D.; Hasenfuss, C.; Palmetshofer, L.; Kolarova, R.; Bauer, P. Masked ion beam irradiation of high-temperature superconductors: patterning of nano-size regions with high point-defect density. *Int. J. Nanotechnol.* **2009**, *6*, 704−14.
(9) Pedarnig, J. D.; Siraj, K.; Bodea, M. A.; Puica, I.; Lang, W.; Kolarova, R.; Bauer, P.; Haselgrübler, K.; Hasenfuss, C.; Beinik, I.; Teichert, C. Surface planarization and masked ion-beam structuring of $YBa_2Cu_3O_7$ thin films. *Thin Solid Films* **2010**, *518*, 7075−80.
(10) Swiecicki, I.; Ulysse, C.; Wolf, T.; Bernard, R.; Bergeal, N.; Briatico, J.; Faini, G.; Lesueur, J.; Villegas, J. E. Strong field-matching effects in superconducting $YBa_2Cu_3O_{7-\delta}$ films with vortex energy landscapes engineered via masked ion irradiation. *Phys. Rev. B: Condens. Matter Mater. Phys.* **2012**, *85*, 224502.
(11) Trastoy, J.; Rouco, V.; Ulysse, C.; Bernard, R.; Palau, A.; Puig, T.; Faini, G.; Lesueur, J.; Briatico, J.; Villegas, J. E. Unusual magneto-transport of $YBa_2Cu_3O_{7-\delta}$ films due to the interplay of anisotropy, random disorder and nanoscale periodic pinning. *New J. Phys.* **2013**, *15*, 103022.
(12) Haag, L. T.; Zechner, G.; Lang, W.; Dosmailov, M.; Bodea, M. A.; Pedarnig, J. D. Strong vortex matching effects in YBCO films with periodic modulations of the superconducting order parameter fabricated by masked ion irradiation. *Physica C* **2014**, *503*, 75−81.
(13) Zechner, G.; Jausner, F.; Haag, L. T.; Lang, W.; Dosmailov, M.; Bodea, M. A.; Pedarnig, J. D. Hysteretic Vortex-Matching Effects in High-T_c Superconductors with Nanoscale Periodic Pinning Landscapes Fabricated by He Ion-Beam Projection. *Phys. Rev. Appl.* **2017**, *8*, 014021.
(14) Yang, C. et al. Quantum coherence across bosonic superconductor-anomalous metal-insulator transitions. arXiv:1901.07706 [cond-mat.supr-con], 2019.
(15) Moshchalkov, V. V.; Fritzsche, J. *Nanostructured Superconductors*; World Scientific: Singapore, 2011.
(16) Welp, U.; Xiao, Z. L.; Jiang, J. S.; Vlasko-Vlasov, V. K.; Bader, S. D.; Crabtree, G. W.; Liang, J.; Chik, H.; Xu, J. M. Superconducting transition and vortex pinning in Nb films patterned with nanoscale hole arrays. *Phys. Rev. B: Condens. Matter Mater. Phys.* **2002**, *66*, 212507.
(17) Hallet, X.; Mátéfi-Tempfli, M.; Michotte, S.; Piraux, L.; Vanacken, J.; Moshchalkov, V. V.; Mátéfi-Tempfli, S. Quasi-Hexagonal Vortex-Pinning Lattice Using Anodized Aluminum Oxide Nanotemplates. *Small* **2009**, *5*, 2413−2416.
(18) Wölbing, R.; Schwarz, T.; Müller, B.; Nagel, J.; Kemmler, M.; Kleiner, R.; Koelle, D. Optimizing the spin sensitivity of grain boundary junction nanoSQUIDs − towards detection of small spin systems with single-spin resolution. *Supercond. Sci. Technol.* **2014**, *27*, 125007.
(19) Thiel, L.; Rohner, D.; Ganzhorn, M.; Appel, P.; Neu, E.; Müller, B.; Kleiner, R.; Koelle, D.; Maletinsky, P. Quantitative nanoscale vortex imaging using a cryogenic quantum magnetometer. *Nat. Nanotechnol.* **2016**, *11*, 677−681.
(20) Martínez-Pérez, M. J.; Müller, B.; Schwebius, D.; Korinski, D.; Kleiner, R.; Sesé, J.; Koelle, D. NanoSQUID magnetometry of individual cobalt nanoparticles grown by focused electron beam induced deposition. *Supercond. Sci. Technol.* **2017**, *30*, 024003.
(21) Rohner, D.; Thiel, L.; Müller, B.; Kasperczyk, M.; Kleiner, R.; Koelle, D.; Maletinsky, P. Real-space probing of the local magnetic response of thin-film superconductors using single spin magnetometry. *Sensors* **2018**, *18*, 3790.
(22) Dam, B.; Huijbregtse, J. M.; Klaassen, F. C.; van-der Geest, R. C. F.; Doornbos, G.; Rector, J. H.; Testa, A. M.; Freisem, S.; Martinez, J. C.; Stäuble-Pümpin, B.; Griessen, R. Origin of high critical currents in $YBa_2Cu_3O_{7-\delta}$ superconducting thin films. *Nature* **1999**, *399*, 439−442.
(23) Castellanos, A.; Wördenweber, R.; Ockenfuss, G.; Hart, A. v. d.; Keck, K. Preparation of regular arrays of antidots in $YBa_2Cu_3O_7$ thin films and observation of vortex lattice matching effects. *Appl. Phys. Lett.* **1997**, *71*, 962−964.
(24) https://www.zeiss.com/microscopy/int/products/multiple-ion-beam/orion-nanofab-for-materials.html.2019-05-17.
(25) Ward, B. W.; Notte, J. A.; Economou, N. P. Helium ion microscope: A new tool for nanoscale microscopy and metrology. *J. Vac. Sci. Technol. B* **2006**, *24*, 2871−2874.
(26) Hlawacek, G., Gölzhäuser, A., Eds.; *Helium Ion Microscopy*; Springer International Publishing: Switzerland, 2016.
(27) Flatabø, R.; Agarwal, A.; Hobbs, R.; Greve, M. M.; Holst, B.; Berggren, K. K. Exploring proximity effects and large depth of field in helium ion beam lithography: large-area dense patterns and tilted surface exposure. *Nanotechnology* **2018**, *29*, 275301.
(28) Emmrich, D.; Beyer, A.; Nadzeyka, A.; Bauerdick, S.; Meyer, J. C.; Kotakoski, J.; Gölzhäuser, A. Nanopore fabrication and characterization by helium ion microscopy. *Appl. Phys. Lett.* **2016**, *108*, 163103.
(29) Cybart, S. A.; Cho, E. Y.; Wong, T. J.; Wehlin, B. H.; Ma, M. K.; Huynh, C.; Dynes, R. C. Nano Josephson superconducting tunnel junctions in $YBa_2Cu_3O_{7-\delta}$ directly patterned with a focused helium ion beam. *Nat. Nanotechnol.* **2015**, *10*, 598.
(30) Cho, E. Y.; Ma, M. K.; Huynh, C.; Pratt, K.; Paulson, D. N.; Glyantsev, V. N.; Dynes, R. C.; Cybart, S. A. $YBa_2Cu_3O_{7-\delta}$ superconducting quantum interference devices with metallic to insulating barriers written with a focused helium ion beam. *Appl. Phys. Lett.* **2015**, *106*, 252601.
(31) Cho, E. Y.; Zhou, Y. W.; Cho, J. Y.; Cybart, S. A. Superconducting nano Josephson junctions patterned with a focused helium ion beam. *Appl. Phys. Lett.* **2018**, *113*, 022604.

DOI: 10.1021/acsanm.9b01006
ACS Appl. Nano Mater. 2019, 2, 5108−5115

(32) Müller, B.; Karrer, M.; Limberger, F.; Becker, M.; Schröppel, B.; Burkhardt, C. J.; Kleiner, R.; Goldobin, E.; Koelle, D. Josephson Junctions and SQUIDs Created by Focused Helium-Ion-Beam Irradiation of $YBa_2Cu_3O_7$. *Phys. Rev. Appl.* **2019**, *11*, 044082.
(33) Sekirnjak, C.; Lang, W.; Proyer, S.; Schwab, P. Novel approach for the analysis of the fluctuation magnetoconductivity in $YBa_2Cu_3O_7$ thin films. *Physica C* **1995**, *243*, 60−68.
(34) Ziegler, J. F.; Ziegler, M. D.; Biersack, J. P. SRIM − The stopping and range of ions in matter (2010). *Nucl. Instrum. Methods Phys. Res., Sect. B* **2010**, *268*, 1818−23.
(35) Mletschnig, K. L.; Lang, W. Nano-patterning of cuprate superconductors by masked He^+ ion irradiation: 3-dimensional profiles of the local critical temperature. *Microelectron. Eng.* **2019**, *215*, 110982.
(36) Niebieskikwiat, D.; Silhanek, A.; Civale, L.; Nieva, G.; Levy, P.; Krusin-Elbaum, L. Suppression of matching field effects by splay and pinning energy dispersion in $YBa_2Cu_3O_7$-with columnar defects. *Phys. Rev. B: Condens. Matter Mater. Phys.* **2001**, *63*, 144504.
(37) Ooi, S.; Mochiku, T.; Yu, S.; Sadki, E. S.; Hirata, K. Matching effect of vortex lattice in $Bi_2Sr_2CaCu_2O_{8+y}$ with artificial periodic defects. *Physica C* **2005**, *426*, 113−117.
(38) Laguna, M. F.; Balseiro, C. A.; Domínguez, D.; Nori, F. Vortex structure and dynamics in kagomé and triangular pinning potentials. *Phys. Rev. B: Condens. Matter Mater. Phys.* **2001**, *64*, 104505.
(39) Misko, V.; Savel'ev, S.; Nori, F. Critical Currents in Quasiperiodic Pinning Arrays: Chains and Penrose Lattices. *Phys. Rev. Lett.* **2005**, *95*, 177007.
(40) Misko, V. R.; Savel'ev, S.; Nori, F. Critical currents in superconductors with quasiperiodic pinning arrays: One-dimensional chains and two-dimensional Penrose lattices. *Phys. Rev. B: Condens. Matter Mater. Phys.* **2006**, *74*, 024522.
(41) Reichhardt, C.; Olson Reichhardt, C. J. Vortex molecular crystal and vortex plastic crystal states in honeycomb and kagomé pinning arrays. *Phys. Rev. B: Condens. Matter Mater. Phys.* **2007**, *76*, 064523.
(42) Kemmler, M.; Gürlich, C.; Sterck, A.; Pöhler, H.; Neuhaus, M.; Siegel, M.; Kleiner, R.; Koelle, D. Commensurability effects in superconducting Nb films with quasiperiodic pinning arrays. *Phys. Rev. Lett.* **2006**, *97*, 147003.
(43) Misko, V. R.; Bothner, D.; Kemmler, M.; Kleiner, R.; Koelle, D.; Peeters, F. M.; Nori, F. Enhancing the critical current in quasiperiodic pinning arrays below and above the matching magnetic flux. *Phys. Rev. B: Condens. Matter Mater. Phys.* **2010**, *82*, 184512.
(44) Bothner, D.; Seidl, R.; Misko, V. R.; Kleiner, R.; Koelle, D.; Kemmler, M. Unusual commensurability effects in quasiperiodic pinning arrays induced by local inhomogeneities of the pinning site density. *Supercond. Sci. Technol.* **2014**, *27*, 065002.
(45) Villegas, J. E.; Montero, M. I.; Li, C.-P.; Schuller, I. K. Correlation length of quasiperiodic vortex lattices. *Phys. Rev. Lett.* **2006**, *97*, 027002.
(46) Silhanek, A. V.; Gillijns, W.; Moshchalkov, V. V.; Zhu, B. Y.; Moonens, J.; Leunissen, L. H. A. Enhanced pinning and proliferation of matching effects in a superconducting film with a Penrose array of magnetic dots. *Appl. Phys. Lett.* **2006**, *89*, 152507.
(47) Kramer, R. B. G.; Silhanek, A. V.; Van de Vondel, J.; Raes, B.; Moshchalkov, V. V. Symmetry-Induced Giant Vortex State in a Superconducting Pb Film with a Fivefold Penrose Array of Magnetic Pinning Centers. *Phys. Rev. Lett.* **2009**, *103*, 067007.
(48) Perez de Lara, D.; Alija, A.; Gonzalez, E. M.; Velez, M.; Martin, J. I.; Vicent, J. L. Vortex ratchet reversal at fractional matching fields in kagomélike array with symmetric pinning centers. *Phys. Rev. B: Condens. Matter Mater. Phys.* **2010**, *82*, 174503.
(49) Latimer, M. L.; Berdiyorov, G. R.; Xiao, Z. L.; Kwok, W. K.; Peeters, F. M. Vortex interaction enhanced saturation number and caging effect in a superconducting film with a honeycomb array of nanoscale holes. *Phys. Rev. B: Condens. Matter Mater. Phys.* **2012**, *85*, 012505.
(50) Cuppens, J.; Ataklti, G. W.; Gillijns, W.; Van de Vondel, J.; Moshchalkov, V. V.; Silhanek, A. V. Vortex Dynamics in a Superconducting Film with a Kagome and a Honeycomb Pinning Landscape. *J. Supercond. Novel Magn.* **2011**, *24*, 7−11.
(51) Libal, A.; Olson Reichhardt, C. J.; Reichhardt, C. Creating artificial ice states using vortices in nanostructured superconductors. *Phys. Rev. Lett.* **2009**, *102*, 237004.
(52) Latimer, M. L.; Berdiyorov, G. R.; Xiao, Z. L.; Peeters, F. M.; Kwok, W. K. Realization of Artificial Ice Systems for Magnetic Vortices in a Superconducting MoGe Thin Film with Patterned Nanostructures. *Phys. Rev. Lett.* **2013**, *111*, 067001.
(53) Xue, C.; Ge, J.-Y.; He, A.; Zharinov, V. S.; Moshchalkov, V. V.; Zhou, Y. H.; Silhanek, A. V.; Van de Vondel, J. Tunable artificial vortex ice in nanostructured superconductors with a frustrated kagome lattice of paired antidots. *Phys. Rev. B: Condens. Matter Mater. Phys.* **2018**, *97*, 134506.
(54) Trastoy, J.; Malnou, M.; Ulysse, C.; Bernard, R.; Bergeal, N.; Faini, G.; Lesueur, J.; Briatico, J.; Villegas, J. E. Freezing and thawing of artificial ice by thermal switching of geometric frustration in magnetic flux lattices. *Nat. Nanotechnol.* **2014**, *9*, 710−715.
(55) Reichhardt, C.; Olson, C. J.; Nori, F. Commensurate and incommensurate vortex states in superconductors with periodic pinning arrays. *Phys. Rev. B: Condens. Matter Mater. Phys.* **1998**, *57*, 7937−7943.
(56) Misko, V. R.; Nori, F. Magnetic flux pinning in superconductors with hyperbolic-tessellation arrays of pinning sites. *Phys. Rev. B: Condens. Matter Mater. Phys.* **2012**, *85*, 184506.
(57) Khalfin, I. B.; Shapiro, B. Y. Relaxation of magnetic flux in a superconductor with a system of columnar defects. *Physica C* **1993**, *207*, 359−365.
(58) Togawa, Y.; Harada, K.; Akashi, T.; Kasai, H.; Matsuda, T.; Nori, F.; Maeda, A.; Tonomura, A. Direct Observation of Rectified Motion of Vortices in a Niobium Superconductor. *Phys. Rev. Lett.* **2005**, *95*, 087002.
(59) Wambaugh, J. F.; Reichhardt, C.; Olson, C. J.; Marchesoni, F.; Nori, F. Superconducting fluxon pumps and lenses. *Phys. Rev. Lett.* **1999**, *83*, 5106−5109.
(60) Hastings, M. B.; Olson Reichhardt, C. J.; Reichhardt, C. Ratchet cellular automata. *Phys. Rev. Lett.* **2003**, *90*, 247004.
(61) Milošević, M. V.; Berdiyorov, G. R.; Peeters, F. M. Fluxonic cellular automata. *Appl. Phys. Lett.* **2007**, *91*, 212501.
(62) Heine, G.; Lang, W. Magnetoresistance of the new ceramic 'Cernox' thermometer from 4.2 to 300 K in magnetic fields up to 13 T. *Cryogenics* **1998**, *38*, 377−379.

DOI: 10.1021/acsanm.9b01006
ACS Appl. Nano Mater. 2019, 2, 5108−5115

Ultradense Tailored Vortex Pinning Arrays in Superconducting $YBa_2Cu_3O_{7-\delta}$ Thin Films Created by Focused He Ion-Beam Irradiation for Fluxonics Applications

Bernd Aichner,[†] Benedikt Müller,[‡] Max Karrer,[‡] Vyacheslav R. Misko,[¶,§,‖] Fabienne Limberger,[‡] Kristijan L. Mletschnig,[†] Meirzhan Dosmailov,[⊥,#] Johannes D. Pedarnig,[⊥] Franco Nori,[§,@] Reinhold Kleiner,[‡] Dieter Koelle,[‡] and Wolfgang Lang[*,†]

[†]*Faculty of Physics, University of Vienna, Wien, Austria*

[‡]*Physikalisches Institut and Center for Quantum Science (CQ) in LISA*$^+$*, Universität Tübingen, Tübingen, Germany*

[¶]*Department of Physics, Universiteit Antwerpen, Antwerpen, Belgium*

[§]*Theoretical Quantum Physics Laboratory, RIKEN Cluster for Pioneering Research, Wako-shi, Saitama, Japan*

[‖]*μFlow group, Department of Chemical Engineering, Vrije Universiteit Brussel, Brussels, Belgium*

[⊥]*Institute of Applied Physics, Johannes Kepler University Linz, Linz, Austria*

[#]*Current address: Al-Farabi Kazakh National University, Almaty, Kazakhstan*

[@]*Physics Department, University of Michigan, Ann Arbor, USA*

E-mail: wolfgang.lang@univie.ac.at

Supporting Information

Critical current and resistance data of a square array of vortex pinning centers fabricated by irradiation in the helium ion microscope

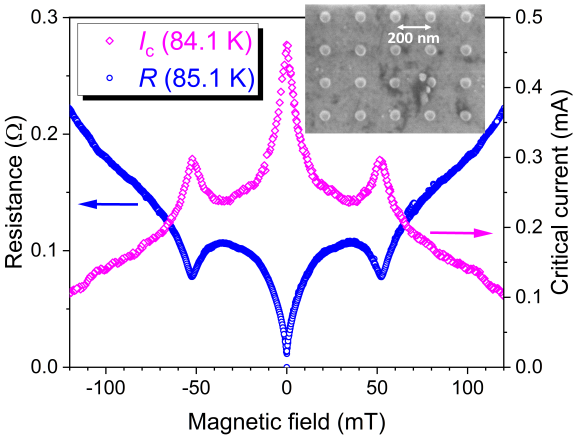

Figure S1: Critical current I_c and resistance R of a 80-nm thick YBCO film, irradiated in a HIM with a square pattern of beam spots (50 nm FWHM) with a lattice constant of 200 nm. The matching field determined from the geometric parameters is $B_m = 52$ mT and leads to a peak in the critical current and a minimum of the resistance. Inset: HIM image of a square array of defects induced by the focused ion beam of the HIM. Irradiation was performed with 5×10^6 ions/spot to visualize the pattern, a much larger fluence than it was used for preparation of the actual sample.

A square array of columnar defect cylinders (CDs) has been fabricated in the helium ion microscope with an intentionally defocused ion beam of FWHM = 50 nm and point-to-point distance $a = 200$ nm in a 80-nm thick YBCO film. The parameters were chosen similar to previous experiments performed with masked ion beam irradiation.[1–4] The critical current $I_c(B_a)$ shows a distinct peak and the magnetoresistance $R(B_a)$ a minimum when each defect is filled with one vortex at an applied magnetic field B_a that fulfils the matching condition for single-vortex occupation of every CD, $B_1 = \Phi_0/a^2$, where Φ_0 is the magnetic

flux quantum and $a = 200\,\mathrm{nm}$ the lattice constant of the square pinning array. The vortex commensurability effects displayed in Fig. S1 appear exactly at the calculated matching field $B_1 = 52\,\mathrm{mT}$.

References

(1) Swiecicki, I.; Ulysse, C.; Wolf, T.; Bernard, R.; Bergeal, N.; Briatico, J.; Faini, G.; Lesueur, J.; Villegas, J. E. Strong field-matching effects in superconducting $YBa_2Cu_3O_{7-\delta}$ films with vortex energy landscapes engineered via masked ion irradiation. *Phys. Rev. B* **2012**, *85*, 224502.

(2) Trastoy, J.; Rouco, V.; Ulysse, C.; Bernard, R.; Palau, A.; Puig, T.; Faini, G.; Lesueur, J.; Briatico, J.; Villegas, J. E. Unusual magneto-transport of $YBa_2Cu_3O_{7-\delta}$ films due to the interplay of anisotropy, random disorder and nanoscale periodic pinning. *New J. Phys.* **2013**, *15*, 103022.

(3) Haag, L. T.; Zechner, G.; Lang, W.; Dosmailov, M.; Bodea, M. A.; Pedarnig, J. D. Strong vortex matching effects in YBCO films with periodic modulations of the superconducting order parameter fabricated by masked ion irradiation. *Physica C* **2014**, *503*, 75–81.

(4) Zechner, G.; Jausner, F.; Haag, L. T.; Lang, W.; Dosmailov, M.; Bodea, M. A.; Pedarnig, J. D. Hysteretic Vortex-Matching Effects in High-T_c Superconductors with Nanoscale Periodic Pinning Landscapes Fabricated by He Ion-Beam Projection. *Phys. Rev. Applied* **2017**, *8*, 014021.

Publication 8

Low Temperature Physics ARTICLE scitation.org/journal/ltp

Angular magnetic-field dependence of vortex matching in pinning lattices fabricated by focused or masked helium ion beam irradiation of superconducting $YBa_2Cu_3O_{7-\delta}$ thin films

Cite as: Fiz. Nizk. Temp. **46**, 402–409 (April 2020); doi: 10.1063/10.0000863
Submitted: 20 February 2020

B. Aichner,[1] K. L. Mletschnig,[1] B. Müller,[2] M. Karrer,[2] M. Dosmailov,[3,4] J. D. Pedarnig,[3] R. Kleiner,[2] D. Koelle,[2] and W. Lang[1,a)]

AFFILIATIONS

[1]University of Vienna, Faculty of Physics, Electronic Properties of Materials, Boltzmanngasse 5, A-I 090 Wien, Austria
[2]Physikalisches Institut and Center for Quantum Science (CQ) in LISA+, Universität Tübingen, Auf der Morgenstelle 14, D-72076 Tübingen, Germany
[3]Johannes-Kepler-University Linz, Institute of Applied Physics, Altenbergerstrasse 69, A-4040 Linz, Austria
[4]Al-Farabi Kazakh National University, Almaty, Kazakhstan

[a)]**Author to whom correspondence should be addressed:** wolfgang.lang@univie.ac.at

ABSTRACT

The angular dependence of magnetic-field commensurability effects in thin films of the cuprate high-critical-temperature superconductor $YBa_2Cu_3O_{7-\delta}$ (YBCO) with an artificial pinning landscape is investigated. Columns of point defects are fabricated by two different methods of ion irradiation — scanning the focused 30 keV ion beam in a helium ion microscope or employing the wide-field 75 keV He^+ beam of an ion implanter through a stencil mask. Simulations of the ion-target interactions and the resulting collision cascades reveal that with both methods square arrays of defect columns with sub-μm spacings can be created. They consist of dense point-defect clusters, which act as pinning centers for Abrikosov vortices. This is verified by the measurement of commensurable peaks of the critical current and related minima of the flux-flow resistance vs magnetic field at the matching fields. In oblique magnetic fields, the matching features are exclusively governed by the component of the magnetic field parallel to the axes of the columnar defects, which confirms that the magnetic flux is penetrated along the defect columns. We demonstrate that the latter dominate the pinning landscape despite of the strong intrinsic pinning in thin YBCO films.

1. INTRODUCTION

Most of the superconducting materials belong to the type II class, into which a magnetic field can penetrate as flux quanta $\Phi_0 = h/(2e)$, where h is Planck's constant and e the elementary charge. These flux quanta are known as Abrikosov vortices, whirls of the supercurrent that confine the magnetic flux into the cylindrical vortex core, a region with vanishing density of superconducting charge carrier pairs. In clean and isotropic bulk superconductors these vortices arrange themselves in a two-dimensional hexagonal lattice with the axes of the vortex cores oriented parallel to the external magnetic field.

In the cuprate high-temperature superconductors (HTSCs) the situation is more complex and vortices can exist in a large range of magnetic fields between a tiny lower critical field $B_{c1}(85\,K) \sim 2$ mT and a high upper critical field $B_{c2}(85\,K) \sim 20$ T at temperatures relevant for the present study and for magnetic fields orthogonal to the CuO_2 atomic layers.[1] The high anisotropy of the HTSCs favors a decomposition of the cylindrical vortices into a stack of coupled "pancake" vortices,[2] which can be visualized, e.g., in $Bi_2Sr_2CaCu_2O_8$.[3]

The arrangement of vortices in type-II superconductors can be tailored by the introduction of artificial defects as pinning sites for vortices. Those defects can be classified by their dimensionality

and can severely disturb the native hexagonal vortex arrangement. Zero-dimensional (0D) point defects can be introduced as tiny non-superconducting impurities *in situ* during fabrication[4] or by postprocessing with electron[5] or light-ion irradiation of HTSCs.[6] One-dimensional (1D) defects are commonly created by irradiation with swift heavy ions that produce amorphous channels with diameters of several nm, i.e., a few times the in-plane coherence length. They have been extensively investigated as a tool to enhance the critical current density.[7] Finally, grain boundaries and, in the prototypical HTSC $YBa_2Cu_3O_{7-\delta}$ (YBCO) also twin planes, can form two-dimensional (2D) defects that can pin vortices.

The dimensionality of the artificial defects is revealed by different angle-dependent behavior in tilted magnetic fields of superconducting properties like the critical current I_c, the vortex-flow resistance R, and B_{c2}. While point defects lead to a marginal angular dependence, randomly distributed yet parallel oriented 1D columnar defects cause narrow features in I_c, R, and magnetization vs field direction, centered around the magnetic field direction parallel to their symmetry axes.[8–10] Similar observations hold for 2D defect planes in YBCO when the magnetic field is rotated through a direction that is oriented parallel to these planes.[11]

In this work, we investigate artificial pinning lattices that are different in two aspects. First, they are neither strictly 0D or 1D, since they consist of dense point defects that form columnar defect clusters (CDs) with diameters at least one order of magnitude larger than the in-plane coherence length $\xi_{ab}(0) = 1.2$ nm in YBCO.[12] Second, these CDs are arranged in a periodic pattern that gives rise to commensurability effects at matching vortex and defect densities. Such commensurability effects have been primarily studied in metallic superconductors using arrays of holes (antidots)[13–19] or magnetic dots[20] in the material, nanogrooves,[21–23] and superlattices[24] but are also found in YBCO perforated with holes.[25]

The fabrication techniques of pinning arrays in our samples are based on the observation that irradiation of YBCO thin films with He^+ ions of moderate energy introduces point defects by displacing mainly oxygen atoms. This leads to a reduction of the transition temperature T_c,[26] which can be well controlled by the ion fluence.[6,27–29] By ion irradiation through a shadow mask[30–38] or using the focused ion beam of a He ion microscope (HIM)[39] an array of CDs can be created that acts as a pinning landscape for vortices.

Only few investigations have addressed the angular dependence of vortex commensurability effects in metallic superconductors with antidots[16,40] and in YBCO thin films patterned with periodic CDs by ion irradiation.[34,37]

The purpose of this study is to explore whether the pinning landscapes created in YBCO by focused He^+ ion irradiation in a HIM act as 1D line-like pinning centers despite of consisting of 0D point defect clusters with inhomogeneous density.

2. EXPERIMENTAL METHODS

Epitaxial thin films of $YBa_2Cu_3O_{7-\delta}$ are grown on (100) MgO single-crystal substrates by pulsed-laser deposition using 248 nm KrF-excimer-laser radiation at a fluence of 3.2 J/cm^2. The thicknesses of the films used in this work are $t_z = (80 \pm 5)$ nm (sample SQ200) and $t_z = (210 \pm 10)$ nm (sample SQ500). The critical temperatures of the as-prepared films are $T_c \sim 90$ K with transition widths $\Delta T_c \sim 1$ K. The films are patterned by photolithography and wet chemical etching to form bridges with a length of 240 μm and a width of $w = 60$ μm. Electrical contacts in a four-probe geometry are established on side arms of the bridges using sputtered Au pads with a voltage probe distance of 100 μm.

In both samples, a tailored vortex pinning landscape was created by different methods of He^+ ion irradiation. Sample SQ200 was irradiated with an intentionally defocused ion beam in a HIM. The setup starts with adjusting the HIM settings to the highest resolution and then changing the working distance (beam focus plane) so that the beam hits the sample surface with a nearly Gaussian fluence profile[41] with a full width at half maximum (FWHM) of about 50 nm. Since the aperture angle of the ion beam is very small the ion beam hits the sample surface almost orthogonally. The method is described in detail elsewhere.[39]

By sequentially scanning the ion beam over the sample surface, a square lattice of columnar defects with $d = 200$ nm spacings is created in the thin YBCO film in an overall area of approximately 200 μm × 100 μm. Every point is irradiated with 30 keV He^+ ions with a dwell time of 2.7 ms and a beam current of 3 pA, corresponding to ~51000 He^+ ions/point. The method is sketched in Fig. 1(a).

Sample SQ500 is patterned by masked ion beam structuring (MIBS)[30] as sketched in Fig. 1(b). A 2 μm-thick Si stencil mask is placed on top of the YBCO film and adjusted in an optical microscope with the help of marker holes. The mask is separated from the surface of the YBCO film by a circumferential spacer layer made of 1.5 μm-thick photoresist. The stencil mask is perforated with holes with diameters $D = (180 \pm 5)$ nm, arranged in a square array of $d = (500 \pm 2)$ nm pitch, which covers the entire bridge. The stencil pattern is shadow projected onto the YBCO surface by irradiating the arrangement with a collinear 75 keV He^+ ion beam, oriented orthogonal to the sample surface, in a commercial ion implanter (High Voltage Engineering Europa B. V.).

Electrical transport measurements are performed in a closed-cycle cryocooler with temperature control by a Cernox resistor, which has a negligible temperature reading error in moderate magnetic fields.[42] The applied magnetic field $\mathbf{B_a}$ is supplied by a revolvable electromagnet with ±1° angular resolution and $B_a = |\mathbf{B_a}|$ is measured by a calibrated Hall probe mounted between the magnet's pole pieces. The Hall probe is connected to a LakeShore 475 gaussmeter, allowing for measurements of $\mathbf{B_a}$ with a zero offset <10 μT, and a reading accuracy <0.1%. The tilt angle α is defined as the angle between the surface normal of the YBCO film and the direction of $\mathbf{B_a}$. The angle-dependent magneto-resistance measurements are performed in constant Lorentz force geometry, i. e., the magnetic field is always perpendicular to the current direction. For all measurements, the current I through the sample is generated by a constant-current source in both polarities to eliminate thermoelectric signals and the voltage V is measured by a Keithley 2182A nano-voltmeter. The critical current $I_c(B_a)$ is determined from isothermal current-voltage (I–V) measurements with a voltage criterion of 100 nV, corresponding to 10 μV/cm. Since the I–V characteristics of a superconductor are nonlinear the resistance curves presented below are defined as $R(B_a) = V(B_a)/I$ at a fixed I. Note that the absolute value of $R(B_a)$ is not important for our analyses.

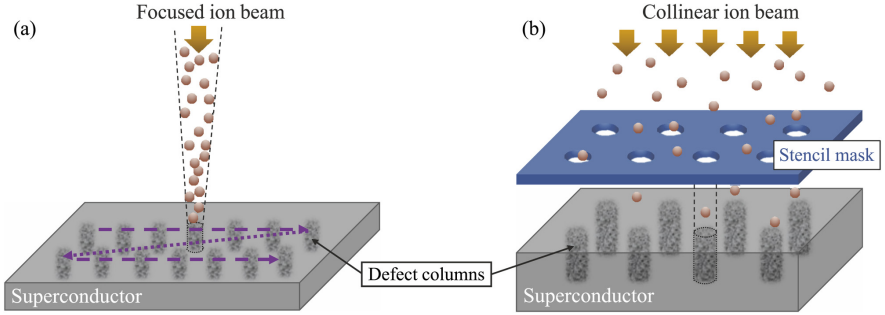

FIG. 1. Two different methods for patterning a YBCO film by He^+ ion irradiation: (a) Irradiation with a slightly defocused beam of a helium-ion microscope produces tailored columnar defect patterns by scanning the beam over the sample surface. The dark regions indicate the defect-rich, nonsuperconducting nanocylinders. (b) Ion beam direct patterning by irradiating through a stencil mask creates a large number of columnar defects in a single step.

3. RESULTS AND DISCUSSION

To compare the shapes of the artificial CD lattices, prepared by the two different irradiation methods, simulations of the defect distributions with the program package SRIM/TRIM[43,44] are performed. It computes the impact of ions on solids using a binary collision approximation of ion-atom and atom-atom collisions, and delivers the full collision cascades. However, ion channeling, thermal effects, diffusion, and recrystallization are not considered.

Details of the crystallographic structure are not considered in SRIM/TRIM as it uses a Monte Carlo method and assumes amorphous targets. For the spatial modulation of superconductivity, the Ginzburg–Landau coherence length is the relevant length parameter and therefore we have determined the average defect density within calculation cells of $2 \times 2 \times 2$ nm^3—a length scale of the order of the in-plane coherence length of YBCO. Note that the investigated point defect densities are below the amorphization limit and a comparison to an experimental visualization is hardly possible. Only by using a larger ion fluence, amorphous channels can be created and detected in cross-section scanning transmission electron microscopy images.[45]

The pinning potential for vortices is provided by a local suppression of T_c, which can be calculated from the defect density on the grounds of the pair-breaking theory of Abrikosov and Gor'kov.[46] Since annealing effects are not considered in SRIM/TRIM and various other effects may lead to substantial uncertainty, a "calibration" curve relating the experimentally observed T_c to the defect density from the simulations is established, using previous experimental T_c values from full-area irradiation of thin YBCO films.[28] Details of this procedure are described elsewhere.[47]

The resulting simulated cross-sectional T_c profiles for the two samples SQ200 and SQ500 are presented in Fig. 2 at the same scale for comparison. Note that sample SQ200 (top panel) was irradiated with a slightly defocused He^+ ion beam with approximately Gaussian normal distributed fluence of FWHM = 50 nm, whereas the fluence was homogeneous in the irradiated parts of sample SQ500. Another important difference is the ion energy of 30 keV for sample SQ200 and 75 keV for sample SQ500.

In thin films with $t_z \leq 80$ nm, 30 keV He^+ ion irradiation creates columns, within which T_c is suppressed, that are clearly separated from each other at 200 nm lattice spacing (Fig. 2, top panel). The suppression of T_c at the fringes of the CDs decays more gradually than for sample SQ500, which was irradiated by MIBS (Fig. 2, bottom panel). Still, the cylindrical envelope of clusters with suppressed T_c provides an efficient pinning landscape as will be discussed below.

Due to the larger penetration depth of the 75 keV He^+ ions, CDs can be patterned into thicker YBCO films with MIBS, as demonstrated in Fig. 2, bottom panel. However, the achievable lateral resolution for CD diameters degrades with increasing thickness of the film, as it can be noticed by the increasing diameter of the CD for film thicknesses larger than 120 nm. We note that increasing the ion energy would improve the resolution on the cost of a lower ion scattering cross-section, which would demand a higher ion fluence.

Although a few dispersed defects are created also outside the CDs by lateral straggling of the incident ions and the secondary collision cascades, their impact on the zero-field electrical transport properties is marginal as demonstrated by the experimentally determined small reduction of the critical temperature $\Delta T_c = 2.6$ K ($\Delta T_c = 4$ K) in sample SQ200 (SQ500) after irradiation.

In electric transport measurements, the commensurability effects evoked by regular pinning lattices are demonstrated in Fig. 3 as peaks in the critical current I_c and corresponding minima of the resistance vs applied field B_a (at $\alpha = 0°$) that appear exactly at the matching fields

$$B_n = n\frac{\Phi_0}{d^2}, \tag{1}$$

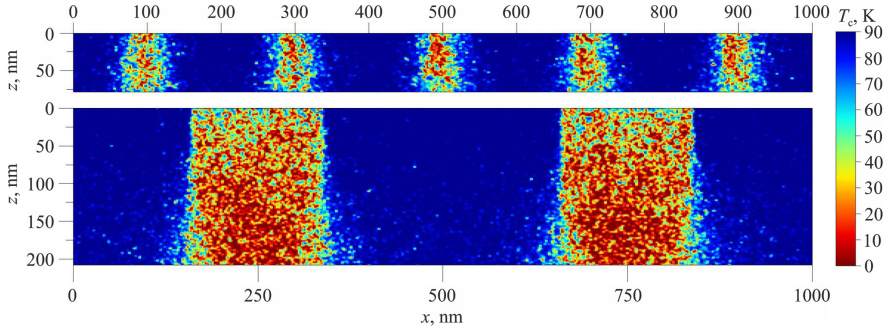

FIG. 2. Cross-sectional view of calculated local T_c profiles within and around the defect columns produced by 50900 ions per dot with 30 keV energy and a Gaussian normal distribution with 50 nm FWHM (sample SQ200, top panel) and 75 keV He^+ ion irradiation of YBCO with a fluence of $3{\cdot}10^{15}$ cm^{-2} (sample SQ500, bottom panel). Both panels are displayed at the same scale for a comparison between the two samples.

where n is a rational number. We use $n = 0$ to denote the absence of vortices and $n < 0$ for the reversed vortex orientation. When the diameters of the CDs are larger than the Ginzburg-Landau coherence length, an integer number $n > 1$ of fluxons can be accommodated per CD.[48] Note the tiny humps of I_c around ±26 mT that indicate a fractional matching pattern with $n = \pm(1/2)$.

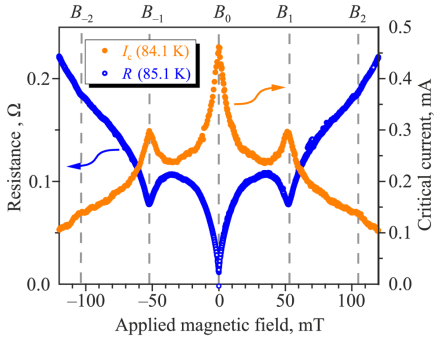

FIG. 3. Resistance $R(I = 50\ \mu A)$ and critical current I_c vs applied magnetic field at $\alpha = 0°$ of an 80-nm thick YBCO film (sample SQ200), irradiated with a slightly defocused He^+ ion beam of 50 nm FWHM to form a square pattern of defect cylinders with a lattice constant of 200 nm. Data were taken after zero-field cooling and then sweeping the field through a full cycle, revealing no hysteresis. The matching field determined from the geometric parameters is $B_1 = 52$ mT and leads to a minimum of the resistance and a peak in the critical current.

The commensurability effects result from two different vortex pinning mechanisms in our samples. On the one hand, n flux quanta can be trapped in the normal-conducting core of a CD, which we will call fluxons to discriminate them from the regular Abrikosov vortices in a plain superconductor. These fluxons remain pinned at the CDs even if a moderate current is applied to the sample. However, by changing the applied magnetic field, the Lorentz force due to increased shielding current exceeds the pinning potential and the fluxons can hop between neighboring CDs.[49]

On the other hand, vortices at interstitial positions between the CDs are pinned mainly by twin boundaries and growth defects in the YBCO films, most of them oriented parallel to the c axis.[50] Their pinning potentials are usually weaker than those of the fluxons trapped in the CDs. At a certain applied magnetic field Ba the critical current shows a peak when the magnetic flux through the sample is penetrating the sample via single fluxons trapped in each CD, which happens exactly at the matching field B_1 of Eq. (1). In this situation, the number of weakly-pinned interstitial vortices is minimized. An equivalent consideration leads to the explanation of the resistance minima observed at the same B_n. Typically, our samples patterned by masked or focused He ion irradiation show clear matching effects in a temperature range from $\sim 0.7T_c$ up to $\sim 0.9T_c$.[36,39] For our further considerations, it is important that the matching fields can be equally well determined from either I_c peaks or resistance minima, the latter allowing for much faster measurements.

An investigation of the angular dependence of the magnetoresistance can shed light on the nature and relative strength of the pinning of fluxons at the CDs and the pinning of interstitial vortices, respectively.

For dominant pinning at CDs, the magnetic flux should be preferentially trapped within the CDs irrespectively of the angle α

by which the applied magnetic field B_a is tilted off the axes of the CDs. Then, the commensurability peaks in I_c (B_a) and dips in $R(B_a)$ should appear if the component of B_a that is parallel to the axes of the CDs,

$$B_{\parallel} = B_a \cos\alpha, \tag{2}$$

fulfills the matching condition of Eq. (1).

Figure 4 shows the magnetoresistance of sample SQ200 for various tilt angles α at a temperature near the onset of dissipation. When the magnetic field B_a is oriented orthogonal to the sample surface and parallel to the axes of the CDs ($\alpha = 0°$) a distinct minimum at $B_1 = 52$ mT and a marginal one at $B_2 = 104$ mT confirms the commensurability effects. With increasing tilt angle α the magnetoresistance curves exhibit very similar matching resistance minima and change their shapes only slightly if data are plotted with the abscissa scaled to $B_{\parallel}$. Even at $\alpha = 70°$ the commensurability effect can be detected.

In sample SQ500 the situation is more complicated due to a hysteresis observed in the magnetic field sweeps. It originates from an unconventional terraced critical state[51] with domains in the sample[52] inside which the pinning centers are occupied by the same number n of fluxons and neighboring domains by $n \pm 1$. Such a hysteretic behavior has been investigated previously[36] and is beyond the scope of this work. Still, the considerations leading to Eq. (2) should hold. Indeed, Fig. 5 demonstrates that all the features observed in the $\alpha = 0°$ orientation of B_a appear at the same positions when the magnetic field is tilted and scaling to $B_{\parallel}$ is used. This not only applies to the first matching fields in upsweep ($B_{-1}^{\uparrow}$) and downsweep ($B_1^{\downarrow}$) conditions, but also to the hysteretic displacement of the minima with zero fluxon occupation of the relevant

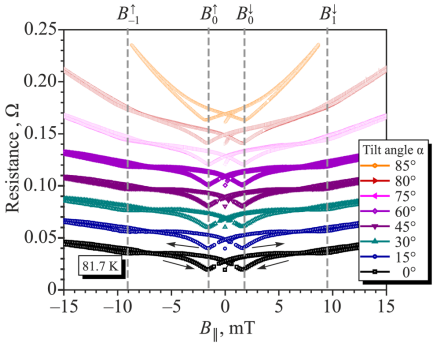

FIG. 5. Resistance ($I = 200$ μA) vs applied field component along the normal of the film surface $B_{\parallel}$ of sample SQ500 for different values of α. Data were taken after zero-field cooling and comprise the virgin curves starting from $B = 0$ and the up and down sweeps as representatively indicated by arrows in the bottom curve. Data for $\alpha > 0°$ are shifted by multiples of 0.02 Ω.

CDs ($B_0^{\uparrow}$ and $B_0^{\downarrow}$). Despite of the more complex fluxon arrangements in this sample, all commensurability effects are governed by $B_{\parallel}$, which confirms that only the component of the magnetic field is relevant that is parallel to the axes of the CDs.

In Fig. 6 the magnetic field components $B_{\parallel}$ at which the resistance dips for single fluxon matching are observed in sample

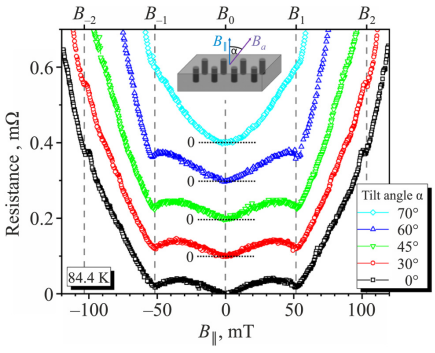

FIG. 4. Resistance ($I = 400$ μA) vs applied field component along the normal of the film surface $B_{\parallel}$ of sample SQ200 for different values of α. Since no hysteresis is observed, only the down sweep branches of the cycle after zero-field cooling are displayed. For $\alpha > 0°$ the curves are shifted by multiples of 0.1 mΩ to enhance visibility. The inset shows a sketch of the experimental situation.

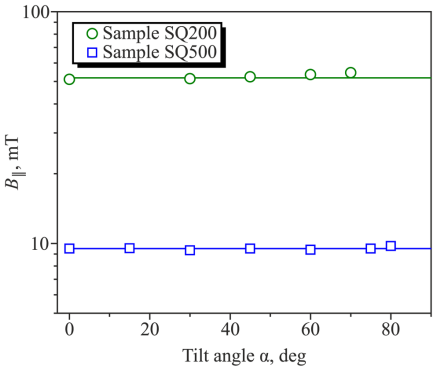

FIG. 6. Angular dependencies of the magnetic field components $B_{\parallel}$ at which the resistance dips for single fluxon matching (sample SQ200) and $B_1^{\downarrow}$ (sample SQ500) are observed. The horizontal lines indicate that $B_{\parallel}$ determines the matching effect, irrespective of the tilt angle α.

SQ200 (B_1) and SQ500 ($B_1^{\downarrow}$) are shown as a function of the tilt angle α. In remarkable agreement with Eq. (2) the experimental values are independent of α as indicated by the horizontal lines. This confirms that at all angles shown in the graph the magnetic flux is penetrated along the CDs. In addition, the adherence to Eq. (2) up to large tilt angles indicates that pinning at the CDs is much stronger than the intrinsic pinning of interstitial vortices in the intermediate regions between the CDs.

Some deviations from the behavior presented in Fig. 6 have been reported in denser pinning lattices. Due to lateral straggling of the collision cascades, a significant number of irradiation defects are created in the spaces between the CDs. This is indicated by $\Delta T_c = 43$ K after MIBS irradiation. In this case the scaling according to Eq. (2) gradually breaks down for $\alpha > 45°$.[37] In thin YBCO films patterned via 110 keV O^+ ion irradiation ($\Delta T_c \simeq 40$ K) a strong modification of the vortex-glass transition and a weakening of the vortex correlations along the c axis has been observed.[34]

Finally, in unirradiated YBCO, due to its anisotropy, the cylindrical vortices change to an elliptical cross-section in oblique magnetic fields $\alpha \neq 0°$ and decompose into a tilted stack of pancake vortices at tilt angles $\alpha \lesssim 54°$.[53] This is reflected by a broad maximum in the critical current extending over a range $\alpha \lesssim 60°$.[11] The feature evolves at temperatures closer to T_c and in moderate magnetic fields. In contrast to the observations in those unirradiated YBCO films, the matching fields B_1 in our samples strictly scale with Eq. (2) up to $\alpha = 72°$ ($\alpha = 80°$) for sample SQ200 (SQ500). Naturally, no pinning of fluxons by the CDs is expected when the CDs and B_a are oriented orthogonally, i.e., near $\alpha = 90°$.

4. CONCLUSIONS

Vortex pinning landscapes in YBCO thin films can be conveniently fabricated by employing He^+ ion irradiation, either by a focused beam in a HIM or by shadow-masking of a wide-field ion beam. As demonstrated by simulations of the defect distributions created in YBCO by the ion impact, the methods are complementary. HIM irradiation is a sequential method and allows for maskless operation and higher resolution of at least 10 nm,[45] but the penetration depth is limited to about 80 nm due to the maximum ion energy of 30 keV. With MIBS the entire pattern can be prepared at the same time and also in thicker films when using higher ion energies, but the lateral resolution is currently limited by a hole diameter of ∼180 nm of the available stencil masks.

Both methods, despite of their different length scales, produce well-defined CDs that provide strong pinning of fluxons, which is supported by the observation that at arbitrary angles of an applied magnetic field only the component parallel to the CDs governs the commensurability effects. Both irradiation methods appear suitable for the creation of well-defined tailored pinning landscapes in cuprate superconductors, which are an important prerequisite for proposed concepts of fluxon manipulation leading to fast and low-dissipation devices.[54–56]

ACKNOWLEDGMENTS

Research was conducted within the framework of the COST Action CA16218 (NANOCOHYBRI) of the European Cooperation in Science and Technology. B.M. acknowledges funding by the German Academic Scholarship Foundation. M.D. acknowledges the European Erasmus Mundus (Target II) program for financial support.

REFERENCES

[1]N. Kobayashi, H. Iwasaki, S. Terada, K. Noto, A. Tokiwa, M. Kikuchi, Y. Syono, and Y. Muto, Physica C **153–155**, 1525 (1988).
[2]J. R. Clem, Phys. Rev. B **43**, 7837 (1991).
[3]A. Correa, F. Mompeán, I. Guillamón, E. Herrera, M. García-Hernández, T. Yamamoto, T. Kashiwagi, K. Kadowaki, A. I. Buzdin, H. Suderow, and C. Munuera, Commun. Phys. **2**, 31 (2019).
[4]T. Haugan, P. N. Barnes, R. Wheeler, F. Meisenkothen, and M. Sumption, Nature **430**, 867 (2004).
[5]R. V. Vovk, G. Y. Khadzhai, and O. V. Dobrovolskiy, J. Mater. Sci. Mater. Electron. **30**, 241 (2019).
[6]W. Lang and J. D. Pedarnig, "Ion irradiation of high-temperature superconductors and its application for nanopatterning," in *Nanoscience and Engineering in Superconductivity*, edited by V. V. Moshchalkov, R. Wördenweber, and W. Lang (Springer, Heidelberg, 2010), p. 81.
[7]L. Civale, Supercond. Sci. Technol. **10**, A11 (1997).
[8]B. Holzapfel, G. Kreiselmeyer, M. Kraus, S. Bouffard, S. Klaumuenzer, L. Schultz, and G. Saemann-Ischenko, Phys. Rev. B **48**, 600 (1993).
[9]R. Prozorov, A. Tsameret, Y. Yeshurun, G. Koren, M. Konczykowski, and S. Bouffard, Physica C **234**, 311 (1994).
[10]A. V. Silhanek, L. Civale, and M. A. Avila, Phys. Rev. B **65**, 174525 (2002).
[11]B. Roas, L. Schultz, and G. Saemann-Ischenko, Phys. Rev. Lett. **64**, 479 (1990).
[12]C. Sekirnjak, W. Lang, S. Proyer, and P. Schwab, Physica C **243**, 60 (1995).
[13]A. T. Fiory, A. F. Hebard, and S. Somekh, Appl. Phys. Lett. **32**, 73 (1978).
[14]A. N. Lykov, Solid State Commun. **86**, 531 (1993).
[15]V. V. Metlushko, M. Baert, R. Jonckheere, V. V. Moshchalkov, and Y. Bruynseraede, Solid State Commun. **91**, 331 (1994).
[16]V. V. Metlushko, L. E. DeLong, M. Baert, E. Rosseel, M. J. Van Bael, K. Temst, V. V. Moshchalkov, and Y. Bruynseraede, Europhys. Lett. **41**, 333 (1998).
[17]M. Kemmler, C. Gürlich, A. Sterck, H. Pöhler, M. Neuhaus, M. Siegel, R. Kleiner, and D. Koelle, Phys. Rev. Lett. **97**, 147003 (2006).
[18]V. R. Misko, D. Bothner, M. Kemmler, R. Kleiner, D. Koelle, F. M. Peeters, and F. Nori, Phys. Rev. B **82**, 184512 (2010).
[19]V. V. Moshchalkov and J. Fritzsche, *Nanostructured Superconductors* (World Scientific, Singapore, 2011).
[20]M. Vélez, J. I. Martín, J. E. Villegas, A. Hoffmann, E. M. González, J. L. Vicent, and I. K. Schuller, J. Magn. Magn. Mater. **320**, 2547 (2008), and references therein.
[21]V. A. Shklovskij and O. V. Dobrovolskiy, Phys. Rev. B **74**, 104511 (2006).
[22]V. A. Shklovskij and O. V. Dobrovolskiy, Phys. Rev. B **78**, 104526 (2008).
[23]O. V. Dobrovolskiy, E. Begun, M. Huth, and V. A. Shklovskij, New J. Phys. **14**, 113027 (2012).
[24]O. V. Dobrovolskiy, V. M. Bevz, M. Y. Mikhailov, O. L. Yuzephovich, V. A. Shklovskij, R. V. Vovk, M. I. Tsindlekht, R. Sachser, and M. Huth, Nat. Commun. **9**, 4927 (2018).
[25]A. Castellanos, R. Wördenweber, G. Ockenfuss, A. v. d. Hart, and K. Keck, Appl. Phys. Lett. **71**, 962 (1997).
[26]X. Z. Wang, B. Hellebrand, D. Bäuerle, M. Strecker, G. Wortmann, and W. Lang, Physica C **242**, 55 (1995).
[27]Z. Sefrioui, D. Arias, E. M. González, C. Léon, J. Santamaria, and J. L. Vicent, Phys. Rev. B **63**, 064503 (2001).
[28]W. Lang, T. Enzenhofer, M. Peruzzi, J. D. Pedarnig, D. Bäuerle, C. Horner, E. Cekan, E. Platzgummer, and H. Loeschner, Inst. Phys. Conf. Ser. **181**, 1549 (2004).
[29]S. A. Cybart, P. X. T. Yen, E. Y. Cho, J. U. Huh, V. N. Glyantsev, C. S. Yung, B. Moeckly, J. W. Beeman, and R. C. Dynes, IEEE Trans. Appl. Supercond. **24**, 1 (2014).

[30]W. Lang, M. Dineva, M. Marksteiner, T. Enzenhofer, K. Siraj, M. Peruzzi, J. D. Pedarnig, D. Bäuerle, R. Korntner, E. Cekan, E. Platzgummer, and H. Loeschner, Microelectron. Eng. **83**, 1495 (2006).
[31]W. Lang, H. Richter, M. Marksteiner, K. Siraj, M. A. Bodea, J. D. Pedarnig, C. Grigoropoulos, D. Bäuerle, C. Hasenfuss, L. Palmetshofer, R. Kolarova, and P. Bauer, Int. J. Nanotechnol. **6**, 704 (2009).
[32]J. D. Pedarnig, K. Siraj, M. A. Bodea, I. Puica, W. Lang, R. Kolarova, P. Bauer, K. Haselgrübler, C. Hasenfuss, I. Beinik, and C. Teichert, Thin Solid Films **518**, 7075 (2010).
[33]I. Swiecicki, C. Ulysse, T. Wolf, R. Bernard, N. Bergeal, J. Briatico, G. Faini, J. Lesueur, and J. E. Villegas, Phys. Rev. B **85**, 224502 (2012).
[34]J. Trastoy, V. Rouco, C. Ulysse, R. Bernard, A. Palau, T. Puig, G. Faini, J. Lesueur, J. Briatico, and J. E. Villegas, New J. Phys. **15**, 103022 (2013).
[35]L. T. Haag, G. Zechner, W. Lang, M. Dosmailov, M. A. Bodea, and J. D. Pedarnig, Physica C **503**, 75 (2014).
[36]G. Zechner, F. Jausner, L. T. Haag, W. Lang, M. Dosmailov, M. A. Bodea, and J. D. Pedarnig, Phys. Rev. Appl. **8**, 014021 (2017).
[37]G. Zechner, K. L. Mletschnig, W. Lang, M. Dosmailov, M. A. Bodea, and J. D. Pedarnig, Supercond. Sci. Technol. **31**, 044002 (2018).
[38]G. Zechner, W. Lang, M. Dosmailov, M. A. Bodea, and J. D. Pedarnig, Phys. Rev. B **98**, 104508 (2018).
[39]B. Aichner, B. Müller, M. Karrer, V. R. Misko, F. Limberger, K. L. Mletschnig, M. Dosmailov, J. D. Pedarnig, F. Nori, R. Kleiner, D. Koelle, and W. Lang, ACS Appl. Nano Mater. **2**, 5108 (2019).
[40]F. N. Womack, P. W. Adams, J. M. Valles, and G. Catelani, Phys. Rev. B **100**, 174505 (2019).
[41]D. Emmrich, A. Beyer, A. Nadzeyka, S. Bauerdick, J. C. Meyer, J. Kotakoski, and A. Gölzhäuser, Appl. Phys. Lett. **108**, 163103 (2016).
[42]G. Heine and W. Lang, Cryogenics **38**, 377 (1998).
[43]J. F. Ziegler, U. Littmark, and J. P. Biersack, *The Stopping and Range of Ions in Solids* (Pergamon, New York, 1985).
[44]J. F. Ziegler, M. D. Ziegler, and J. P. Biersack, Nucl. Instrum. Methods Phys. Res., Sect. B **268**, 1818 (2010).
[45]B. Müller, M. Karrer, F. Limberger, M. Becker, B. Schröppel, C. J. Burkhardt, R. Kleiner, E. Goldobin, and D. Koelle, Phys. Rev. Appl. **11**, 044082 (2019).
[46]A. A. Abrikosov and L. P. Gor'kov, Zh. Eksp. Teor. Fiz. **39**, 1781 (1960) [Sov. Phys. JETP **12**, 1243 (1961)].
[47]K. L. Mletschnig and W. Lang, Microelectron. Eng. **215**, 110982 (2019).
[48]A. I. Buzdin, Phys. Rev. B **47**, 11416 (1993).
[49]M. P. Sørensen, N. F. Pedersen, and M. Ögren, Physica C **533**, 40 (2017).
[50]B. Dam, J. M. Huijbregtse, F. C. Klaassen, R. C. F. van-der Geest, G. Doornbos, J. H. Rector, A. M. Testa, S. Freisem, J. C. Martinez, B. Stäuble-Pümpin, and R. Griessen, Nature **399**, 439 (1999).
[51]L. D. Cooley and A. M. Grishin, Phys. Rev. Lett. **74**, 2788 (1995).
[52]C. Reichhardt, J. Groth, C. J. Olson, S. B. Field, and F. Nori, Phys. Rev. B **54**, 16108 (1996); Erratum: Phys. Rev. B **56**, 14196 (1997).
[53]G. Blatter, M. Feigel'man, V. Geshkenbein, A. Larkin, and V. Vinokur, Rev. Mod. Phys. **66**, 1125 (1994).
[54]J. F. Wambaugh, C. Reichhardt, C. J. Olson, F. Marchesoni, and F. Nori, Phys. Rev. Lett. **83**, 5106 (1999).
[55]M. B. Hastings, C. J. Olson Reichhardt, and C. Reichhardt, Phys. Rev. Lett. **90**, 247004 (2003).
[56]M. V. Milošević, G. R. Berdiyorov, and F. M. Peeters, Appl. Phys. Lett. **91**, 212501 (2007).

Translated by AIP Author Services

Publication 9

Reproduced with permission from
B. Müller *et al.*, 2019 IEEE International Superconductive Electronics Conference (ISEC) Proceedings (2019);
DOI: 10.1109/ISEC46533.2019.8990906.

IEEE International Superconductive Electronics Conference (ISEC), Riverside, CA, USA;
published by IEEE Xplore; DOI: 10.1109/ISEC46533.2019.8990906

$YBa_2Cu_3O_7$ and Nb NanoSQUIDs for the Investigation of Magnetization Reversal of Individual Magnetic Nanoparticles

B. Müller, J. Lin, J. Linek, M. Karrer, F. Limberger, L. Koch, E. Goldobin, R. Kleiner, D. Koelle
Physikalisches Institut and CQ in LISA+
Universität Tübingen
Tübingen, Germany

V. Morosh, T. Weimann, O. F. Kieler
Fachbereich 2.4 Quantenelektronik
Physikalisch Technische Bundesanstalt (PTB)
Braunschweig, Germany

J. Sesé, M. J. Martínez-Pérez
Instituto de Nanociencia de Aragón (INA)
Universidad de Zaragoza - CSIC
Zaragoza, Spain

***Abstract*—We report on the fabrication, performance and application of sensitive $YBa_2Cu_3O_7$ (YBCO) and Nb nanoSQUIDs to magnetization reversal measurements of individual magnetic nanoparticles. The YBCO SQUIDs are based on grain boundary Josephson junctions and are patterned in a single layer of epitaxially grown YBCO films by Ga focused ion beam milling. The Nb SQUIDs contain sandwich-type Josephson junctions with normal conducting HfTi barriers; they are fabricated with a multilayer technology that includes patterning by e-beam lithography and a combination of milling techniques and chemical-mechanical polishing. Due to the small inductance of the SQUID loops, ultralow white flux noise at 4.2 K can be achieved, which yields spin sensitivities of down to a few Bohr magnetons per unit bandwidth for a magnetic nanoparticle placed at 10 nm distance to the SQUID loop.**

Keywords—nanoSQUID; YBCO; Nb; focused ion beam milling; flux noise; magnetic nanoparticle

I. Introduction

Magnetic properties of micro- and nanoscale objects, are currently a topic of intensive research. Their investigation requires the development of appropriate tools, e.g. for detection of the magnetization reversal of individual magnetic nanoparticles (MNPs) [1, 2]. Promising candidates for this task are strongly miniaturized superconducting quantum interference devices (SQUIDs) – so-called nanoSQUIDs [3, 4]. The magnetization hysteresis loop of a ferromagnetic nanoparticle can be detected via the induced change of stray magnetic field coupled to a nanoSQUID by a MNP that is placed in close vicinity to the SQUID loop. The figure of merit for this kind of SQUID application is the spin sensitivity $S_\mu^{1/2}$, defined as the rms flux noise $S_\Phi^{1/2}$ of the nanoSQUID divided by the coupling factor $\phi_\mu=\Phi/\mu$ (flux Φ coupled to the SQUID per magnetic moment μ of the MNP).

B. Müller acknowledges funding by the German Academic Scholarship Foundation. J. Lin acknowledges funding by the Chinese Research Council (CRC). This work was supported by the Deutsche Forschungsgemeinschaft (DFG), via KO 1303/13-1, -2, KI 698/3-1, -2 and GO 1106/6-1, and by the COST action NANOCOHYBRI (CA 16218).

II. Device Fabrication

A. YBCO nanoSQUIDs

We fabricate devices from thin films of $YBa_2Cu_3O_7$ (YBCO), epitaxially grown by pulsed laser deposition on bicrystal $SrTiO_3$ (STO) or MgO substrates, with 24° misorientation angle of the grain boundary. The grain boundary formed in the YBCO film (typically 120 nm thick) acts as a Josephson junction [5]. Subsequently, we deposit in-situ by sputtering or electron beam evaporation 50-70 nm thick Au on top of YBCO. The Au film serves as a protection layer and for providing electrical contacts. Next, we pattern 4-8 µm wide bridges straddling the grain boundary by photolithography and Ar ion milling. As a final patterning step, we use Ga focused ion beam (FIB) milling to pattern the SQUID loop, to define the width of the grain boundary junctions and to pattern a narrow constriction (100-300 nm wide) into the SQUID loop [6-9]. The constriction in the SQUID loop provides the location of highest sensitivity to the stray field produced by a MNP placed on top of the constriction [9]. Moreover, by sending a current I_{mod} through the constriction, the flux coupled to the SQUID can be controlled and modulated. This feature can be conveniently used for on-chip flux modulation of the nanoSQUIDs and for their operation in flux-locked loop readout [8].

B. Nb nanoSQUIDs

The Nb SQUIDs are fabricated by a multilayer process, involving in-situ sputtering of a Nb/HfTi/Nb trilayer plus ex-situ sputtered SiO_2 insulating and Nb wiring layer and a combination of electron beam lithography, various etching steps and chemical-mechanical polishing. The Nb films are typically 160-200 nm thick, and the normal conducting HfTi barriers have typical thicknesses ranging from 17 to 25 nm. For

IEEE International Superconductive Electronics Conference (ISEC), Riverside, CA, USA;
published by IEEE Xplore; DOI: 10.1109/ISEC46533.2019.8990906

details of the fabrication process and superconductor-normal metal-superconductor (SNS) Josephson junction characteristics see [10-13]. The typical nanoSQUID geometry of our devices is of a microstrip-type: two Nb lines (typically 150-250 nm wide) are patterned on top of each other (separated by SiO_2) and are vertically connected by two trilayer Nb/HfTi/Nb Josephson junctions. The lateral spacing of the two junctions is a few μm down to ~100 nm, and the vertical spacing of the two Nb lines is ~200 nm; both quantities together define the size of the SQUID loop with a loop plane that is perpendicular to the substrate surface. This microstrip geometry allows us to conveniently control and modulate magnetic flux coupled to the SQUID loop via a modulation current I_{mod}, which is flowing along one of the two Nb lines [13].

III. NanoSQUID Performance

The YBCO and Nb nanoSQUIDs have nonhysteretic current-voltage characteristics (IVCs) at temperature T=4.2 K that are reasonably well described by the resistively and capacitively shunted junction model. Due to the small inductance L of the SQUID loop (in the pH range), the rms flux noise in the thermal white noise region $S_{\Phi,w}^{1/2}$ is very low – typically a few 100 $n\Phi_0/Hz^{1/2}$ (Φ_0 is the magnetic flux quantum). The lowest values obtained so far are $S_{\Phi,w}^{1/2}$=45 $n\Phi_0/Hz^{1/2}$ [8] and 110 $n\Phi_0/Hz^{1/2}$ [4] for our best YBCO and Nb nanoSQUIDs, respectively. For a MNP placed at 10 nm distance from the SQUID loop, this corresponds to spin sensitivities $S_\mu^{1/2}$~4 $\mu_B/Hz^{1/2}$ and ~10 $\mu_B/Hz^{1/2}$, respectively (μ_B is the Bohr magneton). For the determination of $S_\mu^{1/2}$, we calculate the coupling factor by numerical simulation of the supercurrents flowing in the SQUID loop, for any given planar SQUID geometry. For these simulations we use 3D-MLSI [14], a finite-element-based software, solving the London equations in 2D sheets; this takes into account the thickness of the superconducting films forming the SQUID loop and the value of the London penetration depth [4, 6, 9, 15].

The YBCO nanoSQUIDs offer the advantage of operation over a very wide temperature range, so far from 300 mK up to 80 K [9]. Moreover, due to the huge upper critical field of YBCO, these devices offer the potential for operation up to very strong magnetic fields. So far, we operated devices at 4.2 K up to 3 T, and performed flux noise measurements up to 1 T [7]. A major drawback of the YBCO nanoSQUIDs is their strong low-frequency excess noise, scaling approximately as $S_\Phi \sim 1/f$ (f is the frequency) [8]. This is due to strong critical current fluctuations, as typically observed for SQUIDs based on cuprate superconductors [16]. Moreover, $1/f$ noise may further increase upon applying strong magnetic fields, unless the entry of Abrikosov vortices can be avoided [17].

The temperature range of operation of the Nb nanoSQUIDs is much more restricted, as compared to the YBCO nanoSQUIDs. Typically our devices operate below ~6 K. Upon cooling to below 4.2 K, the devices start to develop hysteresis in their IVCs which can be attributed to Joule heating in the junctions. The temperature below which hysteresis appears increases with increasing critical current density and area of the junctions [18]. Operation in strong magnetic fields, although restricted to below ~1 T is also possible, in particular for devices with strongly reduced linewidths, for which operation up to ~0.5 T has been demonstrated [12].

The mature multilayer technology for Nb nanoSQUID fabrication offers the possibility to develop quite complex device layouts which can be used e.g. to develop gradiometric designs for operation in strong homogeneous magnetic fields. One promising approach is the development of 3D vector nanoSQUIDs that have been realized recently [19]. This device combines two orthogonal microstrip-type Nb nanoSQUIDs (loop normal along the x- and y-axis) with a gradiometric nanoSQUID with loop normal along the z-axis. For a MNP placed in the center of one of the gradiometer loops, the switching of its magnetic moment upon applying a magnetic field in z-direction can then be traced by all three orthogonal nanoSQUIDs, to record simultaneously all three vector components of the magnetic moment of the MNP. This approach shall be particularly useful for studies of the magnetic anisotropy of individual MNPs.

IV. Applications of nanoSQUIDs to Magnetization Reversal Measurements of Magnetic Nanoparticles

We have used YBCO and Nb nanoSQUIDs to perform magnetization reversal measurements of individual MNPs of different geometries: nanopillars, -disks, -wires and -tubes.

A. MNP measurements with YBCO nanoSQUIDs

A Fe nanowire, embedded in a carbon nanotube, has been placed on top of a YBCO nanoSQUID with ~300 nm distance from the SQUID loop (on the side opposite to the constriction in the loop). A magnetic field was applied along the wire axis (the easy axis of magnetization). While sweeping the magnetic field, the flux coupled to the SQUID was recorded, yielding an almost ideal rectangular-shaped magnetization hysteresis curve at 4.2 K, as expected for a single-domain state [8]. The detected flux change of ±82.5 $m\Phi_0$ in the saturated states was in very good agreement with the calculated signal (from the simulated coupling factor integrated over the volume of the Fe wire), assuming the literature value for the saturation magnetization of Fe. The observed switching field ~100 mT was ten times smaller than predicted from a simple Stoner-Wohlfarth reversal mechanism. This low switching field, however, was in very good agreement with estimates based on magnetization reversal via curling mode [8].

We note that further measurements with similar YBCO nanoSQUIDs have been performed on Co nanowires grown by focused-electron-beam-induced deposition (FEBID), as reported in [20]. In this case, the nanowires were suspended above the nanoSQUIDs. These measurements clearly showed improved performance of the nanowires that had been annealed after FEBID growth [21].

In a further series of measurements, we have demonstrated the benefit of using YBCO nanoSQUIDs for MNP measurements over a wide temperature range [9]. In this case, Co nanopillars and nanodisks were grown by FEBID directly on top of the constriction in the SQUID loop. For the Co MNPs that revealed single-domain states, we recorded hysteresis loops from 300 mK up to 80 K. The observed T-dependence of the switching fields was shown to be in very good agreement

with predictions from a model for thermally induced magnetization reversal [9].

B. MNP measurements with Nb nanoSQUIDs

Nb nanoSQUIDs have been integrated into the torque magnetometer setup of the Poggio group at Univ. Basel to investigate individual Ni, permalloy and CoFeB nanotubes. The combined system enables simultaneous measurements of the integral magnetization by dynamic cantilever torque magnetometry and local magnetization by nanoSQUID magnetometry [13]. Combined torque and SQUID measurements on individual Ni nanotubes, supported by micromagnetic simulations of magnetization configurations, suggest reversal via the formation of vortexlike states within the nanotube [22]. Such stray-field free states can have applications for memory and noninvasive sensing.

CONCLUSIONS AND OUTLOOK

YBCO and Nb nanoSQUIDs have been developed for the investigation of magnetization reversal of individual magnetic nanoparticles. Very small SQUID inductances enable the realization of ultralow flux noise of the nanoSQUIDs in the thermal white noise limit. For MNPs placed in 10 nm distance to the SQUID loop, this translates into spin sensitivities down to only a few Bohr magnetons per unit bandwidth, which is appropriate for many studies on individual MNPs. Apart from further suppression of $1/f$ noise, a key challenge is the development of reliable routines for placing MNPs in a controlled way in close vicinity to the nanoSQUIDs, ideally at variable position and temperature. For YBCO nanoSQUIDs, the recently developed creation of Josephson junctions and SQUIDs by focused He ion irradiation [23, 24] can provide new perspectives for creating advanced nanoscale devices

REFERENCES

[1] W. Wernsdorfer, K. Hasselbach, D. Mailly, B. Barbara, A. Benoit, L. Thomas, and G. Suran, "DC-SQUID magnetization measurements of single magnetic particles," J. Magn. Magn. Mater., vol. 145, pp. 33-39, 1995.

[2] W. Wernsdorfer, "Classical and quantum magnetization reversal studied in nanometersized particles and clusters," Adv. Chem. Phys., vol. 118, pp. 99-190, 2001.

[3] C. Granata, and A. Vettoliere, "Nano superconducting quantum interference device: A powerful tool for nanoscale investigations," Phys. Rep., vol. 614, pp. 1-69, 2016.

[4] M. J. Martínez-Pérez, and D. Koelle, "NanoSQUIDs: Basics & recent advances," Phys. Sci. Rev., vol. 2, 20175001, 2017.

[5] H. Hilgenkamp, and J. Mannhart, "Grain boundaries in high-T_c superconductors," Rev. Mod. Phys., vol. 74, pp. 485-549, 2002.

[6] J. Nagel, K. B. Konovalenko, M. Kemmler, M. Turad, R. Werner, E. Kleisz, S. Menzel, R. Klingeler, B. Büchner, R. Kleiner, and D. Koelle, "Resistively shunted $YBa_2Cu_3O_7$ grain boundary junctions and low-noise SQUIDs patterned by a focused ion beam down to 80 nm linewidth," Supercond. Sci. Technol., vol. 24, 015015, 2011.

[7] T. Schwarz, J. Nagel, R. Wölbing, M. Kemmler, R. Kleiner, and D. Koelle, "Low-noise superconducting quantum interference device operating in tesla magnetic fields," ACS Nano, vol. 7, pp. 844-850, 2013.

[8] T. Schwarz, R. Wölbing, C. F. Reiche, B. Müller, M. J. Martínez-Pérez, T. Mühl, B. Büchner, R. Kleiner and D. Koelle, "Low-noise $YBa_2Cu_3O_7$ nano-SQUIDs for performing magnetization reversal measurements on magnetic nanoparticles," Phys. Rev. Applied, vol. 3, 044001, 2015.

[9] M. J. Martínez-Pérez, B. Müller, D. Korinski, R. Kleiner, J. Sesé, and D. Koelle, "NanoSQUID magnetometry of individual cobalt nanoparticles grown by focused electron beam induced deposition," Supercond. Sci. Technol., vol. 30, 024003, 2017.

[10] D. Hagedorn, O. Kieler, R. Dolata, R. Behr, F. Müller, J. Kohlmann, and J. Niemeyer, "Modified fabrication of planar sub-µm superconductor–normal metal–superconductor Josephson junctions for use in a Josephson arbitrary waveform synthesizer," Supercond. Sci. Technol., vol. 19, pp. 294-298, 2006.

[11] J. Nagel, O. F. Kieler, T. Weimann, R. Wölbing, J. Kohlmann, A. B. Zorin, R. Kleiner, D. Koelle, and M. Kemmler, "Superconducting quantum interference devices with submicron Nb/HfTi/Nb junctions for investigation of small magnetic particles," Appl. Phys. Lett., vol. 99, 032506, 2011.

[12] R. Wölbing, J. Nagel, T. Schwarz, O. Kieler, T. Weimann, J. Kohlmann, A. B. Zorin, M. Kemmler, R. Kleiner, and D. Koelle, "Nb nano superconducting quantum interference devices with high spin sensitivity for operation in magnetic fields up to 0.5 T," Appl. Phys. Lett., vol. 102, 192601, 2013.

[13] J. Nagel *et al.*, "Nanoscale multifunctional sensor formed by a Ni nanotube and a scanning Nb nanoSQUID," Phys. Rev. B, vol. 88, 064425, 2013.

[14] M. M. Khapaev, M. Yu. Kupriyanov, E. Goldobin, and M Siegel, "Current distribution simulation for superconducting multi-layered structures," Supercond. Sci. Technol., vol. 16, pp. 24-27, 2003.

[15] R. Wölbing, T. Schwarz, B. Müller, J. Nagel, M. Kemmler, R. Kleiner, and D. Koelle, "Optimizing the spin sensitivity of grain boundary junction nanoSQUIDs—towards detection of small spin systems with single-spin resolution," Supercond. Sci. Technol., vol. 27, 125007, 2014.

[16] D. Koelle, R. Kleiner, F. Ludwig, E. Dantsker, and J. Clarke, "High-transition-temperature superconducting quantum interference devices," Rev. Mod. Phys., vol. 71, pp. 631-686, 1999.

[17] A. H. Miklich, D. Koelle, T. J. Shaw, F. Ludwig, D. T. Nemeth, E. Dantsker, J. Clarke, N. McN Alford, and T. W. Button, "Low-frequency excess noise in $YBa_2Cu_3O_{7-x}$ dc superconducting quantum interference devices cooled in static magnetic fields," Appl. Phys. Lett., vol. 64, pp. 3494-3496, 1994.

[18] V. Morosh *et al.*, "Transport and noise properties of sub-100 nm planar Josephson junctions with metallic barrier for nanoSQUID applications," unpublished.

[19] M. J. Martínez-Pérez, D. Gella, B. Müller, V. Morosh, R. Wölbing, J. Sesé, O. Kieler, R. Kleiner, and D. Koelle, "Three-axis vector vector nano superconducting quantum interference device," ACS Nano, vol. 10, pp. 8308-8315, 2016.

[20] M. J. Martínez-Pérez, J. Pablo-Navarro, B. Müller, R. Kleiner, C. Magén, D. Koelle, J. M. de Teresa, and J. Sesé, "NanoSQUID magnetometry on individual as-grown and annealed Co nanowires at variable temperature," Nano Lett., vol. 18, 7674-7682, 2018.

[21] J. Pablo-Navarro, C. Magén, and J. M. de Teresa, "Purified and crystalline three-dimensional electron-beam-induced deposits: The successful case of cobalt for high performance magnetic nanowires," ACS Appl. Nano Mater., vol. 1, pp. 38-46, 2018.

[22] A. Buchter *et al.*, "Reversal mechanism of an individual Ni nanotube simultaneously studied by torque and SQUID magnetometry," Phys. Rev. Lett., vol. 111, 067202, 2013.

[23] S. A. Cybart, E. Y. Cho, J. T. Wong, B. H. Wehlin, M. K. Ma, C. Huynh, and R. C. Dynes, "Nano Josephson superconducting tunnel junctions in $YBa_2Cu_3O_{7-\delta}$ directly patterned with a focused helium ion beam," Nature Nanotechnol., vol. 10, pp. 598-602, 2015.

[24] B. Müller, M. Karrer, F. Limberger, M. Becker, B. Schröppel, C. J. Burkhadt, R. Kleiner, E. Goldobin, and D. Koelle, "Josephson junctions and SQUIDs created by focused helium-ion-beam irradiation of $YBa_2Cu_3O_7$," Phys. Rev. Applied, vol. 11, 044082, 2019.